Distribution Agreement

In presenting this thesis or dissertation as a partial fulfillment of the requirements for an advanced degree from Emory University, I hereby grant to Emory University and its agents the non-exclusive license to archive, make accessible, and display my thesis or dissertation in whole or in part in all forms of media, now or hereafter known, including display on the world wide web. I understand that I may select some access restrictions as part of the online submission of this thesis or dissertation. I retain all ownership rights to the copyright of the thesis or dissertation. I also retain the right to use in future works (such as articles or books) all or part of this thesis or dissertation.

Signature:

______________________________ _______________

Matthew B. Jones Date

Coordination Mode Versatility and Intramolecular Bond Activation in Metal Complexes Supported by a Family of Tripodal Tris(amidato)amine Ligands

By

Matthew B. Jones
Doctor of Philosophy

Chemistry

____
Dr. Cora E. MacBeth, Ph.D.
Advisor

____
Dr. Craig L. Hill, Ph.D.
Committee Member

____
Dr. Vincent P. Conticello, Ph.D.
Committee Member

Accepted:

____
Lisa A. Tedesco, Ph.D.
Dean of the James T. Laney School of Graduate Studies

____
Date

Coordination Mode Versatility and Intramolecular Bond Activation in Metal Complexes Supported by a Family of Tripodal Tris(amidato)amine Ligands

By

Matthew B. Jones
B.S., Butler University, 2005

Advisor: Cora E. MacBeth, Ph.D.

An abstract of
A dissertation submitted to the Faculty of the
James T. Laney School of Graduate Studies of Emory University
in partial fulfillment of the requirements for the degree of
Doctor of Philosophy
in Chemistry
2010

Abstract

Coordination Mode Versatility and Intramolecular Bond Activation in Metal Complexes Supported by a Family of Tripodal Tris(amidato)amine Ligands

By Matthew B. Jones

In the first part of this dissertation, the synthesis and coordination chemistry of a tris(amidato)amine ligand scaffold is discussed. The amidate acyl substituents can act as regulatory elements to control access to the open coordination site on metal complexes of the ligand. This control is found to have both a steric and electrostatic component, depending on the identity of the acyl substituent. Variation of these acyl substituents can have an effect on both the coordination number and primary coordination sphere of the resultant complexes. The ambidentate nature of the amidate substituents makes this ligand scaffold applicable for binding a variety of metal ions (Co, Ni, Al). The synthetic, spectral, and structural details of a variety of metal complexes supported by these ligands are discussed, and the ability of some of these complexes to bind exogenous anions is detailed.

The second part of this work describes the reactivity of cobalt and iron complex of these ligands towards intramolecular bond activation. It is found that C–H bonds in the ligand acyl substituents can act as traps for high-valent metal-based oxidants. While the cobalt reaction can only be accomplished with the help of a strong oxidant, the C–H bond activation with iron is found to proceed with dioxygen, as confirmed by labeling studies. The similarity between the reactions using the differing oxidants implies that the C–H activation likely proceeds via some Fe–oxo adduct in both cases. When the acyl substituents of the ligands are replaced with perfluoroaryl groups, the iron complex is shown to activate intramolecular C–F bonds instead. This reaction is also shown to proceed in the presence of dioxygen as the terminal oxidant/*O*-atom source.

Coordination Mode Versatility and Intramolecular Bond Activation in Metal Complexes Supported by a Family of Tripodal Tris(amidato)amine Ligands

By

Matthew B. Jones
B.S., Butler University, 2005

Advisor: Cora E. MacBeth, Ph.D.

A dissertation submitted to the Faculty of the
James T. Laney School of Graduate Studies of Emory University
in partial fulfillment of the requirements for the degree of
Doctor of Philosophy
in Chemistry
2010

Acknowledgements

First and foremost, I want to express my gratitude to Dr. Cora MacBeth. From the moment I first began work in the MacBeth group, I found her energy and passion for chemistry inspiring. Her dedication and persistent guidance have not only taught me how to think like a scientist but have also nurtured and grown my passion for research. Even when I felt like I was just spinning my tires in lab, she kept me on my toes without seeming unsupportive, and that kept me optimistic through those tough times. I'm sure that our professional relationship will endure, and I look forward to future advice and maybe even future collaboration!

I also have to thank my committee members, Dr. Craig Hill and Dr. Vince Conticello. Their helpful advice and discussions have been instrumental in my progress towards this degree.

It is important to me that I recognize those influential in sparking my interest in chemistry. First, I have to thank the Belgian artist Peyo for creating the Smurfs. The antagonist, an evil sorcerer named Gargamel, always had complex networks of glassware filled with multi-colored liquids. I was intrigued at an early age by the purpose of these liquids and the mechanics behind his apparatuses. On a more realistic level, Mr. Wizard is responsible for my first exposure to actual chemistry, but the Smurfs gave me the first taste of the field I now love.

My high school chemistry teacher, Dr. Joseph Shane, was an important influence in my decision to pursue chemistry as my major in college, and I thank him for that. His Chemistry 2 class was an exercise in independent thought and experimental design, that while basic in its goals, gave me a real taste of what being a scientist really was. He was very passionate about teaching, and he did an amazing job showing high school students how wonderful chemistry was.

At Butler University, I had several professors that had a huge influence on helping me figure out what kind of chemist I wanted to be. Dr. Anne Wilson was my thesis advisor, and she gave me my first research experience. She allowed me to be very independent, and I learned a huge amount about laboratory technique from her. I also wanted to thank her for showing me the close relationship between synthetic chemistry and cooking. It's also important that I thank Dr. Stacy O'Reilly. First, I want to thank her for telling me not to pursue medical school and go to graduate school instead. Secondly, she is responsible for my interest in Inorganic Chemistry. Her Advanced Inorganic Chemistry class was life changing, to say the least.

I also need to acknowledge the MacBeth group, both current and former members, for all your support and helpful discussions during the course of my degree. Graduate school would have been miserable without your friendship. The current group: Omar Villanueva, Kelly Kluge, and Dr. Savita Sharma are all wonderful scientific minds, and I can always rely on them for helpful feedback. I look forward to seeing all the wonderful things they accomplish. I also need to thank former members: Lei Chu, Dr. Sheri Lense, and Dr. Emma Brown. You all helped start the MacBeth group, and I'll always be happy to have been a part of that with you. I also need to thank all the undergrads that I've worked with, especially Alex Rudd and Zoey Herm. The two of them made working late nights in the lab very entertaining, and I'm glad they both found themselves pursuing doctoral degrees as well.

Last, but certainly not least, I want to thank my family and my fiancée. My parents, Brad and Paula Jones, have always been supportive of every decision I've made, even though those decisions have kept in school for over 20 years. They are the hardest working, most loving people I know, and even as an adult I aspire to be more like them. Needless to say, I'd be nowhere without them. I also want to thank my brother, Jason. There's never been a more kind-hearted, genuine person, and I'm lucky to be able to call him brother. The final thanks goes to my fiancée, Rebecca Allen. For almost two years, she has been the most supportive and loving significant other anyone could ask for. She has put up with more from me in the course of writing this dissertation than anyone should be expected to, and I'll be happy spending the rest of my life making it up to her.

Table of Contents

Part I. Introduction 1

Chapter 1 : Bioinspired Ligand Design for Promoting New Modes of Base Metal Reactivity 1

Section 1-1. Bioinorganic Chemistry 1

Section 1-2. Iron in Base Metal Catalysis 5

Section 1-3. Amidate Ligands in Nature and in Synthetic Complexes 11

Section 1-4. Tripodal, Tetradentate Ligands 17

Section 1-5. Ligand Design 20

Section 1-6. Overview of this Dissertation 22

Part II. Coordination Chemistry of Metal Complexes Supported by a Tris(amidato)amine Ligand Scaffold 24

Chapter 2 : Tripodal Phenylamine-based Ligands and Their Cobalt(II) Complexes 24

Section 2-1. Introduction 24

Section 2-2. Results and Discussion 28

Section 2-3. Experimental 53

Chapter 3: Chelating Tris(amidate) Ligands: Versatile Scaffolds for Nickel(II) 67

Section 3-1. Introduction 67

Section 3-2. Results and Discussion 72

Section 3-3. Experimental 99

Chapter 4: Synthetic, Spectral, and Structural Studies of Mononuclear Tris(κ^2-amidate) Aluminum Complexes Supported by Tripodal Ligands 109

Section 4-1. Introduction 109

Section 4-2. Results and Discussion 115

Section 4-3. Experimental 124

Part III. Intramolecular Bond Activation by Cobalt and Iron Complexes Supported by a Tris(amidato)amine Ligand Scaffold 129

Chapter 5: The Intramolecular Activation of C-H Bonds by Cobalt and Iron Complexes Supported by a Trianionic, Tripodal Ligand 129

Section 5-1. Introduction 129

Section 5-2. Results and Discussion 138

Section 5-3. Experimental 162

Chapter 6: Facile C-F Bond Activation by Fe(II) Complexes Using Dioxygen as Terminal Oxidant and Oxygen Atom Source 171

Section 6-1. Introduction 171

Section 6-2. Results and Discussion 176

Section 6-3. Experimental 202

References 211

Table of Figures

Figure 1-1. Active site of methane monooxygenase (left) and a biomimetic complex (right) from Lippard et al.[3] 3

Figure 1-2. Ligand design from Borovik, et al. (left) inspired by the active site of cytochrome P450 (right).[7] 4

Figure 1-3. Side by side comparison of Casey and coworkers' Fe-based C=O reduction catalyst (left) and the well-known Shvo catalyst (right).[15] 7

Figure 1-4. Dihydroxylation catalyst designed by Que et al.[34-36] 9

Figure 1-5. Active sites of lipoxygenase (left) and isopenicillin N synthase (right) featuring a 2-His-1-carboxylate facial triad.[47, 48] 11

Figure 1-6. Active site of Fe-containing nitrile hydratase. 13

Figure 1-7. Active sites of acetyl-CoA synthase (left) and Ni-containing superoxide dismutase (right). 14

Figure 1-8. Binding modes of amidate ligands. 15

Figure 1-9. Examples of amidate-containing macrocycles used by Kimura and coworkers.[67] 16

Figure 1-10. Representative current generation TAML catalyst from the Collins group. 17

Figure 1-11. Diagram of tetradentate tripodal ligands, showing the constituent parts: (A) tertiary donor, (B) carbon spacers, (C) terminal donors, (D) terminal substituents. 18

Figure 1-12. Generalized binding mode for a tripodal tetradentate ligand. 19

Figure 1-13. Comparison of the tren and [N(*o*-PhNH$_2$)$_3$] ligand scaffolds. 20

Figure 2-1. General structure and binding mode of tetradentate tripodal ligands. 24

Figure 2-2. The tren ligand scaffold (left) and our tris(2-aminophenyl)amine ligand framework (right). 27

Figure 2-3. Solid-state structure of [Co(κ^1-L^{NH2})$_2$(DMF)$_2$(Br)$_2$]. Hydrogen atoms are omitted for clarity. Thermal ellipsoids shown at 50% probability. 31

Figure 2-4. Solid-state structure of [Co(L^{NH2})Br]BPh_4. Hydrogen atoms and counterion are omitted for clarity. Thermal ellipsoids shown at 40% probability. 32

Figure 2-5. Solid-state structure of Et_4N[Co(L^{iPr})]. Counterion and hydrogen atoms omitted for clarity. Thermal ellipsoids shown at 50% probability. 35

Figure 2-6. Job's plot produced by the continuous variation method for the titration of Et_4N[Co(L^{iPr})] with Et_4NCN. The total concentration of the two species was held constant at 4.04 mM (DMF). 38

Figure 2-7. Titration data for CN^- binding to Et_4N[Co(L^{iPr})] 38

Figure 2-8. Cyclic voltammogram of $(Et_4N)_3$[(Co(L^{iPr}))$_2$(μ-CN)]. 39

Figure 2-9. Solid-state structure of $(Et_4N)_3$[(Co(L^{iPr}))$_2$(μ-1,2-CN)]. Counterions and hydrogen atoms omitted for clarity. Thermal ellipsoids shown at 50% probability. 40

Figure 2-10. Solid-state structure of $(Et_4N)_3$[(Co(L^{iPr}))$_2$(μ-1,3-N_3)]. Counterions and hydrogen atoms omitted for clarity. Thermal ellipsoids shown at 50% probability. 42

Figure 2-11. Solid-state structure of Ph_4P[Co(L^{Ph})(MeCN)]. Counterion and hydrogen atoms removed for clarity. Thermal ellipsoids are shown at 30% probability. ... 45

Figure 2-12. Solid-state structure of $Ph_4P[Co(L^{Ph})]$. Counterion and hydrogen atoms omitted for clarity. Thermal ellipsoids shown at 50% probability. 48

Figure 2-13. Solid-state structure of $Ph_4P[Co(L^{Ph})(CNtBu)]$. Counterion and hydrogen atoms omitted for clarity. Thermal ellipsoids shown at 50% probability........... 51

Figure 3-1. The active sites of acetyl-CoA (left) and Ni-containing SOD (right) 68

Figure 3-2. Representative nickel complexes supported by a N_2S_2-type ligand scaffold. 69

Figure 3-3. The possible binding modes of amidate ligands. 72

Figure 3-4. Solid-state structure of $Ph_4P[Ni(L^{iPr})]$. Counterion and hydrogen atoms have been omitted for clarity. Thermal ellipsoids are shown at 50% probability....... 75

Figure 3-5. Solid-state structure for $Ph_4P[Ni(L^{tBu})]$. Counterion and hydrogen atoms have been omitted for clarity. Thermal ellipsoids are shown at 50% probability. 77

Figure 3-6. Solid-state structure of $Ph_4P[Ni(L^{Ph})(MeCN)]$. Counterion and hydrogen atoms have been omitted for clarity. Thermal ellipsoids are shown at 50% probability.. 78

Figure 3-7. Cyclic voltammogram (0.1 V/s) of $[Ni(L^{iPr})]^{-}$ at a glassy carbon electrode in DMF (298 K) with 0.2 M $TBAPF_6$ as supporting electrolyte. 81

Figure 3-8. Solid-state structure of the two crystallographically independent molecules in the unit cell of $(Et_4N)_2[Ni(L^{iPr})(CN)]$. Counterions and hydrogen atoms are omitted for clarity. Thermal ellipsoids are shown at 50% probability. 84

Figure 3-9. Cyclic voltammogram (0.05 V/s) of $[Ni(L^{iPr})(CN)]^{2-}$ at a glassy carbon electrode in DMF (298 K) with 0.2 M $TBAPF_6$ as supporting electrolyte. 86

Figure 3-10. Temperature dependence of magnetic susceptibility for $(Et_4N)_2[Ni(L^{iPr})(CN)]$ obtained at a measuring field of 0.1 T. The red line indicates the best fit. Inset: Magnetization of $(Et_4N)_2[Ni(L^{iPr})(CN)]$ as a function of reduced magnetic field.. 88

Figure 3-11. Temperature dependence of magnetic susceptibility for $Ph_4P[Ni(L^{iPr})]$ obtained at a measuring field of 0.1 T. The red line indicates the best fit. Inset: Magnetization of $Ph_4P[Ni(L^{iPr})]$ as a function of reduced magnetic field............ 89

Figure 3-12. Solid-state structure of $(Et_3N)_3[CoNi(L^{iPr})_2(\mu_2\text{-}CN)]$ (top) and the primary coordination sphere of $(Et_3N)_3[CoNi(L^{iPr})_2(\mu_2\text{-}CN)]$ (bottom). Counterions and hydrogen atoms are removed for clarity. Thermal ellipsoids are shown at 30% probability. 92

Figure 3-13. Temperature dependence of magnetic susceptibility for $(Et_3N)_3[CoNi(L^{iPr})_2(\mu_2\text{-}CN)]$ obtained at a measuring field of 0.1 T. The red line indicates the best fit. Inset: Magnetization of $(Et_3N)_3[CoNi(L^{iPr})_2(\mu_2\text{-}CN)]$ as a function of reduced magnetic field. 95

Figure 3-14. Low temperature expansion of magnetic susceptibility of $[Et_4N]_3[CoNi(L^{iPr})_2(\mu_2\text{-}CN)]$ collected at various fields.................................... 97

Figure 3-15. Fits of the susceptibility data for $(Et_3N)_3[CoNi(L^{iPr})_2(\mu_2\text{-}CN)]$ with *D* fixed (top) and with *D* allowed to refine freely (bottom)... 98

Figure 4-1. Possible coordination modes for amidate $[(RNC(O)R')]^-$ ligands............ 109

Figure 4-2. Ni(II) complex of the ligand $[(L^{tBu})]^{3-}$, featuring an *O*-amidate ligand...... 110

Figure 4-3. Structurally characterized mononuclear Al(III) *O*-amidate from Kakudo, et al.[204] 111

Figure 4-4. ^{13}C NMR study of the titration of *N*-benzylcarboxamide into a toluene-d_8 solution of ($Al_2(NMe_2)_6$). (Reprinted with permission from Hoerter, et al., JACS 2006).[208] 113

Figure 4-5. ^{27}Al NMR spectra of [Al(L^{iPr})]and [Al(L^{tBu})] in $CDCl_3$ referenced against an external $Al(NO_3)_3$ standard. The broad peaks at 57-58 ppm are due to background from the aluminum incorporated into the probe. 117

Figure 4-6. Solid-state structure of [Al(L^{iPr})]. Hydrogen atoms are removed for clarity. Thermal ellipsoids are shown at 50% probability 119

Figure 4-7. Solid-state structure of [Al(L^{tBu})]. Hydrogen atoms are removed for clarity. Thermal ellipsoids are shown at 50% probability 120

Figure 4-8. Illustration of the dihedral angle (trigonal twist angle ϕ) between the vertices of the triangles formed in the trigonal planes of the *O*-amidate (red) and *N*-amidate (blue) donors. 121

Figure 5-1. Comparison of mechanisms of dioxygen activation by mono- and dinuclear iron oxygenases 130

Figure 5-2. Active site of an α-keto-acid-dependent enzyme featuring the 2-His-1-carboxylate facial triad 131

Figure 5-3. Active sites of diiron oxygenases MMOH (left) and R2 (right). 132

Figure 5-4. Solid-state structure of [Co(L^{iPr})]$^-$, indicating the short distance between the cobalt center and the methine hydrogen atoms. 136

Figure 5-5. Solid-state structure of Et_4N[Co(L^{Mod})]. Counterion and hydrogen atoms are removed for clarity. Thermal ellipsoids are shown at 30% probability 139

Figure 5-6. Solid-state structure of $K(Ph_4P)[Fe(L^{iPr})]_2$. Counterions and hydrogen atoms are omitted for clarity. Thermal ellipsoids are shown at 30% probability......... 143

Figure 5-7. Example of windmill-type, dicarboxylate-bridged complex from the Lippard group.[227] 144

Figure 5-8. Cyclic voltammogram of cyanide adduct of $K(Ph_4P)[Fe(L^{iPr})]_2$ (DMF, 0.100 V/s).. 145

Figure 5-9. Solid-state structure of $K_2[Zn(L^{iPr})]_2$. Counterions and hydrogen atoms are omitted for clarity. Thermal ellipsoids are shown at 30% probability. 147

Figure 5-10. Solid-state structure of $Ph_4P[Fe(L^{Mod})]$. Counterion and hydrogen atoms have been removed for clarity. Thermal ellipsoids are shown at 50% probability. 150

Figure 5-11. Cyclic votammogram of $Ph_4P[FeL^{Mod}]$ recorded at 100 mV/s. 152

Figure 5-12. HRESI-MS spectra showing $[Fe(L^{Mod})]^-$ made using $^{16}O_2$ (top) and ^{18}O-labeled O_2 (bottom).. 154

Figure 5-13. Solid-state structure of $Ph_4P[Fe(L^{Ph})(MeCN)]$. Counterion and hydrogen atoms have been removed for clarity. Thermal ellipsoids are shown at 50% probability... 158

Figure 5-14. Cyclic votammogram of the cyanide adduct of $Ph_4P[(Fe(L^{Ph}))(MeCN)]$ in DMF, recorded at 0.050 V/s. 160

Figure 6-1. Rhodium half-sandwich complex from Jones, et al. shown to attack aryl C–F bonds.[258] 172

Figure 6-2. Proposed size-selective C–H hydroxylation reaction (see chapter 5 for detailed explanation. 177

Figure 6-3. Solid-state structure of K[Fe(L^{C6F5})(MeCN)]. Hydrogen atoms and counterion have been omitted for clarity. Thermal ellipsoids shown at 50% probability. 179

Figure 6-4. Cyclic voltammogram of cyanide adduct, [Fe(L^{C6F5})(CN)]$^{2-}$, recorded at 0.1 V/s. 181

Figure 6-5. Solid-state structure of K[Fe(L^{Mod})]. Hydrogen atoms and counterion have been omitted for clarity. Thermal ellipsoids shown at 30% probability. 183

Figure 6-6. UV-Vis absorption data for K[Fe(L^{Mod})] (3.50 x 10^{-5} M in MeCN). 184

Figure 6-7. Overlay of FTIR region showing aryloxide ν(C-O) stretches. 185

Figure 6-8. Cyclic voltammogram of K[Fe(L^{Mod})] recorded at 10 mV/s. 186

Figure 6-9. Solid-state structure of $(Et_4N)_2$[Fe(L^{Mod})]. Counterions and hydrogen atoms are omitted for clarity. Thermal ellipsoids are shown at 40% probability 190

Figure 6-10. Cyclic voltammogram of $(Et_4N)_2$[Fe(L^{Mod})] recorded in DMF (0.2 M $TBAPF_6$) at 0.1 V/s. 192

Figure 6-11. HRESI-MS spectra showing [Fe(L^{Mod})]$^-$ made using $^{16}O_2$ (top) and ^{18}O-labeled O_2 (bottom). 194

Figure 6-12. Solid-state structure of K[Fe(L^{C3F7})(MeCN)]. Counterion and hydrogen atoms are omitted for clarity. Thermal ellipsoids are shown at 40% probability. 199

Figure 6-13. Cyclic voltammogram of K[Fe(L^{C3F7})(MeCN)] recorded in DMF (0.2 M $TBAPF_6$) at 0.1 V/s. 201

Table of Schemes

Scheme 1-1. Fe-catalyzed alkene hydrogenation from Chirik and coworkers.[11-14] 6

Scheme 1-2. The enantioselective transfer hydrogenation reaction from Morris and coworkers.[17] 8

Scheme 1-3. Fe-catalyzed cross-coupling reaction from Bolm and coworkers.[38, 39] 10

Scheme 1-4. General method for creating tris(amide)amines with varied acyl substituents 21

Scheme 2-1. Work from the Schrock lab utilizing tripodal tris(amido)amine ligands. Formation of a stable Fe(IV) cyanide adduct (top) and the molybdenum-mediated reduction of dinitrogen to ammonia (bottom) 25

Scheme 2-2. Notable examples of tris(ureato)amine complexes from the Borovik group. The support of late, first row transition metals in a coordinatively unsaturated geometry (top), and stabilization of an Fe(III) oxo unit through hydrogen bonding (bottom) 26

Scheme 2-3. Synthesis of the triamidoamine (H_3L^R) ligand scaffold 29

Scheme 2-4. Synthesis of $Et_4N[Co(L^{iPr})]$ 34

Scheme 2-5. Synthesis of terminal cyanide adduct, $(Et_4N)_2[Co(L^{iPr})(CN)]$. 37

Scheme 2-6. Synthesis of $Ph_4P[Co(L^{Ph})(MeCN)]$ 44

Scheme 2-7. Synthesis of trigonal monopyramidal $Ph_4P[Co(L^{Ph})]$. 47

Scheme 2-8. Synthesis of $Ph_4P[Co(L^{Ph})(CNtBu)]$. 50

Scheme 3-1. A functional model for glyoxalase I isomerization activity for Berreau, et al.[148] 71

Scheme 3-2. Generalized route to Ni(II) complexes of the H_3L^R ligand (R = iPr, tBu, Ph). 73

Scheme 3-3. Synthesis of cyanide adduct, $(Et_4N)_2[Ni(L^{iPr})(CN)]$. 82

Scheme 3-4. Synthesis of heterobimetallic cyanide adduct, $(Et_3N)_3[CoNi(L^{iPr})_2(\mu_2\text{-}CN)]$. 91

Scheme 4-1. Generalized scheme for Stahl's transamidation reaction (top) and the proposed active catalyst (bottom). 112

Scheme 4-2. Synthesis of the Al(III) complexes, $[Al(L^{iPr})]$ (top) and $[Al(L^{tBu})]$ (bottom), using two different synthetic routes. 116

Scheme 5-1. Pathways proposed by Nam, et al. in the activation of O_2 by $[Fe^{II}(TMC)]^{2+}$. 133

Scheme 5-2. Intramolecular C–H activation by a carboxylate-bridged diiron(II) complex studied by Lippard, et al 135

Scheme 5-3. Proposed size-selective C–H bond activation strategy based on the $[(L^R)]^{3-}$ ligand scaffold 137

Scheme 5-4. Synthesis of the hydroxylated complex $Et_4N[Co(L^{Mod})]$. 138

Scheme 5-5. Intramolecular hydroxylation of $[Tp^{tBu,Me}Co(H)]$ by O_2. Adapted from Theopold et al.[244] 141

Scheme 5-6. Synthesis of the bridged-amidate complex $K(Ph_4P)[Fe(L^{iPr})]_2$. 142

Scheme 5-7. Synthesis of the dimeric zinc complex, $K_2[Zn(L^{iPr})]_2$. 146

Scheme 5-8. Synthesis of the hydroxylated Fe(III) complex, $Ph_4P[Fe(L^{Mod})]$. 149

Scheme 5-9. Synthesis of $Ph_4P[Fe(L^{Mod})]$ using dioxygen as the oxidant. 153

Scheme 5-10. Proposed mechanism for the oxidation of C–H bonds by $[Fe(L^{iPr})]_2^{2-}$ using either O_2 or PhIO as the terminal oxidant and *O*-atom source........................... 156

Scheme 5-11. Synthesis of five-coordinate Fe(II) adduct, $Ph_4P[Fe(L^{Ph})(MeCN)]$........ 157

Scheme 6-1. Known organometallic pathways of metal-mediated C–F cleavage (L = H, R_3Si)... 171

Scheme 6-2. Representative C–F hydroxylation reaction from Stammler, et al.[259]....... 173

Scheme 6-3. C–F cleavage by Fe(II) half-sandwich complex, $[CpFe(Me)(CO)_2]$, reported by Green and coworkers.[277] 175

Scheme 6-4. Synthesis of $K[Fe(L^{C6F5})(MeCN)]$... 178

Scheme 6-5. Synthesis of Fe(III) phenoxide, $K[Fe(L^{Mod})]$.. 182

Scheme 6-6. Synthesis of $Me_4N[Fe(L^{C6F5})(F)]$.. 187

Scheme 6-7. Synthesis of $(Et_4N)_2[Fe(L^{Mod})]$.. 188

Scheme 6-8. Proposed mechanism for C–F hydroxylation by Fe(II)-hydroxide adduct. 189

Scheme 6-9. Synthesis of $K[Fe(L^{Mod})]$ using dioxygen as the oxidant/*O*-atom source. 193

Scheme 6-10. Mechanisms of C-F activation that have been disproven...................... 196

Scheme 6-11. Proposed dinuclear mechanism of C-F activation................................ 197

Scheme 6-12. Synthesis of Fe(II) complex, $K[Fe(L^{C3F7})(MeCN)]$.............................. 198

List of Tables

Table 2-1. Tabulated bond lengths for $[Co(\kappa^1\text{-}L^{NH2})(DMF)_2(Br)_2]$ and $[Co(L^{NH2})Br]BPh_4$ 33

Table 2-2. Selected metrical parameters for $Et_4N[Co(L^{iPr})]$, $(Et_4N)_3[(Co(L^{iPr}))_2(\mu\text{-}1,2\text{-}CN)]$, and $(Et_4N)_3[(Co(L^{iPr}))_2(\mu\text{-}1,3\text{-}N_3)]$. 43

Table 2-3. Selected metrical parameters for $Ph_4P[Co(L^{Ph})(MeCN)]$, $Ph_4P[Co(L^{Ph})]$, and $Ph_4P[Co(L^{Ph})(CNtBu)]$. 52

Table 2-4. Crystal data and structure refinement for solid-state structures. 64

Table 3-1. Selected metrical parameters for $Ph_4P[Ni(L^{iPr})]$, $Ph_4P[Ni(L^{tBu})]$, and $Ph_4P[Ni(L^{Ph})(MeCN)]$ 79

Table 3-2. Selected metrical parameters for the two geometrical isomers of $[Ni(L^{iPr})(CN)]^{2-}$ 85

Table 3-3. Selected metrical parameters for the two metal ions in $[CoNi(L^{iPr})_2(\mu_2\text{-}CN)]^{3-}$ 94

Table 3-4. Crystal data and structure refinement for solid-state structures. 106

Table 4-1. Selected average bond lengths (Å), angles (°), and metrical parameters for $[Al(L^{iPr})]$ and $[Al(L^{tBu})]$. 122

Table 4-2. Crystal data and structure refinement for solid-state structures. 128

Table 5-1. Selected metrical parameters for $Et_4N[Co(L^{Mod})]$. 140

Table 5-2. Selected metrical parameters for $K(Ph_4P)[Fe(L^{iPr})]_2$ and $K_2[Zn(L^{iPr})]_2$. 148

Table 5-3. Comparison of selected metrical parameters for $Et_4N[Co(L^{Mod})]$ and $Ph_4P[Fe(L^{Mod})]$. 151

Table 5-4. Selected metrical parameters for $Ph_4P[Fe(L^{Ph})(MeCN)]$. 159

Table 5-5. Crystal data and structure refinement for solid-state structures. 169

Table 6-1. Selected bond lengths and angles for K[Fe(L^{C6F5})(MeCN)]. 180

Table 6-2. Selected bond lengths and angles for K[Fe(L^{Mod})] and $(Et_4N)_2$[Fe(L^{Mod})]. .. 191

Table 6-3. Selected bond lengths and angles for K[Fe(L^{C3F7})(MeCN)]. 200

Table 6-4. Crystal data and structure refinement for solid-state structures. 209

Part I. Introduction

Chapter 1: Bioinspired Ligand Design for Promoting New Modes of Base Metal Reactivity

Section 1-1. Bioinorganic Chemistry

Bioinorganic chemistry is the study of the roles metal ions play in biology.[1, 2] Many of the processes relevant to biochemistry involve molecules that fall in the realm of inorganic chemistry. Researchers in this field study subjects such as the transport and storage of metal ions within cells and through cell walls, the structure and function of metalloenzymes, as well as the design and mechanism of metal-containing pharmaceuticals. Specifically, the study of metalloenzymes is of interest because of the diverse reactions that are carried out by these proteins. Some of the better-studied classes of metalloenzymes include:

- Oxygen-transport and -activation proteins: This category incorporates the proteins responsible for the transport of dioxygen within organisms (i.e., hemoglobin, hemocyanin), the activation of dioxygen for electron and group transfer chemistry (oxidation and oxygenases), as well as the enzymes responsible for the protection of biological systems from harmful effects of dioxygen and it's oxidized forms (i.e., peroxidases and superoxide dismutase).
- Nitrogenases: This class of enzyme mediates biological nitrogen fixation. The active site of this species contains molybdenum and iron centers, though in some

species the molybdenum is replaced by a vanadium or another iron ion. The cooperation of an electron-transfer protein (see below) is necessary in order for the six-electron reduction of dinitrogen to proceed.

- Bioorganometallic systems: Hydrogenases and methylcobalamin (MeB_{12}) are examples of proteins that contain organometallic species. This class of protein has seen significant attention from environmental chemists, due to the ability of these proteins to act as chemical sensors.
- Electron-transfer proteins: Well-known examples of these proteins include the iron-sulfur proteins (ferredoxin and rubredoxins) and the cytochromes. They are responsible for supplying reducing equivalents to other proteins in order to carry out multi-electron processes.
- Hydrolases: As implied by their classification, these proteins catalyze the hydrolysis of a chemical bond in their corresponding substrate. These enzymes are responsible for diverse transformations such as the oxidation of CO_2 to CO_3^- (carbonic anhydrase) and the cleavage of phosphoesters (phosphatase).

These proteins efficiently use biologically available small molecules in order to execute regiospecific catalytic processes under mild conditions. As such, the chemical information to be garnered from these systems by structural chemists, enzymologists, spectroscopists, biochemists, and synthetic chemists is almost endless.

Many studies of metalloproteins are geared toward the understanding of structure/function relationships within these systems. On one end of the spectrum, scientists study these systems in order to gain a better understanding of the structure of these proteins and the mechanisms at work in the processes that they catalyze. On the other side of bioinorganic chemistry, this information gives synthetic inorganic chemists and medicinal chemists important clues as to what structural and electronic properties are necessary in order to mimic the elegant chemical processes performed in nature.

One strategy toward elucidating the structural and mechanistic aspects of an enzyme, as well to duplicate its functional processes is to generate small molecule mimics of the enzyme.[1] The complexes that result from this synthetic strategy can be divided into two categories, biomimetic and bioinspired, based on the goals inherent to the research. On one hand, biomimetic complexes are synthesized with the structure of the enzyme active site in mind (Figure 1-1).[3-5] The supporting ligands in these complexes are designed to conserve, as much as possible, the connectivity observed in the primary coordination sphere of the protein's active site.

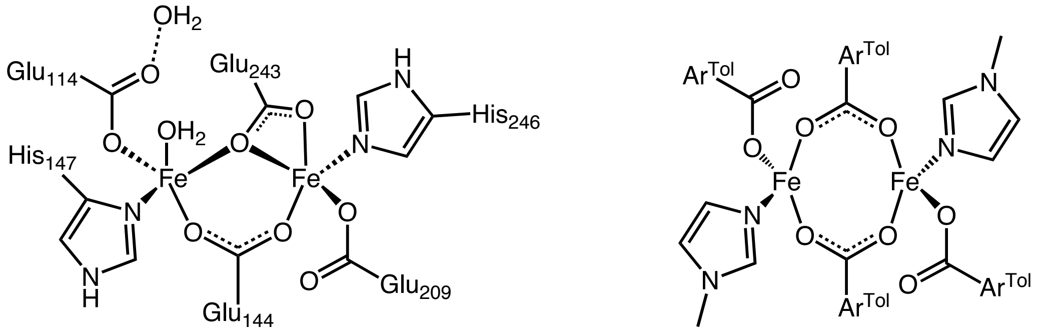

Figure 1-1. Active site of methane monooxygenase (left) and a biomimetic complex (right) from Lippard et al.[3]

These complexes are particularly useful for making spectroscopic comparisons to the native protein, as the small molecule analogue can be analyzed without the presence of the protein backbone, which often makes direct characterization of an enzyme difficult. Duplicating the functional aspects of the proteins, however, is rarely possible with biomimetic complexes. Bioinspired complexes, on the other hand, take specific cues from nature as to which structural and electronic properties of the enzymes are necessary to duplicate the function of the enzymes (Figure 1-2).[6] This allows some freedom in ligand design, as other traits may be incorporated into the complexes that are known to support the desired reactivity.

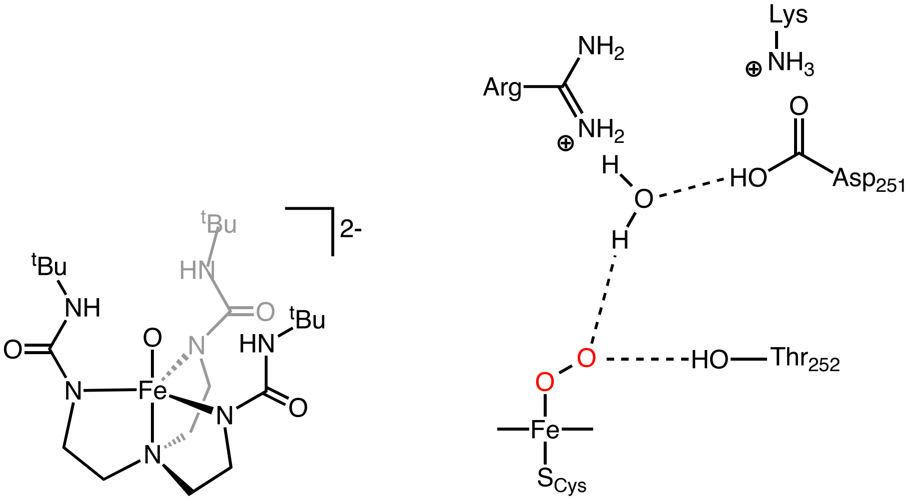

Figure 1-2. Ligand design from Borovik, et al. (left) inspired by the active site of cytochrome P450 (right).[7]

No specific care is taken to preserve the complete structure of the protein active site, so while the complexes generated using this strategy aren't useful for gathering any further information about the protein(s) that led to the inspiration, it represents an effective strategy towards reproducing an enzyme's reactivity in a laboratory setting.

The research presented in this dissertation provides a bioinspired approach to ligand design that incorporates biologically relevant ligands in order to gear naturally abundant metals towards reactivity that is currently performed by more expensive 4d and 5d metals in the industrial setting.

Section 1-2. Iron in Base Metal Catalysis

As mentioned above, metalloproteins make use of the most readily available metals to perform their required functions. Most common among these are manganese, iron, cobalt, nickel, copper, and zinc.[1, 2] Given that living organisms require small quantities of these metals to function, these metals are, in general, less toxic than the other transition elements, and because they are the most naturally abundant metals, they also happen to be the cheapest transition metals, commercially. However, many metal-mediated industrial processes involve the use of more expensive and toxic 4d and 5d metals, such as rhodium, iridium, and platinum.[8] The drastic reduction in cost and environmental impact that could be achieved by engineering late first-row transition metal catalysts for these processes has long driven research in this area.

This disconnect is most obvious in catalysts for reduction-oxidation (redox) reactions, which are not only important in catalysis, but also in the fields of energy production and storage. As the fourth most earth-abundant element (4.7 wt%), iron is particularly interesting for catalytic transformations.[9, 10] Many iron salts, and complexes thereof, are either commercially available on a large scale or relatively easy to synthesize. Owing to its facile redox behavior and considerable Lewis acidity, iron should be useful for myriad transformations including, hydrogenations, oxidations, reductions, polymerizations, additions, substitutions, and coupling reactions. However, the known catalytic reactions of iron are few in number, and those that exist are either limited in scope or lack practicality for large-scale applications. One significant problem presented when developing iron (or other 3d metal) catalysts stems from the difference in the electronic structure of a 3d metal from the noble metals.[8] While the noble metals have a propensity for the two-electron processes that are necessary for maintaining stable catalyst function, the base metals tend to participate in one-electron redox processes that are more difficult to develop into efficient catalytic transformations with high-turnovers. A surge of studies in the field of iron catalysis in the past decade has seen promising advancements that indicate that viable catalysts for industrial-scale processes could be realized in the near future.

Relevant examples of recent achievements in iron catalysis are varied in scope and application. Chirik and coworkers have presented a highly active alkene and alkyne hydrogenation catalyst (Scheme 1-1).[11-14] The Fe(0) precatalyst is supported by a redox-active, bis(imino)pyridine ligand, and redox participation from the ligand in the catalytic cycle is well documented.

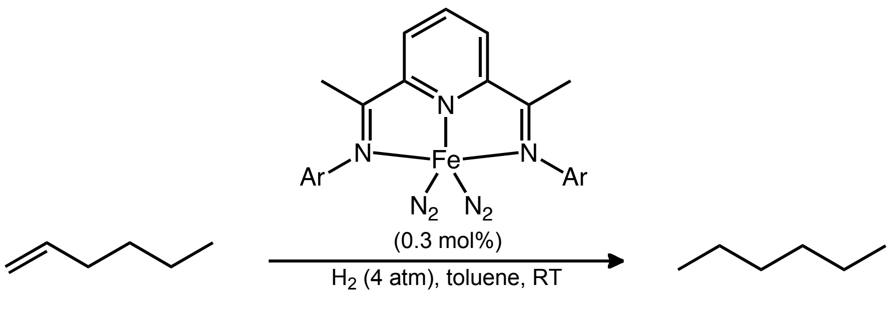

Scheme 1-1. Fe-catalyzed alkene hydrogenation from Chirik and coworkers.[11-14]

While the turnover frequency (TOF) of the catalyst is remarkable (1814 mol h^{-1}), the substrate scope is limited by a lack of functional group tolerance.

More advances have been seen in the hydrogenation of C=O bonds. Casey and coworkers have demonstrated that a half-sandwich complex of iron is capable of the efficient reduction of several ketones, aldehydes, diketones, and imines to the corresponding alcohols and amines.[15, 16] Mechanistic studies have shown that the catalyst behaves similarly to the structurally related, ruthenium-based Shvo catalyst (Figure 1-3). Despite all the advancements in iron-based hydrogenation catalysis, only one example exists of catalytic asymmetric hydrogenation using iron.

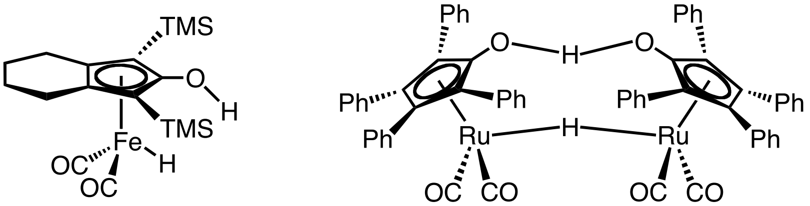

Figure 1-3. Side by side comparison of Casey and coworkers' Fe-based C=O reduction catalyst (left) and the well-known Shvo catalyst (right).[15]

The Morris lab showed that the Fe(II) complex of a phosphorous-containing salen-type ligand was capable of enantioselective transfer hydrogenation of ketones to generate chiral alcohols in as much as 76% enantiomeric excess (*ee*).[17] The high activity of the catalyst (TOF up to 995 h^{-1}) is comparable to the most efficient known ruthenium catalysts (Scheme 1-2). In an indirect route to chiral alcohols from ketones, the Nishiyama group has shown that iron complexes supported by chiral tridentate nitrogen ligands, like bis(oxazolinyl)pyridine (pybox), are capable of the asymmetric hydrosilylation of ketones, which can then be cleaved with an acidic workup to obtain the chiral alcohol in up to 79% *ee*.[18] More recent work by Beller, et al. indicated that using bidentate, chiral phosphine ligands could improve the selectivity of Fe-catalyzed hydrosilylation reactions to upwards of 99% *ee*.[19, 20]

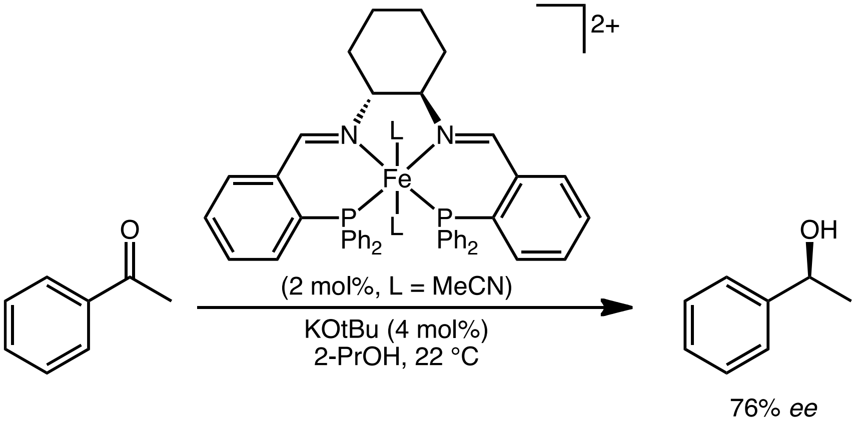

Scheme 1-2. The enantioselective transfer hydrogenation reaction from Morris and coworkers.[17]

Bolm and coworkers have also recently reported examples of catalytic oxidation reactivity using an iron complex supported by a Schiff base ligand.[21-24] A generalized approach to chiral sulfoxides from sulfides using hydrogen peroxides has been developed, giving high yields and selectivities up to 96% *ee*. The labs of Bryliakov[25] and Katsuki[26] reported similar reactivity using salen-supported iron complexes. Bolm and coworkers also reported the oxidation of cycloalkanes and alkylarenes using catalytic amounts of iron salts.[27, 28] These selective C–H oxidation reactions are ligand-free and proceed under mild conditions.

Rose, et al. reported the first entry into catalytic, enantioselective epoxidation by iron.[29] Their binaphthyl-substituted heme complex was shown to epoxidize various styrene-based substrates with impressive selectivity and activity (97% *ee* and TON = 16,000). The necessity of iodosylbenzene (PhIO) as an oxidant, however, belied the limited scope of this transformation. Beller and coworkers improved on this transformation, however, in their three-component catalyst system that employed $FeCl_3$, pyridine-2,6-dicarboxylic acid, and a chiral diamine.[30-33] This system was shown to epoxidize 1,2-disubstituted aromatic olefins with up to 97% *ee* using the more environmentally benign hydrogen peroxide as the oxidant. Using bioinspired N,N,O ligands, Que, et al. demonstrated that a ligand modification could favor a *cis*-dihydroxylation reaction over the previously reported epoxidation reaction (Figure 1-4).[34-36] Under mild reaction conditions, they achieved selectivity of greater than 100:1 diol:epoxide, depending on the substrate.

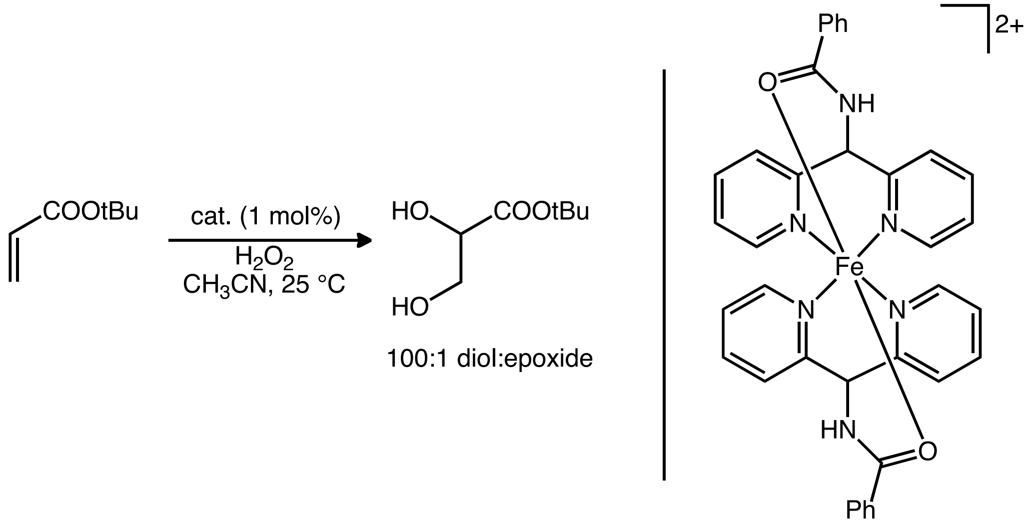

Figure 1-4. Dihydroxylation catalyst designed by Que et al.[34-36]

Oxidation of aliphatic C–H bonds has also been reported by White, et al.[37] Using a tetradentate nitrogen ligand, they demonstrated the iron-mediated hydroxylation of unactivated sp^3 C–H bonds. They showed that the methodology was applicable to a variety of substrates, including a complex molecule.

Recently, examples of Fe-catalyzed cross coupling reactions have been presented. Bolm and coworkers demonstrated the *N*-arylation of aryl iodides and bromides with pyrazole in good yields (up to 87%).[38, 39] The reaction was mediated by $FeCl_3$ with dimethylethylenediamine (dmeda) as the ligand (Scheme 1-3). They've extended the methodology beyond pyrazole to include amides, *N*-heterocycles, and sulfoximes. Later, they adapted their arylation protocol to C–O and C–S bond forming reactions, providing an iron-catalyzed route to aryl ethers and thioethers.[40, 41]

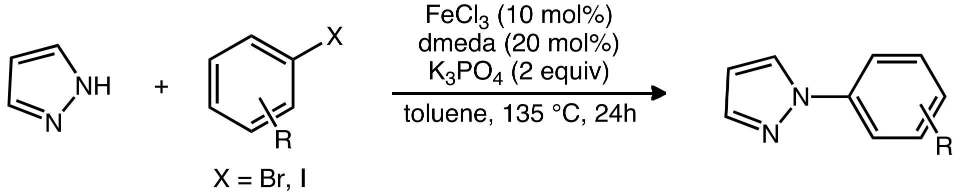

Scheme 1-3. Fe-catalyzed cross-coupling reaction from Bolm and coworkers.[38, 39]

Lastly, Plietker and coworkers demonstrated the first example of an allylic amination reaction by an iron-based catalyst.[42] Using a simple monoanionic iron-carbonyl adduct, they demonstrated that a series of allylcarbonates, when exposed to various amines, gave the corresponding secondary and tertiary allylic amines.

Section 1-3. Amidate Ligands in Nature and in Synthetic Complexes

A small but significant number of structurally characterized metalloproteins of interest to chemists feature amidate-supported transition metal ions in their active sites.[43-50] These proteins feature either Co, Fe, or Ni in their active site, and while the enzymes catalyze a variety of reactions, they are all redox processes. It is likely that the amidate ligands in these systems are responsible for tuning the metal centers in these enzymes towards facile electron transfer.

There are three known examples of Fe-containing enzymes whose crystal structure shows an active site with amidate ligation.[47-50] Two of these enzymes, lipoxygenase and isopenicillin N synthase, feature very similar active site structures (Figure 1-5).[4, 47-49] Each active site features a six-coordinate Fe ion supported by a 2-His-1-carboxylate facial triad, a common feature in nonheme mononuclear iron enzymes.

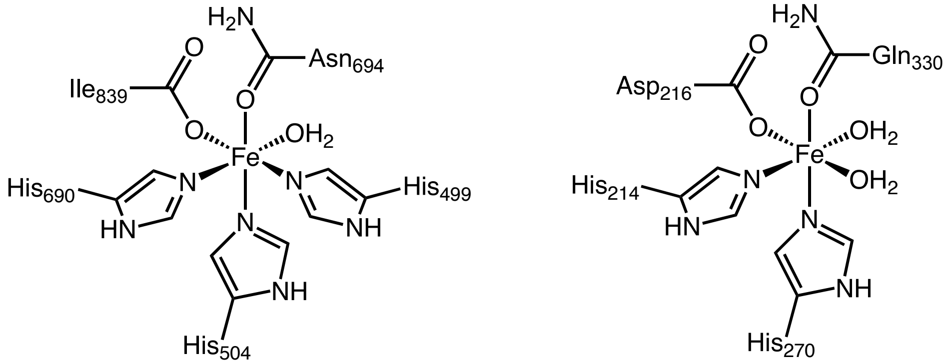

Figure 1-5. Active sites of lipoxygenase (left) and isopenicillin N synthase (right) featuring a 2-His-1-carboxylate facial triad.[47, 48]

Lipoxygenase also features a third histidine donor, an aqua ligand, and an axial *O*-amidate ligand.[47] The remaining sites on the iron in isopenicillin N synthase consist of two aqua ligands and an axial *O*-amidate ligand.[48, 49] Lipoxygenase catalyzed the activation of dioxygen for fatty acid metabolism, and isopenicillin N activates dioxygen in the biosynthesis of penicillin. Site-directed mutagenesis[51-53] and model complex studies[4] indicate that the amidate ligand is necessary for enzyme function and the strongly donating ligand is likely necessary to tune the redox potential of the iron center toward dioxygen activation.

The third iron enzyme is the Fe-containing nitrile hydratase.[50] This enzyme catalyzes the conversion of nitriles to amides and is used on an industrial scale for the production of acrylamide (> 30,000 tons/year). The six-coordinate iron center in the active site is supported by the sulfur atoms of three cysteine residues, the backbone amide nitrogens of two residues and a nitric oxide ligand (Figure 1-6). The nitric oxide ligand is labile and dissociates upon substrate binding. The amide ligation in this case appears to be necessary for activation of the nitrile triple bond. There is also a structurally characterized Co-containing nitrile hydratase. The active site structure is the same as the Fe enzyme, but the NO ligands is replaced with a hydroxide in the structurally characterized form.

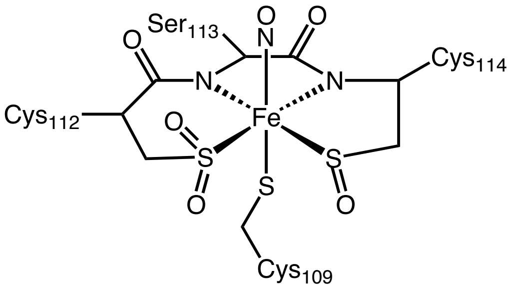

Figure 1-6. Active site of Fe-containing nitrile hydratase.

The enzymes that feature nickel in their active sites are acetyl coenzyme A synthase (Acetyl-CoA)[46] and Ni-containing superoxide dismutase (Ni SOD).[45] Acetyl-CoA catalyzes the synthesis of acetyl-coenzyme A, a molecule important to many metabolic processes in living organisms. The compound serves as the source of a two-carbon acetyl fragment in the enzyme citrate synthase (to produce citrate, the first step in the citric acid cycle),[54] as well as in the biosynthesis of acetylcholine from choline (choline acetyltransferase).[55] Acetyl CoA is also paired with carbon monoxide reductase, in which acetyl coenzyme A is produced as a cofactor for the reversible conversion of CO_2 to CO.[56] The active site of acetyl-CoA synthase contains a $[Fe_4S_4]$ cluster bridged by a cysteine residue to an asymmetric dinickel unit in which one of the nickel ions is bound to two cysteine residues and two carboxamido-N donors in the protein backbone (Figure 1-7, left). The second enzyme that features nickel carboxamidate binding is Ni SOD.[45] This active site is monometallic and contains a Ni ion bound to a two cysteines, the amine of the N-terminus of the protein, and a carboxamidate in the protein backbone (Figure 1-7, right). A histidine acts as a fifth ligand at certain steps in the catalytic cycle. This particular enzyme is responsible for the disproportionation of superoxide radicals to dioxygen and hydrogen peroxide.

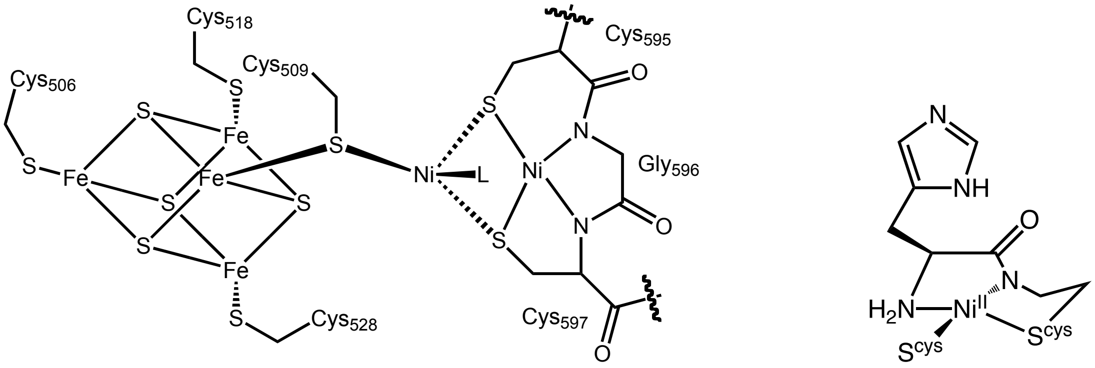

Figure 1-7. Active sites of acetyl-CoA synthase (left) and Ni-containing superoxide dismutase (right).

This antioxidant behavior is important in all living creatures whose cells are exposed to oxygen. The binding motifs around the metal ions in these systems are unusual for metalloenzymes. At this time, it is unclear as to what role these unique metal centers play in catalysis, but it is likely that the ions in the enzymes are responsible for both substrate binding and redox activity.

The discovery of the amidate ligand as a structural feature in biology has resulted in the incorporation of this feature into many biomimetic and bioinspired model complexes for the study of both the structural and functional aspects of the parent enzymes. Beyond their presence in biological systems, ligands that incorporate amidate donors are appealing for several reasons: (1) Due to the ease of amide synthesis from amine precursors, these functionalities are highly modular and can be isolated in high yields. (2) The amide substituents can be modified to affect both the steric and electronic features of the resulting metal complexes.[57-63] (3) Amide functional groups are chemically robust. This is best exemplified in proteins, in which amide linkages (peptides) are used to form the skeleton of the molecules, which must undergo constant oxidative stress. A significant challenge when working with amidate ligands is their ambidentate nature (Figure 1-8).[57] The amidate ligand can coordinate to a metal either through its *O*- or *N*-atom, or in some cases the amidate can chelate to a metal in a κ^2 fashion or bridge two metals using both donor atoms. This can make the isolation of complexes with predictable coordination geometries difficult.

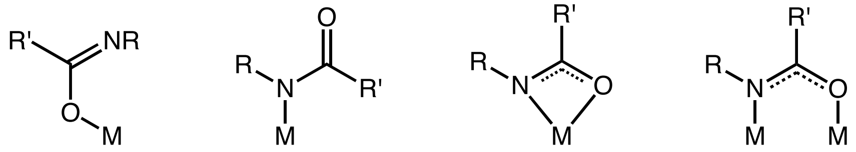

Monodentate *O*-amidate

Monodentate *N*-amidate

Chelating κ^2-amidate

Bridging *N,O*-amidate

Figure 1-8. Binding modes of amidate ligands.

Amidate ligands have seen significant incorporation into macrocyclic and open-chain chelates. Pioneering work in this area by Margerum established that oligopeptide chelates were capable of supporting nickel and copper ions in the 3+ oxidation state.[59, 64, 65] This provided one of first synthetic routes to these rare, biologically important oxidation states. The Kimura group further supported this property of amidate ligands, when they showed that simple azamacrocycles (i.e. cyclam)[66] could be oxidized to generate the corresponding amide-containing ligands (i.e. dioxocyclam) (Figure 1-9).[67] The nickel(II) complexes of these oxidized ligands were demonstrated to form complexes with dioxygen that were best characterized as a Ni(III) superoxide species, whereas the all-amine azamacrocycles complexes were unreactive towards dioxygen.[68, 69] The strongly donating *N*-donor of the amidate moieties provides enough electron density to make the (II/III) couples of these metals accessible.

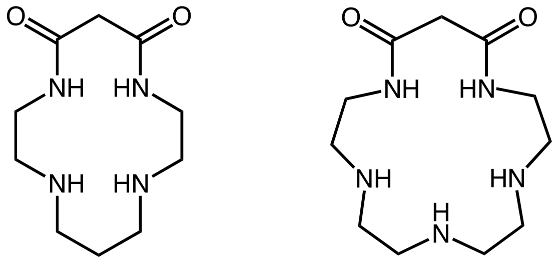

Figure 1-9. Examples of amidate-containing macrocycles used by Kimura and coworkers.[67]

Studies from the Mascharak group using amide-containing, *N*-donor ligands have led insight into the mechanism of acetyl–CoA synthase.[43, 70, 71] Using a chelate that mimics the ligand environment around the distal nickel in the A cluster of the enzyme, they generated a Ni(II) complex. This species could then be bridged to nickel or copper ions supported by more weakly donating ligands to mimic the proximal sulfur-supported proximal metal ion. They showed that CO binding likely occurred at the proximal metal ions in these enzymes, as the distal nickel showed no reactivity with added CO. The Mascharak group has also utilized amidate donors to activate small molecules at iron centers.[72-74] Most notably, their work with nitro and nitrosyl complexes of iron has generated a nonheme system that is capable of catalytic *O*-atom transfer to triphenylphosphine, using the nitro/nitrosyl redox couple with dioxygen as the oxygen atom source.

Another notable example is the Fe–TAML (TAML = tetraamido macrocyclic ligand) framework, made popular by Collins, et al.[75] This macrocyclic scaffold has been shown to support high-valent terminal Fe–oxo fragments, even reporting spectroscopic evidence for an Fe(V) adduct.[76, 77] A great interest has been taken in the Fe(III) complexes of later generation TAML ligands due to their remarkable reactivity for degrading environmental pollutants (Figure 1-10).[75, 78, 79] The complexes are inexpensive, environmentally benign and have found industrial-scale applications for purifying industrial effluent and drinking water.[78, 80]

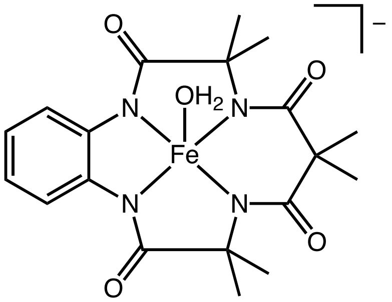

Figure 1-10. Representative current generation TAML catalyst from the Collins group.

Section 1-4. Tripodal, Tetradentate Ligands

Tripodal, tetradentate ligands have a generalized structure that can be divided into four, easily modifiable parts (Figure 1-11). At the center of this type of ligand is a central, tertiary donor. These donors are most often neutral phosphorus or nitrogen atoms, though there have been recent reports of ligands by Peters, et al. with anionic silicon donors in this central position.[81-84]

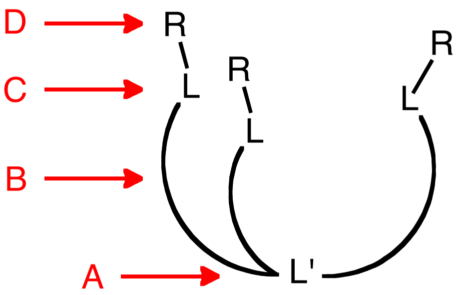

Figure 1-11. Diagram of tetradentate tripodal ligands, showing the constituent parts: (A) tertiary donor, (B) carbon spacers, (C) terminal donors, (D) terminal substituents.

Extending from this central donor, are three carbon-based spacers. These spacers are most often designed to be two or three carbons in length, in order to generate stable 5- or 6-membered chelate rings. Traditionally, these spacers have been alkyl-based, though there have been reports in the literature of ligands with *o*-phenylene spacers.[85-89] Next, each of these carbon spacers is capped with a donor substituent. These donors are more varied in nature, and there have been reports of myriad ligands with nitrogen, oxygen, phosphorus, and sulfur in this role. More recently, carbon-based *N*-heterocyclic carbene donors have been installed as the terminal donors in these tetradentate ligands, as reported by Meyer and coworkers.[90] Depending on their substitution, these donors can be made neutral, or they can be deprotonated to generate anionic ligands. Lastly, the terminal donor atoms are substituted with organic substituents, except in the case of alcohol and thiol ligands. These substituents are varied in nature and can usually be modulated with ease to vary the steric bulk and electronics of the ligands.

The work presented in this dissertation involves the coordination chemistry of a tripodal, tetradentate ligand with an N_3N donor set, meaning that the central donor, and all three terminal donors are nitrogen atoms. The ligand represents a novel entry into the much-studied class of tetraamine ligands.[91] Tripodal, trianionic tris(amido)amines[92] derived from tetraamine precursors have received particular attention because of the ability of this ligand type to support metal complexes with uncommon coordination geometries,[93-97] unique inorganic functionalities,[98-100] and diverse catalytic capabilities.[101-103] The substitution of the primary amine precursors to generate secondary amines, allows for their facile deprotonation to give trianionic ligands. The face-capping binding motif inherent to this ligand framework results in two vacant binding sites in a *cis* relationship at the metal center (Figure 1-12). It has been shown that by adding bulky substituents to the ligand arms, these binding sites can be completely blocked off, leading to a four-coordinate geometry best described as trigonal monopyramidal (TMP).[93-95, 97]

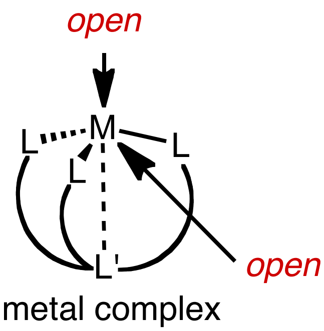

Figure 1-12. Generalized binding mode for a tripodal tetradentate ligand.

This unique geometry generates a ligand field splitting diagram very similar to trigonal bipyramidal. In the absence of one of the axial ligands, the d_{z^2} orbital is reduced in energy, while the lower two sets of degenerate orbitals are proportionately increased in energy.[104]

Section 1-5. Ligand Design

The most common building block for the aforementioned tripodal, trianionic systems are tripodal tetraamine fragments that contain a tertiary amine substituted by three alkylamine moieties, such as tris(2-aminoethyl)amine (tren).[91] We have been interested in exploring alternative building blocks for this type of ligand as a means of varying the electronic features of the resulting transition metal centers. In this context, we were particularly interested in investigating a tripodal tetraamine ligand in which the ligand arms are comprised of *o*-phenylamine moieties (Figure 1-13).

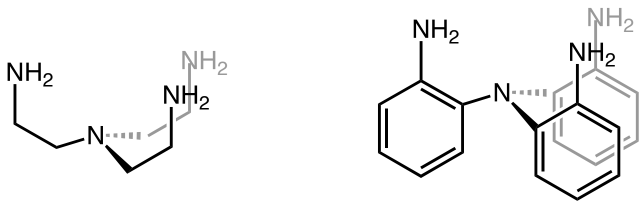

tris(2-aminoethyl)amine
(tren)

tris(2-aminophenyl)amine
N(*o*-$PhNH_2$)$_3$

Figure 1-13. Comparison of the tren and [N(*o*-$PhNH_2$)$_3$] ligand scaffolds.

The incorporation of these units into the ligand backbone is intriguing for several reasons: (1) The *o*-phenylamine backbone should be less flexible upon metal ion chelation than its alkylamine counterparts.[105] This should result in a more rigid structure, thereby inhibiting the isomerism and solution-state fluxionality observed in tren-based systems. (2) Chelating *o*-phenylenediamine[106] units and their derivatives[107] have the potential to act as redox-active or "non-innocent" ligands. Ligand participation in electron-transfer events can allow for multi-electron processes to occur at otherwise redox-inactive metal centers. (3) While tetradentate tripodal ligands of the general form [N(*o*-PhL)$_3$], where L = OH[86-88] or PR$_2$,[85] have been known for some time, the coordination chemistry of [N(*o*-PhNH$_2$)$_3$] and its derivatives had, to the best of our knowledge, not been explored with first row transition metal ions.[108] It came to our attention after the publication of our first manuscript, however, that the Stavropoulos group published studies on a similar tris(amido)amine system and its coordination to late, first row metals.[109-111]

In order to generate our potentially anionic terminal donor ligands, we chose to functionalize the primary amines of our ligand framework with acid chlorides to generate the corresponding amides (Scheme 1-4). This tris(amide)amine now could be deprotonated to generate a chelate with three anionic amidate donor groups. These strongly coordinating ligands should allow us to access high oxidation state metal centers when the ligand is bound to late first-row transition metal ions.

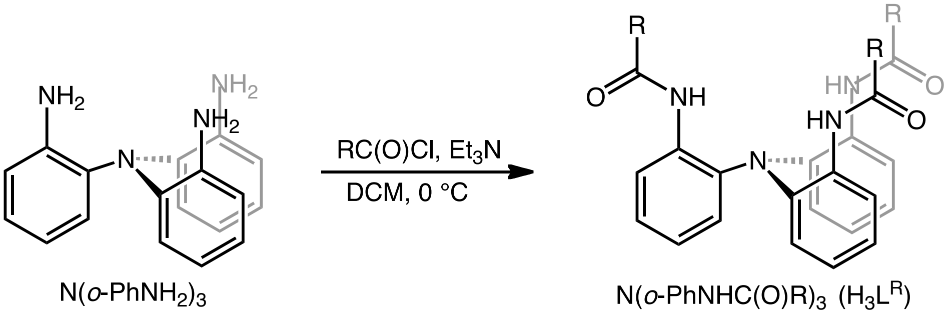

Scheme 1-4. General method for creating tris(amide)amines with varied acyl substituents.

We not only found these amide functionalities appealing because of their ease of synthesis, they are also appealing because of the modularity and chemical robustness. Owing to the great variety of commercially available acid chlorides, the amide acyl substituents can be easily varied to modulate both the steric and electronic influence of the acyl groups on the resulting metal complexes. Lastly, given our interest in the potential oxidation reactivity of our complexes, the chemical robustness of amidate functionalities was of great importance to us. Even under strenuously oxidative conditions, the amidate linkages should remain intact.

Section 1-6. Overview of this Dissertation

In chapter 2 the synthesis of the tris(amide)amine ligand framework will be described. The synthetic, spectral, and structural details of two ligand analogues with Co(II) will also be discussed. The unique anion binding properties engendered on the Co(II) ions by the ligand scaffold indicate that the acyl substituents act as regulatory elements for exogenous ligand binding.[112]

Chapter 3 expands on the coordination chemistry of these tris(amidate)amine ligands by looking at their coordination to Ni(II). A series of complexes with various acyl substituents are synthesized and described structurally and spectroscopically. The acyl substituents are shown to have a significant effect on both the coordination number and primary coordination sphere of the nickel centers. The cyanide binding properties of these complexes and an investigation into their potential use as building blocks for magnetic materials are also reported.[113]

Chapter 4 investigates the ambidentate nature of the amidate ligands by looking at a more oxophilic metal ion, Al(III). It is demonstrated that two of the ligand analogues are capable of generating mononuclear Al(III) adducts, in a rare example of the κ^2-amidate binding motif. The spectral and structural details of these complexes are discussed. These findings indicate that this ligand framework has the potential to bind a variety of metal ions.[114]

The work in chapter 5 explores the reactivity of a series of Co(II) and Fe(II) complexes towards intramolecular bond activation. It is discovered that both the Co(II) and Fe(II) complexes activate weak intramolecular C–H bonds in the presence of an *O*-atom transfer reagent. However, these reactions appear to proceed via different mechanisms. Lastly, it is shown that the hydroxylated Fe(III) species can also be generated using dioxygen as the oxidant/*O*-atom source.

The final chapter in this dissertation discusses a unique example of intramolecular aryl C–F bond activation by iron. The hydroxylation reaction appears to proceed via the intermediacy of a nucleophilic high-valent iron-based oxidant. This transformation can be performed with either an *O*-atom transfer reagent or dioxygen as the terminal oxidant and *O*-atom source.

Part II. Coordination Chemistry of Metal Complexes Supported by a Tris(amidato)amine Ligand Scaffold

Chapter 2: Tripodal Phenylamine-based Ligands and Their Cobalt(II) Complexes

Section 2-1. Introduction

Tetraamine, tripodal ligand systems have been widely employed in many areas of inorganic chemistry.[91] Tripodal, trianionic tris(amido)amines[92] derived from tetraamine precursors have received particular attention because of the ability of this ligand type to support metal complexes with uncommon coordination geometries,[93-97] unique inorganic functionalities,[98-100] and diverse catalytic capabilities.[101-103] The face-capping binding motif inherent to this ligand results in two vacant binding sites in a *cis* relationship at the metal center (Figure 2-1).

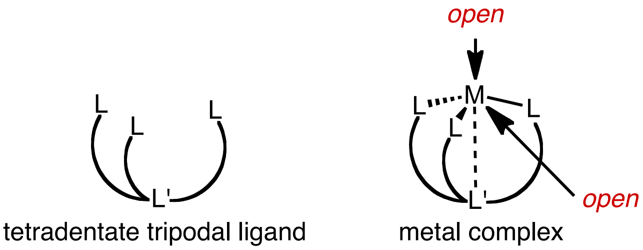

Figure 2-1. General structure and binding mode of tetradentate tripodal ligands.

It has been shown that by adding bulky substituents to the ligand arms, these binding sites can be completely blocked off, leading to a four-coordinate geometry best described as trigonal monopyramidal (TMP).[93-95, 97]

Schrock and coworkers have used silyl-substituted tris(amido)amine ligands to support the first example of an Fe(IV) cyanide,[98] as well as rare examples of tantalum(V) phosphinidene[115] and ethylidene[99] units. They also showed that a Mo(III) complex was capable of catalyzing the 6-electron reduction of dinitrogen to ammonia (Scheme 2-1).[101]

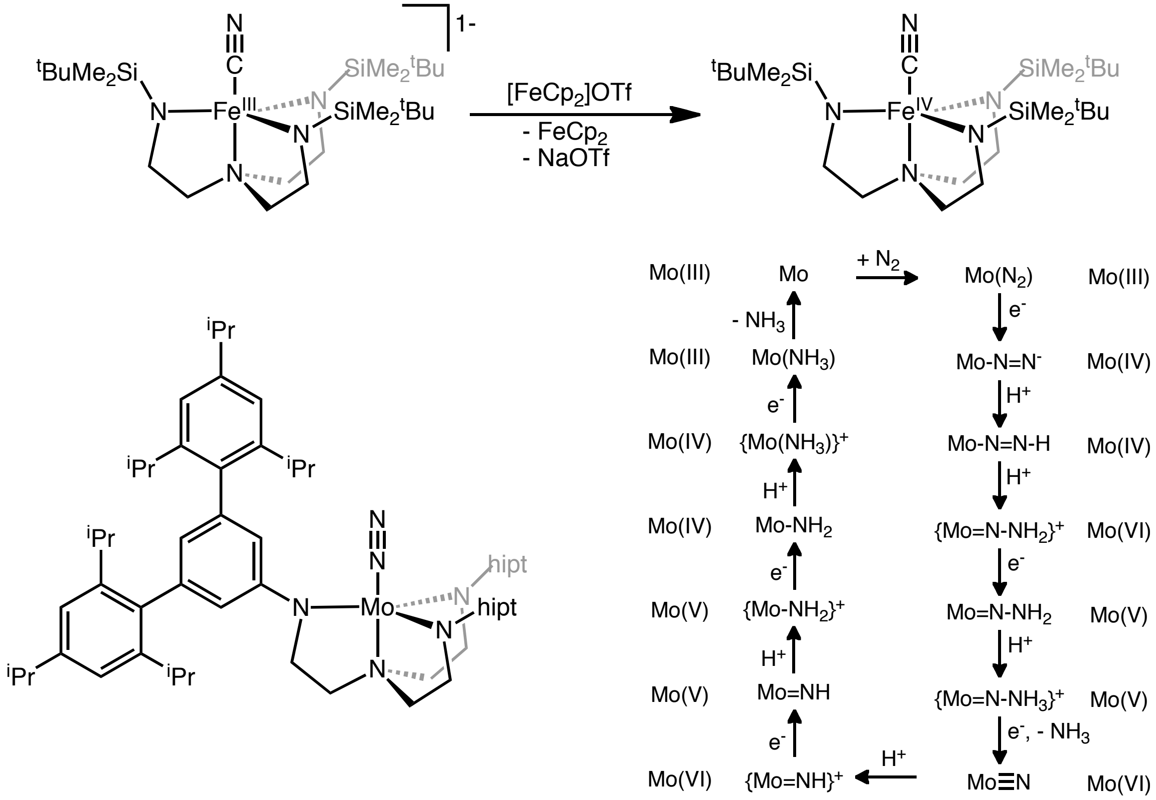

Scheme 2-1. Work from the Schrock lab utilizing tripodal tris(amido)amine ligands. Formation of a stable Fe(IV) cyanide adduct (top) and the molybdenum-mediated reduction of dinitrogen to ammonia (bottom).

Various intermediates in this process, including a Mo(III) dinitrogen complex and a Mo(VI) nitride adduct, could be isolated for study.[116] The Borovik group utilized bulky *tert*-butyl groups on their triamidate ligands to enforce TMP geometry around a series of late, first row transition metal ions (Scheme 2-2).[117] Notably, the Ni(II) congener was shown to be able to be chemically oxidized by one electron to generate a rare example of a Ni(III) complex, as identified by EPR.[58] Also, using a ligand featuring ureate moieties, the Borovik group isolated the first example of a structurally characterized terminal iron oxo complex.[7] The Fe(III) oxo moiety was generated using dioxygen as the O-atom source, and the highly reactive oxo was supported by a network of hydrogen bonds from the remaining protons on the ureate groups.

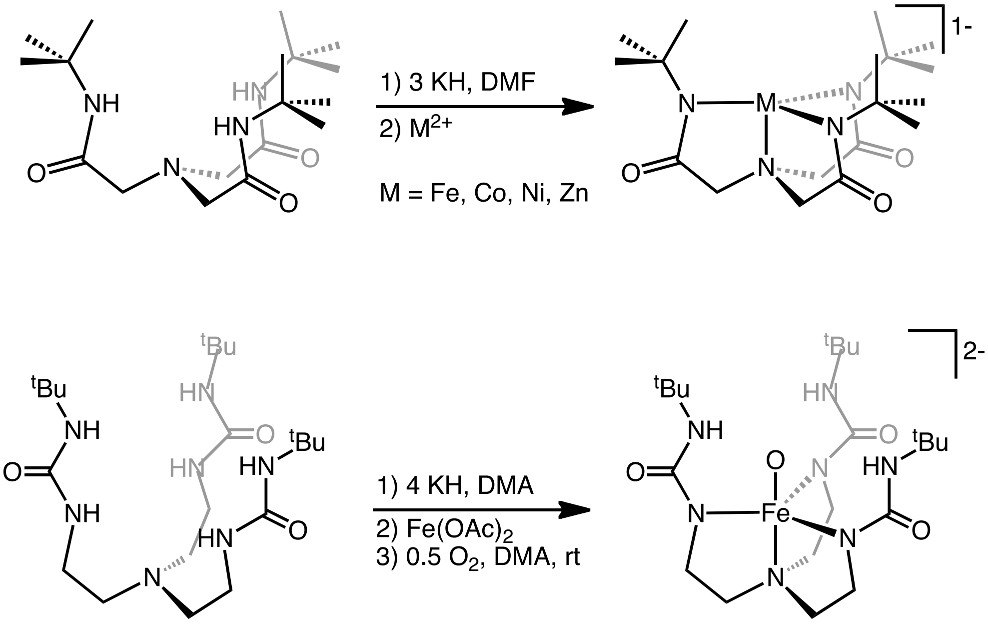

Scheme 2-2. Notable examples of tris(ureato)amine complexes from the Borovik group. The support of late, first row transition metals in a coordinatively unsaturated geometry (top), and stabilization of an Fe(III) oxo unit through hydrogen bonding (bottom).

The most common building block for these types of trianionic systems are tripodal tetraamine fragments that contain a tertiary amine substituted by three alkylamine moieties, such as tris(2-aminoethyl)amine (tren).[91] We have been interested in exploring alternative building blocks for this type of ligand as a means of varying the electronic features of the resulting transition metal centers.

In this context, we were particularly interested in investigating a tripodal tetraamine ligand in which the ligand arms are comprised of *o*-phenylamine moieties (Figure 2-2).

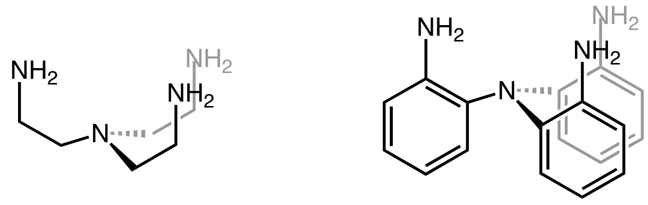

tris(2-aminoethyl)amine (tren)

tris(2-aminophenyl)amine $N(o\text{-}PhNH_2)_3$

Figure 2-2. The tren ligand scaffold (left) and our tris(2-aminophenyl)amine ligand framework (right).

The incorporation of these units into the ligand backbone is intriguing for several reasons: (1) The *o*-phenylamine backbone should be less flexible upon metal ion chelation than its alkylamine counterparts.[105] This should result in a more rigid structure, thereby inhibiting the isomerism and solution-state fluxionality observed in tren-based systems. (2) Chelating *o*-phenylenediamine[106] units and their derivatives[107] have the potential to act as redox-active or "non-innocent" ligands. Ligand participation in electron-transfer events can allow for multi-electron processes to occur at otherwise redox-inactive metal centers. (3) While tetradentate tripodal ligands of the general form [N(*o*-PhL)$_3$], where L = OH[86-88] or PR$_2$,[85] have been known for some time, the coordination chemistry of [N(*o*-PhNH$_2$)$_3$] and its derivatives had, to the best of our knowledge, not been explored with first row transition metal ions.[118] It came to our attention after the publication of our first manuscript, however, that the Stavropoulos group had been studying a similar tris(amido)amine system and its coordination to late, first row metals as well.[109-111]

In this chapter, the synthesis and characterization of the tetraamine ligand tris(2-aminophenyl)amine, N(*o*-PhNH$_2$)$_3$, and its tris(amide)amine derivative, 2, 2', 2"-tris(isobutylamido)triphenylamine [N(*o*-PhNHC(O)^{i}Pr)$_3$] are presented. The synthesis of Co(II) complexes of both of these ligands, as well as their anion binding abilities, will also be detailed.[112]

Section 2-2. Results and Discussion

Few routes exist to generating tertiary arylamine centers. However, we did find one promising route in the literature utilizing the nucleophilic aromatic substitution (S$_N$Ar) of electron-rich aromatics.[119] Using a modified version of their preparation, the trinitroamine ligand N(*o*-PhNO$_2$)$_3$ could be synthesized by the nucleophilic attack of 2-nitroaniline on two equivalents of 2-fluoronitrobenzene (Scheme 2-3). The reaction is run in dimethylsulfoxide (DMSO) and requires high temperature (145°C), but recrystallization of the crude product from hot acetone gives the desired compound is good yield (80%).

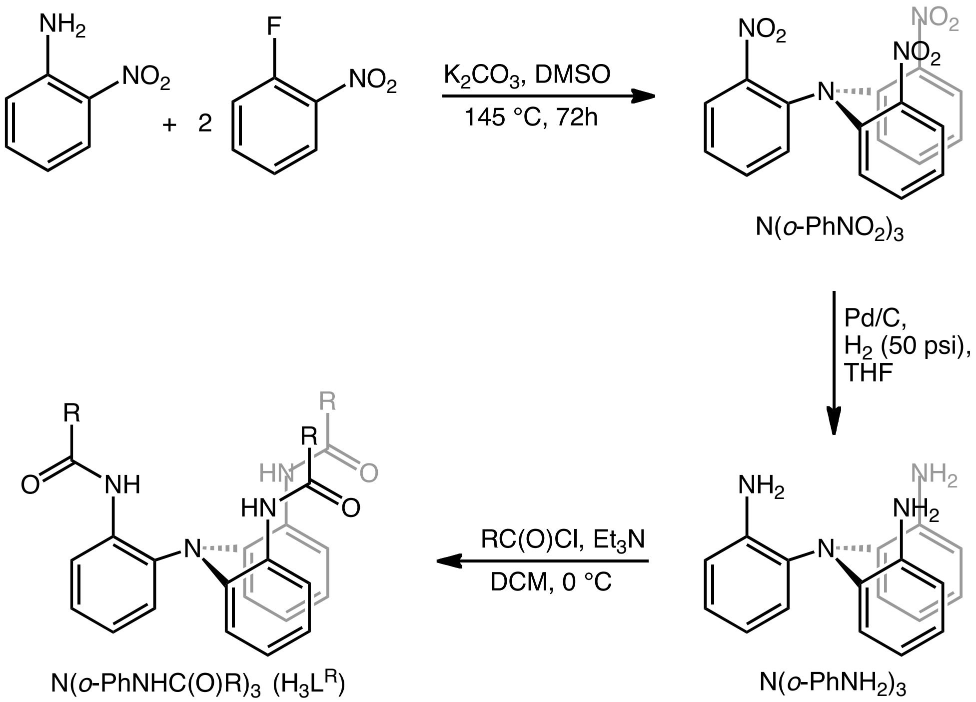

Scheme 2-3. Synthesis of the triamidoamine (H_3L^R) ligand scaffold.

The reduction of the three nitro substituents to generate the parent tetraamine ligand N(*o*-PhNH$_2$)$_3$ (L^{NH2}) can be achieved by hydrogenation over Pd/C at 50 psi. Filtration of the reaction mixture, followed by evaporation of solvent gives the crude product as an off-white solid. Washing the solid with diethyl ether, followed by drying under vacuum gives the pure product as a white solid (85%). Small amounts of palladium impurity in this compound cause a drastic color change in this solid over the course of 1-2 days in air, so the synthesis of the desired triamide ligand requires the use of freshly synthesized tetraamine in order for the reaction to proceed. Once synthesized, however, the tris(amide)amine can be stored in air indefinitely without any observable discoloration or decomposition.

The tris(amide)amine ligands can be synthesized by a standard acylation procedure, using triethylamine, followed by the addition of the appropriate acid chloride at 0 °C to generate the corresponding triamides, N(*o*-PhNHC(O)R)$_3$ (H$_3$L^R), in generally good yields. This chapter discusses only the isopropyl derivative of the ligand (H$_3$L^{iPr}), which is synthesized using isobutyryl chloride. The ligand is purified by multiple extractions of the organic phase with aqueous hydrochloric acid, followed by evaporation of the organic phase to isolate the crude solid. Washing the solid with diethyl ether and drying under vacuum gives the pure product in good yield (93 %).

We began to evaluate the structural properties of L^{NH2} by looking at its coordination to Co(II). We initially attempted to metallate by addition of CoBr$_2$ to a tetrahydrofuran (THF) solution of L^{NH2}. This resulted in the immediate formation of a blue precipitate that was generally insoluble in most solvents. Trying a similar route in acetonitrile, we were able to isolate a purple solid that could be crystallized by vapor diffusion of diethyl ether into a dimethylformamide (DMF) solution of the complex. The structurally characterized complex, however, was not what we expected (Figure 2-3). The structure of [Co(κ^1-L^{NH2})$_2$(DMF)$_2$(Br)$_2$] features a crystallographic center of inversion. The Co(II) ion is in an approximately octahedral geometry with two L^{NH2} ligands bound in a κ^1 fashion through one of the primary amine moieties of the ligand arms. Two bromide ions, as well as two O-bound DMF molecules filled the remaining coordination sites.

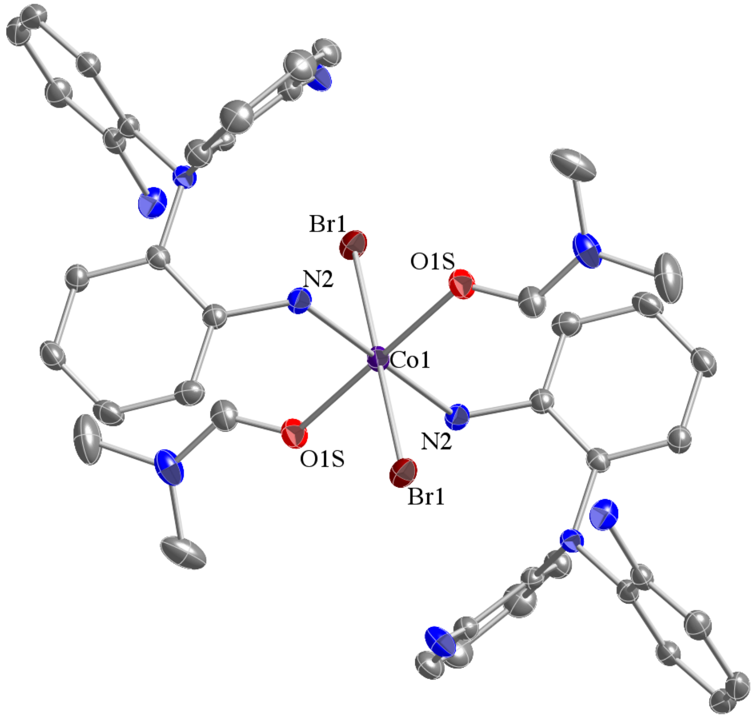

Figure 2-3. Solid-state structure of [Co(κ^1-L^{NH2})$_2$(DMF)$_2$(Br)$_2$]. Hydrogen atoms are omitted for clarity. Thermal ellipsoids shown at 50% probability.

This indicated to us that, despite the fact that our ligand was potentially tetradentate in nature, the neutral donors could be easily replaced by strongly coordinating solvents, such as DMF.

Moving away from coordinating solvents, it was found through the testing of various solvents that a combination MeOH and THF allowed for the efficient dissolution of both the ligand and resultant Co(II) species. In situ exchange of one of the bromide ions using sodium tetraphenylborate resulted in an indigo complex that could be purified by the diffusion of diethyl ether into a THF solution of the metal salt to give

$[Co(L^{NH2})Br]BPh_4$ in good yield (73 %). X-ray quality crystals of this species could be generated by the vapor diffusion of diethyl ether into an acetonitrile solution of the complex.

The solid-state molecular structure shows a five-coordinate Co(II) ion in a trigonal bipyramidal coordination environment with a τ_5 value of 1.0, indicating a near-idealized geometry (Figure 2-4).[120]

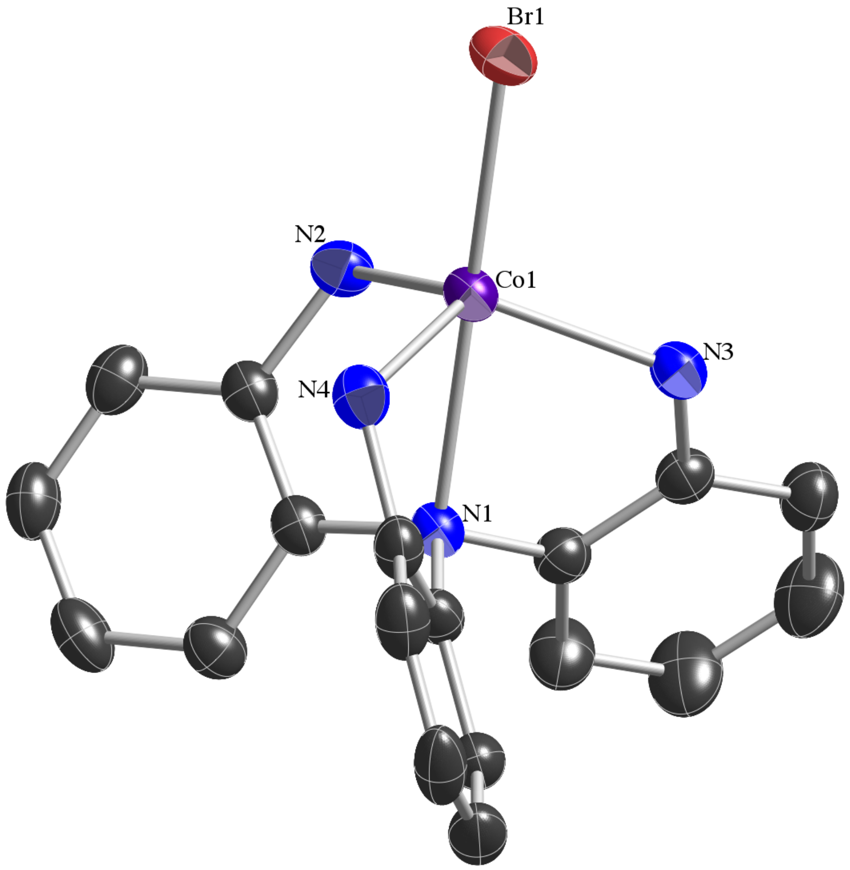

Figure 2-4. Solid-state structure of $[Co(L^{NH2})Br]BPh_4$. Hydrogen atoms and counterion are omitted for clarity. Thermal ellipsoids shown at 40% probability.

The primary coordination sphere of the complex is composed of the three primary amine donors in the equatorial plane, and the axial positions are occupied by the tertiary amine of the ligand and a bromide ion. The Co(II) center is distorted 0.5 Å out of the trigonal plane toward to bromide ion. The C_3-symmetric [Co(L^{NH2})Br]BPh_4 is paramagnetic, and solution state measurements indicate that the metal center has a high-spin S = 3/2 ground state (μ_{eff} = 4.37 μ_B, THF-d_8) at 25 °C.

Table 2-1. Tabulated bond lengths for [Co(κ^1-L^{NH2})$(DMF)_2(Br)_2$] and [Co(L^{NH2})Br]BPh_4

	[Co(κ^1-L^{NH2})$(DMF)_2(Br)_2$]	[Co(L^{NH2})Br]BPh_4
Co–N_{prim} (ave.)	2.1946(17) Å	2.066(3) Å
Co–N_{tert}	--	2.338(2) Å
Co–Br (ave.)	2.6307(3) Å	2.3875(5) Å
Co–O_{DMF}	2.0738(13) Å	--

The coordination chemistry of H_3L^{iPr} was also probed using the Co(II) ion. Deprotonation of a DMF solution of H_3L^{iPr} with 3.1 equivalents of potassium hydride gives the trianionic $K_3[L^{iPr}]$ in solution, as verified by ^{1}H NMR. Transmetallation with $CoBr_2$, followed by salt metathesis with tetraethylammonium bromide gives a deep blue solution. Removal of potassium bromide, followed by evaporation of solvent gives the product as a teal solid in 82% yield (Scheme 2-4).

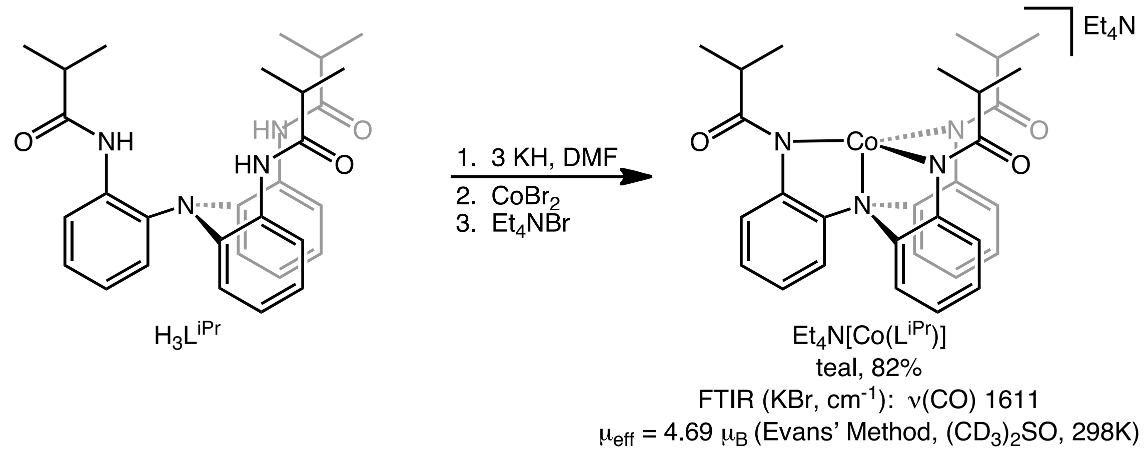

Scheme 2-4. Synthesis of $Et_4N[Co(L^{iPr})]$.

X-ray quality crystals of $Et_4N[Co(L^{iPr})]$ were obtained by slow diffusion of diethyl ether into a DMF solution of the complex. The unit cell of $Et_4N[Co(L^{iPr})]$ contains two crystallographically independent molecules (Figure 2-5). The geometrical parameters of these molecules are indistinguishable within experimental error. The geometry around the cobalt ion is best described as trigonal monopyramidal (TMP), as quantified by the τ_4 value originally described by Houser, et al.[121] This value places four-coordinate geometries on a scale of 0.0 – 1.0, where 0 is idealized square planar, and 1 is equivalent to perfect tetrahedral. Using this equation, $Et_4N[Co(L^{iPr})]$ produces a value consistent with idealized TMP geometry (τ_4 = 0.85). The trigonal plane is composed of the three anionic *N*-amidate donors. The average Co–N_{eq} bond length is 1.959(9) Å.

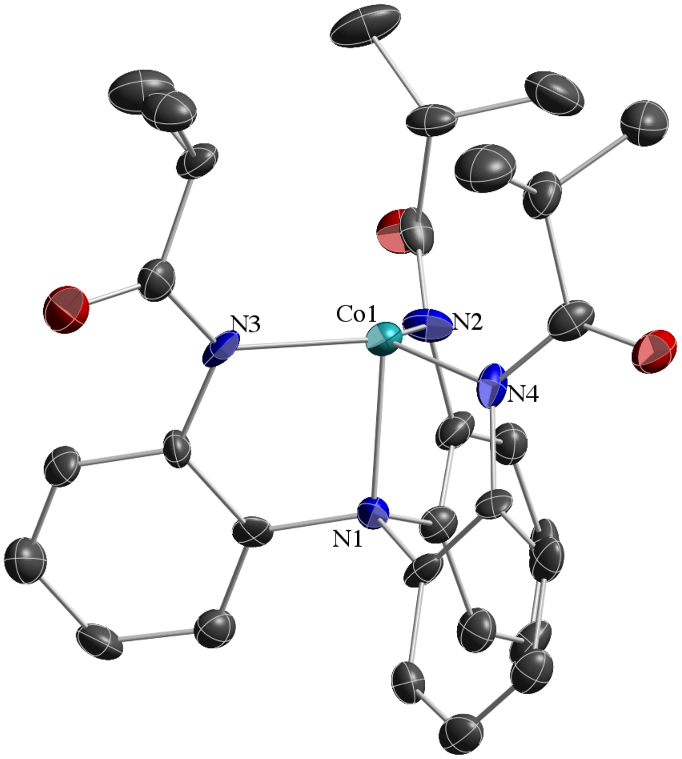

Figure 2-5. Solid-state structure of $Et_4N[Co(L^{iPr})]$. Counterion and hydrogen atoms omitted for clarity. Thermal ellipsoids shown at 50% probability.

The Co ion is slightly distorted (0.182 Å) out of the trigonal plane toward the vacant axial coordination site. The tertiary amine donor of the ligand occupies the opposite axial site with a Co–N bond length of 2.115(8) Å. The vacant coordination site on the Co(II) ion is surrounded by the three amidate isopropyl groups of the ligand. The groups forming this cavity are oriented so that the methine protons of the isopropyl group are positioned inside the protective pocket above the cobalt ion. The trigonal monopyramidal coordination environment observed in $Et_4N[Co(L^{iPr})]$ is rare for cobalt ions, but has been observed with other face-capping ligand systems on both Co(I)[122, 123] and Co(II)[117, 124] centers.

$Et_4N[Co(L^{iPr})]$ displays a high-spin, S = 3/2 electronic configuration in DMSO-d_6 at 25 °C with a $\mu_{eff} = 4.69\ \mu_B$. The electrochemical properties of this complex were investigated by cyclic voltammetry experiments, but the complex did not display any significant or reversible electrochemical events at 25°C in DMF with *n*-tetrabutylammonium hexafluorophosphate ($TBAPF_6$) as the supporting electrolyte.

It was speculated that $Et_4N[Co(L^{iPr})]$ should have an open and accessible axial coordination site given the geometry that it displays in the solid state. This assumption was supported by the behavior of the complex when dissolved in different solvents. The teal crystals give corresponding teal solutions when dissolved in THF or dichloromethane. When dissolved in DMF or MeCN, however, the resulting solutions are purple and magenta, respectively. This implied solvent binding in solution is reversible, however, as recrystallization or solvent removal under reduced pressure results in recovery of the TMP $Et_4N[Co(L^{iPr})]$ species.

In an attempt to generate an isolable, five-coordinate metal complex, anion binding was explored. Addition of one equivalent of Et_4NBr or Ph_4PCl to solutions of $Et_4N[Co(L^{iPr})]$ did not generate the corresponding cobalt halogen adducts. It was observed, however, that the addition of one equivalent of small, linear anions, such as Et_4NCN or sodium azide to a DMF solution of $Et_4N[Co(L^{iPr})]$ resulted in an intensifying of the solution's magenta color. Removal of solvent from the solution under vacuum yields a magenta solid (Scheme 2-5).

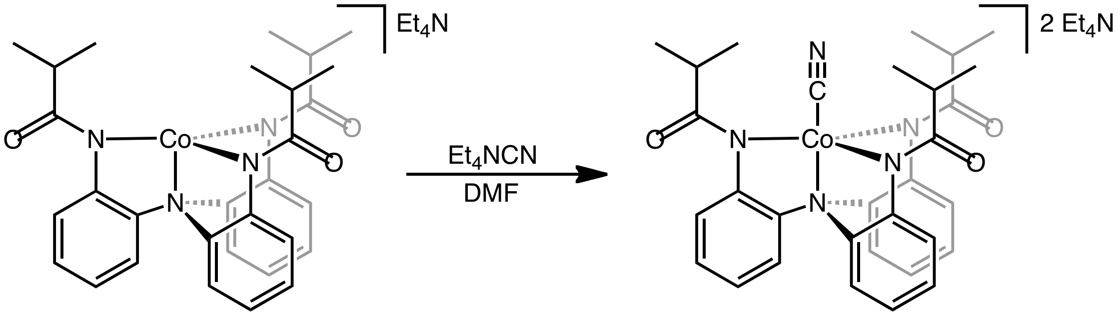

$Et_4N[Co(L^{iPr})]$

$Et_4N[Co(L^{iPr})(CN)]$
FTIR (KBr, cm^{-1}): ν(CN) 2112

Scheme 2-5. Synthesis of terminal cyanide adduct, $(Et_4N)_2[Co(L^{iPr})(CN)]$.

The FTIR spectrum of the cyanide $Et_4N[Co(L^{iPr})]$ adduct shows a ν(CN) stretch at 2112 cm^{-1}, indicative of terminal cyanide binding to a transition metal center.[125] The UV-visible absorption data also support this assignment. The absorption spectrum of $Et_4N[Co(L^{iPr})]$ was monitored while incremental additions of Et_4NCN (between 0 and 1.0 equivalents) were added. The visible absorption spectrum changes after each addition until exactly one equivalent of Et_4NCN has been added. The addition of more than one equivalent causes no additional change in the spectrum. These data are consistent with the formation of a 1:1 CN^- / $Et_4N[Co(L^{iPr})]$ adduct in solution, which may be formulated as $(Et_4N)_2[Co(L^{iPr})(CN)]$. This formulation has been supported by a Job's plot, in which the absorbance at 570 maximizes when the mole fraction of Et_4NCN added is exactly 0.5 (Figure 2-6).

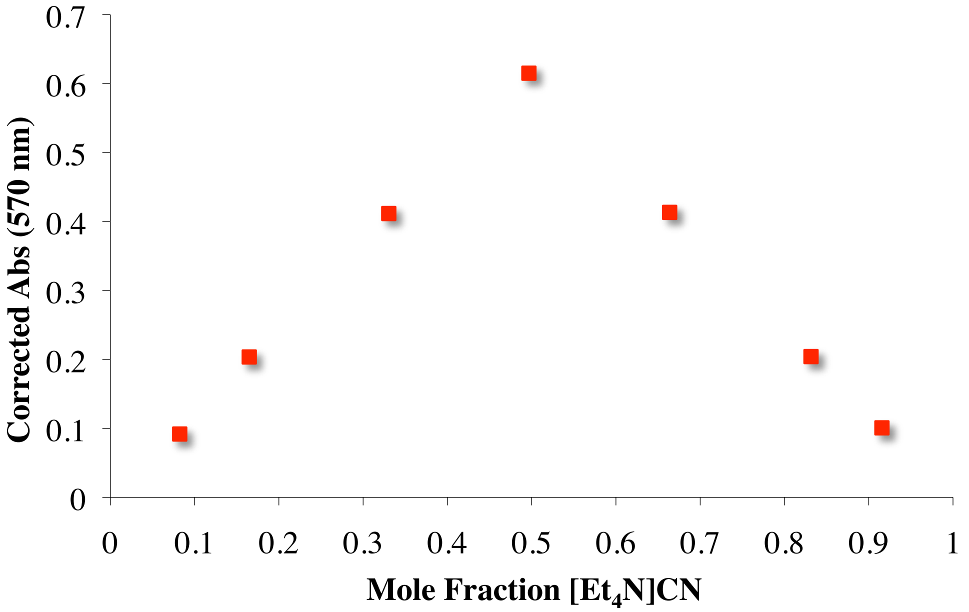

Figure 2-6. Job's plot produced by the continuous variation method for the titration of $Et_4N[Co(L^{iPr})]$ with Et_4NCN. The total concentration of the two species was held constant at 4.04 mM (DMF).

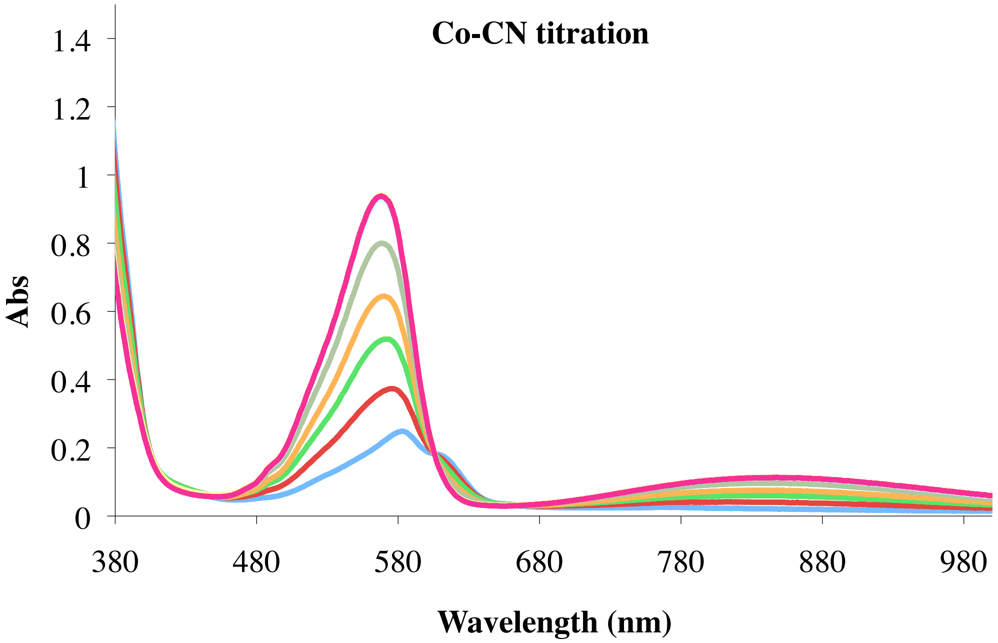

Figure 2-7. Titration data for CN^- binding to $Et_4N[Co(L^{iPr})]$

The binding constant (K_{assoc}) of CN^- binding to $Et_4N[Co(L^{iPr})]$ was determined to be ~ 6 × 10^2 M^{-1} from the titration data (Figure 2-7). $(Et_4N)_2[Co(L^{iPr})(CN)]$ was also examined by cyclic voltammetry (Figure 2-8). The complex displays a single, reversible electrochemical event at -0.145 V (ΔE_p = 0.095 V; i_{pc}/i_{pa}^{-1} = 0.95) vs Fc^0/Fc^+. This one-electron process has been tentatively assigned to the Co^{II}/Co^{III} couple.

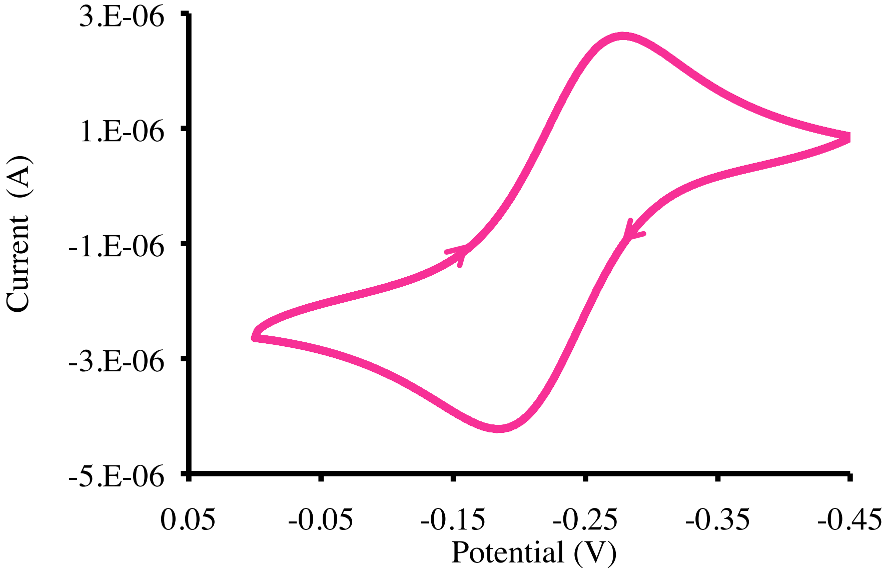

Figure 2-8. Cyclic voltammogram of $(Et_4N)_3[(Co(L^{iPr}))_2(\mu\text{-CN})]$.

Recrystallization of $(Et_4N)_2[Co(L^{iPr})(CN)]$ by slow diffusion of diethyl ether into a DMF solution of the magenta solid yields large magenta crystals suitable for X-ray structural analysis. The crystal structure, however, revealed that the complex did not contain a terminal cyanide adduct but a cyanide-bridged, dicobalt complex (Figure 2-9). The structure of $(Et_4N)_3[(Co(L^{iPr}))_2(\mu\text{-}1,2\text{-CN})]$ features two cobalt centers separated by the bridged cyanide ligand with the tripodal ligands capping the cobalt ions on either end.

The tertiary amine donors are positioned *trans* to the cyano ligand and the bond angles extending from the apical nitrogen of one ligand through the cyanide ion to the other apical nitrogen are all exactly 180°, thus creating a linear array of atoms within the pocket formed by the amidate ligand arms.

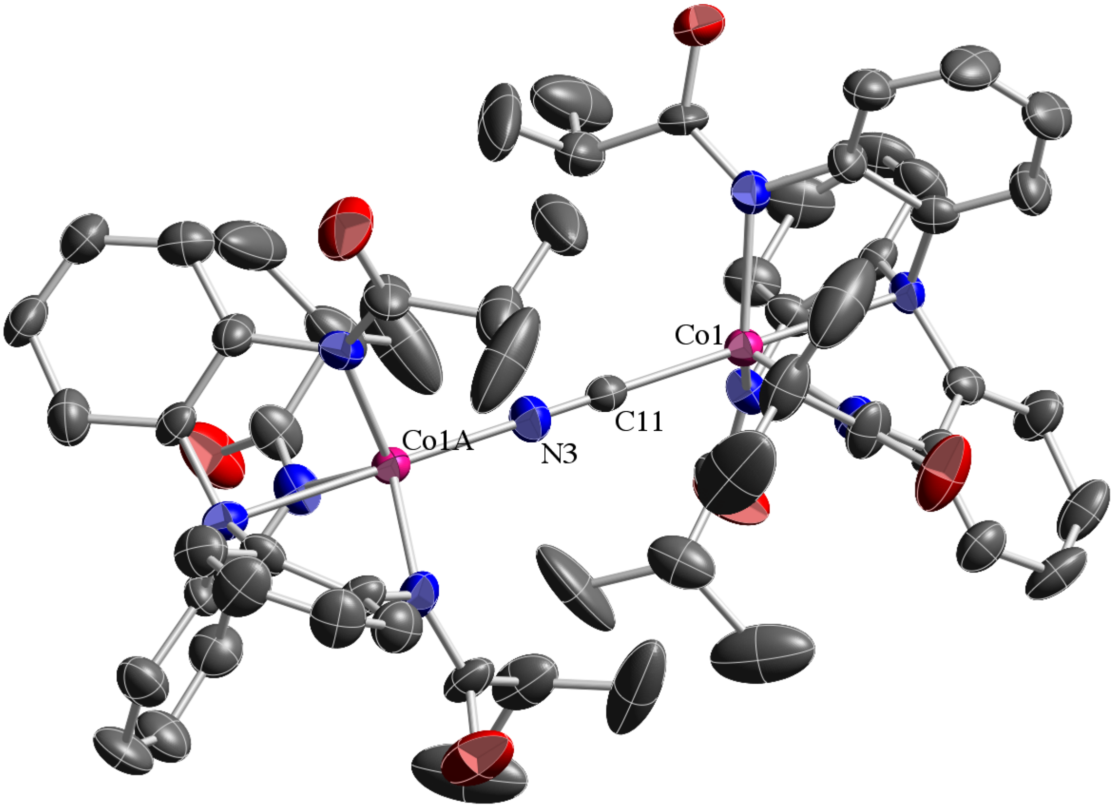

Figure 2-9. Solid-state structure of $(Et_4N)_3[(Co(L^{iPr}))_2(\mu\text{-}1,2\text{-}CN)]$. Counterions and hydrogen atoms omitted for clarity. Thermal ellipsoids shown at 50% probability.

The isopropyl groups of the ligands interlock, encapsulating the dicobalt cyanide unit. This μ-(1,2)-cyanide species, which forms through the loss of 0.5 equivalents of Et_4NCN, is most likely the more thermodynamically stable species, which is favored during the slow recrystallization process. The FTIR data supports this formulation, showing a cyanide stretch at 2125 cm^{-1}, consistent with a bridged cyano complex. Synthesis of $(Et_4N)_3[(Co(L^{iPr}))_2(\mu\text{-}1,2\text{-}CN)]$ by addition of 0.5 equivalents of Et_4NCN to a DMF solution of $Et_4N[Co(L^{iPr})]$ results in the direct synthesis of the bridged species in high yield (82%).

The N_3^- / $Et_4N[Co(L^{iPr})]$ adduct displays two $\nu(N_3)$ stretches in its FTIR spectrum. The stretch seen at 2059 cm^{-1} is consistent with terminal azide binding, while the stretch observed at 2166 cm^{-1} is most like a bridged-1,3 species. Crystallization of this mixture by slow diffusion of diethyl ether into a concentrated DMF solution, results in magenta crystals. The FTIR spectrum of these crystals shows only one azide stretch at 2166 cm^{-1}, indicating that the bridged species is the thermodynamic sink in this species as well. X-ray structural analysis confirms this. The structure of $(Et_4N)_3[(Co(L^{iPr}))_2(\mu\text{-}1,3\text{-}N_3)]$ shows a nearly isostructural arrangement to that of the bridged cyanide species (Figure 2-10). The major difference between the two structures is the increased distance separating the $[Co(L^{iPr})]^-$ units. Both structures show 180° angles from apical nitrogen of one ligand through the apical nitrogen of the opposite ligand, however, the Co•••Co distance is much greater in the azide species (6.309 Å) than in the cyanide dimer (5.270 Å).

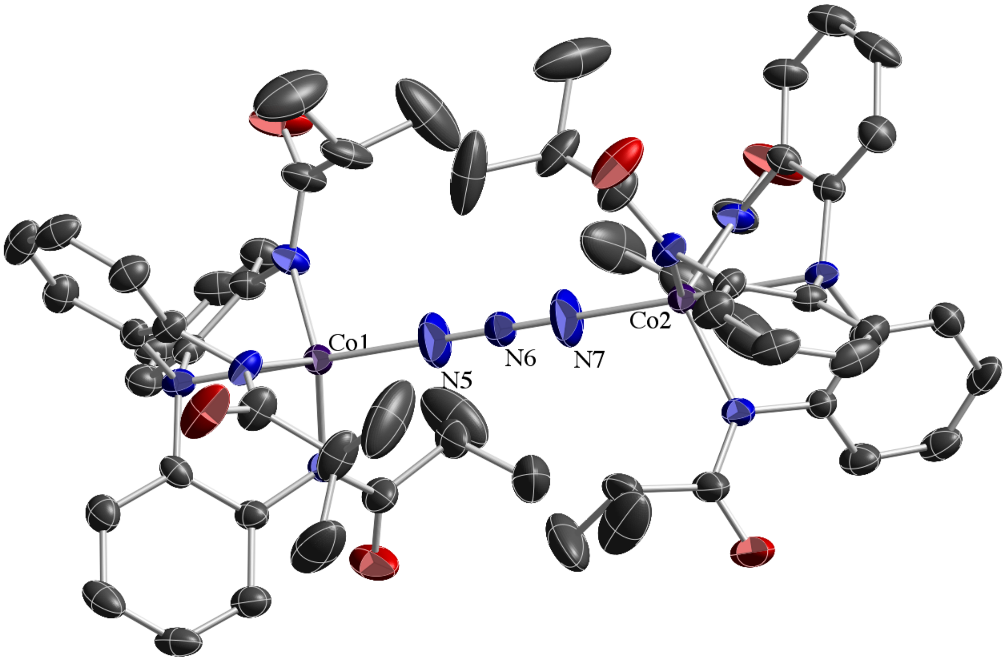

Figure 2-10. Solid-state structure of $(Et_4N)_3[(Co(L^{iPr}))_2(\mu\text{-}1,3\text{-}N_3)]$. Counterions and hydrogen atoms omitted for clarity. Thermal ellipsoids shown at 50% probability.

This results in a decreased interaction between the bulky isopropyl substituents on the arms of the triamidate ligand. The attenuated steric interaction may explain why the bridged azide dimer was observed in the crude FTIR of this complex, but the cyanide dimer was not observed in the spectrum of the crude powder isolated from its reaction. The observation that CN^- and N_3^- bind irreversibly to the cobalt center in $Et_4N[Co(L^{iPr})]$, but DMF, acetonitrile, and bromide ion do not indicates that the cavity surrounding the Co(II) ion is limiting exogenous ligand binding to small or linear anionic donors.

Table 2-2. Selected metrical parameters for $Et_4N[Co(L^{iPr})]$, $(Et_4N)_3[(Co(L^{iPr}))_2(\mu\text{-}1,2\text{-}CN)]$, and $(Et_4N)_3[(Co(L^{iPr}))_2(\mu\text{-}1,3\text{-}N_3)]$.

	$Et_4N[Co(L^{iPr})]$	$(Et_4N)_3[(Co(L^{iPr}))_2$ $(\mu\text{-}1,2\text{-}CN)]$	$(Et_4N)_3[(Co(L^{iPr}))_2$ $(\mu\text{-}1,3\text{-}N_3)]$
Co–N_{ax} (Å, ave.)	2.115(8)	2.458(13)	2.410(6)
Co–N_{eq} (Å, ave.)	1.959(9)	2.039(6)	2.028(2)
Co–N_{CN} (Å)	--	2.075(15)	--
Co–C_{CN} (Å)	--	2.058(17)	--
Co–N_{N3} (Å, ave.)	--	--	2.013(8)
Distance out of plane (Å)	0.182	0.593	0.550
N_{ax}–Co–N_{CN} (°)	--	180.0(2)	180.0(2)
N_{ax}–Co–C_{CN} (°)	--	180.0(2)	180.0(2)

In order to further explore the characteristics of the cavity formed by our acyl substituents, we looked at substituting the ligand with phenyl groups. Using a similar procedure to that for H_3L^{iPr}, we acylated the parent amine, L^{NH2} with benzoyl chloride to generate the corresponding phenyl derivative, H_3L^{Ph}. Triply deprotonating a DMF solution of this ligand with KH, followed by addition of $CoBr_2$ gives the corresponding cobalt complex. Salt metathesis with Ph_4PBr, followed by removal of solvent gives a magenta solid (Scheme 2-6). Removal of KBr, followed by recrystallization from acetonitrile/diethyl ether gives magenta crystals suitable for x-ray analysis.

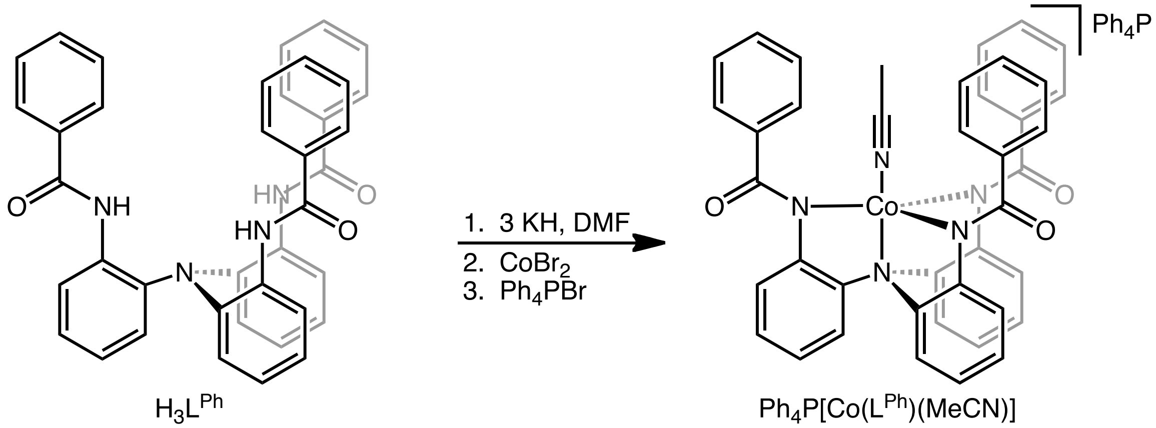

Scheme 2-6. Synthesis of $Ph_4P[Co(L^{Ph})(MeCN)]$

The solid-state structure of $Ph_4P[Co(L^{Ph})(MeCN)]$ shows a five-coordinate Co(II) ion in an approximately trigonal bipyramidal geometry (Figure 2-11). Like the isopropyl analogue, the trigonal plane is comprised of the three amidate groups of the ligand arms, and one axial site is occupied by tertiary amine central to the ligand. In this case, an acetonitrile molecule from the recrystallization solvent occupies the second axial site. The effect of this extra ligand is seen is the Co–N bond lengths of the complex. The axial Co–N distance of 2.184(6) Å is significantly longer than that of the isopropyl ligand, owing to the trans influence of the bound solvent molecule. The average equatorial Co–N distance of 2.045(5) Å is also notably longer. The Co ion sits 0.447 Å above the trigonal plane towards the acetonitrile ligand ($Co–N_{MeCN}$ 2.064(6)).

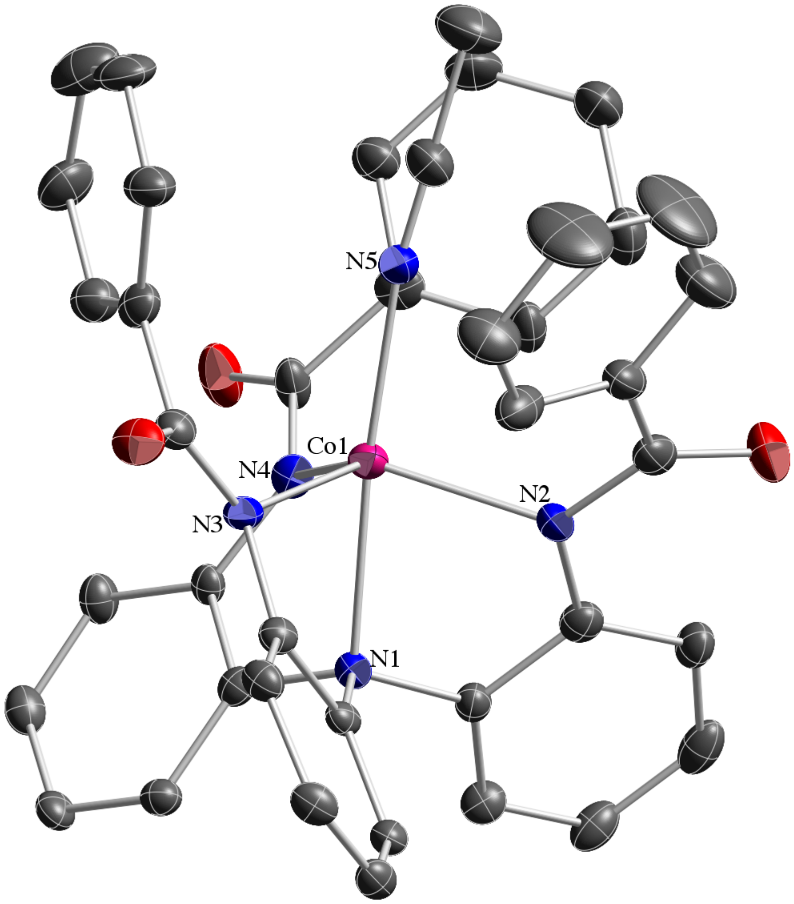

Figure 2-11. Solid-state structure of $Ph_4P[Co(L^{Ph})(MeCN)]$. Counterion and hydrogen atoms removed for clarity. Thermal ellipsoids are shown at 30% probability.

The phenyl rings of the acyl substituents line up around axial coordination site, with the faces of the rings pointed in towards the MeCN ligand. The ability of this complex to bind MeCN indicates the cavity in this ligand is much larger than the one formed by the isopropyl substituents, as indicated by this complex's ability to bind solvent. Solution-state magnetic data in DMSO-d_6 at 25 °C indicate a high-spin, S = 3/2 Co(II) ion (μ_{eff} = 4.53 μ_B). The electrochemical properties of this complex were investigated by cyclic voltammetry experiments, but the complex did not display any significant or reversible electrochemical events at 25 °C in DMF with *n*-tetrabutylammonium hexafluorophosphate ($TBAPF_6$) as the supporting electrolyte.

In order to make direct comparisons of the cavities formed by the isopropyl and phenyl ligand analogues, we sought to make the cyanide adduct of $Ph_4P[Co(L^{Ph})(MeCN)]$. The addition of one equivalent of Et_4NCN to a DMF solution of $Ph_4P[Co(L^{Ph})(MeCN)]$ resulted in deepening of the magenta color. FTIR of the crude oil collected from this reaction shows two ν(CN) at 2111 and 2069 cm^{-1}, the first being consistent with terminal cyanide binding and the latter with free cyanide. This observation indicated the reaction was not going to completion, as free cyanide still existed in the reaction mixture. Recrystallization of the solid resulted in recovery of the starting material. Observing this reaction by UV-vis spectroscopy showed small changes in the absorption spectrum, indicative of some binding of CN^- to the Co(II) center, but these changes were deemed too insignificant to be used to calculate a binding constant. In order to avoid ligand competition from coordinating solvent, as well as to generate a species with a more distinct absorption spectrum, the synthesis of the TMP adduct, $Ph_4P[Co(L^{Ph})]$ was pursued.

It was discovered that the phenyl ligand, H_3L^{Ph}, could be cleanly deprotonated in THF over two days to generate the trianion $K_3[L^{Ph}]$ (Scheme 2-7). Addition of $CoBr_2$ to the resultant slurry resulted in the formation of a deep blue solution over 12 hours. The subsequent addition of Ph_4PBr resulted in the slow precipitation of a teal solid. The teal solid was collected, dissolved in dichloromethane (DCM), and filtered to remove KBr.

Addition of THF to the filtrate resulted in slow precipitation of teal microcrystalline material.

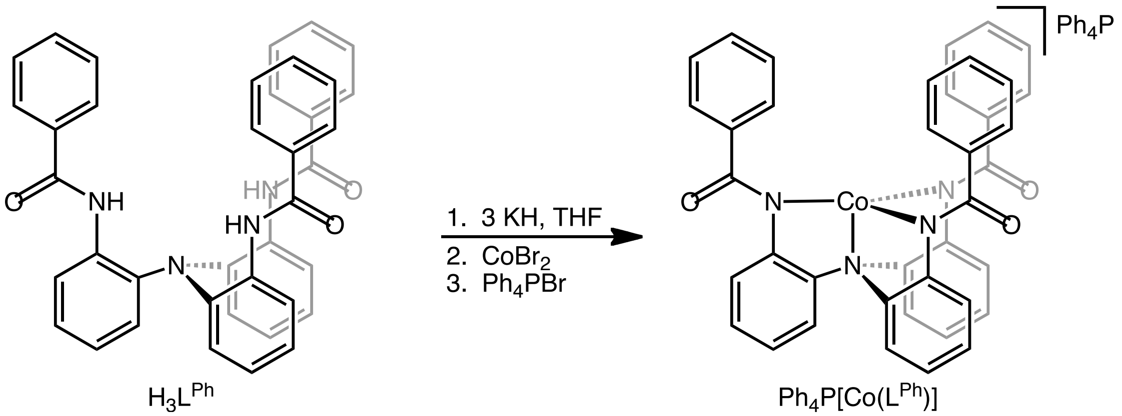

Scheme 2-7. Synthesis of trigonal monopyramidal $Ph_4P[Co(L^{Ph})]$.

Despite the involved procedure, the desired complex is formed in high yield (93%). Crystals suitable for x-ray analysis could be obtained from a cold DCM/hexanes mixture. The structure of $Ph_4P[Co(L^{Ph})]$ shows the desired four-coordinate geometry around the cobalt ion ($\tau_4 = 0.85$). As one would expect, removal of the axial MeCN ligand results in a contraction of all of the Co–N bonds in the complex (Figure 2-12). The axial Co–N bond shortens to 2.126(6) Å, and the average equatorial Co–N bond becomes 1.976(6) Å. These bonds are closer to those seen in the TMP analogue of the isopropyl ligand, $Et_4N[Co(L^{Ph})]$, however they are all slightly longer. Consistent with this observation, the Co(II) ion extends out of the trigonal plane a greater distance away from the apical nitrogen (0.283 Å) compared to $Et_4N[CoL^{iPr}]$ (0.182 Å). Solution-state magnetic data in CD_2Cl_2 at 25 °C indicate a high-spin, $S = 3/2$ Co(II) ion ($\mu_{eff} = 4.44\ \mu_B$). The electrochemical properties of this complex were investigated by cyclic voltammetry experiments, but the complex did not display any significant or reversible electrochemical events at 25 °C in DCM with *n*-tetrabutylammonium hexafluorophosphate ($TBAPF_6$) as the supporting electrolyte.

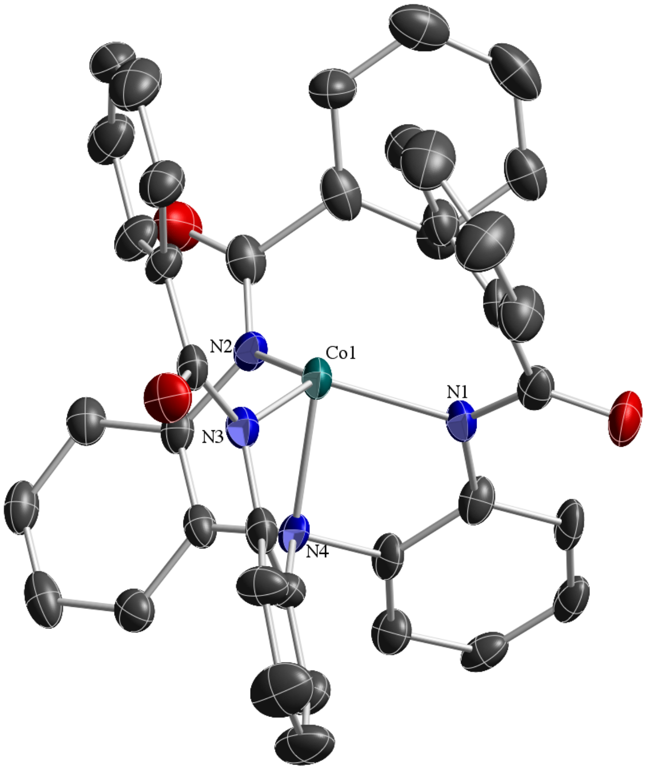

Figure 2-12. Solid-state structure of $Ph_4P[Co(L^{Ph})]$. Counterion and hydrogen atoms omitted for clarity. Thermal ellipsoids shown at 50% probability.

Addition of Et_4NCN to DCM or DMF solutions of $Ph_4P[Co(L^{Ph})]$ results in an immediate color change to bright pink. The UV-vis spectrum of this species is distinct in comparison to that of the starting material. However, attempts to isolate this species only result in mixtures that only partially include the desired CN^- adduct. FTIR spectra of these mixtures are nearly identical to those seen for the reaction of Et_4NCN with the solvento adduct, $Ph_4P[Co(L^{Ph})(MeCN)]$. The electrochemical properties of $Ph_4P[Co(L^{Ph})]$ in the presence of Et_4NCN were studied by cyclic voltammetry experiments, but the complex did not display any significant or reversible electrochemical events at 25 °C in DCM or DMF with *n*-tetrabutylammonium hexafluorophosphate ($TBAPF_6$) as the supporting electrolyte. This goes against expectation for a cyanide adduct, given that a one-electron event was observed for $Et_4N[Co(L^{iPr})(CN)]$. This was thought to indicate that cyanide binding in solution was disfavored. Using the same method as in the case of $Et_4N[Co(L^{iPr})]$, the binding constant of CN^- binding to $Ph_4P[Co(L^{Ph})]$ was determined to be $\sim 2 \times 10^2$ M^{-1} from titration data. This lower binding constant was initially surprising, as the more open cavity surrounding the open axial site should better accommodate exogenous ligands. However, we find we are unable to cleanly isolate a cyanide adduct for analysis. Upon further thinking, however, we postulated that perhaps the considerable electron density inherent to the phenyl rings might be repelling the electron-rich cyanide ligand by coulombic repulsion. This effect would explain why the acetonitrile adduct could be cleanly isolated and structurally characterized, whereas a better ligand, cyanide, would seem to only bind reversibly.

To test this theory, we looked at the binding of an isocyanate ligand. The zwitterionic *tert*-butyl isocyanide supports a partial negative charge on its terminal carbon atom, making it good ligand, and a partial positive charge on its adjacent nitrogen atom, making it electron-deficient and less likely to repel the electron-rich phenyl groups of the ligand arms. As such, an excess of *tert*-butyl isocyanide was added to a DMF solution of $Ph_4P[Co(L^{Ph})(MeCN)]$ (Scheme 2-8). The solution immediately changed from magenta to a coral color.

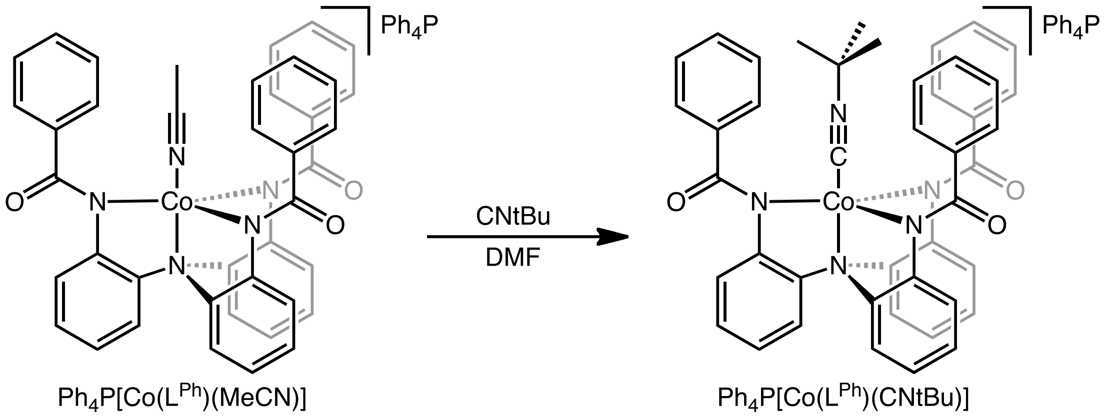

Scheme 2-8. Synthesis of $Ph_4P[Co(L^{Ph})(CNtBu)]$.

After 1.5 hours of stirring, the complex was recrystallized by slow diffusion of diethyl ether into the homogeneous reaction mixture. The FTIR spectrum of the resultant x-ray quality crystals shows one isocyanide stretch at 2190 cm^{-1} that is consistent with binding to a cobalt ion. This indicated that the desired complex, $Ph_4P[Co(L^{Ph})(CNtBu)]$, had been isolated.

The crystallographically determined structure of the complex shows a five-coordinate Co(II) ion in an approximately trigonal bipyramidal geometry (Figure 2-13). Like the MeCN adduct, $Ph_4P[Co(L^{Ph})(MeCN)]$, the trigonal plane contains the three amidate groups of the ligand arms, and one axial site is occupied by tertiary amine central to the ligand. The isonitrile ligand occupies the second axial site.

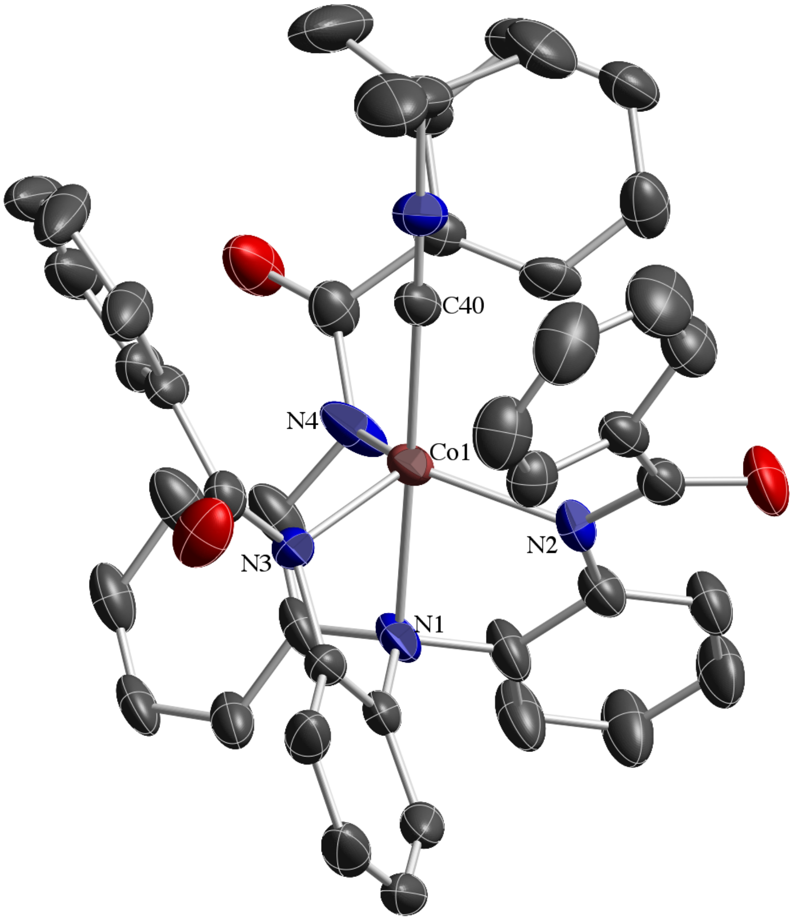

Figure 2-13. Solid-state structure of $Ph_4P[Co(L^{Ph})(CNtBu)]$. Counterion and hydrogen atoms omitted for clarity. Thermal ellipsoids shown at 50% probability.

The effect of this more electron-donating ligand is seen in the Co–N bond lengths of the complex. The axial Co–N_{ax} distance of 2.210(2) Å is significantly longer than that observed in the acetonitrile adduct, $Ph_4P[Co(L^{Ph})(MeCN)]$, owing to greater trans influence exerted by the zwitterionic isonitrile ligand. The Co ion is distorted 0.460 Å above the trigonal plane towards the isonitrile ligand (Co–C_{CNtBu} 2.048(2)), a greater distortion than observed for the MeCN adduct (0.447 Å), once again supporting the greater binding strength in the isonitrile adduct.

Table 2-3. Selected metrical parameters for $Ph_4P[Co(L^{Ph})(MeCN)]$, $Ph_4P[Co(L^{Ph})]$, and $Ph_4P[Co(L^{Ph})(CNtBu)]$.

	$Ph_4P[Co(L^{Ph})]$	$Ph_4P[Co(L^{Ph})(MeCN)]$	$Ph_4P[Co(L^{Ph})(CNtBu)]$
Co–N_{ax}	2.126(6)	2.184(4)	2.210(2)
Co–N_{eq} (Å, ave.)	1.976(6)	2.045(5)	2.038(2)
Co–N_{MeCN} (Å)	--	2.064(6)	--
Co–C_{CNtBu}(Å)	--	--	2.048(3)
Co Distance out of plane (Å)	0.283	0.447	0.460
N_{ax}–Co–N_{MeCN} (°)	--	175.29(19)	--
N_{ax}–Co–C_{CNtBu} (°)	--	--	178.76(9)

This work has demonstrated that varying the acyl substituents on our ligand scaffold can have both a steric and electronic influence over the nature of exogenous ligand binding at our cobalt centers. The complex substituted with bulky isopropyl groups allows only small linear anions access to its open coordination site. The less bulky phenyl substituted ligand creates a more open cavity around the open coordination site, but the electron-rich aromatic rings seem to destabilize the binding of exogenous anionic ligands. Coworkers in our lab are exploring this effect further. It has been shown that by varying the substituents on the aromatic rings to include electron-withdrawing fluoride groups, anion binding is favored and the corresponding binding constants increase as aryl rings with greater positive electrostatic potentials are introduced.[126]

Section 2-3. Experimental

General Considerations

All manipulations were carried out using standard Schlenk techniques or conducted in an MBraun Labmaster 130 drybox under a nitrogen atmosphere. All reagents used were purchased from commercial vendors and used as received unless otherwise noted. Anhydrous solvents were purchased from Sigma-Aldrich and further purified by sparging with Ar gas followed by passage through activated alumina columns. Deuterated dimethyl sulfoxide (DMSO-d_6) was purchased from Aldrich and degassed and dried according to standard procedures prior to use.[127] Elemental analyses were performed by Desert Analytics, Tucson, AZ. ^{1}H and ^{13}C NMR spectra were recorded on a Varian Mercury 300 MHz spectrometer at ambient temperature. Chemical shifts were referenced to residual solvent peaks. Infrared spectra were recorded as KBr pellets on a Varian Scimitar 800 Series FT-IR spectrophotometer. UV-Visible absorption spectra were recorded on a Cary 50 spectrophotometer using 1.0 cm quartz cuvettes. Solution state magnetic moments were measured using the Evans method.[128] Mass spectra were recorded in the Mass Spectrometry Center at Emory University on a JEOL JMS-SX102/SX102A/E mass spectrometer. X-ray diffraction studies were carried out in the

X-ray Crystallography Laboratory at Emory University on a Bruker Smart 1000 CCD diffractometer. Cyclic voltammetric experiments were carried out using a CH Instruments (Austin, TX) Model 660C potentiostat. All experiments were conducted in either DMF with 0.10 M tetrabutylammonium hexafluorophosphate or in DCM with 0.20 M tetrabutylammonium hexafluorophosphate as the supporting electrolyte. Electrochemical experiments were conducted in a three-component cell consisting of a Pt auxiliary electrode, a non-aqueous reference electrode ($Ag/AgNO_3$), and a platinum working electrode. All electrochemical measurements are referenced and reported versus the ferrocene/ferrocenium couple.

Tris(2-nitrophenyl)amine [$N(o\text{-}PhNO_2)_3$]

A mixture of 2-nitroaniline (10.0 g, 72.4 mmol), 1-fluoro-2-nitrobenzene (30.5 mL, 289.6 mmol), and K_2CO_3 (60.0 g, 434.4 mmol) was stirred under N_2 in dimethyl sulfoxide (DMSO, 60 mL) at 150 °C for 84 h. The reaction mixture was then cooled to room temperature, diluted with water (1.0 L) and filtered to give a light orange-brown solid. The solid was stirred in boiling MeOH (1.0 L) for 20 min and filtered hot through a medium porosity frit to yield a bright yellow solid. The solid was washed with additional MeOH (3 x 100 mL, room temperature) and dried under vacuum to afford the dry product. (62%, 17.2 g). ^1H NMR (δ, $CDCl_3$, 300 MHz): 7.84 (dd, 3H, J = 1.2 Hz, J = 6.3 Hz), 7.54 (td, 3H, J = 1.2 Hz, J = 5.7 Hz), 7.31 (td, 3H, J = 0.9 Hz, J = 5.4 Hz), 7.22 (dd, 3H, J = 0.9 Hz, J = 6.3 Hz). ^{13}C NMR (δ, $CDCl_3$, 300 MHz): 143.95, 138.83, 134.02, 128.47, 126.42, 126.15. HRMS(ESI): $C_{18}H_{12}N_4O_6$ *m/z* Calcd. 381.08351 Found

381.08352 $[M+1]^+$. FTIR (KBr, cm^{-1}): ν(NO_2) 1516, 1337. UV-vis ($CHCl_3$) λ_{max}, nm (ε, M^{-1} cm^{-1}): 377 (4410).

Tris(2-aminophenyl)amine [N(*o*-$PhNH_2$)$_3$] (L^{NH2})

To a THF (50.0 mL) solution of N(*o*-$PhNO_2$)$_3$ (10.0 g, 26.3 mmol) was added 5% Pd/C (5.6 g, 2.6 mmol, 10 mol%). The reaction mixture was placed in a pressure safe reaction bottle and shaken under H_2 at 50 psi for 2 h. The reaction mixture was filtered through a pad of celite and washed with THF. The filtrate was concentrated in vacuo to give an off-white solid. The resulting solid was isolated on a medium porosity frit and washed with diethyl ether (3 x 100 mL) and dried overnight under vacuum to yield a white solid (92%, 7.03 g). ^{1}H NMR (δ, $CDCl_3$, 300 MHz): 6.99 (td, 3H, *J* = 1.5 Hz, *J* = 7.5 Hz, ArH), 6.92 (dd, 3H, *J* = 1.2 Hz, *J* = 7.8 Hz, ArH), 6.73 (dd, 3H, *J* = 0.9 Hz, *J* = 7.2 Hz, ArH), 6.71 (td, 3H, *J* = 1.5 Hz, *J* = 7.5 Hz, ArH), 3.70 (bs, 6H, NH). ^{13}C NMR (δ, CD_3CN, 300 MHz): 143.36, 133.21, 126.40, 118.58, 116.65. HRMS(ESI): $C_{18}H_{18}N_4$ *m/z* Calcd. 291.16097 Found 291.16007 $[M+1]^+$. FTIR (KBr, cm^{-1}): ν(NH_2) 3455, 3360.

(N(*o*-PhNHC(O)^{i}Pr)$_3$ (H_3L^{iPr})

A suspension of L^{NH2} (0.9 g, 3.1 mmol) in dichloromethane (DCM, 40 mL) was lowered to 0 °C under an atmosphere of N_2. Triethylamine (1.56 mL, 11.2 mmol) was then added, followed by isobutyryl chloride (1.19 mL, 11.2 mmol). The mixture stirred at 0 °C for 1 h. The reaction mixture was slowly warmed to room temperature and stirred for an additional 20 h. The resulting pale green solution was washed with aqueous HCl (0.1 M, 100 mL), dried over magnesium sulfate, and concentrated in vacuo. The resulting solid was washed with diethyl ether, and the white solid was collected by filtration (70%, 1.09 g). ^{1}H NMR (δ, $CDCl_3$, 300 MHz): 8.03 (s, 3H, NH), 7.81 (d, 3H, *J* = 7.8 Hz, ArH), 7.12 (td, 3H, *J* = 7.5 Hz, ArH), 7.03 (td, 3H, *J* = 1.5 Hz, *J* = 7.5 Hz, ArH), 6.81 (d, 3H, *J* = 7.5 Hz, ArH), 2.25 (5, 3H, *J* = 6.9 Hz, CH), 1.01 (d, 9H, *J* = 6.9 Hz, CH_3), 0.82 (d, 9H, *J* = 6.9 Hz, CH_3). ^{13}C NMR (δ, $CDCl_3$, 300 MHz): 175.51, 138.30, 131.64, 126.01, 125.10, 124.51, 36.02, 19.41. HRESI-MS: $C_{30}H_{37}O_3N_4$ *m/z* Calcd. 501.28602 Found 501.28409 $[M+1]^+$. FTIR (KBr, cm^{-1}): *ν*(NH) 3252, *ν*(CO) 1657.

(N(*o*-PhNHC(O)Ph)$_3$ (H$_3$L^{Ph})

A suspension of L^{NH2} (2.01 g, 6.93 mmol) in dichloromethane (DCM, 40 mL) was lowered to 0°C under an atmosphere of N_2. Triethylamine (3.09 mL, 22.2 mmol) was then added, followed by benzoyl chloride (2.57 mL, 22.2 mmol). The mixture stirred for 90 minutes as the reaction warmed from 0°C to rt. The solution was washed with aqueous HCl (0.1 M, 100 mL), dried over magnesium sulfate, and concentrated in vacuo; yielding a green oil. Crystals of the product were obtained by layering petroleum ether onto a concentrated DCM solution and cooling to -40 °C (3.53 g, 85%). ^{1}H NMR (δ, CD_3CN, 300 MHz): 9.16 (s, 3H, NH), 7.66 (t, 3H, *J* = 4.2 Hz, ArH), 7.45 (t, 3H, *J* = 7.5 Hz, ArH), 7.40 (d, 6H, *J* = 7.2 Hz, ArH), 7.30 (t, 6H, *J* = 7.5 Hz, ArH), 7.10 (t, 6H, *J* = 3.9 Hz, ArH), 6.90 (m, 3H, ArH). ^{13}C NMR (δ, CD_3CN, 300 MHz): 166.55, 139.46, 135.43, 133.09, 133.03, 129.50, 128.52, 127.45, 126.69, 126.13, 125.76. HRESI-MS: $C_{39}H_{31}O_3N_4$ m/z Calcd. 603.23907 Found 603.23914 $[M+1]^+$. FTIR (KBr, cm^{-1}): *ν*(NH) 3273, ν(CO) 1655.

[Co(L^{NH2})Br]BPh_4

To a solution of L^{NH2} (71.0 mg, 0.25 mmol) in dry 1:1 MeOH:THF (12 mL) was added $CoBr_2$ as a blue THF solution. After 10 minutes, sodium tetraphenylborate (168.0 mg, 0.50 mmol) was added as a THF solution to the deep blue reaction mixture. After stirring for 1 h, the reaction mixture was concentrated in vacuo to yield a blue powder. The complex was recrystallized by slow diffusion of diethyl ether into a THF solution containing the metal salt and provided indigo crystals (73%, 133 mg). X-ray quality crystals were grown by slow diffusion of diethyl ether into a concentrated acetonitrile solution of the complex. ^{1}H NMR (δ, CD_3CN, 300 MHz): 13.65 (br), 12.55 (br), 9.97 (s), 7.25 (s, 4H), 6.96 (t, 8H), 6.81 (t, 8H), 4.07 (br). FTIR (KBr, cm^{-1}): ν(NH) 3174. μ_{eff} = 4.37 μ_B (Evans' Method, d_8-THF, 298K). UV-vis (THF) λ_{max}, nm (ε, M^{-1} cm^{-1}): 553(sh), 613(308), 673(sh). Anal. Calcd (found) for [Co(L^{NH2})Br]BPh_4: C, 67.40 (67.36); H, 5.12 (5.14); N, 7.49 (7.47).

Et_4N[Co(L^{iPr})]

To a solution of H_3L^{iPr} (115.0 mg, 0.23 mmol) in dry dimethylformamide (DMF, 10 mL) was added potassium hydride (31.0 mg, 0.76 mmol) as a solid. A colorless precipitate formed. When gas evolution ceased, $CoBr_2$ (51.0 mg, 0.23 mmol) was added as a blue DMF solution. When the reaction mixture became homogenous, tetraethylammonium bromide (49.0 mg, 0.23 mmol) was added to the deep blue solution as a DMF slurry. After stirring for 3 h, the solution was concentrated in vacuo. The resulting blue powder was dissolved in DMF (10 ml) and filtered through a medium porosity frit. The product was recrystallized by slow diffusion of diethyl ether into DMF solution to yield teal crystals (82%, 130 mg). ^{1}H NMR (δ, $CDCl_3$, 300 MHz): 24.20 (br), 12.53 (s), 5.97 (br,m), 3.65 (s), 0.39 (s), -21.33 (br). FTIR (KBr, cm^{-1}): ν(CO) 1611. μ_{eff} = 4.69 μ_B (Evans' Method, $(CD_3)_2SO$, 298K). UV-vis (DMF) λ_{max}, nm (ε, $M^{-1}cm^{-1}$): 582(103), 606(sh). Anal. Calcd (found) for $Et_4N[Co(L^{iPr})]$: C, 66.46 (66.43); H, 7.78 (7.87); N, 10.20 (10.62).

$[Et_4N]_2[Co(L^{iPr})(CN)]$

To a solution of H_3L^{iPr} (131.0 mg, 0.26 mmol) in dry dimethylformamide (DMF, 4 mL) was added potassium hydride (35.0 mg, 0.86 mmol). After 2 hours of stirring, $CoBr_2$ (58.0 mg, 0.26 mmol) was added as a solid. The reaction was stirred for an hour and tetraethylammonium bromide (55.0 mg, 0.22 mmol) was added to the deep blue solution as a solid. This solution stirred for an hour, at which point tetraethylammonium cyanide ($[Et_4N]CN$) (41.0 mg, 0.26 mmol) was added as a solid. After stirring for 1 hour, the solution was filtered and concentrated in vacuo to yield a magenta powder. FTIR (KBr, cm^{-1}): ν(CN) 2112. λ_{max}(ε, $M^{-1}cm^{-1}$) (DMF): 569(381), 844(49). $E_{1/2}$ = -0.145 V vs Fc/Fc^+ at 25 °C in DMF (0.10 M $[TBA]PF_6$).

Stoichiometry Determination of $[Et_4N]_2[Co(L^{iPr})(CN)]$

A Job's plot[129] was used to confirm the stochiometry of the cyano adduct formed when $[Et_4N]CN$ was added to $Et_4N[Co(L^{iPr})]$. The plot in Figure S1 was generated using the method of continuous variations. The following procedure was used to generate a single data point on the Job's plot: A stock solution of $[Et_4N][Co(L^{iPr})]$ (4.04 mM, DMF) and a stock solution of $[Et_4N]CN$ (4.04 mM, DMF) were prepared. 2.75 mL of the $[Et_4N]CN$ solution and 0.25 mL of the $[Et_4N][Co(N(o\text{-}PhNC(O)^iPr)_3)]$ solution were thoroughly mixed in a quartz cuvette and the UV-visible absorption spectrum recorded.

Titration of $[Et_4N]_2[Co(L^{iPr})]$ with $[Et_4N]CN$

Under an N_2 atmosphere, $Et_4N[Co(L^{iPr})]$ (19.4 mg, 0.028 mmol) was placed in a 5.0 mL volumetric flask and dissolved in enough DMF to produce 5.0 mL of solution (5.65 mM). An aliquot was removed from the flask and transferred to a 1.0 cm quartz cuvette and a spectrum was taken. The sample from the cuvette was recombined with the remaining solution in the volumetric flask and 0.25 equivalents of $[Et_4N]CN$ (1.1 mg, 0.007 mmol) was added as a solid and thoroughly mixed. The cuvette was rinsed several times with the solution containing both the $Et_4N[Co(L^{iPr})]$ and $[Et_4N]CN$ to ensure proper mixing before the UV-visible absorption spectrum was recorded. This procedure was repeated until a total of 1.25 equivalents of $[Et_4N]CN$ had been added to the solution. To generate a more complete titration curve, the procedure above was repeated using stock solutions of both $Et_4N[Co(L^{iPr})]$ and $Et_4N[CN]$. The titration experiment was repeated three times and the binding curve was generated. The nonlinear fitting of the titration curve (assuming a 1:1 stoichiometry) yields a binding constant of ca. 6×10^2 M^{-1}.[130]

$[Et_4N]_3[Co_2(L^{iPr})_2(\mu\text{-}1,2\text{-}CN)]$

To a solution of H_3L^{iPr} (139.0 mg, 0.28 mmol) in dry dimethylformamide (DMF, 3 mL) was added potassium hydride (37.0 mg, 0.92 mmol) as a solid. A colorless precipitate formed. When all of the solid dissolved, $CoBr_2$ (61.0 mg, 0.28 mmol) was added as a solid. After 2 hours of stirring, tetraethylammonium bromide (59.0 mg, 0.28 mmol) was added to the deep blue solution as a solid. This solution stirred for an hour; at which point tetraethylammonium cyanide (22.0 mg, 0.14 mmol) was added as a solid. After stirring for 1 hour, the solution was filtered and concentrated in vacuo. The product was recrystallized from the slow diffusion of diethyl ether into DMSO to yield magenta, x-ray quality crystals (349 mg, 82%). ^{1}H NMR (δ, DMSO-d_6, 300 MHz): 17.68, 15.30, 13.05, 10.44, 8.95, 6.15, 0.55, -1.70. FTIR (KBr, cm^{-1}): ν(CN) 2125, ν(CO) 1610. λ_{max}(ε, M^{-1}cm^{-1}) (DMF): 569(381), 844(49).

$[Et_4N]_3[Co_2(L^{iPr})_2(\mu\text{-}1,3\text{-}N_3)]$

To a solution of $Et_4N[Co(L^{iPr})]$ (126.0 mg, 0.28 mmol) in dry dimethylformamide (DMF, 3 mL) was added sodium azide (9.0 mg, 0.14 mmol) as a solid. After 30 minutes of stirring, tetraethylammonium bromide (29.0 mg, 0.14 mmol) was added as a solid. After stirring for 1 hour, the solution was filtered and the filtrate was isolated. The product was recrystallized from the slow diffusion of diethyl ether into the DMF filtrate to yield purple, x-ray quality crystals (122 mg, 92%). FTIR (KBr, cm^{-1}): ν(N_3) 2169, ν(CO) 1611.

$Ph_4P[Co(L^{Ph})(MeCN)]$

To a stirred solution of H_3L^{Ph} (161 mg, 0.27 mmol) in DMF (3 mL) was added KH (35 mg, 0.88 mmol) as a solid. When H_2 evolution ceased, $CoBr_2$ (59 mg, 0.27 mmol) was added as a solid. The pale yellow solution turned magenta. After 15 minutes of stirring, Ph_4PBr (112 mg, 0.27 mmol) was added as a solid. After 30 minutes of stirring, solvent was removed in vacuo. The resultant magenta oil was taken up in acetonitrile (20 mL) and filtered to remove KBr. The filtrate was concentrated in vacuo, and the resultant magenta solid was recrystallized from acetonitrile (235 mg, 93%). X-ray quality crystals were obtained by vapor diffusion of diethyl ether into a concentrated acetonitrile solution. ^{1}H NMR (δ, $CDCl_3$, 600 MHz): 25.25, 17.62, 15.15, 11.29, 5.30, 3.88, 1.64, -1.97, -24.66. FTIR (KBr, cm^{-1}): ν(CO) 1596, 3057, 3023, 2988, 2928, 2248, 1584, 1546, 1473, 1442, 1356, 1269, 1109, 1072, 1040, 997, 914, 762, 723, 687, 527, 486. μ_{eff} = 4.53 μ_B (Evans' Method, DMSO-d_6, 298K). λ_{max}(ε, $M^{-1}cm^{-1}$) (MeCN): 533(190), 739(24). Anal. Calcd (found) for $Ph_4P[CoN(o\text{-}PhNC(O)Ph)_3(MeCN)]$: C, 73.92 (74.09); H, 5.03 (5.16); N, 8.75 (8.56).

$Ph_4P[Co(L^{Ph})]$

To a stirred solution of H_3L^{Ph} (182 mg, 0.30 mmol) in THF (10 mL) was added KH (40 mg, 1.00 mmol) as a solid. After 2 days of stirring, $CoBr_2$ was added as a solid to the white slurry. Over 12 hours the solution became dark blue as most of the solid went into solution, and Ph_4PBr (127 mg, 0.30 mmol) was added as a solid. A teal precipitate formed as the mixture stirred for 2 hours. Solvent was removed in vacuo. The resultant teal solid was taken up in DCM and filtered over Celite. The purple filtrate was concentrated to dryness, and the resultant purple solid was suspended in THF (3 mL). The product precipitated out of the slurry as a microcrystalline solid over 12 hours while stirring (282 mg, 93%). X-ray quality crystals were obtained by adding several drops of hexanes to a concentrated DCM (0.5 mL) solution, and placing it in the freezer. ^{1}H NMR (δ, $CDCl_3$, 300 MHz): 25.95, 11.12, 9.12, 4.05, -1.60, -20.57. FTIR (KBr, cm$^-$

^{1}): ν(CO) 1602, 1562, 1476, 1441, 1355, 1108, 753, 722, 690, 527. $\mu_{eff} = 4.44\ \mu_B$ (Evans' Method, CD_2Cl_2, 298K). λ_{max}(ε, $M^{-1}cm^{-1}$) (DCM): 584(51), 605(sh), 754(11).

$Ph_4P[Co(L^{Ph})(CNtBu)]$

To a solution of $Ph_4P[Co(L^{Ph})(MeCN)]$ (33.0 mg, 0.03 mmol) in dry dimethylformamide (DMF, 2 mL) was added *tert*-butyl isonitrile (13.0 mg, 0.15 mmol) by weight. After stirring for 1.5 hours, the solution was filtered and the filtrate was isolated. The product was recrystallized by slow diffusion of diethyl ether into the DMF filtrate to yield coral-colored, x-ray quality crystals (28 mg, 82%). FTIR (KBr, cm^{-1}): *ν*(C≡NR) 2190, *ν*(CO) 1596.

Crystallography

Suitable crystals were coated with Paratone-N oil, suspended on a small fiber loop and placed in a cooled nitrogen gas stream at 173K on a Bruker D8 APEX II CCD sealed tube diffractometer with graphite monochromated Mo-Ka (0.71073 Å) radiation, except in the case of $Ph_4P[Co(L^{Ph})]\bullet 3CH_2Cl_2$ in which Cu-Ka (1.54178 Å) radiation was utilized. Data were measured using a series of combinations of phi and omega scans with 10 s frame exposures and 0.5° frame widths. Data collection, indexing and initial cell refinements were all carried out using APEX II software.[131] Frame integration and final cell refinements were done using SAINT software.[132] The final cell parameters were determined from least-squares refinement on 2159 reflections. The structure was solved using Direct methods and difference Fourier techniques (SHELXTL, V6.12).[133] Hydrogen atoms were placed in their expected chemical positions using the HFIX command and were included in the final cycles of least squares refinement using a riding model. All non-hydrogen atoms were refined anisotropically. Scattering factors and anomalous dispersion corrections are taken from the *International Tables for X-ray Crystallography*.[134] Structure solution, refinement, graphics and generation of publication materials were performed using SHELXTL, V6.12 software.[133]

Table 2-4. Crystal data and structure refinement for solid-state structures.

	[Co(κ^1-L^{NH2})(DMF)$_2$(Br)$_2$]	[Co(L^{NH2})Br]BPh$_4$	Et$_4$N[Co(L^{iPr})]
Empirical formula	$C_{42}H_{50}Br_2CoN_{10}O_2$	$C_{42}H_{38}BBrCoN_4$	$C_{38}H_{53}CoN_5O_3$
Formula weight	945.67	748.41	686.78
T (K)	173(2)	173(2)	173(2)
λ (Å)	0.71073	0.71073	0.71073
Crystal System	Triclinic	Tetragonal	Monoclinic
Space group	P-1	I4(1)/a	P2(1)
a (Å)	9.0477(10)	34.5691(18)	14.609(11)
b (Å)	9.4110(10)	34.5691(18)	15.421(12)
c (Å)	14.1809(15)	13.4536(10)	15.668(12)
α (°)	92.561(2)	90	90
β (°)	106.999	90	90.116(16)
γ (°)	115.787	90	90
V (Å^3)	1018.81(19)	16077.4(17)	3530(5)
Z	1	16	4
ρ_{calc} (Mg/m^3)	1.541	1.237	1.292
GOF on F^2	1.104	1.022	1.049
R	0.0331	0.0600	0.0855
wR	0.0804	0.1274	0.1905

	$(Et_4N)_3[(Co(L^{iPr}))_2(\mu\text{-}CN)]$	$(Et_4N)_3[(Co(L^{iPr}))_2(\mu\text{-}N_3)]$
Empirical formula	$C_{73}H_{96}Co_2N_{10.50}O_6$	$C_{84}H_{126}Co_2N_{14}O_6$
Formula weight	1334.46	1545.85
T (K)	173(2)	173(2)
λ (Å)	0.71073	0.71073
Crystal System	Rhombohedral	Rhombohedral
Space group	R3	R3
a (Å)	13.1201(3)	18.4932(3)
b (Å)	13.1201(3)	18.4932(3)
c (Å)	13.1201(3)	23.4210(10)
α (°)	92.14	90
β (°)	92.14	90
γ (°)	92.14	120
V (Å^3)	2253.59(9)	6936.8(3)
Z	1	3
ρ_{calc} (Mg/m^3)	0.983	1.110
GOF on F^2	1.079	0.727
R	0.0871	0.0396
wR	0.2279	0.0966

	$Ph_4P[Co(L^{Ph})(MeCN)]$ •2MeCN	$Ph_4P[Co(L^{Ph})]$ •$3CH_2Cl_2$	$Ph_4P[Co(L^{Ph})(CNtBu)]$ •DMF
Empirical formula	$C_{69}H_{56}CoN_7O_3P$	$C_{66}H_{51}Cl_6CoN_4O_3P$	$C_{71}H_{63}CoN_6O_4P$
Formula weight	1121.11	1250.71	1154.7
T (K)	173(2)	173(2)	173(2)
λ (Å)	0.71073	1.54178	0.71073
Crystal System	Monoclinic	Triclinic	Triclinic
Space group	P2(1)/c	P-1	P-1
a (Å)	10.8872(8)	12.1956(9)	13.354(7)
b (Å)	25.8888(19)	13.6621(9)	14.166(7)
c (Å)	20.0306(15)	19.0773(12)	16.830(8)
α (°)	90	106.644(4)	74.884(8)
β (°)	90.38(6)	98.504(4)	84.038(8)
γ (°)	90	95.383(4)	88.722(8)
V ($Å^3$)	5645.6(7)	2980.7(3)	3057(3)
Z	4	2	2
ρ_{calc} (Mg/m^3)	1.319	1.394	1.254
GOF on F^2	1.007	1.031	1.017
R	0.0836	0.1052	0.0529
wR	0.1951	0.2766	0.1191

Chapter 3: Chelating Tris(amidate) Ligands: Versatile Scaffolds for Nickel(II)

Section 3-1. Introduction

A number of biological systems of interest to bioinorganic chemists feature amidate-supported nickel ions in their active sites.[43] Notable among these are acetyl coenzyme A synthase (Acetyl-CoA) and Ni superoxide dismutase (Ni SOD). Acetyl-CoA catalyses the synthesis of acetyl-coenzyme A, a molecule important to many metabolic processes in living organisms. The compound serves as the source of a two-carbon acetyl fragment in the enzyme citrate synthase (to produce citrate, the first step in the citric acid cycle),[54] as well as in the biosynthesis of acetylcholine from choline (choline acetyltransferase).[55] Acetyl CoA is also paired with carbon monoxide reductase, in which acetyl coenzyme A is produced as a cofactor for the reversible conversion of CO_2 to CO.[56] The active site of acetyl-CoA synthase contains a $[Fe_4S_4]$ cluster bridged by a cysteine residue to an asymmetric dinickel unit in which one of the nickel ions is bound to two cysteine residues and two carboxamido-N donors in the protein backbone (Figure 3-1, left). The second enzyme that features nickel carboxamidate binding is Ni SOD.[45] This active site is monometallic and contains a Ni ion bound to a two cysteines, the amine of the N-terminus of the protein, and a carboxamidate in the protein backbone (Figure 3-1, right). A histidine acts as a fifth ligand at certain steps in the catalytic cycle. This particular enzyme is responsible for the disproportionation of superoxide radicals to dioxygen and hydrogen peroxide. This antioxidant behavior is important in all living creatures whose cells are exposed to oxygen. The binding motif around nickel in these systems is unusual for metalloenzymes. At this time, it is unclear as to what role these unique nickel centers play in catalysis. However, it is likely that the nickel centers in both enzymes are responsible for substrate binding.

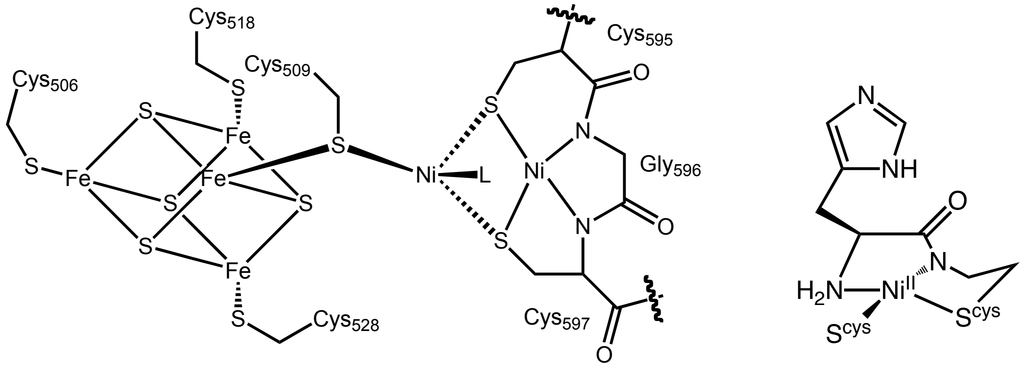

Acetyl CoA Synthase

Superoxide Dismutase

Figure 3-1. The active sites of acetyl-CoA (left) and Ni-containing SOD (right)

Model systems for these nickel-containing enzymes are attractive for a number of reasons. Not only would they lend a better understanding of the processes at work in the enzymes, they provide the opportunity to glean important information about the way nature does catalysis. Functional models of these enzymes could possibly be more efficient and far cheaper (Ni metal = ~ $ 0.01 per gram) than anything we currently have available in our laboratories. Studies towards modeling these enzymes have mostly employed either macrocyclic[67, 135, 136] or open-chain[5, 137-145] chelating ligands that stabilize Ni(II) ions in square planar coordination geometries. Most common among these are simple N_2S_2 open-chain ligands. These ligands feature central *N*-amide moieties with two ligand arms that terminate in thiolate donor substituents. The majority of this work has come from the groups of Holm, Shearer, and Riordan (Figure 3-2).[5, 137, 138]

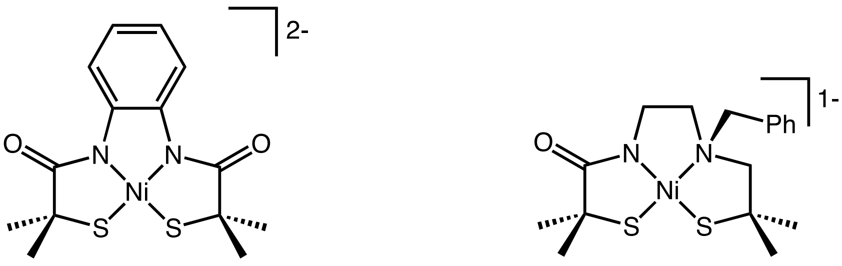

$K_2[Ni^{II}(phmi)]$ $Me_4N[Ni^{II}(BEEAM)]$

Figure 3-2. Representative nickel complexes supported by a N_2S_2-type ligand scaffold.

In studies related to the acetyl-CoA enzymes, Holm and coworkers showed that Ni(II) complexes of these ligands features low-potential Ni(II)/Ni(III) couples (+0.13 to -0.74 V vs. SCE, DMF, 25 °C) that were consistent with that of the acetyl-CoA active site. Using controlled potential coulometry, they generated the corresponding Ni(III) analogues as semi-stable species that gave EPR spectra consistent with the presence of Ni(III) centers (g = 1.96 to 2.44, DMF, 77-100 K).[137] Riordan and coworkers used a variation on this ligand-type to generate dinickel species that could serve as a model for the methylnickel intermediate proposed for the catalytic cycle of acetyl-CoA.[5] They used their model to lend insight into the mechanism of ligand binding to the acetyl-CoA active site. In studies targeting mimics for Ni SOD, the Shearer group utilized a mixed amine/amide analogue of the N_2S_2 framework to act as a structural mimic for the enzyme active site.[138] They conclude that, based on electrochemical data and comparisons with diamine and diamidate analogues, this unique donor set in the protein likely helps balance the redox potential of the active site to prevent either degradation of the protein or overoxidation of the nickel center.

Open-chain ligands that contain amidate donors and stabilize Ni(II) in alternative coordination geometries have received less attention but have been used to prepare nickel complexes that display unique coordination geometries[58, 117, 146] and biomimetic reactivities.[147, 148] As mentioned in the previous chapter, the Borovik group utilized a tripodal open-chain amidate ligand to stabilize a series of late, first row metal ions in trigonal monopyramidal geometries. The bulk of the amide nitrogen's substituents helped enforce this coordinatively unsaturated ligand arrangement around the metal ions. The Ni(II) congener was particularly interesting due to the accessibility of its Ni(II)/(III) couple (0.56 V vs. SCE).[58] Using bulk electrolysis, a short-lived purple species could be observed. It was found that at low temperature (-75 °C), the Ni(II) complex could be chemically oxidized with Ce(IV) or Fe(bpy)$_3$ to generate the purple species, and it was stable in solution at low temperature for ~ 48h. EPR of the purple complex indicated that it contained a Ni(III) S = ½ metal center, however, the complexes structural details were not determined. In a study by the Berreau group, the Ni(II) complex of an amidate-substituted tris(2-pyridylmethyl)amine (tpa) was found to be useful for the glyoxalase I (GlxI)-inspired isomerization of hemithioacetals to thioesters (Scheme 3-1).[147, 148] It was found that the presence of both the Ni(II) ion and the deprotonated *O*-amidate substituent was essential to catalysis, therefore supporting the proposed proton-transfer mechanism for the native protein.

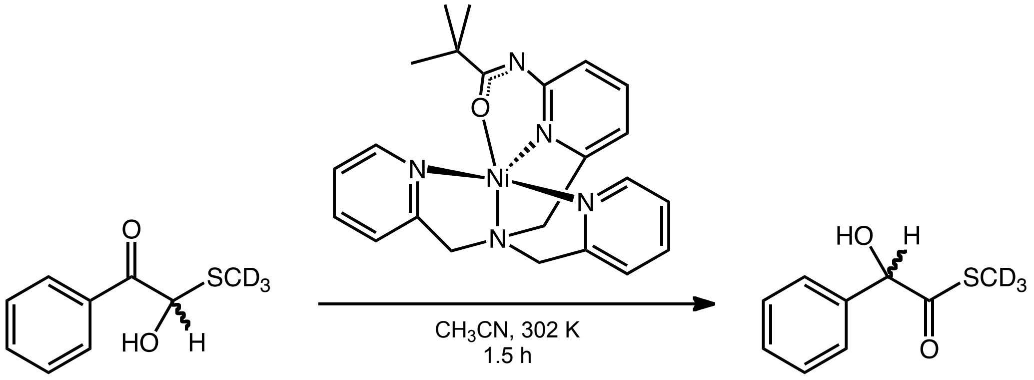

Scheme 3-1. A functional model for glyoxalase I isomerization activity for Berreau, et al.[148]

Ligand systems that incorporate amidate donors are attractive for a number of reasons. Firstly, due to the ease of amide synthesis from amine precursors, these functionalities are highly modular. Secondly, as seen in the case of the Borovik work, amide substituents can be modified to effect both the steric and electronic features of the resulting metal complexes.[57-63] Lastly, amide functional groups are chemically robust. This is best exemplified in proteins, in which amide linkages (peptides) are used to form the skeleton of the molecules, which must undergo constant oxidative stress. A significant challenge when working with amidate ligands is their ambidentate nature (Figure 3-3).[57] The amidate ligand can coordinate to a metal either through its *O*- or *N*-atom, or in some cases the amidate can chelate to a metal in a κ^2 fashion or bridge two metals using both donor atoms.

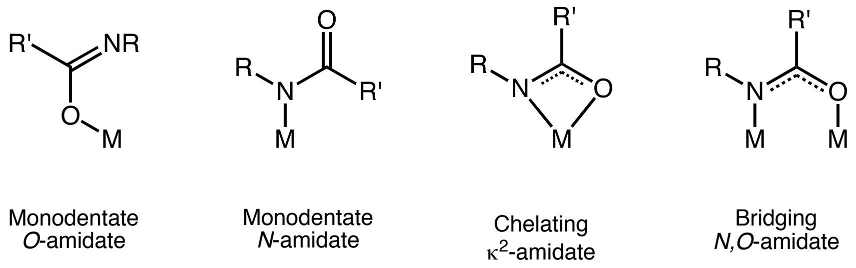

Monodentate *O*-amidate

Monodentate *N*-amidate

Chelating κ^2-amidate

Bridging *N,O*-amidate

Figure 3-3. The possible binding modes of amidate ligands.

Consideration must be taken in order to generate complexes with predictable coordination geometries.

As reported in the previous chapter, our H_3L^R ligand scaffold is capable of supporting metal ions with unique structural properties, and the studies suggested that the amide acyl substituents could be used to regulate exogenous ligand binding.[112] In this chapter, I report the synthesis and characterization of nickel complexes supported by a series of H_3L^R ligands (R = iPr, tBu, Ph).[113] It is demonstrated that the ligand's acyl substituents can be used to control both the coordination number of the nickel center and the coordination mode of the amidate donors in the resulting metal complexes. The cyanide binding properties of these complexes are also discussed.

Section 3-2. Results and Discussion

The *tert*-butyl derivative of the ligand, H_3L^{tBu}, was synthesized in good yield (85%) using a procedure analogous to that for the phenyl and isopropyl derivatives presented in chapter 2 (see Experimental section for complete details). The Ni(II) complexes of all three ligands $Ph_4P[Ni(L^{iPr})]$, $Ph_4P[Ni(L^{tBu})]$, and $Ph_4P[Ni(L^{Ph})(MeCN)]$

were prepared using a generalized route (Scheme 3-2). In a typical preparation, the desired ligand is reacted with a slight excess (3.1 equivalents) of potassium hydride and transmetallated in situ with $NiBr_2$. These steps yield the corresponding potassium salt of the complex (e.g., K[Ni(L^{iPr})]) and two equivalents of KBr as the byproduct.

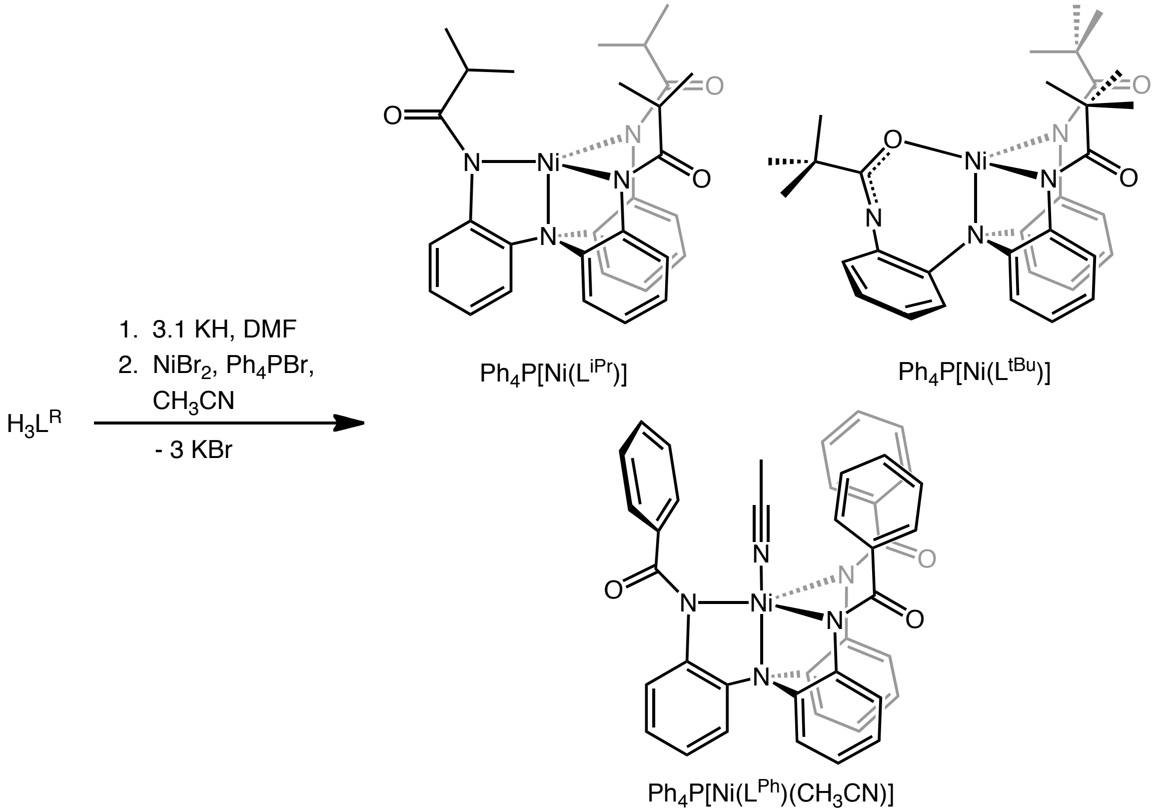

Scheme 3-2. Generalized route to Ni(II) complexes of the H_3L^R ligand (R = iPr, tBu, Ph).

The potassium salts are isolable but difficult to crystallize. It was found that in situ salt metathesis with tetraphenylphosphonium bromide (Ph_4PBr) readily affords the Ph_4P^+ salt (e.g., $Ph_4P[Ni(L^{iPr})]$) of the complex in reasonable yield (see Experimental details for specific yields), as well as loss of the third equivalent of KBr. For each complex, the tetraphenylphosphonium and potassium salts exhibit nearly identical spectroscopic signatures (IR, UV-visible, and ^{1}H NMR), indicating that the countercation is not having a significant effect on the overall coordination chemistry of the ligand in either case. The Ph_4P^+ salts can be crystallized to produce analytically pure materials suitable for X-ray crystallography.

The nickel complexes $Ph_4P[Ni(L^{iPr})]$, $Ph_4P[Ni(L^{tBu})]$, and $Ph_4P[Ni(L^{Ph})(MeCN)]$ have all been characterized by single-crystal x-ray diffraction (For a table of selected metrical parameters, see Table 3-1). Full crystallographic data and refinement parameters are presented in the Experimental section. Orange crystals of $Ph_4P[Ni(L^{iPr})]$ suitable for X-ray diffraction were obtained by diffusion of diethyl ether into a concentrated DMF solution of the complex (Figure 3-4). The Ni(II) ion in $[Ni(L^{iPr})]^-$ possesses a distorted trigonal bipyramidal coordination geometry.

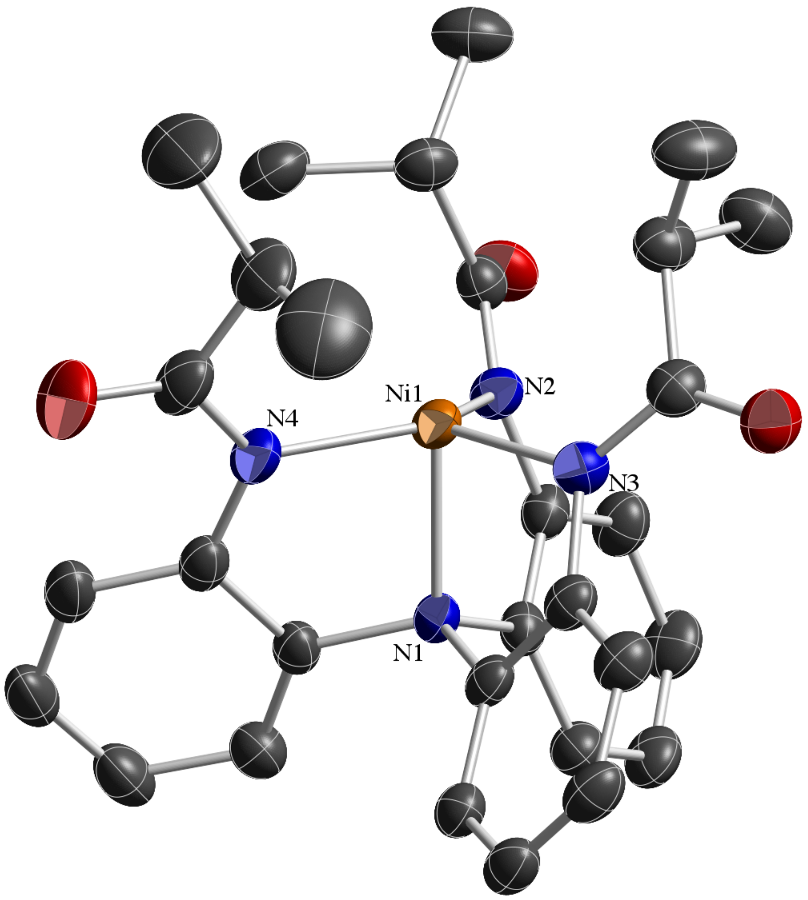

Figure 3-4. Solid-state structure of $Ph_4P[Ni(L^{iPr})]$. Counterion and hydrogen atoms have been omitted for clarity. Thermal ellipsoids are shown at 50% probability.

The three N-amidate donors of the ligands coordinate to the nickel center, making up the equatorial plane, and the tertiary amine donor of the ligand backbone occupies one of the axial sites on the metal ion. All together, these donors make up three five-membered chelate rings around the nickel ion. The complex displays Ni–N_{eq} bond lengths of 1.9542(15), 1.9570(16), and 1.9493(16) Å and an Ni–N_{ax} bond length of 2.0189(15) Å. The N_{eq}–Ni–N_{ax} bond angles (127.19(7), 118.29(7), and 112.67(7)°) are close to the idealized value of 120° expected for a perfect trigonal pyramid. The nickel ion rises

~0.15 Å above the trigonal plane defined by the three amidate donors toward the vacant axial coordination site. The isopropyl substituents of the ligand are positioned above the equatorial plane so that they completely surround the open axial coordination site. This type of arrangement has been observed in other nickel complexes supported by open-chain tris(amidato)amine ligands.[58, 117]

The geometry of four-coordinate metal centers can be quantitatively evaluated using the τ_4 parameter recently described by Houser and coworkers.[121] This parameter is useful, as the extreme values of 0.0 and 1.0 correspond to idealized tetrahedral and square planar geometries, respectively, and idealized intermediate geometries (see-saw and trigonal monopyramidal) fall between these two values. The τ_4 value of 0.82 exhibited by $[\mathrm{Ni}(\mathrm{L}^{\mathrm{iPr}})]^-$ is close to the value expected for an idealized trigonal monopyramidal ligand arrangement (0.85).

Unlike the nickel ion in $[\mathrm{Ni}(\mathrm{L}^{\mathrm{iPr}})]^-$, the equatorial plane surrounding the nickel center in $[\mathrm{Ni}(\mathrm{L}^{\mathrm{tBu}})]^-$ consists of two *N*-amidate donors, and one *O*-amidate donor (Figure 3-5). The two *N*-amidate donors are positioned so that their *tert*-butyl substituents are significantly shielding the nickel center. The third arm of the ligand coordinates through the *O*-amidate donor, which results in the formation of a seven-membered chelate ring within the complex. This coordination mode positions the *tert*-butyl substituent a greater distance from the nickel center, reducing the overall steric strain induced on the complex by the chelate. The bond lengths of the NCO moiety (N–C 1.290(4) and C–O 1.302(3) Å) comprising the *O*-amidate donor indicate that the anionic charge is delocalized throughout the unit.

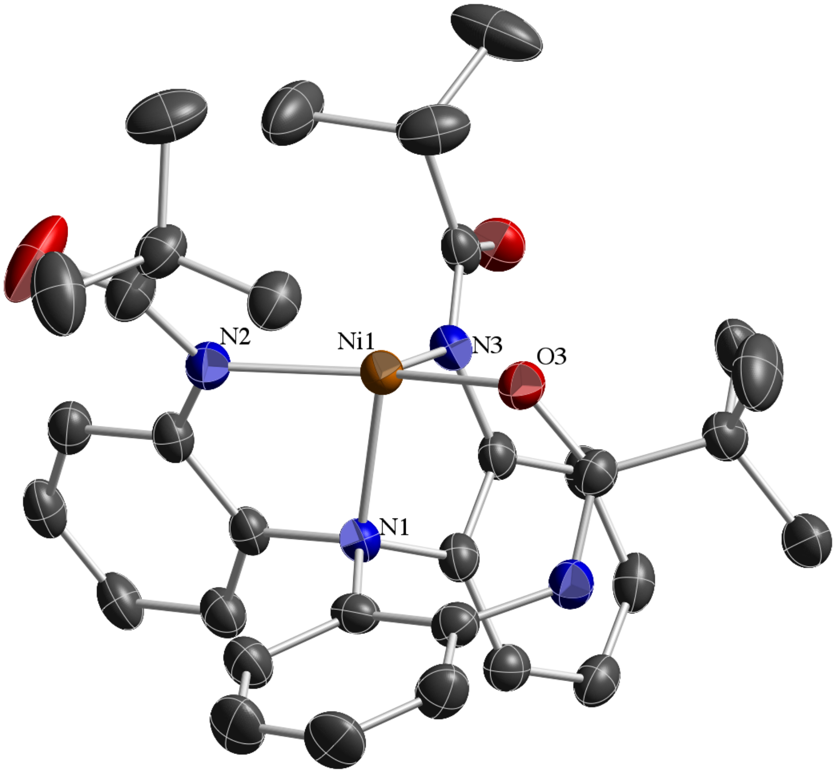

Figure 3-5. Solid-state structure for $Ph_4P[Ni(L^{tBu})]$. Counterion and hydrogen atoms have been omitted for clarity. Thermal ellipsoids are shown at 50% probability.

In this coordination environment, the nickel ion is nearly coplanar with the equatorial donors and deviates only 0.032 Å from the plane. The overall geometry around the Ni(II) ion is distorted trigonal monopyramidal ($\tau_4 = 0.71$). The Ni–N_{eq} bond lengths (1.976(2) and 2.009(2) Å) in $[Ni(L^{tBu})]^-$ are longer than those observed in $[Ni(L^{iPr})]^-$. This lengthening may, in part, be due to the *trans* influence exerted by the stronger *O*-amidate donor. The much shorter Ni–O_{eq} bond length is 1.9167(19) Å.

In contrast to the structures of $[Ni(L^{iPr})]^-$ and $[Ni(L^{tBu})]^-$, in which the nickel ions are four-coordinate, 16 e^- species, the nickel complex of the $[L^{Ph}]^{3-}$ ligand is isolated as a five-coordinate, 18 e^- species, $[Ni(L^{Ph})(MeCN)]^-$ (Figure 3-6).

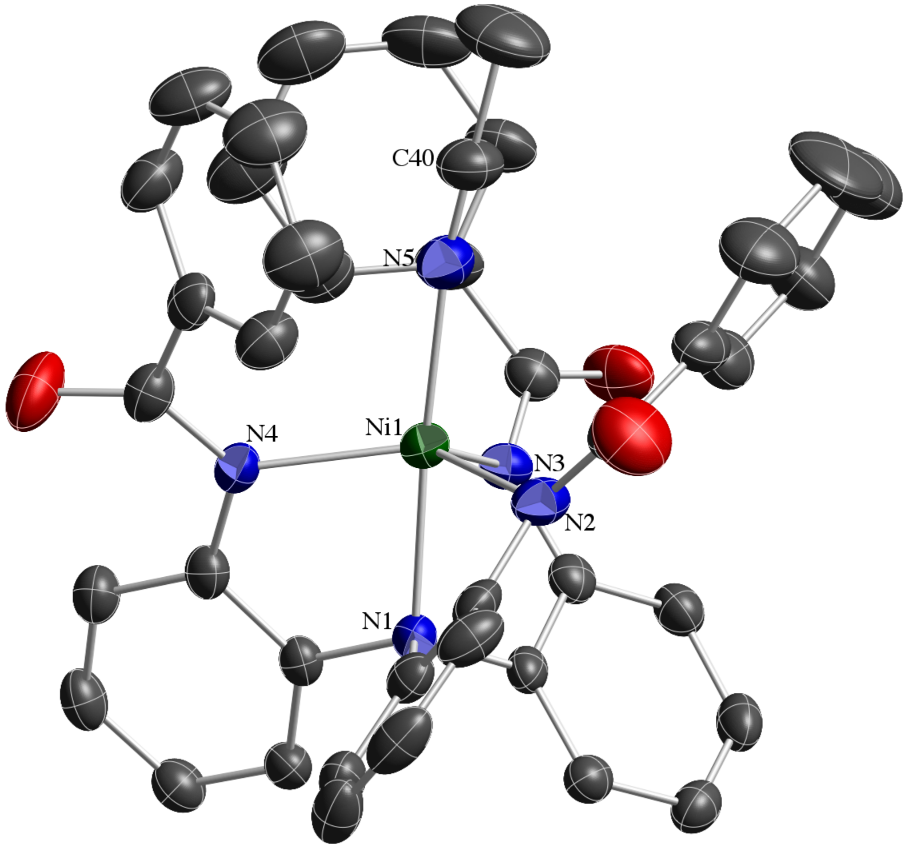

Figure 3-6. Solid-state structure of $Ph_4P[Ni(L^{Ph})(MeCN)]$. Counterion and hydrogen atoms have been omitted for clarity. Thermal ellipsoids are shown at 50% probability.

The phenyl rings of the ligand acyl substituents line up around the cavity with the faces of the rings pointed in towards the open axial coordination site, thus creating a binding site that is much less crowded than those observed in $[Ni(L^{iPr})]^-$ and $[Ni(L^{tBu})]^-$. As such $[Ni(L^{Ph})(MeCN)]^-$ is isolated with a coordinated acetonitrile ligand. The $Ni–N_{eq}$ bond lengths of 2.078(3), 2.056(3), and 2.039(3) Å exhibited by $[Ni(L^{Ph})(MeCN)]^-$ are all longer than the $Ni–N_{eq}$ bond lengths observed in both $[Ni(L^{iPr})]^-$ and $[Ni(L^{tBu})]^-$. In addition, the $Ni–N_{ax}$ bond length (2.080 Å) in $[Ni(L^{Ph})(MeCN)]^-$ is longer than the $Ni–N_{ax}$

bond lengths observed in the four-coordinate species, presumably due to the *trans* influence exerted by the acetonitrile ligand. The N_{ax}–Ni–N_{MeCN} bond angle is nearly linear (175.14(13)°) allowing the phenyl substituents of the ligand to orient about the coordinated acetonitrile in a bowl-like cavity structure.

Table 3-1. Selected metrical parameters for $Ph_4P[Ni(L^{iPr})]$, $Ph_4P[Ni(L^{tBu})]$, and $Ph_4P[Ni(L^{Ph})(MeCN)]$

	$Ph_4P[Ni(L^{iPr})]$	$Ph_4P[Ni(L^{tBu})]$	$Ph_4P[Ni(L^{Ph})(MeCN)]$
Ni–N_{ax}	2.0189(15)	2.043(2)	2.080(3)
Ni–N_{eq} (Å, ave.)	1.9535(16)	1.993(2)	2.058(3)
Ni–N_{MeCN} (Å)	--	--	2.012(3)
Ni–O (Å)	--	1.9167(19)	--
N1–Ni–N2 (°)	86.32(6)	84.25(9)	79.33(12)
N1–Ni–N3 (°)	85.39(7)	82.16(9)	80.01(11)
N1–Ni–N4 (°)	84.85(7)	--	80.13(12)
N1–Ni–O3 (°)	--	102.78	--
N1–Ni–N5 (°)	--	--	175.14(13)
N2–Ni–N3 (°)	112.68(7)	110.16(9)	112.35(13)
N2–Ni–N4 (°)	127.19(7)	--	124.93(13)
N3–Ni–N4 (°)	118.29(7)	--	113.45(12)
Ni–N5–C40 (°)	--	--	170.4(4)

Taken together, these structural data suggest that the relative size of the ligands' amidate acyl substituents can significantly influence both the coordination mode of the ligand and the coordination number of the resulting transition metal complexes. To further probe this trend, attempts were made to synthesize the methyl congener of this series using the H_3L^{Me} ligand. Unfortunately, these experiments led only to complicated reaction mixtures. This result suggests that larger acyl substituents are required to ensure the formation of mononuclear complexes with these ligands. This point will be addressed further in the proceeding chapter.

The nickel complexes have been characterized by ^{1}H NMR, FTIR, and UV-visible absorption spectroscopies. All three complexes, ($[Ni(L^{iPr})]^-$, $[Ni(L^{tBu})]^-$, and $[Ni(L^{Ph})(MeCN)]^-$), exhibit paramagnetically shifted ^{1}H NMR spectra. The ^{1}H NMR (25 °C, CD_3CN) spectra of $[Ni(L^{iPr})]^-$ and $[Ni(L^{Ph})(MeCN)]^-$ are indicative of pseudo C_3-symmetric species in solution (see Experimental section). In contrast, the spectrum of $[Ni(L^{tBu})]^-$, under identical experimental conditions is significantly more complicated, exhibiting seventeen paramagnetically shifted resonances consistent with a lower symmetry (C_1) species. Variable temperature (-60 to 30 °C) ^{1}H NMR spectroscopy was conducted on both $[Ni(L^{iPr})]^-$ and $[Ni(L^{tBu})]^-$ in acetone-d_6 and confirmed the non-fluxional solution-state behavior of these species over this range of temperatures.

The magnetic moments of $[Ni(L^{iPr})]^-$, $[Ni(L^{tBu})]^-$, and $[Ni(L^{Ph})(MeCN)]^-$ were obtained using solution phase ^{1}H NMR methods.[128, 149] The four-coordinate species, $[Ni(L^{iPr})]^-$ and $[Ni(L^{tBu})]^-$, exhibit μ_{eff} values of 3.03 and 3.37 μ_B, respectively, indicative of $S = 1$ ground states. The five-coordinate $[Ni(L^{Ph})(MeCN)]^-$ exhibits a μ_{eff} value of 3.27

μ_B (25 °C, DMSO-d_6), similar to other five-coordinate Ni(II) species having high-spin, S = 1 ground states.[150-156] The UV-visible absorption spectra for $[Ni(L^{iPr})]^-$, $[Ni(L^{tBu})]^-$, and $[Ni(L^{Ph})(MeCN)]^-$ were recorded at room temperature as DMF solutions. The four-coordinate complexes $[Ni(L^{iPr})]^-$ and $[Ni(L^{tBu})]^-$, exhibit similar spectra with λ_{max} values at 525 and 520 nm, respectively. The five-coordinate species, $[Ni(L^{Ph})(MeCN)]^-$, exhibits a broad absorbance centered at 707 nm. A similar broad absorbance (694 nm) has been observed and its transitions assigned ($^3E'(F) \rightarrow {}^3A_1'(F), {}^3A_2'(F)$) for a trigonal bipyramidal Ni(II) complex containing an N_2O_3 donor set.[151, 157]

All three complexes were also examined by cyclic voltammetry, however, only the isopropyl complex, $[Ni(L^{iPr})]^-$, displays reversible electrochemical events (Figure 3-7).

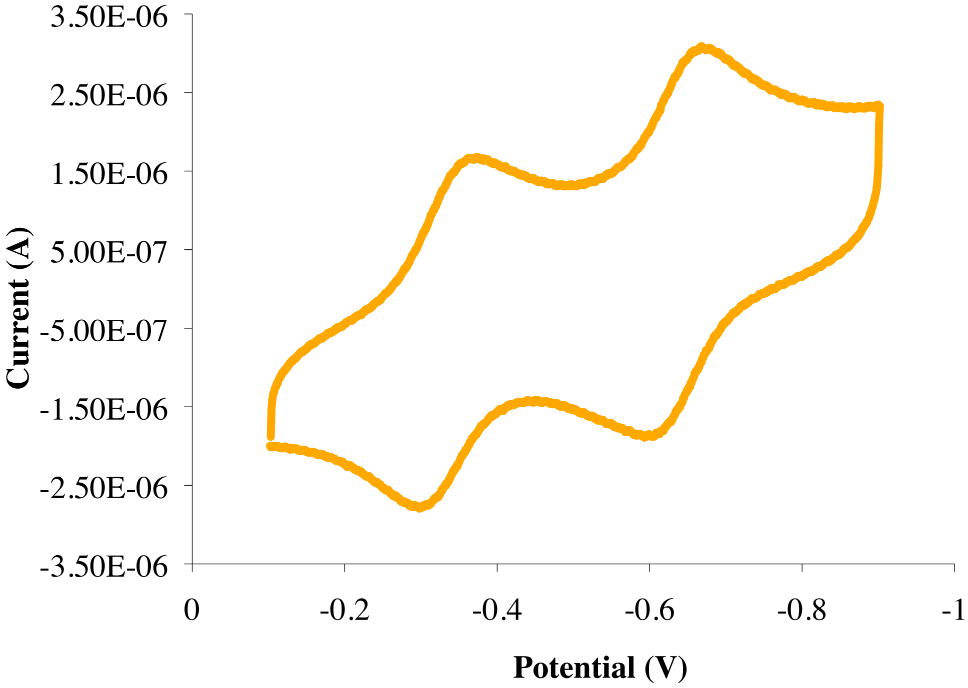

Figure 3-7. Cyclic voltammogram (0.1 V/s) of $[Ni(L^{iPr})]^-$ at a glassy carbon electrode in DMF (298 K) with 0.2 M $TBAPF_6$ as supporting electrolyte.

The complex displays two, reversible electrochemical events at -0.374 V (ΔE_p = 0.075 V; i_{pc}/i_{pa}^{-1} = 0.98) and -0.669 V (ΔE_p = 0.075 V; i_{pc}/i_{pa}^{-1} = 1.28) vs Fc^0/Fc^+. These one-electron processes have not been assigned, however, they are most likely metal- or ligand-based oxidation events. Attempts to generate these species chemically have only yielded mixtures consistent with demetallation of the ligand.

The differences in coordination number and environment exhibited by $[Ni(L^{iPr})]^-$, $[Ni(L^{tBu})]^-$, and $[Ni(L^{Ph})(MeCN)]^-$ prompted us to explore the ability of these complexes to coordinate exogenous ligands. Specifically, the ability of these complexes to bind cyanide was probed because it is a small, linear donor. The orange $[Ni(L^{iPr})]^-$ complex reacts readily with one equivalent of tetraethylammonium cyanide (Et_4NCN) to produce a green solution (Scheme 3-3).

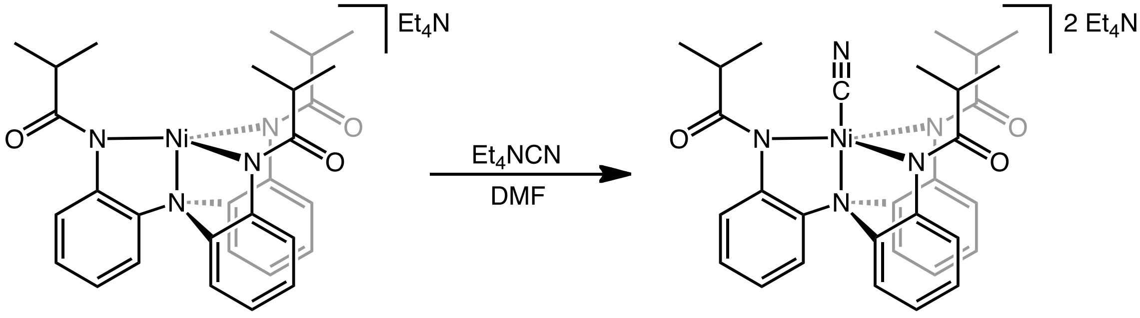

$Et_4N[Ni(L^{iPr})]$

$(Et_4N)_2[Ni(L^{iPr})CN]$

μ_{eff} = 3.25 μ_B (Evans' Method, $(CD_3)_2SO$, 298K)

FTIR (KBr, cm^{-1}) ν(CN) 2112

Scheme 3-3. Synthesis of cyanide adduct, $(Et_4N)_2[Ni(L^{iPr})(CN)]$.

The nickel-containing product of this reaction is formulated to be $[Ni(L^{iPr})(CN)]^{2-}$ by spectroscopic match to an authentic sample prepared directly from the protio ligand in a one-pot procedure (see Experimental section for details).

The dianionic cyanide complex, $[Ni(L^{iPr})(CN)]^{2-}$, exhibits a cyanide stretch in the IR spectrum at 2112 cm^{-1} consistent with a terminally-bound cyanide ligand. [158] This complex is paramagnetic and exhibits a μ_{eff} value of 3.25 μ_B (25 °C, DMSO-d_6) indicative of a high-spin, $S = 1$ system (*vide supra*). This species can be recrystallized by the slow diffusion of diethyl ether into a concentrated DMF solution of the complex to afford X-ray quality crystals. Results of the single crystal X-ray diffraction studies carried out on $(Et_4N)_2[Ni(L^{iPr})(CN)]$ indicate that the complex crystallizes in a $P2_1/n$ space group with $Z = 8$. There are two crystallographically independent and geometrically dissimilar $[Ni(L^{iPr})(CN)]^{2-}$ units within the asymmetric unit cell (Figure 3-8). Both nickel centers are five-coordinate and contain the same donor atoms within their primary coordination sphere (see table 3-2 for selected metrical parameters).

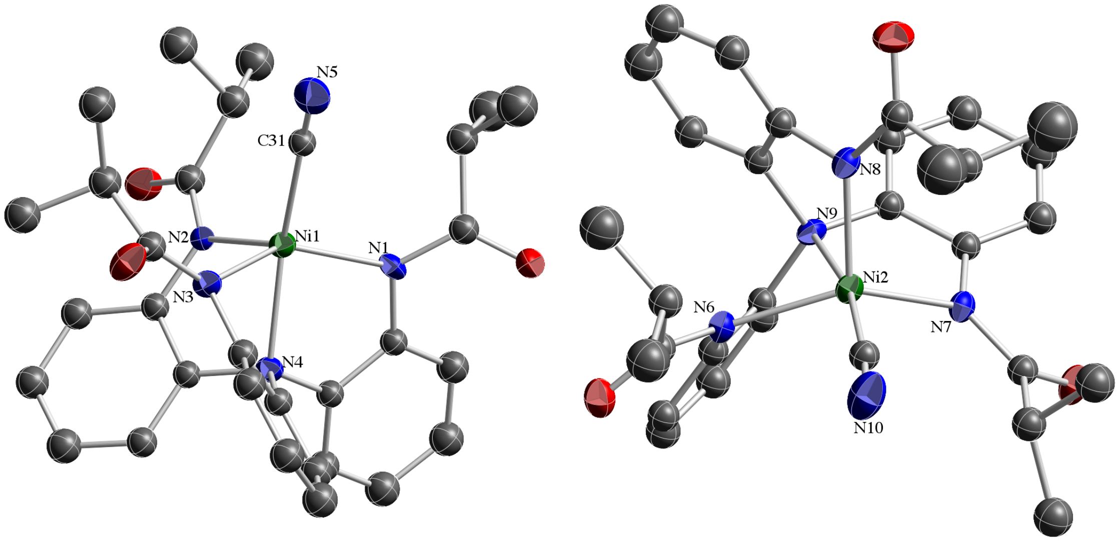

Figure 3-8. Solid-state structure of the two crystallographically independent molecules in the unit cell of $(Et_4N)_2[Ni(L^{iPr})(CN)]$. Counterions and hydrogen atoms are omitted for clarity. Thermal ellipsoids are shown at 50% probability.

Each Ni(II) ion is coordinated by three *N*-amidate and one tertiary amine donor of the chelating ligand and a terminal cyanide ligand. In one of the anions, $[Ni\mathbf{1}(L^{iPr})(CN)]^{2-}$, the nickel center displays a distorted trigonal bipyramidal geometry. The other nickel center, $[Ni\mathbf{2}(L^{iPr})(CN)]^{2-}$, exhibits a distorted square pyramidal coordination geometry. For five-coordinate species, the degree of distortion between idealized trigonal bipyramidal and square pyramidal geometries can be quantified by using the τ_5 parameter defined by Addison and Reedijk.[120] The value of τ_5 varies between 0.0 for idealized square pyramidal geometry and 1.0 for idealized trigonal bipyramidal geometry. Applying this structural parameter to $[Ni\mathbf{1}(L^{iPr})(CN)]^{2-}$ and $[Ni\mathbf{2}(L^{iPr})(CN)]^{2-}$ gives rise to τ_5 values of 0.59 and 0.26, respectively, illustrating their intermediate geometries.

Table 3-2. Selected metrical parameters for the two geometrical isomers of $[Ni(L^{iPr})(CN)]^{2-}$

	$[Ni\mathbf{1}(L^{iPr})(CN)]^{2-}$	$[Ni\mathbf{2}(L^{iPr})(CN)]^{2-}$
Ni–N_{amide} (ave.)	2.071(5) Å	2.067(4) Å
Ni–N_{amine}	2.139(4) Å	2.122(5) Å
Ni–C_{CN}	2.019(7) Å	2.018(6) Å
N_{amine}–Ni–C_{CN}	169.0(2)°	158.9(2)°
Ni–C_{CN}–N_{CN}	173.6(6)°	167.2(6)°

Co-crystallization of geometrical[120, 159-164] or polytopal isomers[164-166] within the same unit cell has been observed for other transition metal systems. Co-crystallization of these species is rare, however, because compounds with different molecular structures typically possess different crystallization kinetics and crystal lattice packing energies.[167] These structural data suggest that the two geometries observed for $[Ni(L^{iPr})(CN)]^{2-}$ in the solid-state are very similar in energy and that, in solution, a distribution of these geometries must exist. In solution, $[Ni(L^{iPr})(CN)]^{2-}$ displays a single, quasi-reversible electrochemical event (0.050 V s^{-1}) in its cyclic voltammogram centered at -0.251 V (ΔE_p = 0.116 V; i_{pc}/i_{pa}^{-1} = 0.76) vs Fc^0/Fc^+ (Figure 3-9).

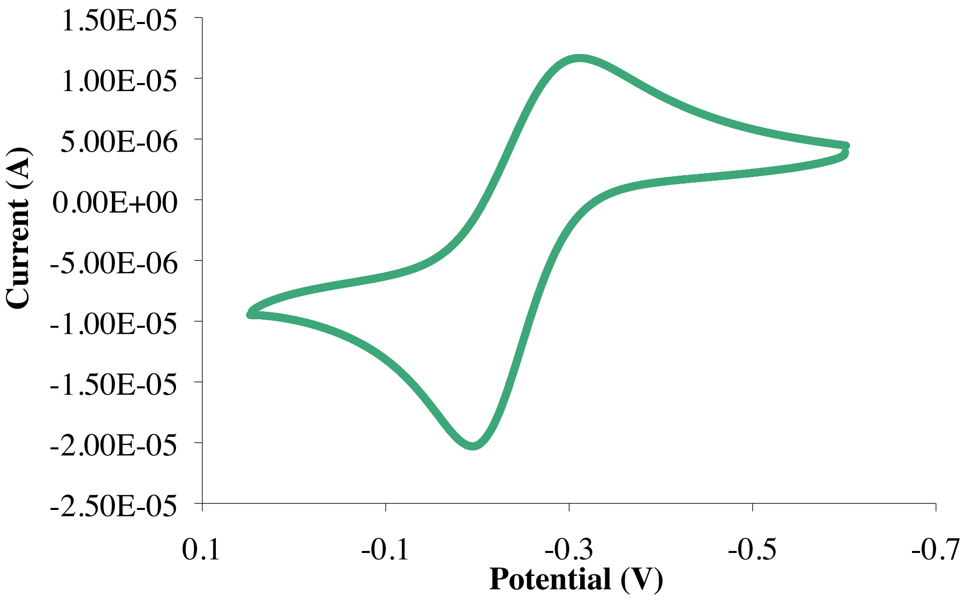

Figure 3-9. Cyclic voltammogram (0.05 V/s) of $[Ni(L^{iPr})(CN)]^{2-}$ at a glassy carbon electrode in DMF (298 K) with 0.2 M $TBAPF_6$ as supporting electrolyte.

We have tentatively assigned this process to the Ni(II)/(III) couple. Attempts to chemically oxidize $(Et_4N)_2[Ni(L^{iPr})(CN)]$ by one electron have been unsuccessful.

When the $[Ni(L^{tBu})]^-$ complex is treated with cyanide, a slight color change from orange to red-orange is observed. This reaction, however, does not give rise to a single, well-defined product in solution. Both solution-state IR and ^1H NMR spectroscopy indicate that cyanide does interact to some extent with the nickel center. For example, in the solution-state FTIR spectrum (MeCN) a major ν(CN) stretching band appears at 2109 cm^{-1}, suggesting coordination of the cyanide ligand in a terminal fashion,[158] similar to what is observed for the isolated $[Ni(L^{iPr})(CN)]^{2-}$ species. However, several lower intensity, higher frequency bands also appear (2150 and 2186 cm^{-1}) that cannot be definitively assigned. The ^1H NMR spectrum (CD_3CN) also reveals the presence of at least two major species in solution. One of the species is paramagnetic and exhibits a spectrum nearly identical to the $[Ni(L^{tBu})]^{-}$ starting material. The second species is diamagnetic and exhibits three distinct *tert*-butyl CH_3 resonances. These data are consistent with the existence of a solution-state equilibrium between a diamagnetic, square planar complex and a paramagnetic species. It is likely that cyanide coordination to the nickel center in $[Ni(L^{tBu})]^{-}$ may cause one of the coordinated ligand arms to dissociate to afford a square planar species. Similar solution-state equilibria have recently been observed for nickel complexes supported by scorpionate ligands.[168] The $[Ni(L^{Ph})(MeCN)]^{-}$ complex also reacts with cyanide to produce a complex reaction mixture that contains both paramagnetic and diamagnetic products. This result was somewhat surprising as the solid-state data obtained for $[Ni(L^{Ph})(MeCN)]^{-}$ clearly demonstrates the ability of this ligand to support five-coordinate Ni(II) species. Most likely, as with the Co(II) analogue of this complex described in chapter 2, the close proximity of the electron-rich phenyl rings of the ligand arms to the open axial site on the metal center results in coulombic repulsion of approaching anions, destabilizing anion binding, while conserving the ability to bind neutral ligands (i.e., MeCN).

The unusual ligand field environment for Ni(II) ions provided by the triamidate ligand architecture may influence magnetic anisotropy parameters, which are of interest in the field of molecular magnetism.[169, 170] As such, a collaboration with the Shores group at Colorado State was developed in order to obtain solid-state magnetic data for $Ph_4P[Ni(L^{iPr})]$ and $(Et_4N)_2[Ni(L^{iPr})(CN)]$. The temperature dependence of $\chi_M T$ for $(Et_4N)_2[Ni(L^{iPr})(CN)]$ was plotted (Figure 3-10).

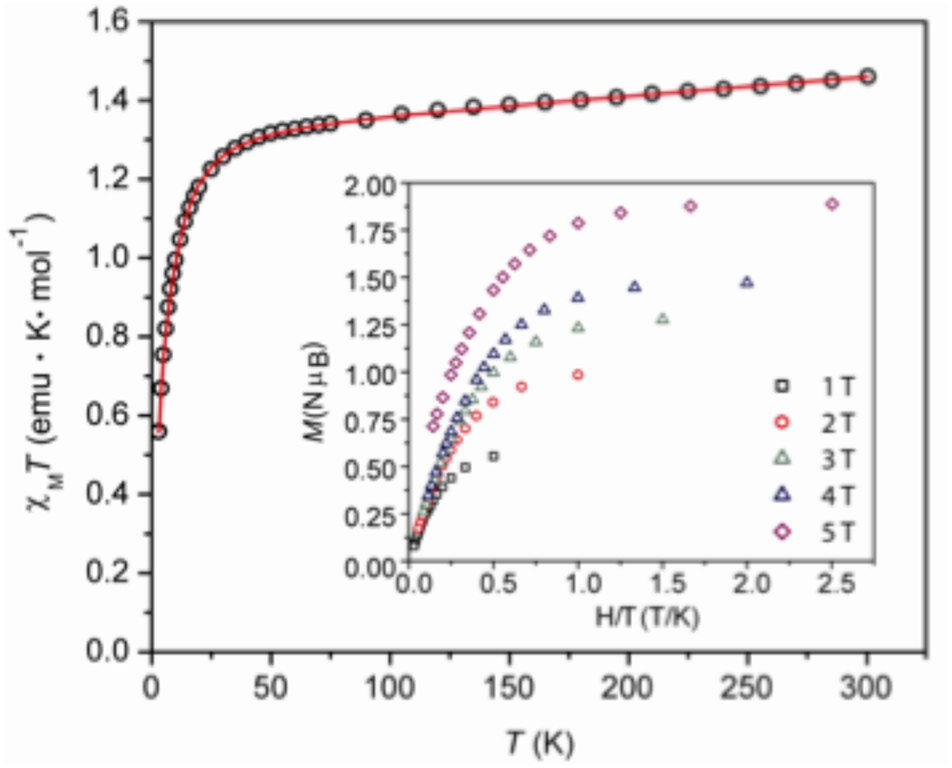

Figure 3-10. Temperature dependence of magnetic susceptibility for $(Et_4N)_2[Ni(L^{iPr})(CN)]$ obtained at a measuring field of 0.1 T. The red line indicates the best fit. Inset: Magnetization of $(Et_4N)_2[Ni(L^{iPr})(CN)]$ as a function of reduced magnetic field.

The $\chi_M T$ value of 1.46 emu K mol^{-1} at 300K is significantly larger than that expected for a mononuclear Ni(II) complex with S = 1 and g = 2.00 (1.00 emu K mol^{-1}). The product decreases gradually to 1.32 emu K mol^{-1} at 50 K, followed by a steep drop to 0.56 emu K mol^{-1} at 2 K. Qualitatively similar data are obtained for $Ph_4P[Ni(L^{iPr})]$ (Figure 3-11).

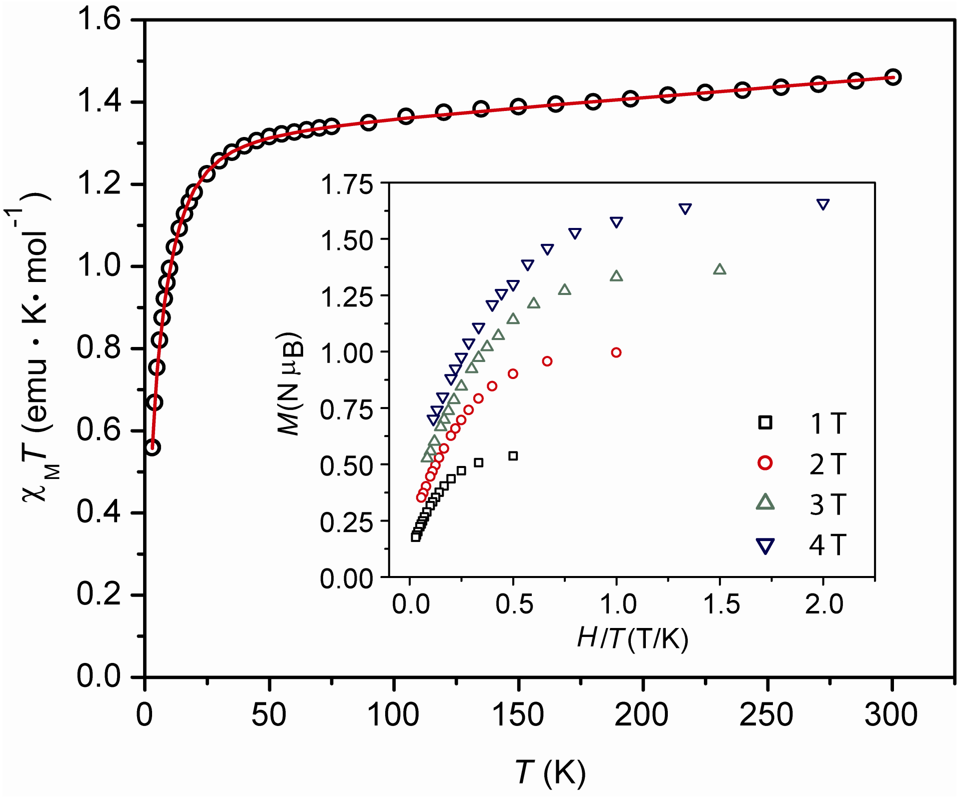

Figure 3-11. Temperature dependence of magnetic susceptibility for $Ph_4P[Ni(L^{iPr})]$ obtained at a measuring field of 0.1 T. The red line indicates the best fit. Inset: Magnetization of $Ph_4P[Ni(L^{iPr})]$ as a function of reduced magnetic field.

For fitting the susceptibility data to a magnetic model, the first scenario considered was the most likely one, in which the unpaired spin was localized on the nickel center (i.e., Ni(II), $S = 1$). For $Ph_4P[Ni(L^{iPr})]$, the best fit affords $g = 2.35$, $D = -19.44$ cm^{-1}, $E = -1.46$ cm^{-1}, temperature independent paramagnetism (TIP) = 808 × 10^{-6} emu mol^{-1}, and relative error $f = 0.018$. Similarly, the best fit for $(Et_4N)_2[Ni(L^{iPr})(CN)]$ gives $g = 2.295$, $D = -23.03$ cm^{-1}, $E = -2.60$ cm^{-1}, TIP = 475 × 10^{-6} emu mol^{-1}, and relative error $f = 0.005$. In both cases, the fitted $|D|$ and TIP values are significantly larger than might be expected. The former may be due to weak intermolecular interactions being incorporated into the phenomenological *D* parameter (although no obvious exchange pathways exist in the crystal structure); the latter may be indicative of low lying excited spin states, and similar values have been reported for a Ni(II) porphyrin complex.[171] Nevertheless, two other alternative scenarios were considered. The potential coupling of a Ni(II) center (S = ½) with a radical dianionic ligand did not result in any reasonable fits to the data. Alternatively, antiferromagnetic coupling of a high-spin Ni(III) center (S = 3/2) with a radical tetraanionic ligand (S = ½) afforded large intramolecular exchange coupling ($J \sim -5000\ \text{cm}^{-1}$) and a reasonable g_{Ni} of ~2.3, but only when the radical g was fixed at 2.00; even then, the fits were inferior to the original scenario.

To examine magnetic anisotropy in more detail, magnetization data at various fields between 2 and 35 K were collected. The data collected at different fields do not overlay each other and deviate significantly from the Brillouin function expected for S = 1, indicating significant zero-field splitting. However, modeling the data with ANISOFIT[172] does not afford satisfactory fits, even when fitting is restricted to the lowest temperatures (< 14 K). The lack of agreement is likely due to the presence of low-lying excited spin states; unfortunately ANISOFIT requires well-isolated ground spin states to give the best fits. Overall, it seems most likely that an S = 1 Ni(II) ion with significant (but complicated) zero-field splitting is operative in these compounds.

The ability of $[\text{Ni}(\text{L}^{\text{iPr}})]^{-}$ to irreversibly bind cyanide in solution is unique for this series of complexes. We next sought to investigate whether $[\text{Ni}(\text{L}^{\text{iPr}})(\text{CN})]^{2-}$ could be used to form heterobimetallic complexes. Our motivation for this study is based upon the widespread utility of terminal cyanide complexes in the assembly of molecular, cyanide-bridged clusters via the "building block approach."[169, 170, 173-175] Cyanide complexes with terminal cyanide ligands or open binding sites are often used as capping or blocking groups in the construction of these species. Thus, the reaction of green $[\mathrm{Ni(L^{iPr})(CN)}]^{2-}$ with a four-coordinate, trigonal monopyramidal Co(II) complex of the same ligand, $[\mathrm{Co(L^{iPr})}]^{-}$,[112] immediately produces a reddish-purple solution (Scheme 3-4).

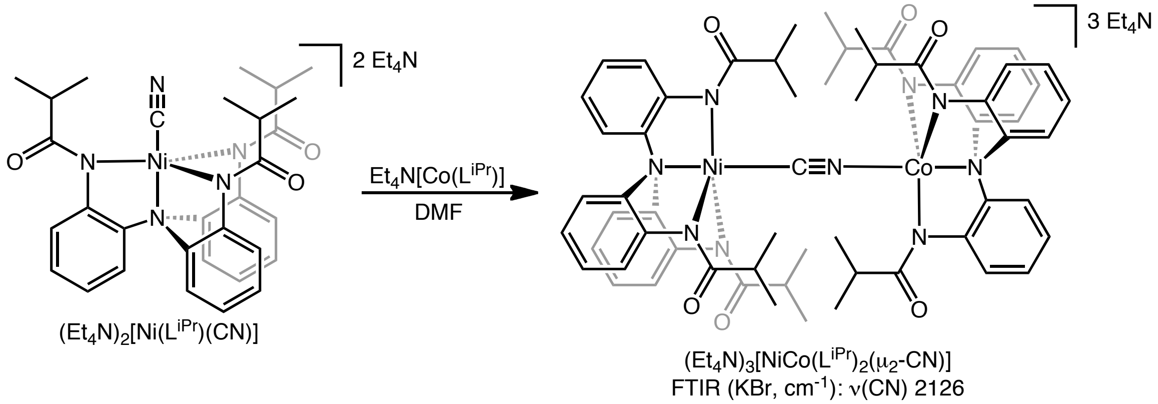

Scheme 3-4. Synthesis of heterobimetallic cyanide adduct, $\mathrm{(Et_3N)_3[CoNi(L^{iPr})_2(\mu_2\text{-}CN)]}$.

The product of this reaction is isolated as a reddish-purple solid in good yield (83%). FTIR studies suggest a bridging coordination mode of the cyanide ligand, as the product exhibits a single ν(CN) (KBr) stretch at 2126 cm^{-1}. The increase in cyanide stretching frequency observed for the product compared to the mononuclear nickel cyanide precursor is consistent with the formation of a cyanide-bridged species.[173]

Crystals of a quality suitable for X-ray diffraction were grown by the diffusion of diethyl ether into a concentrated DMF solution of the product. The molecular structure of the heterobimetallic complex, $\mathrm{(Et_3N)_3[CoNi(L^{iPr})_2(\mu_2\text{-}CN)]}$ crystallizes in a rhombohedral space group (*R*3) and adopts 3-fold symmetry (Figure 3-12).

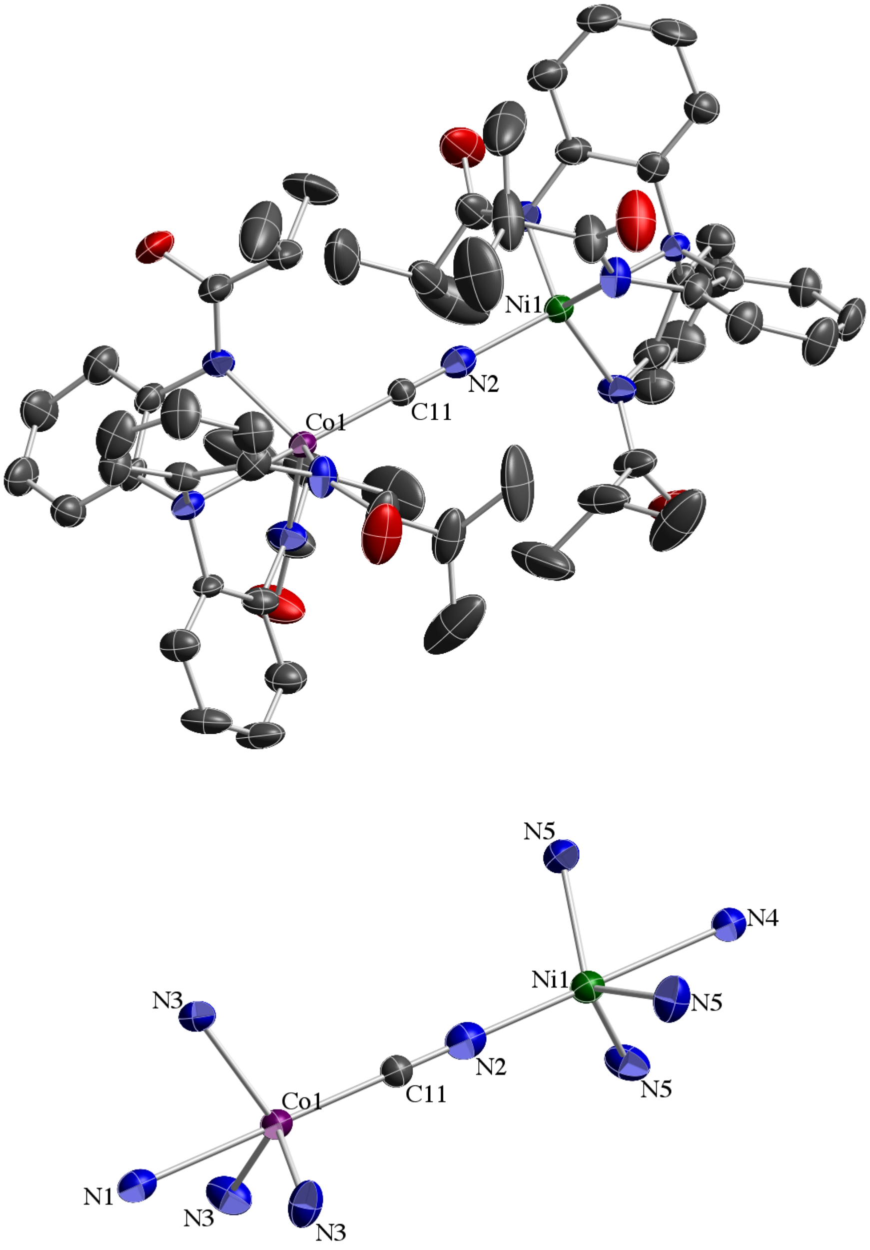

Figure 3-12. Solid-state structure of $(Et_3N)_3[CoNi(L^{iPr})_2(\mu_2\text{-}CN)]$ (top) and the primary coordination sphere of $(Et_3N)_3[CoNi(L^{iPr})_2(\mu_2\text{-}CN)]$ (bottom). Counterions and hydrogen atoms are removed for clarity. Thermal ellipsoids are shown at 30% probability.

The crystals contained poorly resolved solvent peaks and there was some disorder in the pendant arms of the tetraethylammonium cations. Nevertheless, the $[CoNi(L^{iPr})_2(\mu_2\text{-}CN)]^{3-}$ unit is well resolved. To be confident that the correct molecular geometry had been assigned, the nickel and cobalt atoms were exchanged as well as the carbon and nitrogen atoms of the bridging cyanide ligand and their final positions verified after least squares analysis by critical evaluation of their respective atomic displacement parameters. Note that the orientation of the cyanide bridging ligand in $[CoNi(L^{iPr})_2(\mu_2\text{-}CN)]^{3-}$ is different from that observed in the $[Ni(L^{iPr})(CN)]^{2-}$ precursor, i.e., the cyanide ligand in coordinated to the nickel center via the nitrogen atom. This type of cyanide flipping or linkage isomerism has been observed in the formation of other bridged cyanide clusters.[176] The Ni(II) and Co(II) centers both display distorted trigonal bipyramidal coordination geometries with $M(II)–N_{eq}$ bond lengths similar to those observed in the mononuclear complexes (for selected metrical parameters, see Table 3-3). Each metal center displays relatively long (> 2.3 Å) $M(II)–N_{ax}$ bond lengths.[177] Long $M(II)–N_{tert.\ amine}$ bond distances have been observed in other dinuclear Ni(II)[178-182] and Co(II)[183-185] complexes supported by sterically demanding ligands. The $M(II)–N_{ax}$ elongation observed in $[CoNi(L^{iPr})_2(\mu_2\text{-}CN)]^{3-}$ is likely due to the geometric distortions that occur upon formation of the bimetallic complex.

Table 3-3. Selected metrical parameters for the two metal ions in $[\mathrm{CoNi}(\mathrm{L}^{\mathrm{iPr}})_2(\mu_2\text{-CN})]^{3-}$

	$[\mathbf{Co}\mathrm{Ni}(\mathrm{L}^{\mathrm{iPr}})_2(\mu_2\text{-CN})]^{3-}$	$[\mathrm{Co}\mathbf{Ni}(\mathrm{L}^{\mathrm{iPr}})_2(\mu_2\text{-CN})]^{3-}$
M–$\mathrm{N}_{\mathrm{amide}}$ (ave.)	2.035(4) Å	2.030(4) Å
M–$\mathrm{N}_{\mathrm{amine}}$	2.354(9) Å	2.390(9) Å
Co–C_{CN}	2.029(13) Å	--
Ni–N_{CN}	--	2.063(12) Å

Specifically, the two $[(\mathrm{L}^{\mathrm{iPr}})]^{3-}$ ligands which cap the Co(II) and Ni(II) centers are positioned so that the isopropyl substituents are interlocked about the bridging cyanide ligand, forcing a completely linear N1–Co–C≡N–Ni–N4 arrangement of atoms within the molecule. In addition, both the Co(II) and Ni(II) centers are distorted ~0.55 Å away from the trigonal planes formed by the *N*-amidate donors of the $[(\mathrm{L}^{\mathrm{iPr}})]^{3-}$ ligands toward the bridging cyanide. This type of co-linear arrangement of atoms within multimetallic assemblies has been previously observed in binuclear Cu(II) cryptates[186, 187] and in Co(II) cyanide clusters assembled with capping ligands.[188] These results suggest that transition metal complexes supported by $[(\mathrm{L}^{\mathrm{R}})]^{3-}$-type ligands may be useful as capping species in the assembly of larger molecular clusters.[189]

The Shores group also gathered solid-state magnetic data for $(\mathrm{Et}_3\mathrm{N})_3[\mathrm{CoNi}(\mathrm{L}^{\mathrm{iPr}})_2(\mu_2\text{-CN})]$. A plot of the temperature dependence of $\chi_{\mathrm{M}}T$ (obtained at 0.1 T) shows a value for $\chi_{\mathrm{M}}T$ of 5.07 emu K mol^{-1} at 300 K, which is significantly larger than expected for non-interacting $S = 1$ Ni(II) and $S = 3/2$ Co(II) spin centers (2.875 emu

K mol^{-1}) (Figure 3-13). The product decreases linearly (due to Co(II) orbital moment and/or TIP) to 3.59 emu K mol^{-1} at 70 K.

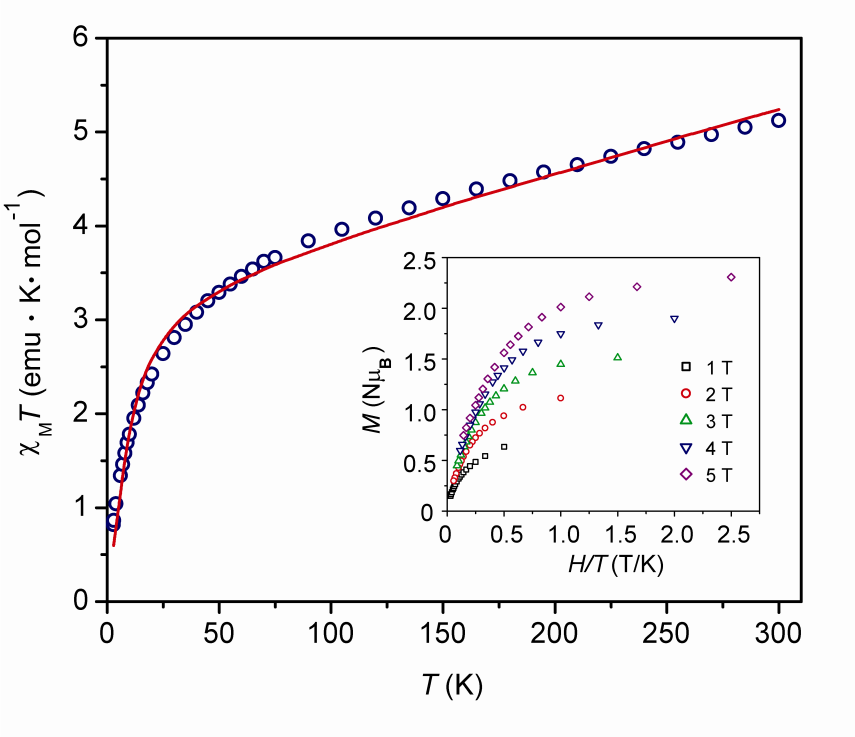

Figure 3-13. Temperature dependence of magnetic susceptibility for $(Et_3N)_3[CoNi(L^{iPr})_2(\mu_2\text{-}CN)]$ obtained at a measuring field of 0.1 T. The red line indicates the best fit. Inset: Magnetization of $(Et_3N)_3[CoNi(L^{iPr})_2(\mu_2\text{-}CN)]$ as a function of reduced magnetic field.

At lower temperatures, the susceptibility drops off more rapidly to 0.86 emu K mol^{-1} at 3 K. Using JulX,[190] and assuming no zero-field splitting, the best fit to the data indicates weak antiferromagnetic coupling between the Co(II) and Ni(II) ions (J = -2.04 cm^{-1}). This is consistent with expected weak superexchange (through cyanide π* orbitals) between the singly-occupied molecular orbitals of the constituent ions, which for Ni(II) and Co(II) ions should have the same symmetries.[169] A large TIP value is observed, consistent both with the Ni–CN complex $(Et_4N)_2[Ni(L^{iPr})(CN)]$, as well as distortion of the local coordination sphere around the Co(II) ion, which is known to give large TIP and Zeeman contributions to the susceptibility.[191]

As with the mononuclear complexes, magnetization data clearly show significant magnetic anisotropy; however, this data does not yield reasonable fits using ANISOFIT. In addition to the issues described above for the mononuclear Ni(II) precursor, it has been shown that fitting magnetization data with Co(II) complexes can be difficult due to mixing of low-lying excited states into the ground state,[192] as well as the presence of Zeeman effects. Evidence for this is shown in the susceptibility data, where at higher fields the data tracks under those obtained at lower fields (Figure 3-14).[193]

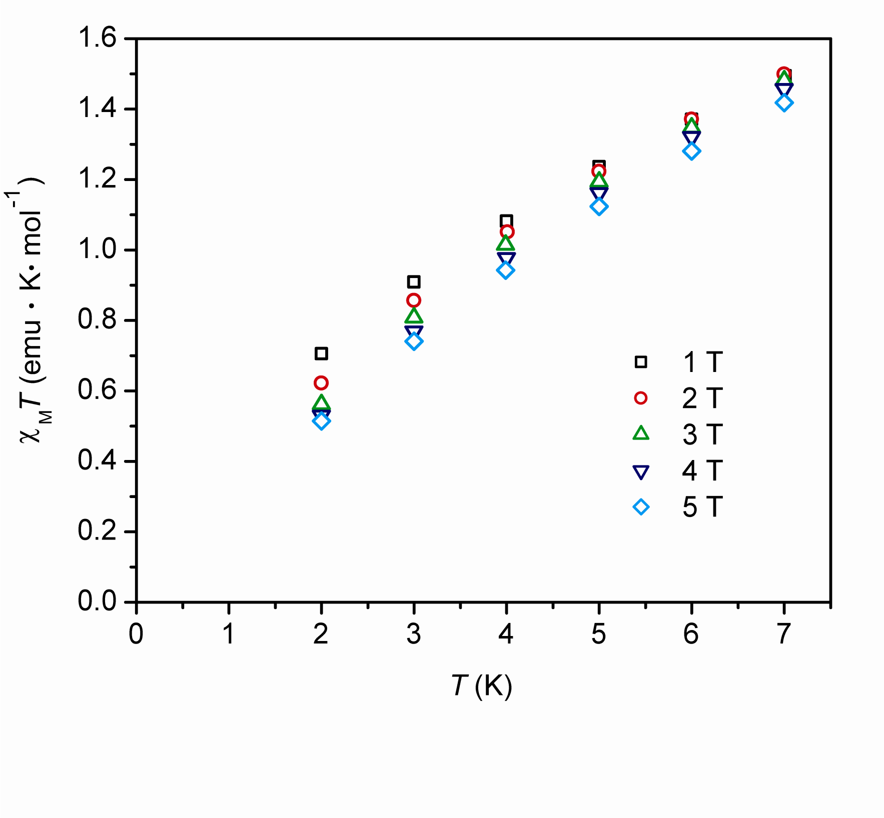

Figure 3-14. Low temperature expansion of magnetic susceptibility of $[Et_4N]_3[CoNi(L^{iPr})_2(\mu_2\text{-}CN)]$ collected at various fields.

If D is included in the fits to the susceptibility data, the quality improves somewhat when the parameter is allowed to refine freely, affording $D = 20\ cm^{-1}$ (Figure 3-15). As $|D|$ values for Co(II) complexes are typically 1 cm^{-1} to 5 cm^{-1},[194] this large value would appear to trace back to the presence of Ni(II), similar to the mononuclear species. In spite of rather weak coupling, the apparently large values of magnetic anisotropy merit further study.

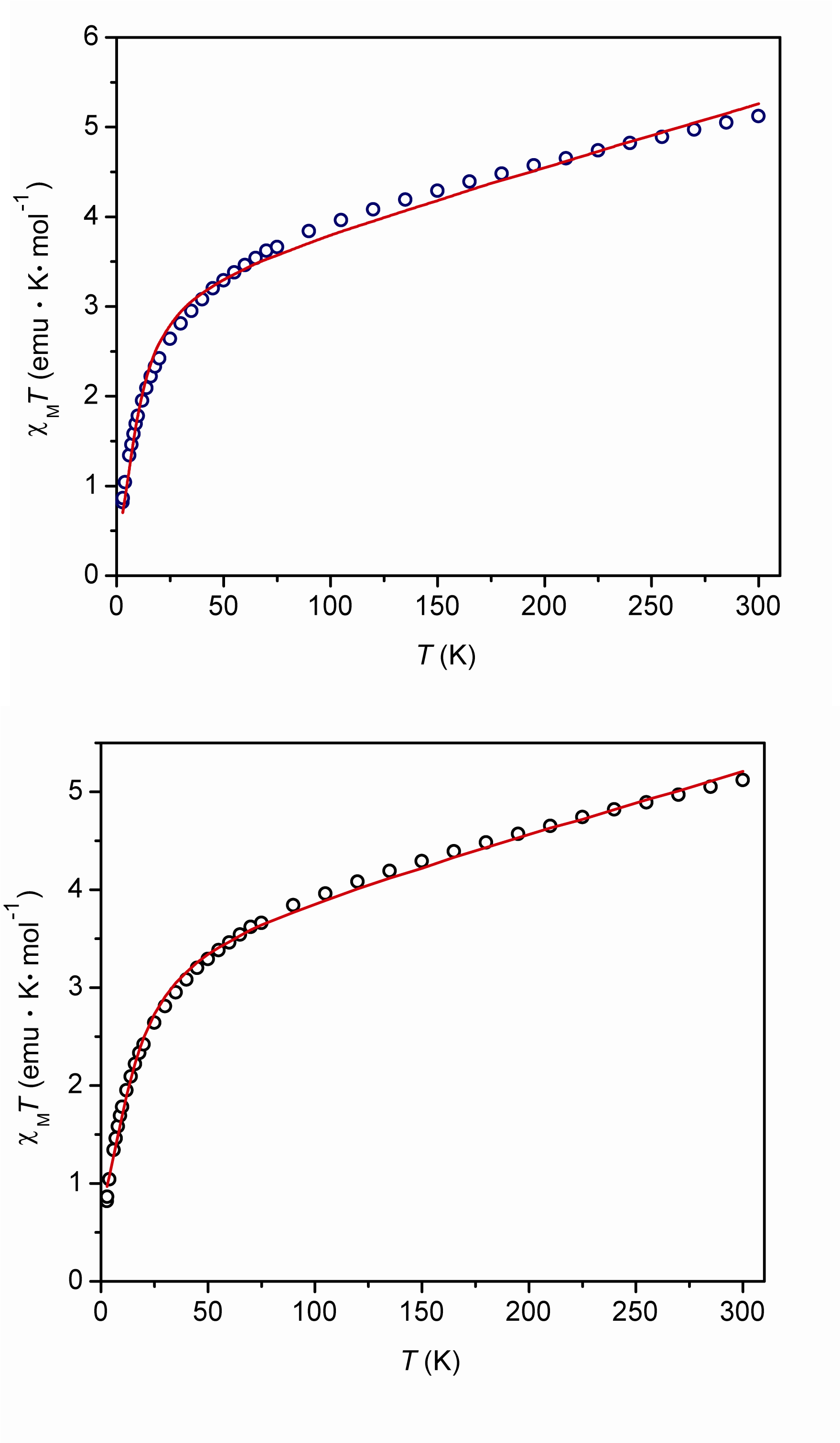

Figure 3-15. Fits of the susceptibility data for $(Et_3N)_3[CoNi(L^{iPr})_2(\mu_2\text{-}CN)]$ with D fixed (top) and with D allowed to refine freely (bottom).

The work in this chapter has demonstrated that the amidate substituents on the ligand scaffold $[(L^R)]^{3-}$ can be varied to control both the coordination mode of the ligands' amidate donors as well as the coordination number of the transition metal centers in the resulting complexes. It has also been shown that the unusual ligand fields presented by this family of ligands engender interesting magnetic behavior in the Ni(II) complexes studied, and merit more in depth investigation into their possible use as monomers for magnetic materials. Overall, these studies demonstrate that these chelating triamidate ligands offer highly tunable and versatile scaffolds for Ni(II).

Section 3-3. Experimental

General Considerations

All manipulations were carried out using standard Schlenk techniques or conducted in an MBraun Labmaster 130 drybox under a nitrogen atmosphere. All reagents used were purchased from commercial vendors and used as received unless otherwise noted. Anhydrous solvents were purchased from Sigma-Aldrich and further purified by sparging with Ar gas followed by passage through activated alumina columns. Deuterated dimethylsulfoxide (DMSO-d_6) was purchased from Aldrich and degassed and dried according to standard procedures prior to use.[127] Elemental analyses were performed by Desert Analytics, Tucson, AZ and Atlantic Microlab, Norcross Georgia. ^{1}H and ^{13}C NMR spectra were recorded on a Varian Mercury 300 MHz spectrometer at ambient temperature. Chemical shifts were referenced to residual solvent peaks. Infrared spectra were recorded as KBr pellets on a Varian Scimitar 800 Series FT-IR spectrophotometer. UV-Visible absorption spectra were recorded on a Cary 50 spectrophotometer using 1.0 cm quartz cuvettes. Solution state magnetic moments were measured using the Evans method.[128] Mass spectra were recorded in the Mass Spectrometry Center at Emory University on a JEOL JMS-SX102/SX102A/E mass spectrometer. X-ray diffraction studies were carried out in the X-ray Crystallography Laboratory at Emory University on a Bruker Smart 1000 CCD diffractometer. Cyclic voltammetric experiments were carried out using a CH Instruments (Austin, TX) Model 660C potentiostat. All experiments were conducted in either DMF with 0.20 M tetrabutylammonium hexafluorophosphate or in DCM with 0.10 M tetrabutylammonium hexafluorophosphate as the supporting electrolyte. Electrochemical experiments were conducted in a three-component cell consisting of a Pt auxiliary electrode, a non-aqueous reference electrode ($Ag/AgNO_3$), and a platinum working electrode. All electrochemical measurements are referenced and reported versus the ferrocene/ferrocenium couple.

N(*o*-PhNHC(O)^{t}Bu)$_3$ (H_3L^{tBu})

A suspension of L^{NH2} (1.79 g, 6.2 mmol) in dichloromethane (DCM, 80 mL) was cooled to 0°C under an atmosphere of N_2. Triethylamine (3.20 mL, 23.0 mmol) was then added, followed by pivaloyl chloride (2.71 mL, 22.0 mmol). The mixture stirred for 20 hours as it slowly warmed to room temperature. The crude reaction mixture was washed with aqueous HCl (0.1 M, 3 x 50 mL), dried over magnesium sulfate, and concentrated in vacuo. The resulting solid was washed with diethyl ether (~10 mL) and ethyl acetate (~10 mL), and the white solid was collected by filtration (69%, 2.29 g). ^{1}H NMR (δ,

$CDCl_3$, 300 MHz): 7.95 (s, 3H, NH), 7.79 (dd, 3H, *J* = 1.2, 7.8 Hz, ArH), 7.11 (td, 3H, *J* = 1.2, 7.5 Hz, ArH), 7.02 (td, 3H, *J* = 1.2 Hz, *J* = 7.5 Hz, ArH), 6.84 (dd, 3H, *J* = 1.2, 7.8 Hz, ArH), 0.95 (s, 27H, $C(CH_3)_3$). ^{13}C NMR (δ, $CDCl_3$, 300 MHz): 176.64, 137.94, 131.56, 126.01, 125.67, 124.78, 124.42, 39.44, 27.22. HRESI-MS: $C_{33}H_{43}O_3N_4$ *m/z* Calcd. 543.33297 Found 543.33352 $[M+1]^+$. FTIR (KBr, cm^{-1}): *ν*(NH) 3258, *ν*(CO) 1653, 3387, 3309, 2959, 2909, 2871, 1680, 1653, 1594, 1516, 1479, 1439, 1303, 1265, 1160, 928, 756, 734, 625, 480.

$Ph_4P[Ni(L^{iPr})]$

To a solution of H_3L^{iPr} (117 mg, 0.23 mmol) in dry DMF (3 mL) was added solid potassium hydride (31 mg, 0.77 mmol). A colorless precipitate formed. When all of the solid dissolved, $NiBr_2$ (51 mg, 0.23 mmol) was added as a solid and the reaction stirred for four hours. Tetraphenylphosphonium bromide (98 mg, 0.23 mmol) was added to the deep orange solution as a solid. After stirring for 1 hour, the solution was concentrated in vacuo. The resultant orange powder was dissolved in MeCN and filtered to yield the final product as an orange solid. X-ray quality crystals could be obtained by the slow diffusion of diethyl ether into DMF to give orange crystals (109 mg, 68 %). ^1H NMR (δ, CD_3CN, 300 MHz): 21.38(br), 19.98(sh), 7.59(Ph_4P), 2.16(br). FTIR (KBr, cm^{-1}): ν(CO) 1604, 3059, 3020, 2959, 2926, 2866, 1601, 1578, 1476, 1440, 1386, 1295, 1276, 1207, 1108, 1040, 967, 767, 724, 690, 527. $\mu_{eff} = 3.30\ \mu_B$ (Evans' Method, $(CD_3)_2SO$, 298K). $\lambda_{max}(\varepsilon, M^{-1}cm^{-1})$ (DMF): 401(sh). Anal. Calcd (found) for $Ph_4P[Ni(L^{iPr})](DMF)_2$: C, 69.17 (69.35); H, 6.48 (6.35); N, 8.07 (8.15).

$(Et_4N)_2[Ni(L^{iPr})(CN)]$

To a solution of H_3L^{iPr} (68 mg, 0.14 mmol) in dry DMF (3 mL) was added solid potassium hydride (18 mg, 0.45 mmol). A colorless precipitate formed. When all of the solid had dissolved, $NiBr_2$ (30 mg, 0.14 mmol) was added as a solid and the reaction stirred for four hours. Tetraethylammonium bromide (29 mg, 0.14 mmol) was added to the deep orange solution as a solid and stirred for 1 hour. Tetraethylammonium cyanide (21 mg, 0.14 mmol) was then added as a solid and the reaction stirred for one hour. Solvent was removed in vacuo and the brown-green solid was washed with THF to yield a light green solid. Green, X-ray quality crystals were obtained by vapor diffusion of diethyl ether into DMF (97 mg, 85 %). ^1H NMR (δ, CD_3CN, 300 MHz): 37.41(br), 12.70(sh), 10.56(sh), 5.34(sh), 3.12(Et_4N), 1.16(Et_4N), -7.38(sh), -15.49(sh). FTIR (KBr, cm^{-1}): ν(CN) 2112, 3053, 2962, 2865, 1594, 1551, 1476, 1444, 1394, 1309, 1280, 1230, 1173, 1158, 1089, 1037, 1003, 956, 788, 770, 747, 624, 493. $\mu_{eff} = 3.25\ \mu_B$ (Evans' Method, $(CD_3)_2SO$, 298K). $\lambda_{max}(\varepsilon, M^{-1}cm^{-1})$ (MeCN): 654(32). Anal. Calcd (found) for $(Et_4N)_2[Ni(L^{iPr})(CN)]$: C, 66.98 (66.65); H, 8.73 (8.45); N, 11.63 (11.64).

$Ph_4P[Ni(L^{Ph})(MeCN)]$

To a stirred solution of H_3L^{Ph} (361 mg, 0.60 mmol) in DMF (5 mL) was added KH (79 mg, 1.98 mmol) as a solid. When H_2 evolution ceased, $NiBr_2$ (131 mg, 0.60 mmol) was added as a solid. The pale yellow solution turned orange as the metal salt dissolved over four hours. Tetraphenylphosphonium bromide (251 mg, 0.60 mmol) was added as a solid. After 30 minutes of stirring, solvent was removed in vacuo. The resultant yellow oil was taken up in acetonitrile (40 mL) and filtered to remove KBr. The filtrate was concentrated in vacuo, and the resultant yellow-green solid was recrystallized from acetonitrile (409 mg, 66 %). X-ray quality crystals were obtained by vapor diffusion of diethyl ether into a concentrated acetonitrile solution of the complex. ^{1}H NMR (δ, CD_3CN, 300 MHz): 48.36(br), 21.14(sh), 12.41(sh), 9.18(sh), 7.66(Ph_4P), -8.63(sh), -29.87(br). FTIR (KBr, cm^{-1}): ν(MeCN) 2247, ν(CO) 1596, 3056, 3021, 2927, 1596, 1584, 1552, 1473, 1442, 1357, 1109, 1041, 997, 914, 754, 723, 690, 527. μ_{eff} = 3.27 μ_B (Evans' Method, DMSO-d_6, 298K). λ_{max}(ε, $M^{-1}cm^{-1}$) (DMF): 707(16). Anal. Calcd (found) for $Ph_4P[Ni(L^{Ph})(MeCN)]DMF$: C, 73.45 (73.32); H, 5.17 (5.01); N, 7.56 (7.67).

$Ph_4P[Ni(L^{tBu})]$

To a solution of H_3L^{tBu} (426 mg, 0.79 mmol) in dry DMF (50 mL) was added solid potassium hydride (104 mg, 2.59 mmol). A colorless precipitate formed. When all of the solid dissolved, $NiBr_2$ (172 mg, 0.79 mmol) was added as a solid and the reaction stirred for four hours. Tetraphenylphosphonium bromide (329 mg, 0.79 mmol) was added to the deep orange solution as a solid. After stirring for 1 hour, the solution was concentrated in vacuo. The resultant orange powder was dissolved in MeCN and filtered to yield the final product as an orange solid. X-ray quality crystals could be obtained by the slow diffusion of diethyl ether into DMF to give orange crystals (271 mg, 37 %). ^{1}H NMR (δ, CD_3CN, 300 MHz): 53.99(br), 39.64(br), 31.00(br), 25.07(br), 22.44(sh), 21.93(br), 21.27(br), 17.15(sh), 14.32(br), 13.70(sh), 9.89(sh), 7.70(Ph_4P), 0.17(br), -1.51(sh), -3.11(br), -5.09(sh), -18.83(br), -19.41(sh). FTIR (KBr, cm^{-1}): ν(CO) 1597, 3057, 2949, 2919, 2861, 1597, 1557, 1475, 1439, 1387, 1328, 1244, 1195, 1172, 1108, 1045, 997, 951, 756, 724, 691, 528, 483. μ_{eff} = 3.37 μ_B (Evans' Method, CD_3CN, 298K). λ_{max}(ε, M^-

^{1}cm^{-1}) (DMF): 520(119). Anal. Calcd (found) for $Ph_4P[Ni(L^{tBu})]$: C, 71.29 (70.88); H, 6.58 (6.61); N, 6.93 (6.80).

$(Et_4N)_3[NiCo(L^{iPr})_2(CN)]$

To a solution of $(Et_4N)_2[Ni(L^{iPr})(CN)]$ (117 mg, 0.14 mmol) in DMF (~ 4 mL) was added $Et_4N[Co(L^{iPr})]$ (95 mg, 0.14 mmol) as a DMF solution. After 2 hours of stirring, diethyl ether (~ 5 mL) was added to precipitate the product as a reddish-purple solid. The solid was collected by filtration, washed with acetonitrile (~ 5 mL) and diethyl ether (~ 5 mL), and dried in vacuo (175 mg, 83%). X-ray quality crystals were grown by slow diffusion of diethyl ether into a concentrated solution of the product. ^{1}H NMR (δ, $(CD_3)_2SO$, 400 MHz): 37.29(br), 21.25(br), 20.15(br), 17.72(sh), 12.96(br), 12.65(sh), 10.68(sh), 9.34(br), 7.58(sh), 6.36(br), 5.55(sh), 3.21(Et_4N), 1.16(Et_4N), 0.39(br), -1.37(br), -7.16(sh), -15.68(sh). FTIR (KBr, cm^{-1}): ν(CN) 2126, 3053, 2963, 2935, 2867, 1596, 1558, 1478, 1447, 1388, 1277, 1250, 1172, 1089, 1036, 1001, 965, 772, 746, 625, 498. λ_{max}(ε, M^{-1}cm^{-1}) (DMF): 572(281), 834(40). Anal. Calcd (found) for $(Et_4N)_3[NiCo(L^{iPr})_2(CN)](DMF)_2$: C, 65.22 (65.49); H, 8.42 (8.19); N, 11.70 (11.36).

Addition of cyanide ion to $Ph_4P[Ni(L^{tBu})]$

To a solution of $Ph_4P[Ni(\mathbf{L^{tBu}})]$ (41 mg), 0.04 mmol) in acetonitrile (4 mL) was added tetraphenylphosphonium cyanide (16 mg, 0.04 mmol) as a solid and the reaction stirred for one hour. Solvent was removed in vacuo and the solid was washed with THF (3 x 2 mL) to yield a dark red-orange solid (56 mg, 98 %). ^{1}H NMR (δ, CD_3CN, 400 MHz): diamagnetic resonances: 8.22, 7.92, 7.75, 7.55, 7.36, 7.22, 7.07, 6.96, 6.78, 6.52, 6.06, 1.27, 1.23, 0.93. paramagnetic resonances: 53.29, 39.49, 30.79, 25.60, 22.16, 21.77, 21.35, 17.02, 14.52, 13.62, 10.13, -1.48, -2.99, -5.04, -18.74, -19.28. FTIR (MeCN, cm^{-1}): ν(CN) 2109, 2975, 2868, 2187, 2150, 1590, 1293, 1224, 1187, 1165, 1110, 763, 725, 693, 529. λ_{max}(ε, $M^{-1}cm^{-1}$) (MeCN): 408(sh).

Crystallography

Suitable crystals were coated with Paratone-N oil, suspended on a small fiber loop and placed in a cooled nitrogen gas stream at 173K on a Bruker D8 APEX II CCD sealed tube diffractometer with graphite monochromated Mo-Ka (0.71073 Å) radiation. Data were measured using a series of combinations of phi and omega scans with 10 s frame exposures and 0.5° frame widths. Data collection, indexing and initial cell refinements were all carried out using APEX II software.[131] Frame integration and final cell refinements were done using SAINT software.[132] The final cell parameters were determined from least-squares refinement on 2159 reflections. The structure was solved using Direct methods and difference Fourier techniques (SHELXTL, V6.12).[133] Hydrogen atoms were placed in their expected chemical positions using the HFIX command and were included in the final cycles of least squares refinement using a riding model. All non-hydrogen atoms were refined anisotropically. Scattering factors and anomalous dispersion corrections are taken from the *International Tables for X-ray Crystallography*.[134] Structure solution, refinement, graphics and generation of publication materials were performed using SHELXTL, V6.12 software.[133]

Table 3-4. Crystal data and structure refinement for solid-state structures.

	$Ph_4P[Ni(L^{iPr})]\cdot 2DMF$	$Ph_4P[Ni(L^{tBu})]$ $\cdot DMF\cdot 0.6\ Et_2O$	$Ph_4P[Ni(L^{Ph})(MeCN)]$ $\cdot 2MeCN$
Empirical formula	$C_{60}H_{67}N_6NiO_5P$	$C_{62.40}H_{72}N_5NiO_{4.6}P$	$C_{69}H_{56}N_7NiO_3P$
Formula weight	1041.88	1055.33	1120.89
T (K)	173(2)	173(2)	173(2)
λ (Å)	0.71073	0.71073	0.71073
Crystal System	Triclinic	Triclinic	Monoclinic
Space group	P-1	P-1	P2(1)/c
a (Å)	11.3871(10)	14.4575(8)	10.9218(3)
b (Å)	16.0284(2)	15.1016(8)	25.9666(9)
c (Å)	16.8718(2)	15.4786(8)	20.1405(7)
α (°)	115.3630(10)	64.786(3)	90
β (°)	102.2649(10)	72.689(3)	90.153(17)
γ (°)	91.6840(10)	77.867(3)	90
V (Å^3)	2693.69(5)	2905.3(3)	5711.9(3)
Z	2	2	4
ρ_{calc} (Mg/m^3)	1.285	1.206	1.303
GOF on F^2	1.036	1.041	1.021
R	0.0438	0.0505	0.0673
wR	0.1162	0.1414	0.1795

	$(Et_4N)_2[Ni(L^{iPr})(CN)]$	$(Et_4N)_3[CoNi(L^{iPr})_2(\mu\text{-}CN)]$
Empirical formula	$C_{47}H_{73}N_7NiO_3$	$C_{85}H_{126}CoN_{12}NiO_6$
Formula weight	842.83	1529.62
T (K)	173(2)	173(2)
λ (Å)	0.71073	0.71073
Crystal System	Monoclinic	Rhombohedral
Space group	P2(1)/n	R3
a (Å)	11.412(6)	19.0019(17)
b (Å)	18.653(10)	19.0019(17)
c (Å)	43.91(2)	21.787(4)
α (°)	90	90
β (°)	96.676(14)	90
γ (°)	90	120
V ($Å^3$)	9285(8)	6812.7(15)
Z	8	3
ρ_{calc} (Mg/m^3)	1.206	1.118
GOF on F^2	1.056	1.021
R	0.0793	0.0733
wR	0.1873	0.1488

Magnetic Susceptibility Measurements

DC magnetic susceptibility data were collected using a Quantum Design MPMS XL SQUID magnetometer at temperatures ranging from 2 to 300 K. Powdered microcrystalline samples were packed in gelatin capsules, inserted into a straw and transported to the magnetometer under dinitrogen. Contributions to the magnetization from the gelatin capsule and the straw were measured independently and subtracted from the total measured signal. Data were corrected for diamagnetic contributions using Pascal's constants. Samples for magnetization measurements were suspended in eicosane to prevent torquing of the crystallites at high magnetic fields. Susceptibility data were fit with theoretical models using a relative error minimization routine (JulX).[190] Attempts to fit magnetization data employed JulX or ANISOFIT 2.[172] Reported coupling constants are based on exchange Hamiltonians of the form $\hat{H} = -2J(\hat{S}_i \cdot \mathrm{E}\hat{S}_j)$.

Chapter 4: Synthetic, Spectral, and Structural Studies of Mononuclear Tris(κ^2-amidate) Aluminum Complexes Supported by Tripodal Ligands

Section 4-1. Introduction

Deprotonated organic amides (amidates) have recently been recognized as potent ligand scaffolds for metal-ion mediated catalytic and stoichiometric transformations.[57, 195] Amidate ligands can interact with metal centers through a variety of coordination modes (Figure 4-1), including: (1) monodentate (where the amidate coordinates through either *N*- or *O*-amidato donor), (2) bridging (where *N*- and *O*- donors coordinate to two separate metal ions), and (3) chelating (where the *N*- and *O*-donors coordinate to a single metal ion).

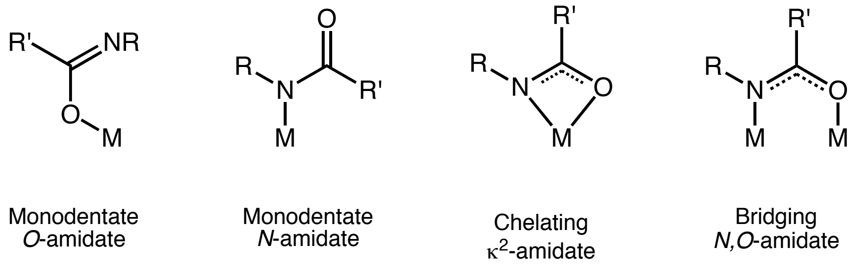

Figure 4-1. Possible coordination modes for amidate $[(RNC(O)R')]^-$ ligands.

The previous chapters reported the synthesis of a tripodal tris(amidato)amine ligand scaffold, [N(*o*-PhNHC(O)R)] (H_3L^R), and the coordination chemistry of the ligand variants with cobalt[112] and nickel.[113] The majority of these complexes feature a metal ion that is bound through the three *N*-donor atoms of the amidate substituents. However, it was observed that when the *tert*-butyl analogue of the ligand was metallated with Ni(II), only two of the amidate arms coordinated through the *N*-donor atoms, and the third amidate coordinated through the *O*-donor (Figure 4-2). It is believed that the flipping of the amidate moiety is mostly due to the relative bulk of the *tert*-butyl substituent.

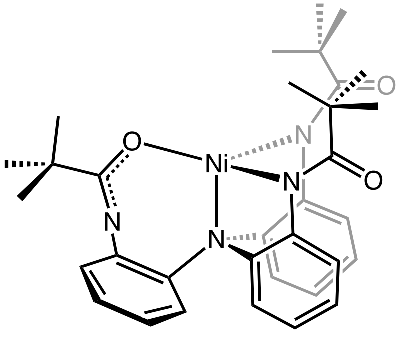

$Ph_4P[Ni(L^{tBu})]$

Figure 4-2. Ni(II) complex of the ligand $[(L^{tBu})]^{3-}$, featuring an *O*-amidate ligand.

The observation that this ligand scaffold was capable of supporting an *O*-amidate binding mode was intriguing, as it reveals the many coordination motifs available to this ligand scaffold, and it opens up the possibility of using these ligands with a variety of hard and soft metal ions. In order to further explore the coordination modes available to our ligand, we chose to look at a more oxophilic metal ion, Al(III). The harder aluminum ion should, in theory, favor a binding mode that incorporates the *O*-donors of the amidate into the chelate, possibly resulting in all three amidate substituents binding to a metal ion through the *O*-donor.

The majority of structurally characterized aluminum amidate complexes are multinuclear or oligomeric species in which the amidate donors bridge more than one aluminum center.[196-203] However, two separate studies have identified monomeric aluminum complexes stabilized by *O*-amidate ligands.[204, 205] In their efforts to better understand the mechanism of Al(III)-catalyzed polymerization of acetaldehyde, the Kakudo group undertook the structural analysis of a series of catalytically active species. Least reactive among these was a comparatively stable, mononuclear complex featuring an *O*-amidate ligand, [Me_2Al-(PhNC(O)Ph)($ONMe_3$)] (Figure 4-3).[204]

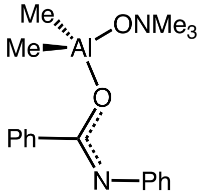

Figure 4-3. Structurally characterized mononuclear Al(III) *O*-amidate from Kakudo, et al.[204]

The relatively long amide C–O bond (1.330(9) Å) and short amide C–N bond (1.263 Å) of the aluminum complex indicate the amide C–N distance can be qualified as an almost completely localized double bond. They postulated that the more stable *trans* configuration of the substituents on amide ligand's C–N bond were most likely responsible for the complex's remarkable stability, as well as for its lack of catalytic activity. In another study, Barron, et al. studied the interactions of Al(III) aryloxide complexes (i.e., [$AlMe(BHT)_2$] BHT = butylated hydroxytoluene) with various organic carbonyl compounds.[205] They found that amides featuring tertiary amines favored coordination through the neutral *O*-donor of the ligand. In the presence of an amide with a secondary amine functionality, however, resulted in the loss of CH_4 with the concurrent formation of the complex $[Al(\kappa^2\text{-}(OC(NMe)Ph))(BHT)_2]$. The assignment of a chelating amidate ligand was based upon an ^{27}Al NMR shift diagnostic for four-coordinate aluminum, as well as solution-state molecular weight determination.

Recently, Stahl and coworkers have demonstrated that the dimeric, homoleptic aluminum amido complex ($Al_2(NMe_2)_6$) can be used to efficiently catalyze the transamidation of carboxamides (Scheme 4-1).[206] Given the importance of the amide functional group in protein and polymer chemistry, the ability to manipulate or functionalize these molecules under mild conditions with an innocuous catalyst is an intriguing target for research. Known examples of transamidation reactions are scarce, and those that do exist require harsh conditions in order to cleave the chemically robust amide bond.

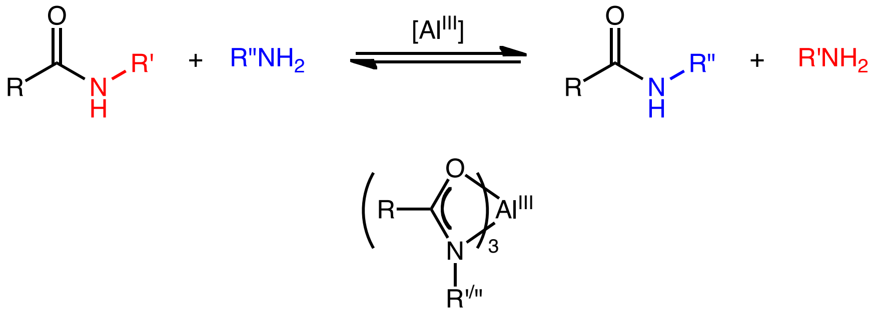

Scheme 4-1. Generalized scheme for Stahl's transamidation reaction (top) and the proposed active catalyst (bottom).

Stahl's transamidation reaction can take a secondary or tertiary amide ($RC(O)(NR_1R_2)$), and, in the presence of a primary or secondary amine (HNR_3R_4) and the Al(III) catalyst, exchange the $[NR_xR_y]^-$ units to generate $RC(O)(NR_3R_4)$ and (HNR_1R_2). The reactions proceed at low catalyst loading (2-5 mol%) and at relatively mild temperatures (~90 °C).

In subsequent mechanistic studies,[207, 208] they were able to use NMR spectroscopy to characterize the resting state of the catalyst, an Al(III) tris(κ^2-amidate) species. They observed by ^1H NMR that the addition of six or greater equivalents of carboxamido to the precatalyst, $(Al_2(NMe_2)_6)$, results in the quantitative formation of dimethylamine in solution. The complex resonance forms of the species in solution precluded characterization of the other products using this technique. Greater insight was gained through the careful monitoring of the titration of *N*-benzylcarboxamide into a toluene-d_8 solution of $(Al_2(NMe_2)_6)$ by ^{13}C NMR (Figure 4-4). At a 1:1 ratio of amide to Al(III), two peaks were observed, with chemical shifts of 179.4 and 183.5 ppm. These peaks were not identified definitively, but they remarked that neither corresponds to that of free carboxamide (171.8 ppm).

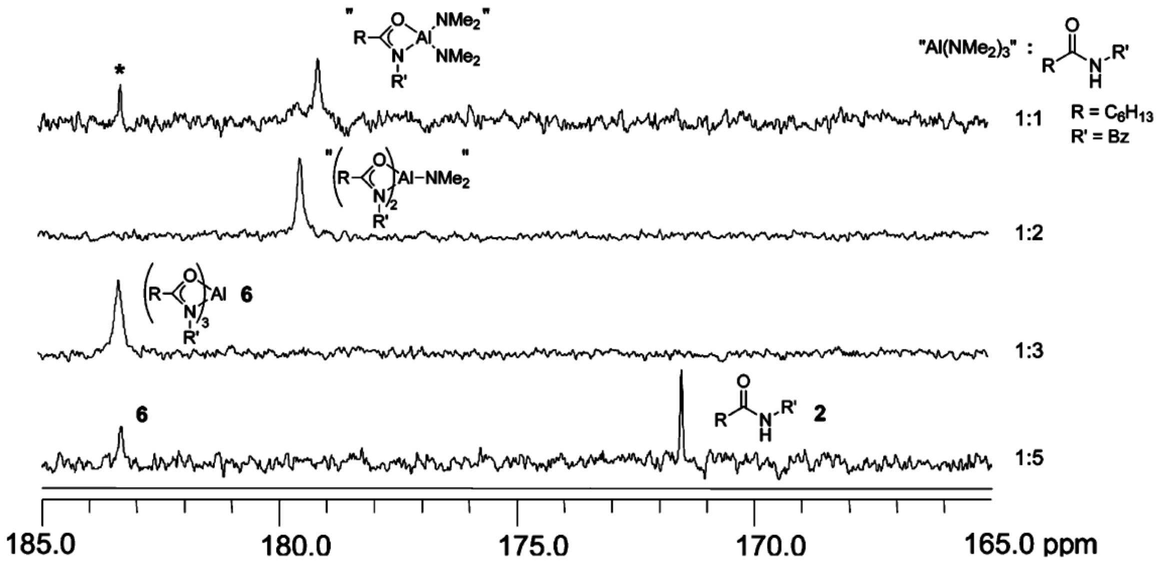

Figure 4-4. ^{13}C NMR study of the titration of *N*-benzylcarboxamide into a toluene-d_8 solution of $(Al_2(NMe_2)_6)$. (Reprinted with permission from Hoerter, et al., JACS 2006).[208]

Increasing the ratio of amide to Al(III) to 2:1 and 3:1, distinct single peaks are observed at 179.8 and 183.6 ppm, respectively. If the ratio of amide to Al(III) exceeds 3:1, two peaks are observed, one of which corresponds to peak observed at a 3:1 ratio (183.6 ppm), and the second peak is identical to that of the amide carbon of the free *N*-benzylcarboxamide. These data support the formation of a single, mononuclear Al(III) adduct with three amidate ligands. Literature precedent dictates that these ligands are likely bound to the metal center in a κ^2-amidate binding mode.

The number of reported complexes featuring κ^2-binding of amidates is relatively small, and the bulk of these examples are confined to complexes of early transition metals.[57] Much more rare are tris(κ^2-amidate) complexes, where a metal center has three amidates chelated to a single metal center. Most examples are characterized solely by solution state data. At the time of this study, only three structurally characterized tris(κ^2-amidate) complexes existed. Two of them were complexes of vanadium, one V(III)[209] and the other V(V)[210, 211], and the other example was an Y(III)[195] adduct. The above examples stress the necessity of hard metal ions to coordinate κ^2-amidate ligands.

The spectroscopic studies of Stahl and coworkers, coupled with the dearth of structurally characterized tris(κ^2-amidate) metal complexes[195, 210, 211] prompted us to explore the coordination chemistry of Al(III) with a series of tripodal, triamidate ligands, $[(L^R)]^{3-}$, synthesized in our lab. Specifically, we sought to use the bulky acyl substituents of our ligands to stabilize monomeric aluminum amidates. Given the tripodal, open-chain arrangement of our ligand, we were in a good position to address the feasibility of Stahl's proposed intermediate, as well as explore the possibility of generating the first structurally characterized complex of Al(III) featuring a κ^2-amidate functionality. In this chapter, the synthesis and characterization of two mononuclear Al(III) tris(κ^2-amidate) metal complexes are discussed.

Section 4-2. Results and Discussion

For the synthesis and characterization of the triamide ligands discussed in this chapter, please see the Experimental sections of chapters 2 and 3. The aluminum complex [Al(L^{iPr})]is readily obtained by reacting the ligand, H_3L^{iPr}, with three equivalents of potassium hydride in DMF to generate the trianion, $[(L^{iPr})]^{3-}$. This step is followed by in situ transmetallation with $AlCl_3$ to generate the desired complex along with three equivalents of KCl (Scheme 4-2, top). Removal of the solvent in vacuo yields a colorless solid. The resulting complex is soluble in a variety of organic solvents including benzene, toluene, and chloroform, making removal and quantification of the potassium chloride byproduct simple. In contrast, the aluminum complex of the *tert*-butyl ligand derivative, [Al(L^{tBu})], is prepared by reacting the ligand directly with one equivalent of $AlMe_3$ in toluene (Scheme 4-2, bottom).

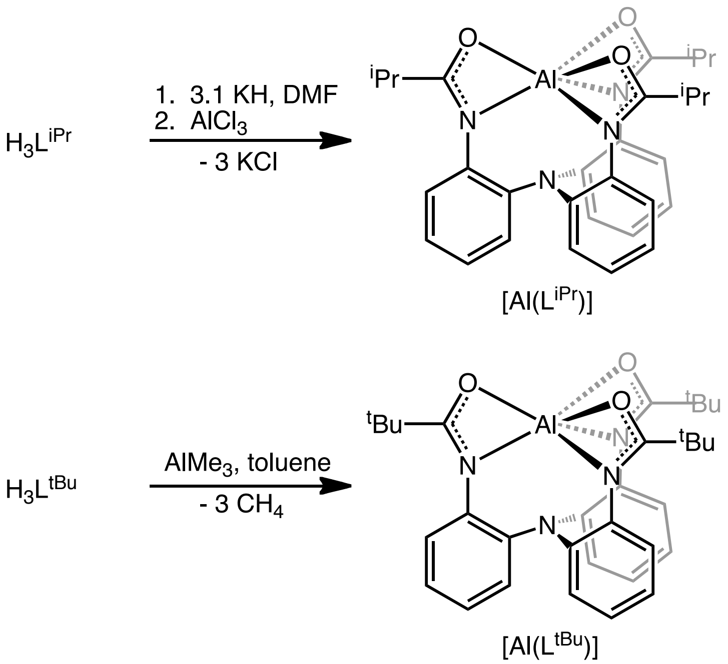

Scheme 4-2. Synthesis of the Al(III) complexes, $[Al(L^{iPr})]$ (top) and $[Al(L^{tBu})]$ (bottom), using two different synthetic routes.

Attempts to synthesize $[Al(L^{iPr})]$ directly from the reaction of the protio ligand with $AlMe_3$ were unsuccessful and lead to a complex reaction mixture, presumably due to the insolubility of the ligand in toluene. Attempts were made to synthesize and isolate the aluminum complexes of the methyl, $[Al(L^{Me})]$, and phenyl, $[Al(L^{Ph})]$, ligand congeners using analogous synthetic strategies. These reactions, however, yielded complicated product mixtures that contained a number of inseparable aluminum species.

The ^{1}H and ^{13}C NMR spectra of $[Al(L^{iPr})]$ and $[Al(L^{tBu})]$ in deuterated chloroform are indicative of pseudo C_3-symmetric species in solution. The ^{1}H spectrum shows the disappearance of the peak associated with the amide proton, and the remaining peaks (7 in $[Al(L^{iPr})]$, 6 in $[Al(L^{tBu})]$) are the number expected for three magnetically equivalent ligand arms. The ^{13}C spectra of both complexes exhibit single carbonyl resonances at approximately 185 ppm consistent with the central carbon of chelating amidate donors.[195, 208] Both [Al(L^{iPr})]and [Al(L^{tBu})]exhibit single peaks in their ^{27}Al NMR spectra (CDCl$_3$, 25 °C) at 26 and 27 ppm, respectively (Figure 4-5).

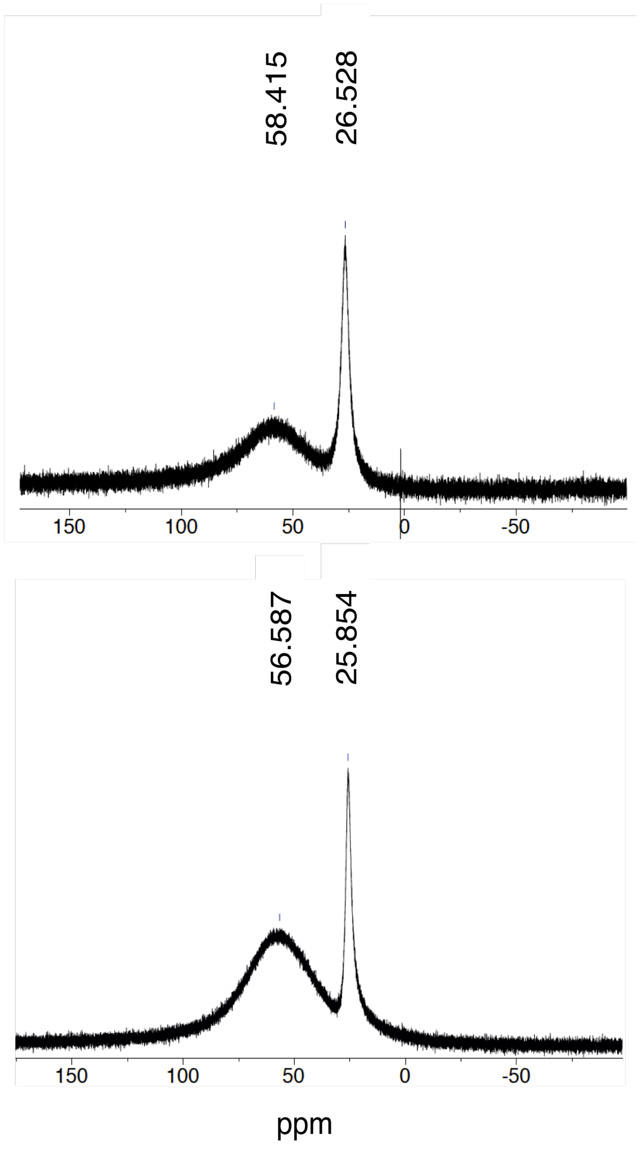

Figure 4-5. ^{27}Al NMR spectra of [Al(L^{iPr})]and [Al(L^{tBu})] in CDCl$_3$ referenced against an external Al(NO$_3$)$_3$ standard. The broad peaks at 57-58 ppm are due to background from the aluminum incorporated into the probe.

These data are consistent with non-fluxional, octahedral Al(III) centers with mixed donor ligands.[212, 213] Due to the overlap of the signal associated with the Al(III) complexes with that of the background signal generated by the aluminum in the probe (~57 ppm), the base width of the peak could only be estimated. Infrared spectroscopy can also be used to determine the coordination mode of the amidate ligands. Specifically, the absence of amide ν(N–H) bands at ca. 3260 cm^{-1} and the appearance of new medium to strong intensity ν(Al–O) and ν(Al–N) bands between ~620–740 cm^{-1} are indicative of κ^2-coordination. The diagnostic ν(CO) bands of the free ligands (~1650 cm^{-1}) are also shifted to significantly lower energies (~1580 cm^{-1}) upon coordination to the aluminum centers. The ν(CO) bands observed for these κ^2-amidate complexes are also significantly lower in energy than the ν(CO) frequency observed in four-coordinate transition complexes of the same ligands (i.e., $Et_4N[Co(L^{iPr})]$, 1610 cm^{-1}) in which the ligand coordinates through three monodentate, *N*-amidate donors and the tertiary amine of the ligand backbone.[112]

The molecular structures of $[Al(L^{iPr})]$ (Figure 4-6) and $[Al(L^{tBu})]$ (Figure 4-7) were determined by X-ray diffraction studies. These studies confirm the chelating tris(κ^2-amidate) coordination mode of each ligand in the solid state. The coordination geometries about the aluminum centers are intermediate between octahedral and trigonal prismatic.

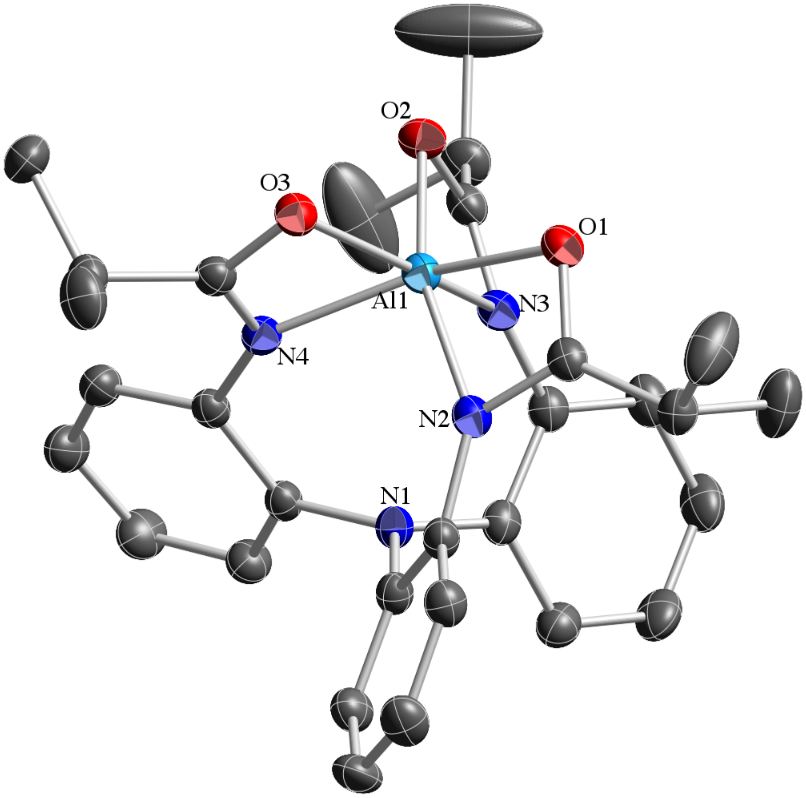

Figure 4-6. Solid-state structure of [Al(L^{iPr})]. Hydrogen atoms are removed for clarity. Thermal ellipsoids are shown at 50% probability.

The degree of distortion between these two idealized geometries can be quantified by measuring the dihedral twist angle (ϕ) between the two trigonal coordination planes (Figure 4-8).[214-217] A twist angle of 60° is indicative of ideal octahedral geometry, whereas a twist angle of 0° indicates an ideal trigonal prismatic ligand arrangement.

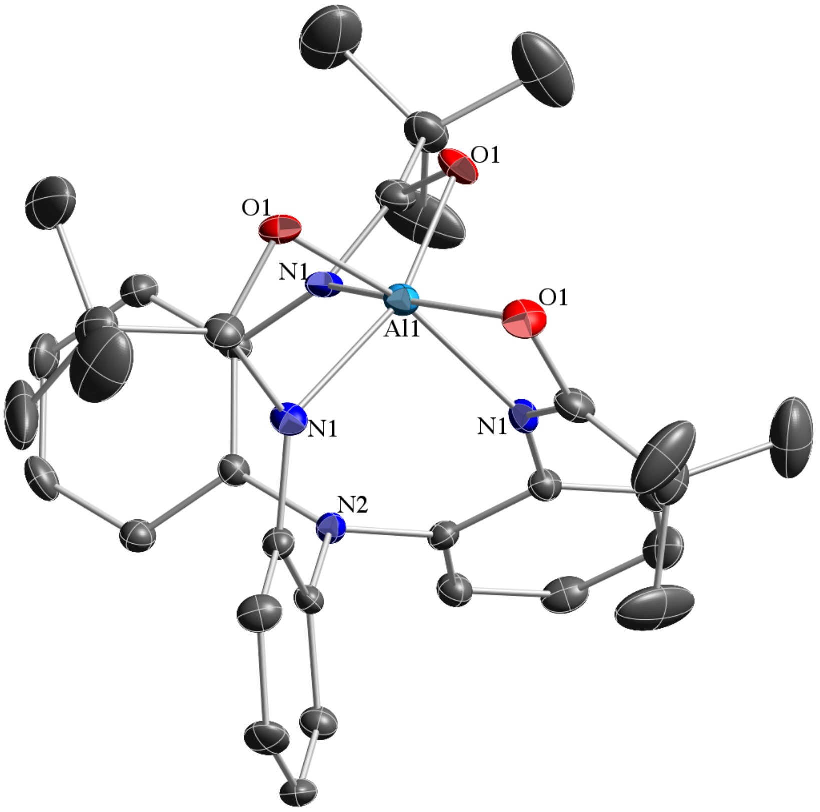

Figure 4-7. Solid-state structure of [Al(L^{tBu})]. Hydrogen atoms are removed for clarity. Thermal ellipsoids are shown at 50% probability.

The average trigonal twist angles for [Al(L^{iPr})] and [Al(L^{tBu})] are 35.7° and 36.3°, respectively, indicating a significant degree of distortion away from octahedral geometry.

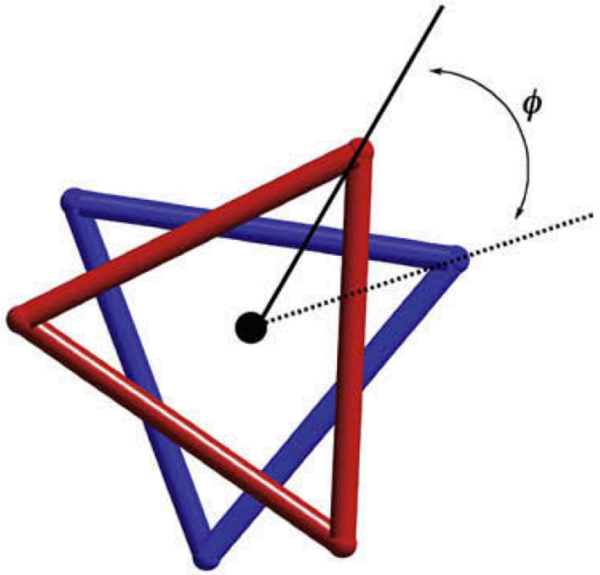

Figure 4-8. Illustration of the dihedral angle (trigonal twist angle ϕ) between the vertices of the triangles formed in the trigonal planes of the *O*-amidate (red) and *N*-amidate (blue) donors.

This distortion can be explained by considering the relatively small chelate bite angles (O–Al–N) and bite distances (non-bonded N· · ·O distance) afforded by the chelating κ^2-amidate ligands. These parameters can be described by the normalized bite, *b*, of the bidentate, chelating ligands ($b = 2 \sin(\alpha/2)$, where α = the O–Al–N bond angle).[218] Both [Al(L^{iPr})] and [Al(L^{tBu})] give rise to normalized bite values of 1.10. This value is similar to normalized bite values (1.12-1.23) observed for tris(*N*,*N*-disubstituted-dithiocarbamato) metal complexes with similar, four-membered chelate rings.[219] Complexes exhibiting *b* values of this magnitude are expected to significantly distort away from an idealized octahedral geometry in order to reduce electrostatic repulsion between the donor atoms.[218, 219] The primary coordination spheres of [Al(L^{iPr})] and [Al(L^{tBu})] are very similar. The average Al–O bond lengths of [Al(L^{iPr})] and [Al(L^{tBu})]

(1.927 and 1.895 Å, respectively) are significantly longer than the Al–O bond length (1.77 Å) observed in the previously reported mononuclear aluminum complex, [Me_2Al-(PhNC(O)Ph)($ONMe_3$)] (vide supra), that contains an *O*-amidate donor and has been characterized by X-ray diffraction.[204]

Table 4-1. Selected average bond lengths (Å), angles (°), and metrical parameters for [Al(L^{iPr})] and [Al(L^{tBu})].

	[Al(L^{iPr})]	[Al(L^{tBu})]
Al–O (ave.)	1.927(1)	1.895(3)
Al–N (ave.)	1.967(1)	1.980(4)
C–O (ave.)	1.300(2)	1.301(5)
C–N (ave.)	1.306(2)	1.302(5)
O–Al–N (ave.)	67.07	67.10
Al···N_{tert}[a]	3.14	3.15
N···O (ave.)[b]	2.15	2.15
ϕ(O/N)[c]	35.7	36.3
b (ave.)[d]	1.10	1.10

[a] Through space distance between Al(III) center and non-coordinated, tertiary amine of the ligand

[b] Bite distance between the chelating *O*- and *N*-donors.

[c] Ligand twist angle.

[d] Normalized bite of the ligand.

The delocalization of anionic charge within the chelating κ^2-amidate OCN group is apparent from the similarities in C–O and C–N bond lengths. The average C–O bonds in the amidate groups of [Al(L^{iPr})] and [Al(L^{tBu})] (1.300(2) and 1.301(5) Å, respectively) are nearly equal to that of their average C–N bonds (1.306(2) and 1.302(5) Å, respectively), indicative of near-complete delocalization of the amide double bond.

In the structure of [Al(L^{iPr})], each amidate acyl substituent is oriented so that either a methyl group or the methine proton of the isopropyl group is positioned between adjacent phenyl rings of the ligand backbone. Replacing the isopropyl substituents with larger *tert*-butyl substituents does not result in a significant change in solid-state structure, suggesting that subtle changes in the amidate substituents do not significantly alter the coordination geometries of these species. However, attempts to synthesize the analogous [Al(L^{Me})] complex using similar synthetic strategies were unsuccessful and gave rise only to complex reaction mixtures by spectroscopic analysis. These results indicate that the bulky acyl substituents may be required to prevent the formation of multinuclear or oligomeric aluminum species. Similar observations have been reported for triamido aluminum complexes in which small amido substituents give rise to dimeric aluminum species in solution.[220, 221]

The six-coordinate geometries observed for [Al(L^{iPr})] and [Al(L^{tBu})] were not unexpected, as hard metal ions tend to favor either the κ^2-amidate binding mode or a binding mode in which the *O*-amidate donor spans two different metal centers.[57] However, given the large number of well-characterized four-coordinate azaalumatranes supported by tripodal tetradentate, triamido[220] ligand systems that contain bulky amide substituents (i.e., [Al(N($CH_2CH_2NSiMe_3$)$_3$]), four-coordinate geometries and/or fluxional solution-state behavior in these systems could not be ruled out. The work described in this chapter shows how the ambidentate amidate substituents of the $[(L^R)]^{-3}$ ligand framework can bind to metals in a κ^2-amidate fashion. This coordination mode flexibility allows for our ligand framework to be applicable to a variety of metal ions, regardless of HSAB theory, due to the number of binding modes incorporating combinations of hard oxygen and softer nitrogen donor atoms. The pair of aluminum complexes described above represent not only a model system for the active catalyst in Stahl's transamidation reaction, but are also the first structurally characterized κ^2-amidate aluminum complexes.

Section 4-3. Experimental

General Considerations

All manipulations were carried out using standard Schlenk techniques or conducted in an MBraun Labmaster 130 drybox under a nitrogen atmosphere. All reagents used were purchased from commercial vendors and used as received unless otherwise noted. Anhydrous solvents were purchased from Sigma-Aldrich and further purified by sparging with Ar gas followed by passage through activated alumina columns. Deuterated chloroform ($CDCl_3$) was purchased from Aldrich and degassed and dried according to standard procedures prior to use.[127] Elemental analyses were performed by Atlantic Microlab, Norcross Georgia. ^1H and ^{13}C NMR spectra were recorded on a Varian Unity Plus 600 MHz spectrometer at ambient temperature. Chemical shifts were referenced to residual solvent peaks. The ^{27}Al spectrum was recorded in $CDCl_3$ on a Varian Unity Plus 600 MHz spectrometer (156.2 MHz) and referenced to an external standard (0.2 M

$Al(NO_3)_3$ in D_2O). The ^{27}Al background signal[222] was determined using a $CDCl_3$ blank. The background signal appeared as a very broad singlet centered at 57 ppm. Infrared spectra were recorded as KBr pellets on a Varian Scimitar 800 Series FT-IR spectrophotometer. Mass spectra were recorded in the Mass Spectrometry Center at Emory University on a JEOL JMS-SX102/SX102A/E mass spectrometer. X-ray diffraction studies were carried out in the X-ray Crystallography Laboratory at Emory University on a Bruker Smart 1000 CCD diffractometer.

[Al(L^{iPr})]

To a stirred solution of H_3L^{iPr} (98 mg, 0.20 mmol) in DMF (2 mL) was added KH (26 mg, 0.65 mmol) as a solid. When H_2 evolution ceased, $AlCl_3$ (26 mg, 0.20 mmol) was added as a solid. Upon complete dissolution of the metal salt, solvent was removed in vacuo. The colorless solid was extracted into toluene and filtered to remove KCl (3 equiv.). X-ray quality crystals were obtained by vapor diffusion of hexanes into a concentrated toluene solution. (38 mg, 37%). ^1H NMR (δ(ppm), $CDCl_3$, 600 MHz): 7.45 (dd, 3H, J = 7.8, 1.2 Hz, ArH), 7.09 (dt, 3H, J = 7.8, 1.2 Hz, ArH), 7.04 (dt, 3H, J = 7.8, 1.8 Hz, ArH), 6.95 (dd, 3H, J = 7.8, 1.8 Hz, ArH), 2.94 (7, 3H, J = 7.2 Hz, CH), 1.28 (d, 9H, J = 7.2 Hz, CH_3), 0.55 (d, 9H, J = 6.6 Hz, CH_3). ^{13}C NMR (δ(ppm), $CDCl_3$, 600 MHz): 184.84, 141.22, 140.48, 130.67, 126.29, 124.25, 122.25, 28.32, 19.14, 17.97. ^{27}Al NMR (δ(ppm), $CDCl_3$, 600 MHz): 26 ($W_{1/2}$ = 3000 Hz). FTIR (KBr, cm^{-1}): ν(CO) 1580, 1474, 1435, 1373, 1295, 1271, 1079, 976, 751, 507. Anal. Calcd (found) for [Al(L^{iPr})]: C, 68.69 (68.35); H, 6.34 (6.41); N, 10.68 (10.57).

[Al(L^{tBu})]

To a stirred suspension of H_3L^{tBu} (250 mg, 0.46 mmol) in toluene (4 mL) was added $AlMe_3$ via syringe(2.0M in toluene, 0.23 mL, 0.46 mmol). After 20 minutes of stirring, the reaction mixture became homogeneous and solvent was removed in vacuo; leaving a colorless solid. X-ray quality crystals were obtained by vapor diffusion of petroleum ether into a concentrated toluene solution of the complex (154 mg, 59%). ^{1}H NMR (δ(ppm), $CDCl_3$, 600 MHz): 7.24 (dd, 3H, *J* = 7.8, 1.2 Hz, ArH), 7.01 (m, 9H, ArH), 0.917 (s, 27H, CH_3C). ^{13}C NMR (δ(ppm), $CDCl_3$, 600 MHz): 184.706, 141.409, 140.62, 129.45, 125.17, 125.00, 124.21, 38.51, 28.15. ^{27}Al NMR (δ(ppm), $CDCl_3$, 600 MHz): 27 ($W_{1/2}$ = 3000 Hz). FTIR (KBr, cm^{-1}): ν(CO) 1562, 1480, 1363, 1302, 1190, 968, 760, 749, 623, 529. Anal. Calcd (found) for [Al(L^{tBu})]: C, 69.94 (69.97); H, 6.94 (6.84); N, 9.89 (9.80).

Crystallography

Suitable crystals were coated with Paratone-N oil, suspended on a small fiber loop and placed in a cooled nitrogen gas stream at 173K on a Bruker D8 APEX II CCD sealed tube diffractometer with graphite monochromated Mo-Ka (0.71073 Å) radiation. Data were measured using a series of combinations of phi and omega scans with 10 s frame exposures and 0.5° frame widths. Data collection, indexing and initial cell refinements were all carried out using APEX II software.[131] Frame integration and final cell refinements were done using SAINT software.[132] The final cell parameters were determined from least-squares refinement on 2159 reflections. The structure was solved using Direct methods and difference Fourier techniques (SHELXTL, V6.12).[133] Hydrogen atoms were placed in their expected chemical positions using the HFIX command and were included in the final cycles of least squares refinement using a riding model. All non-hydrogen atoms were refined anisotropically. Scattering factors and anomalous dispersion corrections are taken from the *International Tables for X-ray Crystallography*.[134] Structure solution, refinement, graphics and generation of publication materials were performed using SHELXTL, V6.12 software.[133]

Table 4-2. Crystal data and structure refinement for solid-state structures.

	[Al(L^{iPr})]	[Al(L^{iPr})]
Empirical formula	$C_{30}H_{33}AlN_4O_3$	$C_{33}H_{39}AlN_4O_3$
Formula weight	524.58	566.66
T (K)	173(2)	173(2)
λ (Å)	0.71073	0.71073
Crystal System	Orthorhombic	Trigonal
Space group	Pbca	P3(1)c
a (Å)	15.9429(3)	11.2793(8)
b (Å)	9.8814(2)	11.2793(8)
c (Å)	34.5625(7)	28.563(4)
α (°)	90	90
β (°)	90	90
γ (°)	90	120
V (Å^3)	5444.91(19)	3147.0(6)
Z	8	4
ρ_{calc} (Mg/m^3)	1.280	1.196
GOF on F^2	1.028	1.115
R	0.0499	0.0713
wR	0.1205	0.1679

Part III. Intramolecular Bond Activation by Cobalt and Iron Complexes Supported by a Tris(amidato)amine Ligand Scaffold

Chapter 5: The Intramolecular Activation of C-H Bonds by Cobalt and Iron Complexes Supported by a Trianionic, Tripodal Ligand

Section 5-1. Introduction

The chemistry of iron is of central importance in chemical biology largely due to its role in the myriad oxidation reactions catalyzed by heme and nonheme iron enzymes.[44] The pivotal role that high-valent iron intermediates play in biocatalytic transformations has prompted interest in creating synthetic systems to explore the nature of their bonding and reactivity. Specifically, models of nonheme iron enzymes are particularly attractive synthetic targets due to the variety of reactions they catalyze, as well as the ease with which model complexes can be generated relative to model heme complexes.[3, 223] This class of enzyme performs a variety of reactions including dioxygen transport, oxidation of unactivated C–H bonds, and the detoxification of biologically harmful radicals. Some of the best-studied enzymes under this heading are those that utilize dioxygen as a terminal oxidant and *O*-atom source. Known as oxygenases, these enzymes can be classified into two subgroups, monoiron and diiron enzymes.

These enzymes activate dioxygen by similar yet distinct mechanisms (Figure 5-1).[44] Nonheme monoiron enzymes feature a single iron atom in their active site. The mechanism of O_2 activation at the enzyme active site may be dependent on the presence of a cofactor. In those operating with a cofactor, oxygen binds to the reduced Fe(II) form of the enzyme, generating an Fe(III) alkyl or aryl peroxy adduct with the cofactor that decomposes to an Fe(IV) oxo intermediate. Those enzymes without a cofactor contain endogenous electron-transfer agents, such as iron-sulfur clusters, to aid in reduction of the bound dioxygen. In these cases, dioxygen is bound to the Fe(II) center to generate an Fe(III) superoxo or hydroperoxo intermediate. The oxygen is then further reduced to form an Fe(V) oxo/hydroxo species that is the active oxidant in catalysis.

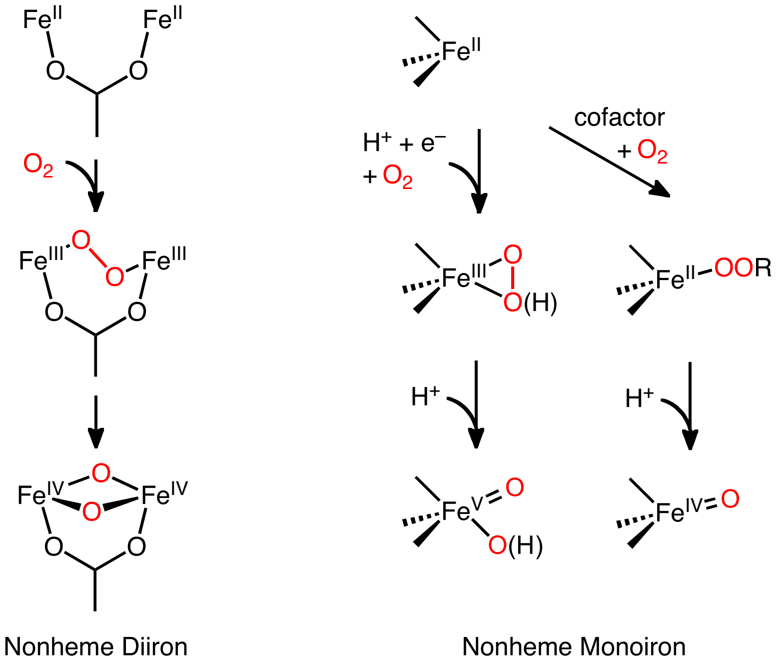

Figure 5-1. Comparison of mechanisms of dioxygen activation by mono- and dinuclear iron oxygenases.

The best-known examples of nonheme monoiron enzymes are the α-keto-acid-dependent enzymes and the Rieske dioxygenases. Both families feature the 2-His-1-carboxylate facial triad as the binding motif of the iron center in the enzyme active site (Figure 5-2). This ligand arrangement features the iron ion supported on one face by two histidines and one carboxylate residue. The facial arrangement leaves the other three sites open to bind exogenous ligands, such as substrate, cofactor, O_2, or water. The α-keto-acid-dependent enzymes require an α-keto-acid (αKA) as a cofactor to reduce O_2 for a variety of oxidative transformations. While the coordination environment about the Fe center in the active site is very similar, the Rieske dioxygenases do not require the use of a cofactor for dioxygen reduction. An endogenous Fe_2S_2 cluster is in close proximity to the monoiron center.

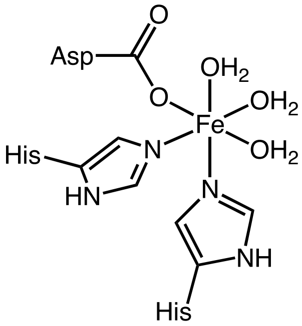

Figure 5-2. Active site of an α-keto-acid-dependent enzyme featuring the 2-His-1-carboxylate facial triad.

This cluster delivers electrons to the mononuclear center, eliminating the need for an exogenous source of electrons

Nonheme diiron enzymes feature two Fe(II) ions in the active site that are in close proximity. Upon approach of O_2, this proximity results in the formation of a diiron(III) peroxo adduct. The peroxo ligand is further reduced to form a high-valent diiron(IV) bis–μ–oxo that acts as the oxidant in catalysis.

.

The two best-known nonheme diiron oxygenases are the hydroxylase component of soluble methane monooxygenase (MMOH) and the R2 subunit of ribonucleotide reductase (RNR). The MMOH enzyme is responsible for the oxidation of methane to methanol, and RNR catalyzes the conversion of nucleotides to deoxynucleotides (Figure 5-3). Both enzymes feature carboxylate-rich active sites, each diiron center being coordinated by two histidines and four carboxylate residues, along with coordinated solvent molecules.

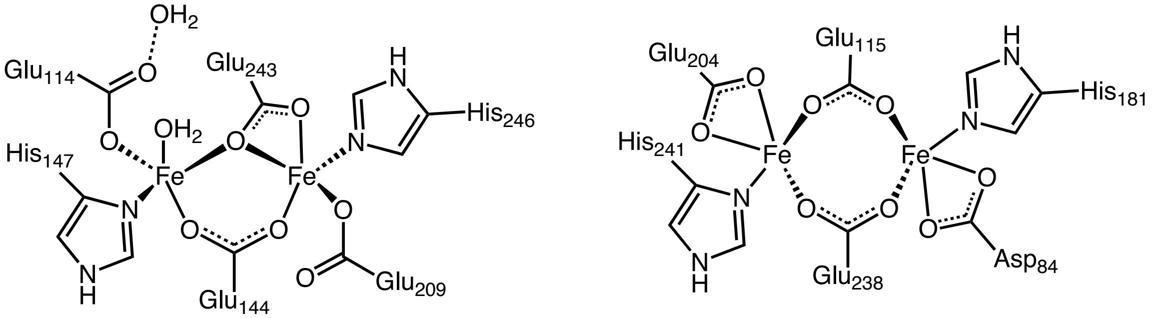

Figure 5-3. Active sites of diiron oxygenases MMOH (left) and R2 (right).

A great deal of work has been done to generate model systems to attempt to understand and mimic the functional aspects of these enzymes.[3, 223-226] For the most part these studies have employed artificial oxidants, such as H_2O_2, organic peroxides, and iodosylarenes to form synthetic iron-oxygen adducts. Dioxygen, however, is employed as both the sacrificial oxidant and oxygen atom source in enzymatic systems, and therefore its use in studies on iron-oxygen complexes is of fundamental importance. Due to the problems inherent to dioxygen activation, only a few examples exist of its use as the oxygen source in studies on synthetic iron systems.[6, 7, 227-235]

Nam and coworkers have shown that mononuclear nonheme Fe(II) complexes of the TMC ligand (TMC = 1,4,8,11-tetramethyl-1,4,8,11-tetraazacyclotetradecane) can reduce dioxygen to generate the corresponding oxoiron(IV) species, $[Fe^{IV}(TMC)(O)]^{2+}$.[236-238] If the reaction was run in MeCN/alcohol mixtures and in the absence of external reductants or protons, they postulated that the reaction proceeds via a dinuclear mechanism.[236] In the presence of a proton source ($HClO_4$) and an external reductant (1-benzyl-1, 4-dihydronicotinamide (BNAH), an NADH analogue) in MeCN, however, a mononuclear mechanism that proceeds via a hydroperoxy intermediate was implicated (Scheme 5-1, pathway A).[237] The solvent dependence of the former reaction on the presence of alcohols or ethers indicates that a hydrogen atom transfer step is possible, and the reactions are likely proceeding by similar mechanisms. In a third study, they found that while $[Fe^{II}(TMC)]^{2+}$ is air-stable in MeCN, the addition of an olefin (i.e., cyclohexene) resulted in the formation of $[Fe^{IV}(TMC)(O)]^{2+}$ along with the allylic oxidation and dehydrogenation products expected from hydrogen atom abstraction (HAT) (Scheme 5-1, pathway B).[238]

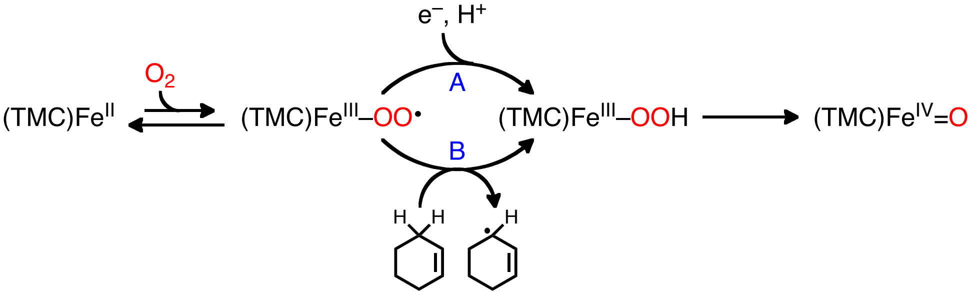

Scheme 5-1. Pathways proposed by Nam, et al. in the activation of O_2 by $[Fe^{II}(TMC)]^{2+}$.

This HAT process implies that the initial iron-dioxygen adduct is likely an Fe(III)-superoxo species. They also observed that, among the complexes they've studied that are known to generate stable iron(IV)-oxo complexes, the TMC-supported complex is the only one that can be generated directly from dioxygen. Given that the TMC complex is the only one that is high-spin Fe(II), it was ascertained that the spin-state may be a necessary consideration in generating complexes that can predictably reduce O_2. The dioxygen-derived $[Fe^{IV}(TMC)(O)]^{2+}$ was found to be capable of oxidizing benzyl alcohol to benzaldehyde.

Lippard and coworkers have reported the activation of dioxygen by bridged, nonheme diiron carboxylates.[3] Lippard, Tolman, and Que contemporaneously discovered that by using sterically bulky terphenyl-substituted carboxylates, discrete diiron complexes can be synthesized that bear a strong structural resemblance to the first coordination sphere of carboxylate-rich diiron oxygenases.[239, 240] These systems have been observed to react with dioxygen to form μ-1,2-peroxo and bis-μ-oxo intermediates.[241, 242] In two instances, Lippard's group has shown that these systems can be used for the oxidation of organic substrates. In one study, they found that the addition of pyridyl ethyl substituents to the requisite pyridine ligands of their complexes resulted in the intramolecular oxidation of the benzyl C–H bonds to yield the corresponding alcohol upon O_2 addition (Scheme 5-2).[227, 243]

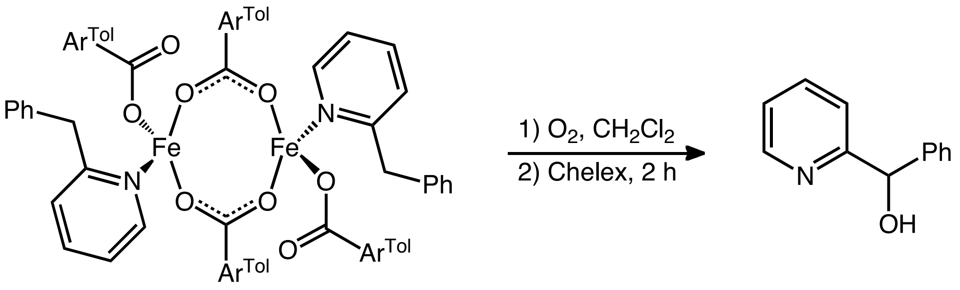

Scheme 5-2. Intramolecular C–H activation by a carboxylate-bridged diiron(II) complex studied by Lippard, et al.

In a second system, it was found that addition of O_2 to a THF solution of the complex resulted in the oxidation of the C-H bonds in the tetrahydrofuran molecules to introduce the corresponding alcohol and ketone moieties.[228]

In Part I of this dissertation, the coordination chemistry of the triamidate ligand scaffold $[N(o\text{-}PhNC(O)R)_3]^{3-}$ with Co, Ni, and Al was disscussed.[112-114] We have demonstrated that these systems, which incorporate *ortho*-substituted phenylene units into the ligand backbone, can be used to stabilize metals with unique structural properties. These studies suggested that the ligand's acyl substituents could be used to regulate exogenous anion binding. Our current research seeks to use the modular nature of the amide acyl groups to give steric protection to or act as traps for high-valent metal-oxygen intermediates. The cavity surrounding the open coordination site in $[Co(L^{iPr})]^-$ is arranged so that the methine protons of the ligand isopropyl substituents lie an average of 2.67 Å from the Co(II) center (Figure 5-4).

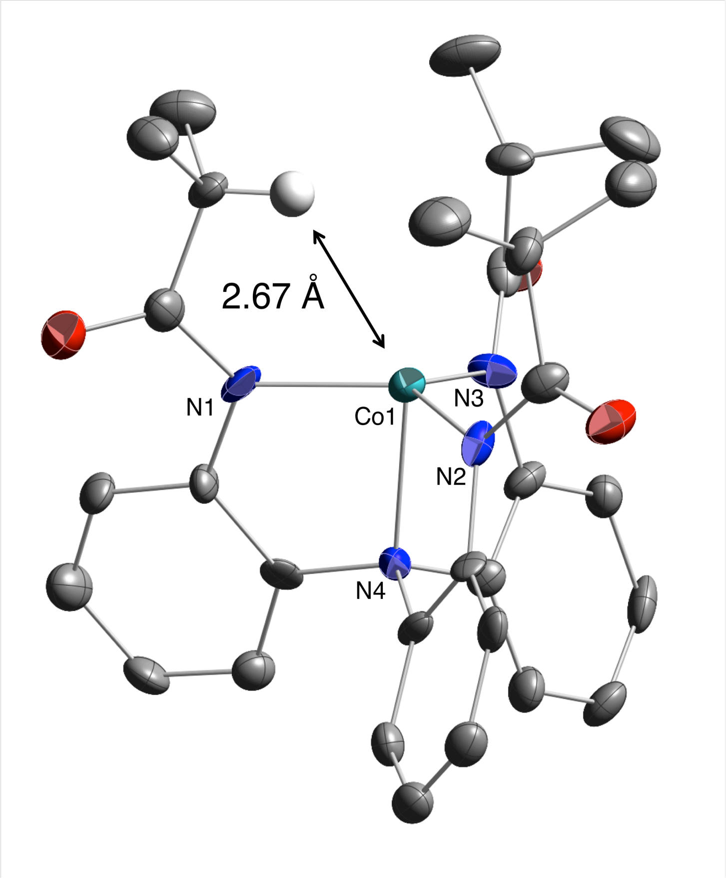

Figure 5-4. Solid-state structure of [Co(L^{iPr})]$^-$, indicating the short distance between the cobalt center and the methine hydrogen atoms.

This short distance indicates that the methine C–H bonds of the ligand arms will be positioned in close proximity to reactive "Co–O$_x$" fragments, thereby allowing an intramolecular reaction, thereby creating an intramolecular trap for the high-valent intermediate. The results of trapping reactions would give insight into the nature of our transient oxidants and would show that they are capable of C–H activation.[244-246] By varying the metal ion and ligand acyl substituents, the complex could then be tuned towards intermolecular C–H activation. Ideally, by synthesizing these sterically crowded oxidants, one could imagine using these complexes to selectively oxidize C–H bonds based on the size of the alkyl substituent (Scheme 5-3).

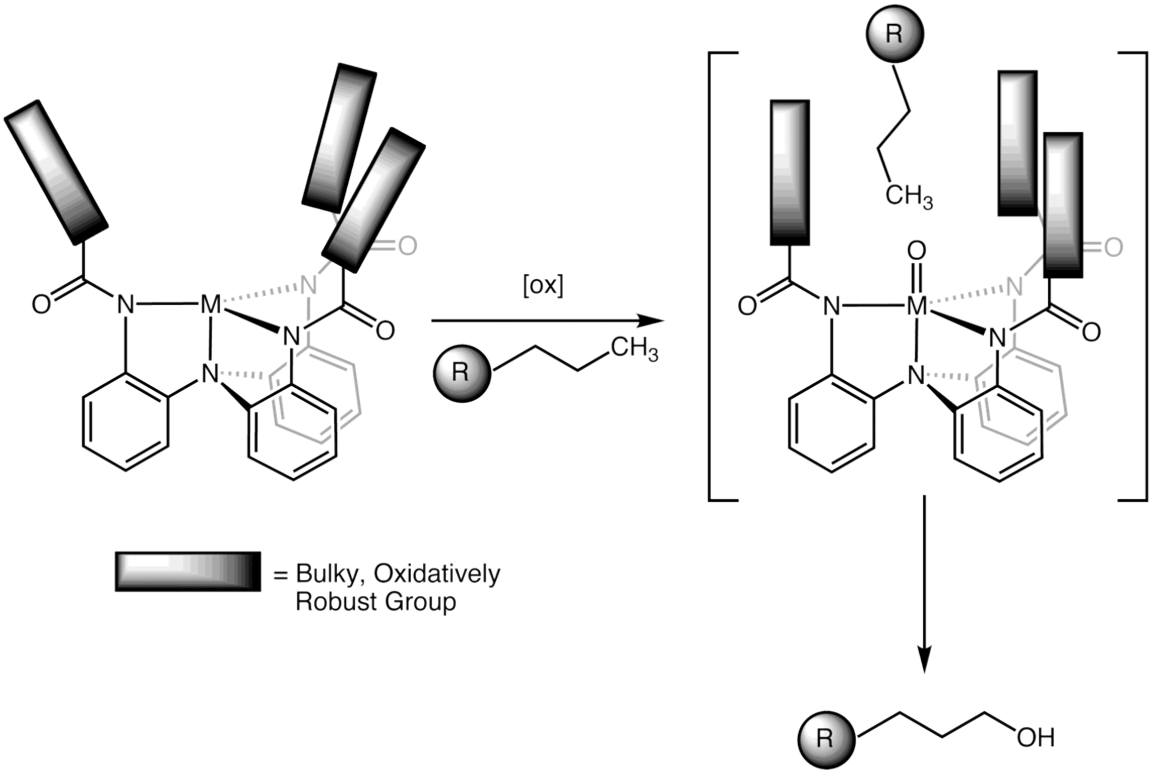

Scheme 5-3. Proposed size-selective C–H bond activation strategy based on the $[(L^R)]^{3-}$ ligand scaffold.

This would represent a new strategy in selective C–H bond activation, eliminating the need for directing groups to favor the activation of stronger C–H bonds. In this chapter, our efforts toward base metal-mediated C–H bond activation with Co(II) and Fe(II) are discussed. The synthesis and characterization of a high-spin, amidate-bridged, nonheme diiron complex is reported. Its ability to activate O_2 for an intramolecular oxidation reaction is also discussed.

Section 5-2. Results and Discussion

The synthesis and characterization of the ligand H_3L^{iPr} and its Co(II) complex, $Et_4N[Co(L^{iPr})]$, is described in chapter 2. Addition of one equivalent of the oxygen atom-transfer reagent iodosylbenzene (PhIO) to a blue DMF solution of $Et_4N[Co(L^{iPr})]$ results in a slow color change to reddish-purple as the solid dissolved. Subsequent workup and recrystallization gives deep burgundy crystals of a paramagnetic species in 66% yield (Scheme 5-4).

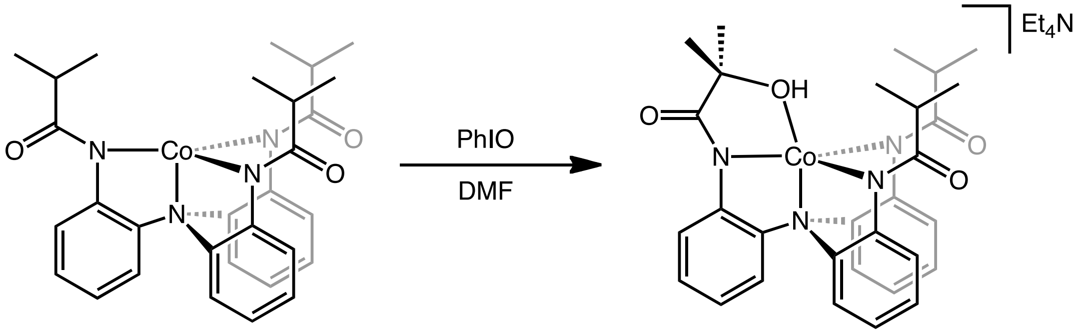

$Et_4N[Co(L^{iPr})]$

$Et_4N[Co(L^{Mod})]$
purple, 66%
FTIR (KBr, cm^{-1}): ν(CO) 1599
$\mu_{eff} = 4.32\ \mu_B$ (Evans' Method, CD_3CN, 298K)

Scheme 5-4. Synthesis of the hydroxylated complex $Et_4N[Co(L^{Mod})]$.

The paramagnetically broadened ^{1}H NMR spectrum contains ~12 signals, which indicates that the complex is of low symmetry. X-ray crystallographic analysis, FTIR, and ESI-MS indicate that this complex is the Co(II) alkoxide complex $Et_4N[Co(L^{Mod})]$. The complex results from alkyl hydroxylation at the methine C–H bond of one of the ligand isopropyl groups.

The solid-state structure of $Et_4N[Co(L^{Mod})]$ shows a five-coordinate cobalt ion bound equatorially by the three *N*-amidate donors of the ligand arms (Figure 5-5). The axial coordination sites are occupied by the tertiary amine of the ligand and the *O*-donor of the newly formed alcohol moiety.

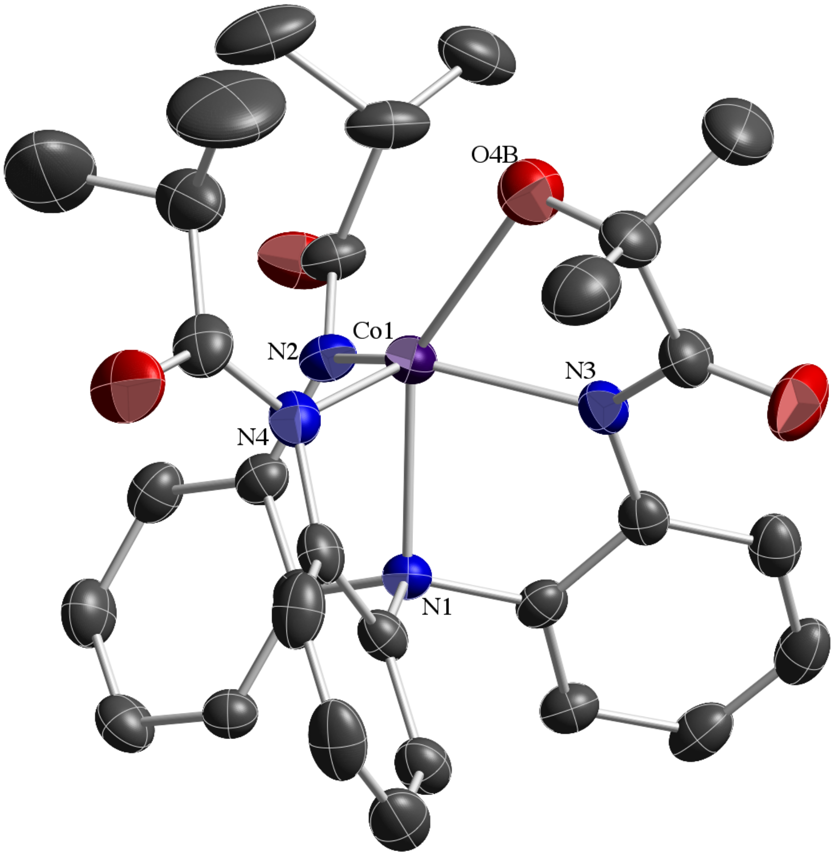

Figure 5-5. Solid-state structure of $Et_4N[Co(L^{Mod})]$. Counterion and hydrogen atoms are removed for clarity. Thermal ellipsoids are shown at 30% probability.

The ligands assume a distorted square pyramidal geometry around the cobalt ion (τ_5 = 0.19).[120] The long Co–O bond is consistent with a dative bond, indicating that the hydroxylated arm is protonated, and the complex is best described as a Co(II) complex with a coordinated alcohol. The FTIR spectrum of the complex supports this assignment, as the ν(OH) is observed at 3386 cm^{-1}. Only one ν(C=O) stretch is observed at 1599 cm^{-1}, but given how similar the asymmetric arm is to the unsubstituted arms, there is a strong possibility that these stretches overlap. The ESI-MS spectrum shows an $[M]^-$ peak at 572.4 m/z, consistent with the coordinate anion of the hydroxylated species. The magnetic moment was determined by Evans' method ($\mu_{eff} = 4.32\ \mu_B$, CD_3CN, 298 K) and is consistent with a high-spin ($S = 3/2$) Co(II) center.

Table 5-1. Selected metrical parameters for $Et_4N[Co(L^{Mod})]$.

	$Et_4N[Co(L^{Mod})]$
$Co–N_{amide}$ (ave.)	1.993(3) Å
$Co–N_{amine}$	2.195(3) Å
Co–O	2.365(18) Å
$N_{amine}–Co–O$	142.5(5)°
N3–Co–O	66.5(5)°
τ_5	0.19

The electrochemical properties of this complex were investigated by cyclic voltammetry experiments, but the complex did not display any significant or reversible electrochemical events at 25 °C in DMF with *n*-tetrabutylammonium hexafluorophosphate ($TBAPF_6$) as the supporting electrolyte.

Intramolecular reactivity similar to this has been observed previously. The Theopold group showed that exposing a Co(II) hydride complex, [Tp^{tBu,Me}Co(H)], to O_2 in the solid state resulted in oxidation of the *tert*-butyl C–H bonds of the ligand (Scheme 5-5).[244] Inspired by their result, we looked into using O_2 as an oxidant. We were somewhat surprised to discover, however, that solutions of $Et_4N[Co(L^{iPr})]$ were stable in the presence of dry O_2.

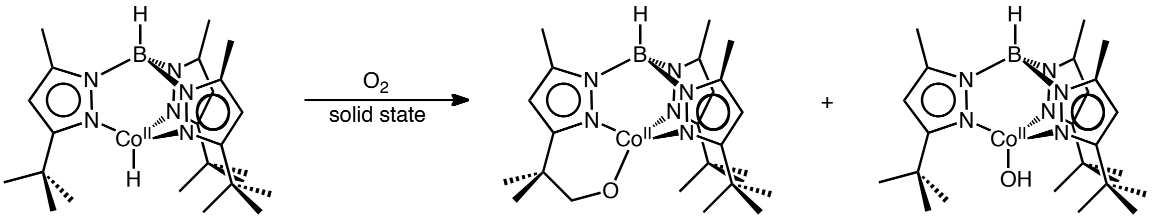

Mechanism:

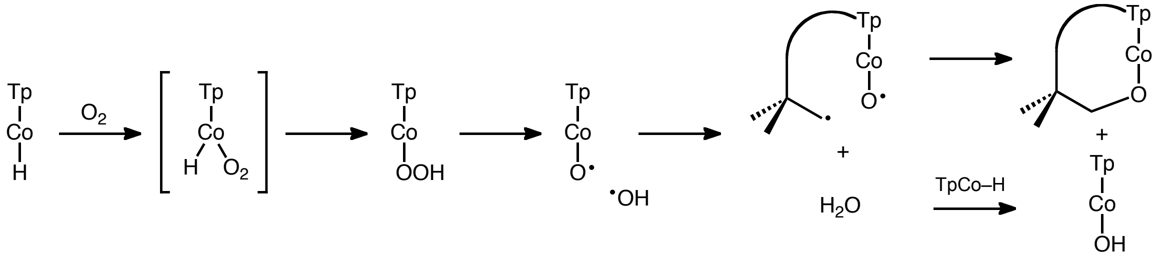

Scheme 5-5. Intramolecular hydroxylation of [Tp^{tBu,Me}Co(H)] by O_2. Adapted from Theopold et al.[244]

This result indicated that our tripodal ligand scaffold was not going to be useful for aerobic oxidations employing cobalt. In order to generate complexes more sensitive to oxidation, we moved to the more biologically relevant metal Fe(II). Given the more negative potentials expected for the Fe(II/III) couple versus that of Co(II/III), the oxidation of the analogous complexes in the presence of dioxygen should be facile.

Complexation of iron by the isopropyl ligand, H_3L^{iPr}, is accomplished by first deprotonating the three amide nitrogens with KH (3.1 equiv.) to generate the trianion, $[(L^{iPr})]^{3-}$. This is followed by metallation with $Fe(OAc)_2$ to generate the potassium salt, $K_2[Fe(L^{iPr})]_2$, concomitant with loss of two equivalents of potassium acetate. In situ salt metathesis with Ph_4PBr followed by subsequent work up and recrystallization gives $K(Ph_4P)[Fe(L^{iPr})]_2$ in 78% yield (Scheme 5-6). Attempts to exchange the second 0.5 equivalent of potassium for Ph_4P^+ proved unsuccessful.

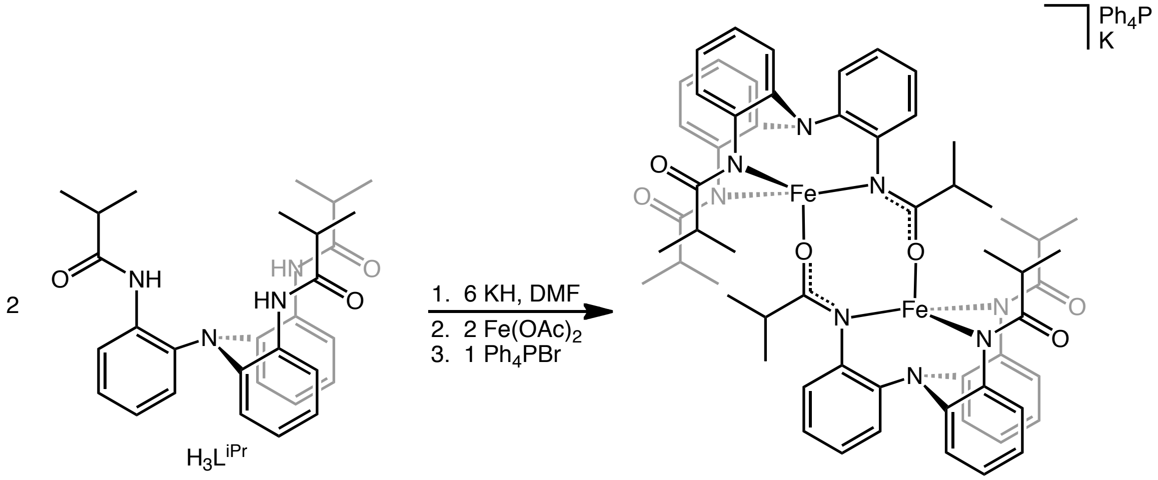

$K(Ph_4P)[Fe(L^{iPr})]_2$
yellow, 78%
FTIR (KBr, cm^{-1}): ν(CO) 1594
$\mu_{eff} = 7.27\ \mu_B$ (Evans' Method, $(CD_3)_2SO$, 298K)

Scheme 5-6. Synthesis of the bridged-amidate complex $K(Ph_4P)[Fe(L^{iPr})]_2$.

The solid-state structure of $K(Ph_4P)[Fe(L^{iPr})]_2$ reveals a dimeric *N,O*-amidate-bridged diiron structure resulting from bridging of one of the amidate arms of each ligand between the iron(II) metal ions (Figure 5-6). The remaining amidate ligands are all *N*-coordinated, and the overall geometry of the metal ions is tetrahedral ($\tau_4 = 0.94, 0.99$).[121]

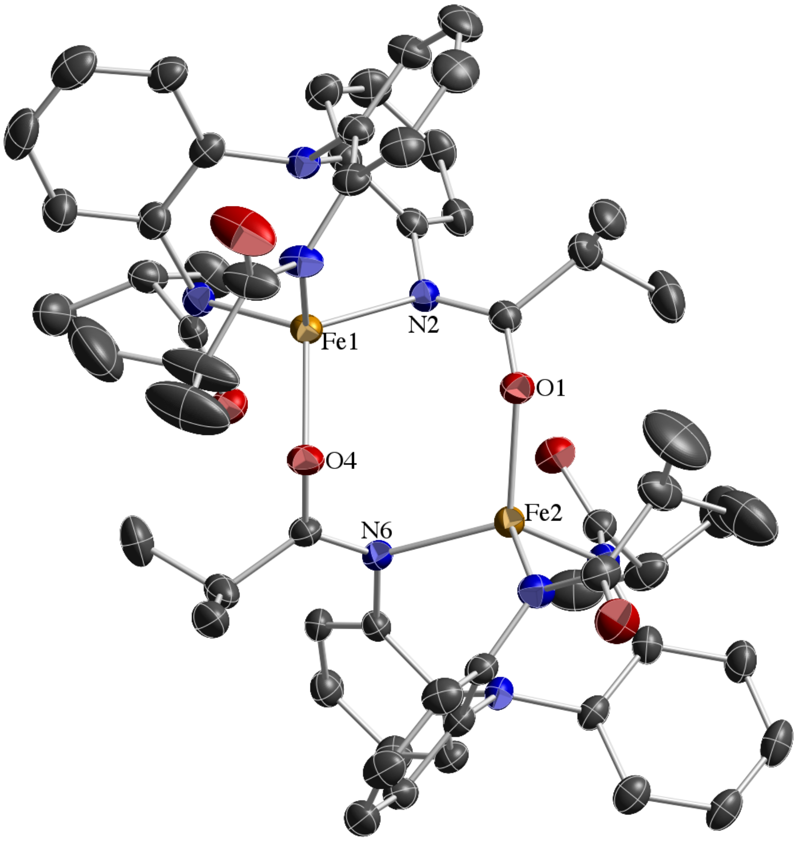

Figure 5-6. Solid-state structure of $K(Ph_4P)[Fe(L^{iPr})]_2$. Counterions and hydrogen atoms are omitted for clarity. Thermal ellipsoids are shown at 30% probability.

The tertiary nitrogen of the ligands lie an average of 2.527 Å from their respective iron ions, which is consistent with the absence of a bond to iron. The doubly amidate-bridged diiron(II) complex features a long Fe•••Fe distance of 4.138 Å. This intermetal distance compares well to those observed in the carboxylate-bridged diiron(II) complexes isolated by Lippard and coworkers. The distance between iron atoms in their windmill-type dicarboxylate-bridged complexes (those most similar in coordination to the present complex) fall between 3.4-4.4 Å (Figure 5-7).[3] In two specific cases, the complexes $[Fe_2(\mu\text{-}OTf)(\mu\text{-}XDK)(N\text{-}MeIm)_3(MeOH)(H_2O)](OTf)$ (4.120 Å) and $[Fe_2(\mu\text{-}O_2CAr^{Tol})_2(O_2CAr^{Tol})_2(N\text{-}MeIm)_2]$ (4.197 Å) were found to have magnetic moments of 7.19 and 7.45 μ_B, respectively.[247, 248]

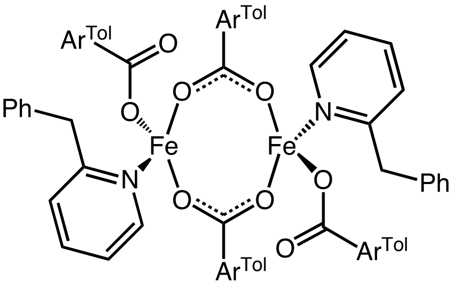

Figure 5-7. Example of windmill-type, dicarboxylate-bridged complex from the Lippard group.[227]

The solution-state magnetic moment of $K(Ph_4P)[Fe(L^{iPr})]_2$ was determined to be 7.27 μ_B (Evans' method, DMSO-d_6, 298 K), which, along with the Fe•••Fe distance, is consistent with two uncoupled $S = 2$ iron centers.

The electrochemical properties of $K(Ph_4P)[Fe(L^{iPr})]_2$ were investigated by cyclic voltammetry experiments, but the complex did not display any significant or reversible electrochemical events at 25 °C in DMF with $TBAPF_6$ as the supporting electrolyte. Under the same conditions, however, the addition of ~1 equivalent of Et_4NCN to the electrochemical cell gave rise to a reversible event at $E_{1/2} = -0.774$ ($\Delta E_p = 0.070$ V; $i_{pc}/i_{pa}^{-1} = 0.98$) vs. Fc/Fc$^+$. The event is tentatively assigned to the Fe(II)/Fe(III) couple for an uncharacterized cyanide adduct, $[Fe(L^{iPr})(CN)]^{2-}$ (Figure 5-8).

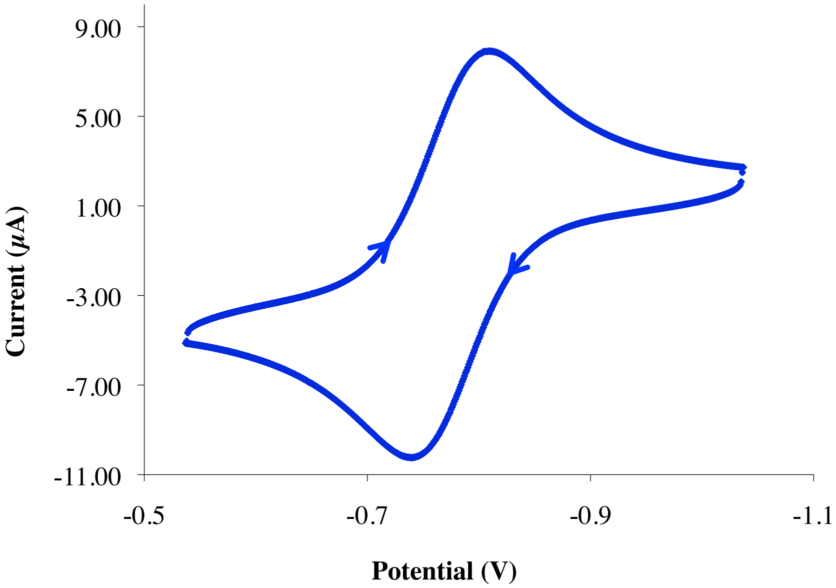

Figure 5-8. Cyclic voltammogram of cyanide adduct of $K(Ph_4P)[Fe(L^{iPr})]_2$ (DMF, 0.100 V/s).

It has been observed that the Fe(II) complexes of the ligand scaffold, $[(L^R)]^{3-}$, do not give significant or reversible electrochemical data without the presence of an anionic fifth ligand in the axial coordination site. All electrochemical data regarding the Fe(II) complexes in this chapter and in subsequent chapters will be in reference to the cyanide adducts generated in situ during electrochemical experiments.

The ^1H NMR spectrum of $K(Ph_4P)[Fe(L^{iPr})]_2$ shows a set of signals (>10) that is consistent with a complex of low symmetry, indicating that the dimer is maintained in solution. To test this theory, we ran a mixing experiment with the Zn(II) analogue of the Fe(II) complex. The complex, $K_2[Zn(L^{iPr})]_2$, is synthesized in a manner similar to that of the iron species, with the omission of the salt metathesis step; thus we isolate the complex as the dipotassium salt (Scheme 5-7).

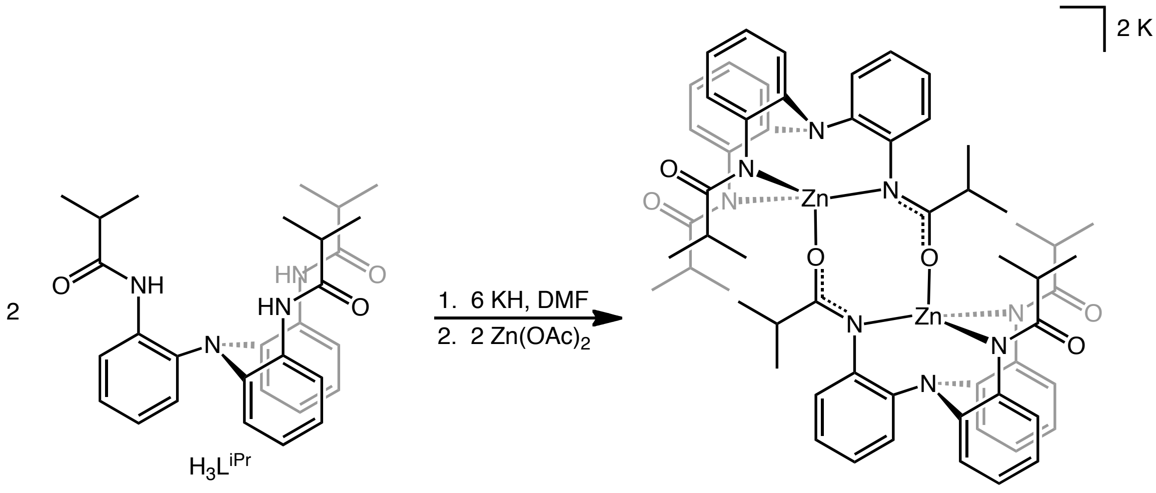

H_3L^{iPr}

$K_2[Zn(L^{iPr})]_2$
colorless, 43%
FTIR (KBr, cm^{-1}): ν(CO) 1597,1553

Scheme 5-7. Synthesis of the dimeric zinc complex, $K_2[Zn(L^{iPr})]_2$.

The solid-state structure of $K_2[Zn(L^{iPr})]_2$ reveals the same primary coordination sphere as $K(Ph_4P)[Fe(L^{iPr})]_2$, with one amidate from each ligand coordinated in an *N*, *O*-bridging mode with the zinc of the opposite ligand (Figure 5-9).

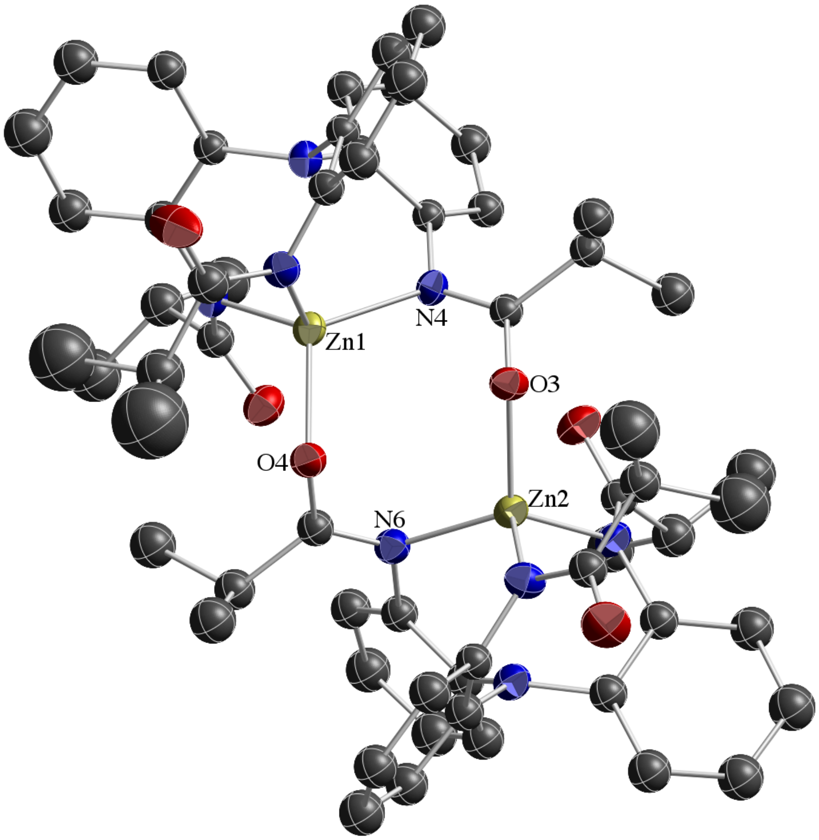

Figure 5-9. Solid-state structure of $K_2[Zn(L^{iPr})]_2$. Counterions and hydrogen atoms are omitted for clarity. Thermal ellipsoids are shown at 30% probability.

Each Zn(II) ion is in a tetrahedral geometry ($\tau_4 = 0.96, 0.97$)[121], and the tertiary nitrogen of each ligand remains unbound with the average Zn•••N distance slightly longer (2.578 Å) than in the Fe(II) case. The Zn•••Zn distance, however, is shorter in this species (4.053 Å) than was observed in the iron structure (4.138 Å).

Table 5-2. Selected metrical parameters for $K(Ph_4P)[Fe(L^{iPr})]_2$ and $K_2[Zn(L^{iPr})]_2$.

	$K(Ph_4P)[Fe(L^{iPr})]_2$	$K_2[Zn(L^{iPr})]_2$
$M–N_{amid.}$ (ave.)	2.105(4) Å	2.040(4) Å
M–O (ave.)	1.992(3) Å	1.991(3) Å
M•••M	4.138 Å	4.053 Å
Out of plane distance (ave.)	0.688 Å	0.664 Å
τ_4	0.94, 0.99	0.96, 0.97

The diamagnetic ^{1}H NMR data for $K_2[Zn(L^{iPr})]_2$ shows that it is C_3-symmetric, indicating that, in this case, the dimer breaks up to generate the monomeric species in solution. By mixing this complex with $K(Ph_4P)[Fe(L^{iPr})]_2$ in DMSO-d_6, the NMR should show the formation of a third species if the $K(Ph_4P)[Fe(L^{iPr})]_2$ dimer breaks up in solution, resulting from the formation of a mixed Fe/Zn dimer. Therefore, a concentrated DMSO-d_6 solution containing a 1:1 mixture of $K_2[Zn(L^{iPr})]_2$ and $K(Ph_4P)[Fe(L^{iPr})]_2$, was prepared, and an ^{1}H NMR spectrum was acquired. A comparison of this spectrum with the reference spectra of the two original compounds shows all of the peaks of the parent complexes but gives no indication that any new species (diamagnetic or paramagnetic) are formed. This result points to the fact that $K(Ph_4P)[Fe(L^{iPr})]_2$ likely maintains its dimeric structure in solution.

Treatment of $K(Ph_4P)[Fe(L^{iPr})]_2$ with PhIO in DMF results in rapid color change from yellow to deep red (Scheme 5-8). Workup yields a dark red solid that is crystallized by diffusion of diethyl ether into a concentrated DMF solution of the crude product to give crystals of $Ph_4P[Fe(L^{Mod})]$ in 86% yield.

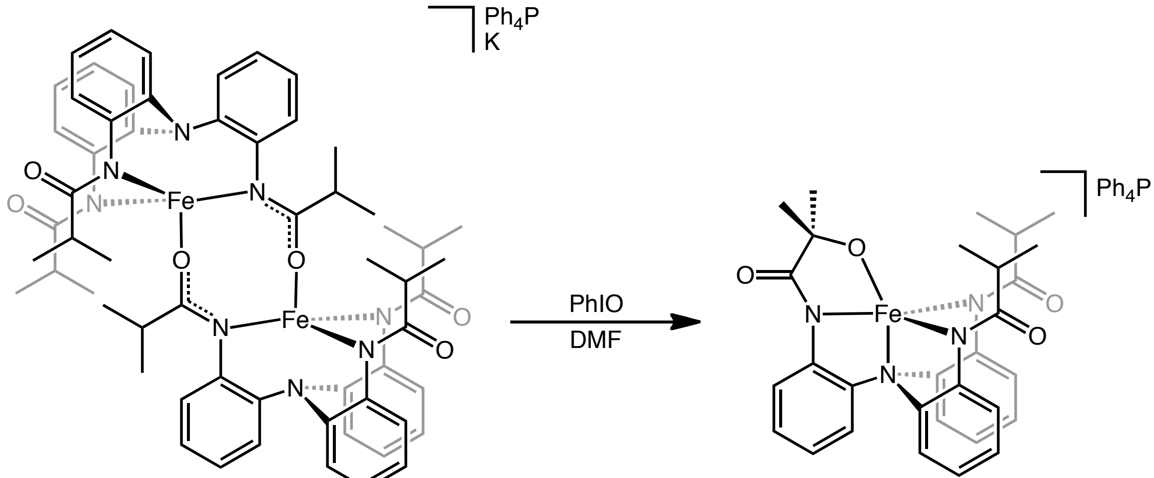

$K(Ph_4P)[Fe(L^{iPr})]_2$

$Ph_4P[Fe(L^{Mod})]$
red, 60% with respect to Ph_4P^+
FTIR (KBr, cm^{-1}): ν(CO) 1611
$\mu_{eff} = 5.86\ \mu_B$ (Evans' Method, DMF-d_7, 298K)

Scheme 5-8. Synthesis of the hydroxylated Fe(III) complex, $Ph_4P[Fe(L^{Mod})]$.

The solid-state structure of $Ph_4P[Fe(L^{Mod})]$ reveals a monomeric complex in which, much like $Et_4N[Co(L^{Mod})]$, hydroxylation has occurred at one of the methine positions of the isopropyl substituents, resulting in a five-coordinate complex with an alkoxide ligand (Figure 5-10). In the *trans* position to the alkoxide ligand, the tertiary amine of the chelate is coordinated, and the three remaining sites are filled by the *N*-donors of the amidate arms, which, all together, result in an intermediate geometry around the iron center (τ_5 = 0.55).[120] The short Fe–O bond length (1.878 Å) is consistent with the assignment of an alkoxide ligand. This complex is best assigned as an Fe(III) alkoxide complex.

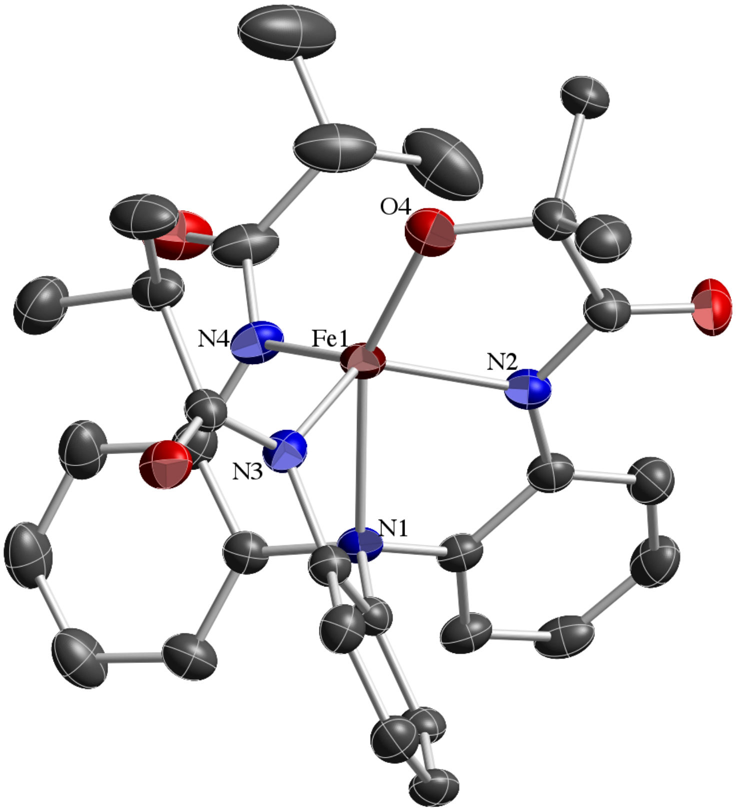

Figure 5-10. Solid-state structure of $Ph_4P[Fe(L^{Mod})]$. Counterion and hydrogen atoms have been removed for clarity. Thermal ellipsoids are shown at 50% probability.

The other characterization data is in support of this assignment. The FTIR spectrum of the complex shows no indication of a ν(OH) stretch, and the UV-visible absorption spectrum shows a strong band at 450 nm (ε = 3000 $M^{-1}cm^{-1}$, DMF), which is representative of an Fe(III) alkoxide LMCT event.[249] The solution-state magnetic measurements indicate a μ_{eff} of 5.86 μ_B (Evans' method, DMF-d_7, 298 K), which is consistent with a high-spin (S = 5/2) Fe(III) center. Given the differences in product oxidation state and ligand protonation from the otherwise identical reactions, $Et_4N[Co(L^{Mod})]$ and $Ph_4P[Fe(L^{Mod})]$ are likely the result of two different mechanistic pathways that are currently unknown. Given the demonstrated propensity for bridging between the iron complexes of the isopropyl ligand, it seems reasonable to propose that the reaction proceeds via a diiron, oxo, or hydroxo-bridged intermediate. This seems even more reasonable when one considers the fact that the single *O*-atom donor, PhIO, as well as the possible two-atom donating dioxygen are effective for alkoxide formation. The cobalt hydroxylation could then be explained by a mononuclear HAT/radical rebound mechanism.

Table 5-3. Comparison of selected metrical parameters for $Et_4N[Co(L^{Mod})]$ and $Ph_4P[Fe(L^{Mod})]$.

	$Et_4N[Co(L^{Mod})]$	$Ph_4P[Fe(L^{Mod})]$
$M–N_{amid.}$ (ave.)	1.993(3) Å	1.992(4) Å
$M–N_{amine}$	2.195(3) Å	2.275(4) Å
M–O	2.365(18) Å	1.878(4) Å
$N_{amine}–M–O$	142.5(5)°	155.04(17)°
$N_{amide}–M–O$	66.5(5)°	81.72(18)°
τ_5	0.19	0.55

Analysis of $Ph_4P[Fe(L^{Mod})]$ by cyclic voltammetry (25 °C, DMF, 0.2 M $TBAPF_6$) gives rise to a single, reversible event at $E_{1/2} = -1.533$ ($\Delta E_p = 0.080$ V; $i_{pc}/i_{pa}^{-1} = 0.99$) vs. Fc/Fc^+ (Figure 5-11). This feature is tentatively assigned to the Fe(II)/Fe(III) couple.

This data supports the necessity for an anionic, fifth ligand in order to gain access to Fe(III) complexes of the $[(L^{R})]^{3-}$ ligand scaffold.

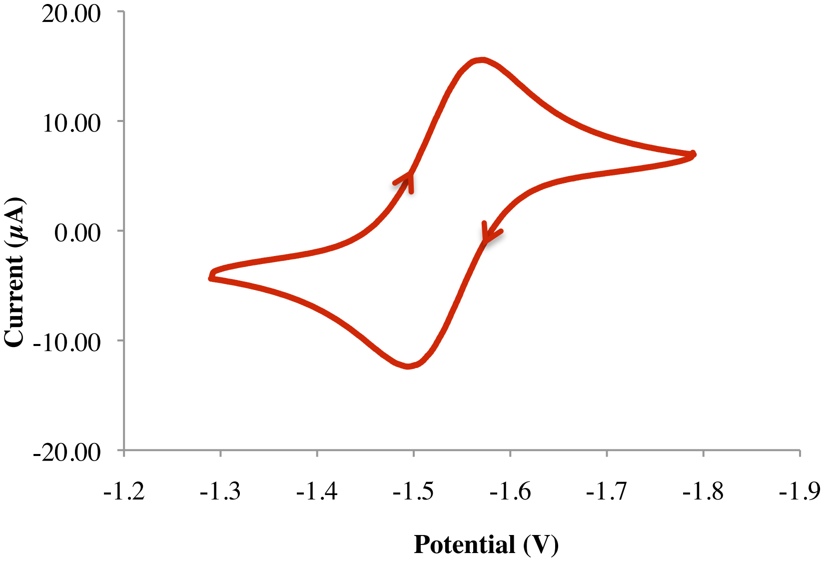

Figure 5-11. Cyclic votammogram of $Ph_4P[FeL^{Mod}]$ recorded at 100 mV/s.

In order to probe the reactivity of $K(Ph_4P)[Fe(L^{iPr})]_2$ with O_2, a UV-visible absorption spectroscopy study was undertaken, in which excess O_2 was added to a cuvette containing an anaerobic solution of $K(Ph_4P)[Fe(L^{iPr})]_2$ (6.2 mM, DMF), and the reaction was monitored over time. After about 15 minutes, the solution had changed from pale yellow to orange-red, and the spectra showed the steady growth of a band at 455 nm (ε = 2800 $M^{-1}cm^{-1}$), which is very similar to that of the spectrum of $Ph_4P[Fe(L^{Mod})]$, with no observed intermediates. This was an indication that the same bond activation reaction may have been occurring with dioxygen as the oxidant/*O*-atom source. The extinction coefficient of the final spectrum is consistent with approximately 93% conversion to $[Fe(L^{Mod})]^-$.

The reaction was repeated on a bench top scale using standard Schlenk technique (Scheme 5-9). The addition of dry dioxygen to an anaerobic solution of $K(Ph_4P)[Fe(L^{iPr})]_2$ elicited the same color change from yellow to dark orange-red over the course of an hour. Work up of the reaction under an inert atmosphere gives a dark red solid that can be recrystallized by diffusion of diethyl ether into a concentrated DMF solution of the solid.

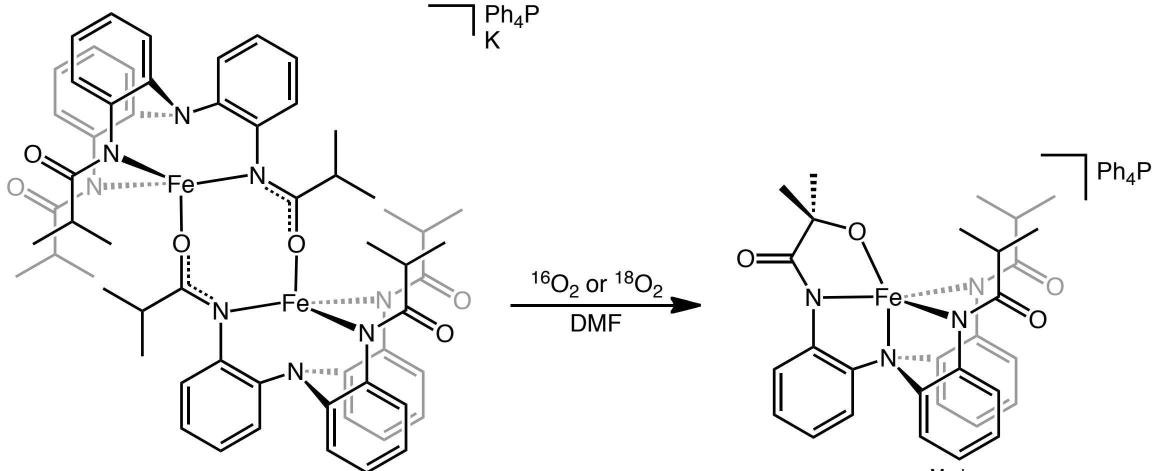

$K(Ph_4P)[Fe(L^{iPr})]_2$

$Ph_4P[Fe(L^{Mod})]$
FTIR (KBr, cm^{-1}): ν(CO) 1611

Scheme 5-9. Synthesis of $Ph_4P[Fe(L^{Mod})]$ using dioxygen as the oxidant.

Analysis of the crystalline material by NMR, FTIR, UV-vis, and ESI-MS confirms the identity of the product as $Ph_4P[Fe(L^{Mod})]$. To verify that dioxygen was indeed the source of the oxygen atom incorporated into the alkoxide ligand, the reaction was repeated with 98% ^{18}O-labeled dioxygen as the oxidant. Work up of the reaction using the standard procedure yields dark red crystalline material. High-resolution ESI-MS of the crystals confirms the presence of [Fe(L$^{\mathrm{Mod}}$)]$^{-}$ with an *m/z* consistent with ^{18}O incorporation into the ion ([Fe(L$^{\mathrm{Mod}}$)]$^{-}$: *m/z* 568.178 (^{16}O), 570.184 (^{18}O)) (Figure 5-12).

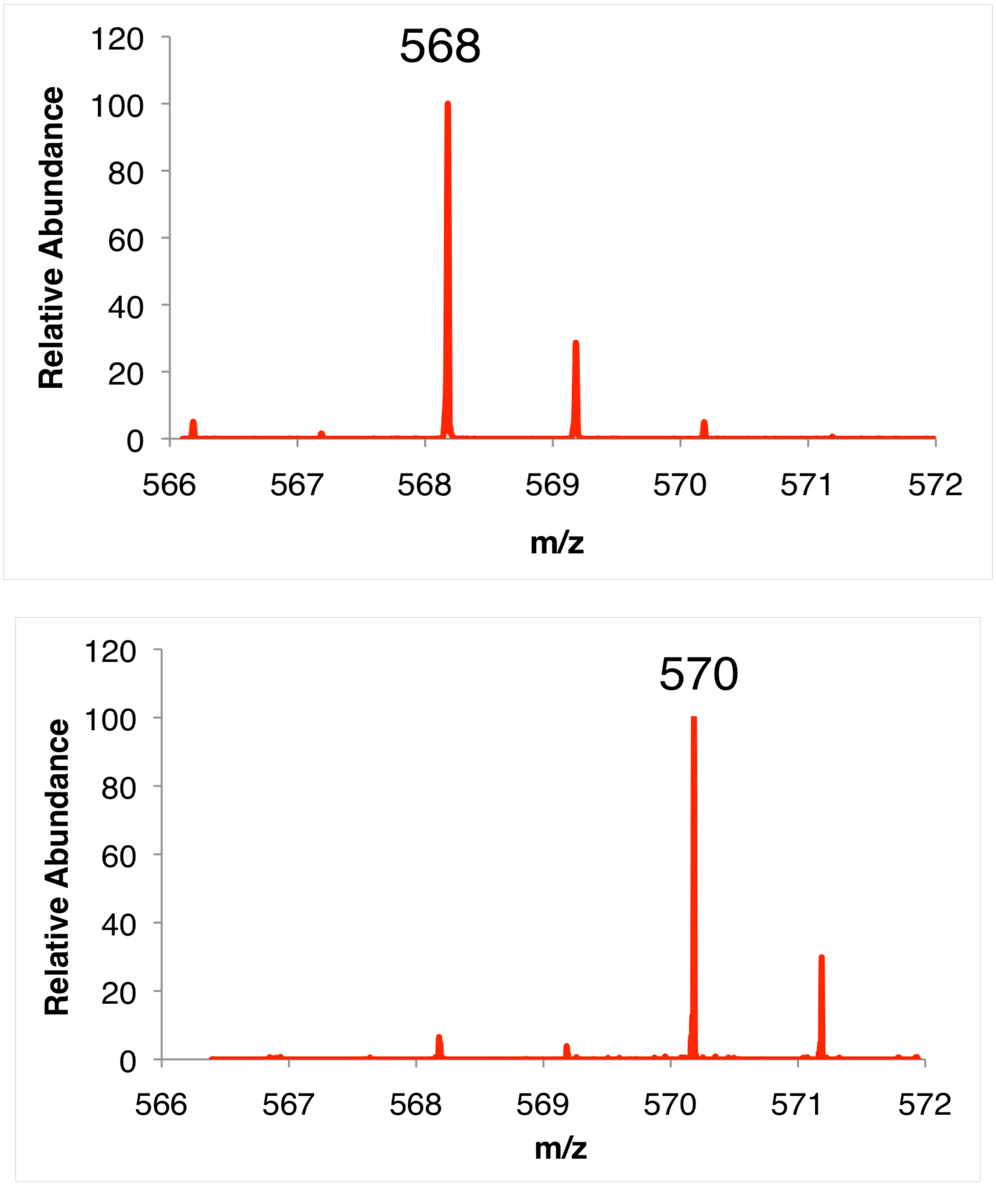

Figure 5-12. HRESI-MS spectra showing [Fe(L$^{\mathrm{Mod}}$)]$^{-}$ made using $^{16}O_2$ (top) and ^{18}O-labeled O_2 (bottom).

FTIR of this material yields a nearly identical spectrum to that of the ^{16}O-containing material, with no peaks identifiable as either alkoxide C–O or Fe–O bonds. Given the complexity of the vibrational spectrum of this species, however, the absence of these peaks is not surprising. The exact mechanism of this reaction is currently unknown, although given the strength of the C–H bond in question, the similarity of the reaction when PhIO is used as the *O*-atom source, and literature precedent for similar reactivity observed in Fe/O_2 systems,[227, 236] the facile formation of the alkoxide moiety is likely attributable to a high-valent bis-μ-oxo intermediate (Scheme 5-10). The observation that the dimeric structure of $[Fe(L^{iPr})]_2^{2-}$ is maintained in solution is in support of this. It is possible that dioxygen could bridge the gap between the two iron centers to form a bridged-1,2-peroxo Fe(III) species that could then be further reduced to generate the diiron(IV) bis-μ-oxo species, which would be capable of C–H bond activation by a radical rebound mechanism.

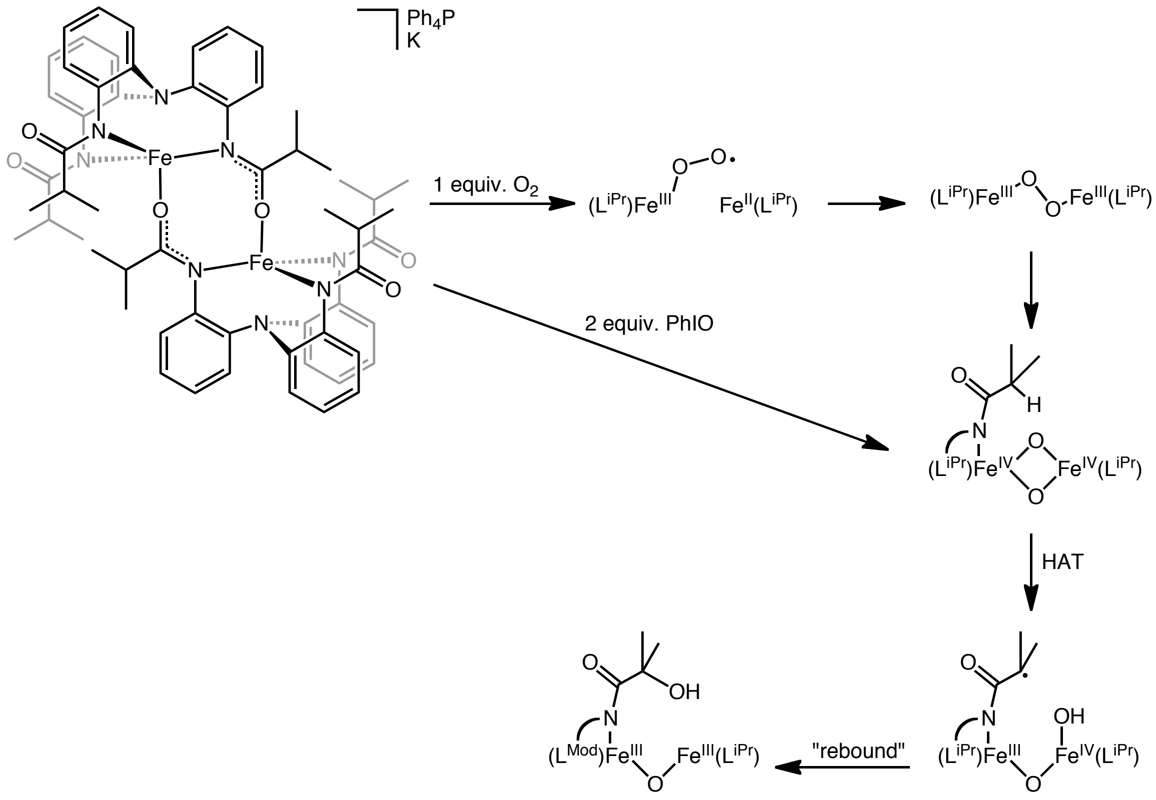

Scheme 5-10. Proposed mechanism for the oxidation of C–H bonds by $[Fe(L^{iPr})]_2^{2-}$ using either O_2 or PhIO as the terminal oxidant and *O*-atom source.

This reactivity represents not only a rare example of dioxygen cleavage by a synthetic nonheme Fe(II)-based system, but also demonstrates that the O_2-derived oxidant has the ability to activate strong intramolecular C–H bonds.[227, 228, 236]

In order to explore this reactivity further, we looked toward a ligand in which the acyl substituents should be more robust in the presence of strong oxidants, $[(L^{Ph})]^{3-}$. The stronger aryl C–H bonds should by less prone to abstraction by the "Fe–O_x" fragment. The synthesis of the phenyl derivative of the $[(L^{R})]^{3-}$ ligand scaffold is presented in chapter 2. The Fe(II) complex of the ligand is synthesized using a route similar to those for the Co(II) and Ni(II) analogues of this ligand (chapters 2 and 3, respectively). The ligand, H_3L^{Ph}, is deprotonated with three equivalents of KH in DMF to yield the tripotassium salt of the ligand, $K_3[(L^{Ph})]$, in situ (Scheme 5-10). The ligand is then transmetallated with $Fe(OAc)_2$ to generate the potassium salt, $K[Fe(L^{Ph})]$, coupled with loss of two equivalents of KOAc.

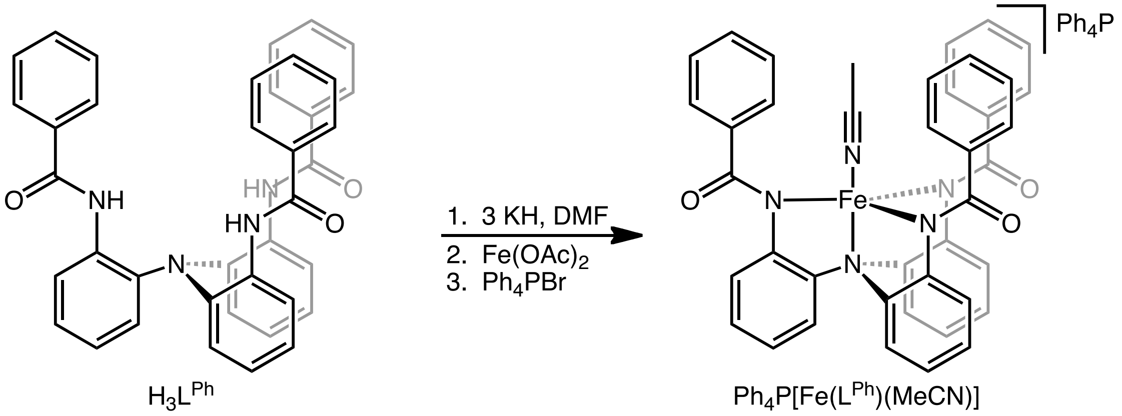

Scheme 5-11. Synthesis of five-coordinate Fe(II) adduct, $Ph_4P[Fe(L^{Ph})(MeCN)]$.

The last step of the one-pot synthesis involves the addition of Ph_4PBr to generate the desired complex, $Ph_4P[Fe(L^{Ph})]$, and one equivalent of KBr. Work up to remove the potassium salts and recrystallization by diffusion of diethyl ether into an MeCN solution of the complex, gives $Ph_4P[Fe(L^{Ph})(MeCN)]$ as bright yellow, X-ray quality crystals in good yield (74%). The solid-state structure of $Ph_4P[Fe(L^{Ph})(MeCN)]$ is very similar to those of $Ph_4P[Co(L^{Ph})(MeCN)]$ and $Ph_4P[Ni(L^{Ph})(MeCN)]$, featuring a five-coordinate Fe(II) center in approximately trigonal bipyramidal geometry ($\tau_5 = 0.95$) (Figure 5-13).

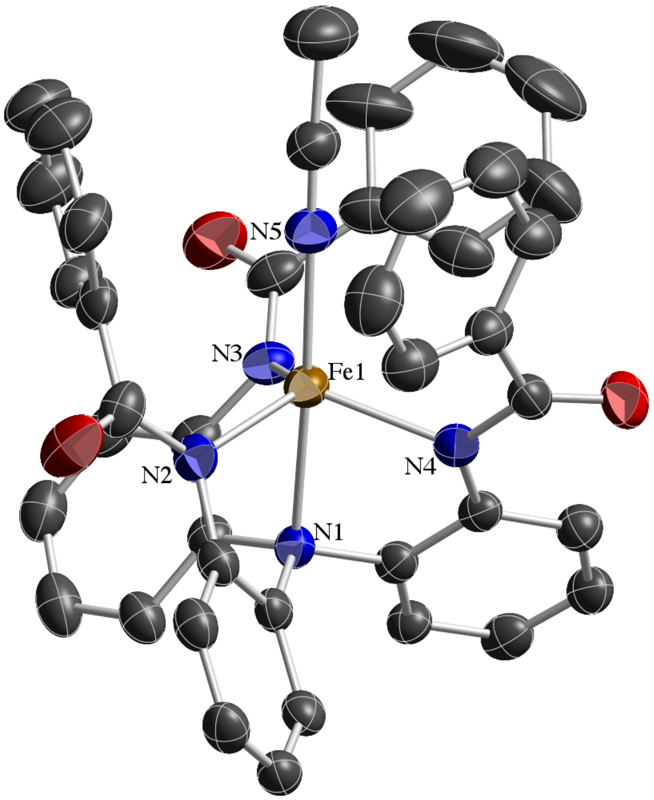

Figure 5-13. Solid-state structure of $Ph_4P[Fe(L^{Ph})(MeCN)]$. Counterion and hydrogen atoms have been removed for clarity. Thermal ellipsoids are shown at 50% probability.

The primary coordination sphere around the iron center consists of the three *N*-amidate donors of the ligand scaffold occupying the trigonal plane, with the tertiary amine of the chelate coordinated to one of the axial sites. The second axial site contains an MeCN solvent molecule from the recrystallization solvents.

Table 5-4. Selected metrical parameters for $Ph_4P[Fe(L^{Ph})(MeCN)]$.

	$Ph_4P[Fe(L^{Ph})(MeCN)]$
$Fe–N_{amid.}$ (ave.)	2.089(5) Å
$Fe–N_{amine}$	2.229(4) Å
$Fe–N_{MeCN}$	2.089(5) Å
$N_{amine}–Fe–N_{MeCN}$	174.29(18)°
τ_5	0.95

The paramagnetically-shifted ^1H NMR of $Ph_4P[Fe(L^{Ph})(MeCN)]$ contains seven signals, indicating that the complex maintains C_3-symmetry in solution. Solution-state magnetic moment measurements give a μ_{eff} of 5.47 μ_B (Evans' method, CD_3CN, 25 °C), consistent with the assignment of a high-spin ($S = 2$) Fe(II) center. The electrochemical properties of $Ph_4P[Fe(L^{Ph})(MeCN)]$ were investigated by cyclic voltammetry experiments, but the complex did not display any significant or reversible electrochemical events at 25 °C in DMF with $TBAPF_6$ as the supporting electrolyte. As such, the CV was attempted once more in the presence of ~1 equivalent of Et_4NCN added directly to the electrochemical cell (Figure 5-15). As was the case for $K(Ph_4P)[Fe(L^{iPr})]_2$, the addition of cyanide ion to $Ph_4P[Fe(L^{Ph})(MeCN)]$ gave rise to a reversible electrochemical event at $E_{1/2} = -0.507$ V ($\Delta E_p = 0.081$ V; $i_{pc}/i_{pa}^{-1} = 0.85$) vs. Fc/Fc^+. The shift to more positive potentials relative to that observed for the cyanide adduct of

$K(Ph_4P)[Fe(L^{iPr})]_2$ is consistent with the change in acyl substituents from electron donating isopropyl groups to electron withdrawing phenyl groups.

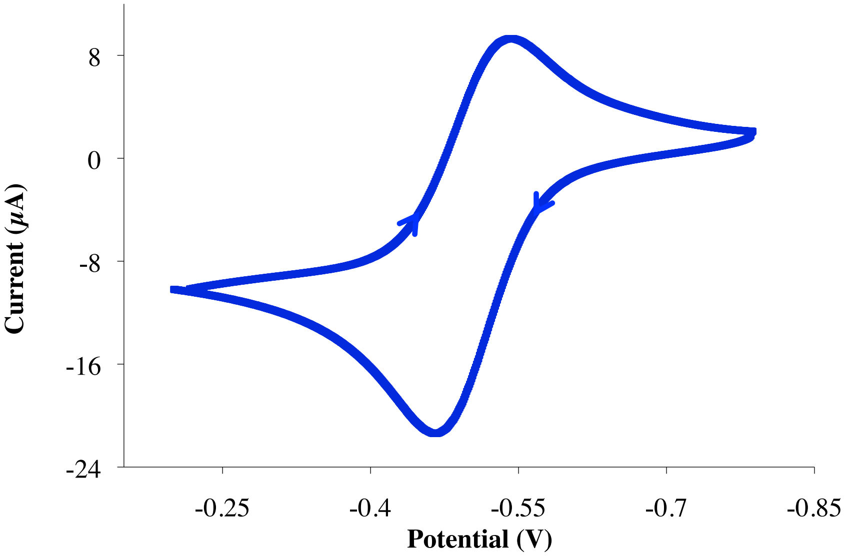

Figure 5-14. Cyclic votammogram of the cyanide adduct of $Ph_4P[(Fe(L^{Ph}))(MeCN)]$ in DMF, recorded at 0.050 V/s.

As was the case for $[Fe(L^{iPr})(CN)]^{2-}$, the signal is tentatively assigned to the Fe(II)/Fe(III) couple for a cyanide adduct, $[Fe(L^{Ph})(CN)]^{2-}$, that is uncharacterized at the time of writing.

The addition of one equivalent of PhIO to solutions of $Ph_4P[Fe(L^{Ph})(MeCN)]$ results in the formation of a red species. The color change is consistent with an oxidation of the Fe(II) center to an Fe(III) species. However, the product of the reaction has yet to be identified. Mass spectrometry (ESI) of the crude solid indicates that the ligand remains unperturbed during the reaction, and the product may be an Fe(III) hydroxide. Dark red, X-ray quality crystals have been isolated from the reaction mixtures. The X-ray data reveal well-resolved $[Fe(L^{Ph})]^-$ units, each with a single associated Ph_4P^+ ion. The data indicates the presence of an fifth, axial ligand on the iron center, but the ligand is highly disordered and the site may be partially occupied by a DMF solvent molecule. A possible explanation as to why this species eludes characterization lies in the ligand acyl substituents. In chapter 2, the inability of the Co(II) complex, $Ph_4P[Co(L^{Ph})(MeCN)]$, to bind cyanide was discussed. The close proximity of the phenyl substituents to the axial binding site on the cobalt center discourages anion binding as a result of coulombic repulsion between the anion and the electron-rich, aromatic rings. It is likely that in this analogous complex the same repulsion exists between the aryl rings of the ligand and whatever exogenous ligand (presumably anionic) binds to the metal center during the course of the reaction.

Similar problems are faced in the oxidation of $Ph_4P[Fe(L^{Ph})(MeCN)]$ with dioxygen. The addition of dry O_2 to an anaerobic MeCN or DMF solution of $Ph_4P[Fe(L^{Ph})(MeCN)]$ results in the slow change from yellow to dark orange-red over the course of an hour. If the reaction is performed in DCM, the color change is much faster. Monitoring this reaction by UV-vis at 25 °C in any of the aforementioned solvents results in subtle changes to the spectrum that are consistent with the formation of a new species. Work up and recrystallization of the products of these reactions, however, result in the isolation of starting material, along with small amounts of decomposition products, as verified by FTIR and UV-vis. There are two possible explanations for these results. Either (1) the phenyl rings of the ligand are preventing the formation of adducts of reduced dioxygen by coulombic repulsion (see chapter 2 for similar observations in cyanide coordination by $Ph_4P[Co(L^{Ph})(MeCN)]$), or (2) the complexes reversibly bind O_2

(i.e., Hemerythrin)[44], and the starting material is thermodynamically favored. Either way, further study is needed in this system to characterize the unique interactions of $Ph_4P[Fe(L^{Ph})(MeCN)]$ with both PhIO and dioxygen.

Section 5-3. Experimental

General Considerations

All manipulations were carried out using standard Schlenk techniques or conducted in an MBraun Labmaster 130 drybox under a nitrogen atmosphere. All reagents used were purchased from commercial vendors and used as received unless otherwise noted. Anhydrous solvents were purchased from Sigma-Aldrich and further purified by sparging with Ar gas followed by passage through activated alumina columns. Deuterated dimethyl sulfoxide (DMSO-d_6) was purchased from Aldrich and degassed and dried according to standard procedures[127] prior to use. Labeled dioxygen gas (^{18}O, 98%) was obtained from ICON Isotopes, Summit, NJ. Elemental analyses were performed by Midwest Microlabs, Indianapolis, IN. ^1H NMR spectra were recorded on Varian Inova 400 MHz and Mercury 300 MHz spectrometers at ambient temperature. Chemical shifts were referenced to residual solvent peaks. Infrared spectra were recorded as KBr pellets on a Varian Scimitar 800 Series FT-IR spectrophotometer. UV-Visible absorption spectra were recorded on a Cary 50 spectrophotometer using 1.0 cm quartz cuvettes. Solution state magnetic moments were measured using the Evans method.[128] Mass spectra were recorded in the Mass Spectrometry Center at Emory University on a JEOL JMS-SX102/SX102A/E mass spectrometer. X-ray diffraction studies were carried out in the X-ray Crystallography Laboratory at Emory University on a Bruker Smart 1000 CCD diffractometer. Cyclic voltammetric experiments were carried out using a CH Instruments (Austin, TX) Model 660C potentiostat. All experiments were conducted in DMF with 0.20 M tetrabutylammonium hexafluorophosphate as the supporting electrolyte. Electrochemical experiments were conducted in a three-component cell consisting of a Pt auxiliary electrode, a non-aqueous reference electrode ($Ag/AgNO_3$), and a glassy carbon working electrode. All electrochemical measurements are referenced and reported versus the ferrocene/ferrocenium couple.

$Et_4N[Co(L^{Mod})]$

To a stirred solution of $Et_4N[Co(L^{iPr})]$ (64 mg, 0.09 mmol) in DMF was added iodosylbenzene (21 mg, 0.09 mmol) as a solid. The blue solution turned deep red-purple as the solid dissolved. After 2h of stirring, solvent was removed in vacuo. The deep red-purple solid was taken up in MeCN, filtered, and the filtrate was concentrated to dryness. X-ray quality crystals were obtained by vapor diffusion of diethyl ether into a concentrated MeCN solution of $Et_4N[Co(L^{Mod})]$ (43 mg, 66%). ^1H NMR (δ, CD_3CN, 400 MHz): 33.80, 28.67, 22.25, 18.44, 17.77, 15.37, 13.46, 12.14, 3.37(q, 8H, Et_4N), 1.35(bs, 12H, Et_4N), -1.96, -3.90, -16.29. FTIR (KBr, cm^{-1}) ν: 3386 (OH), 3058, 2964, 2929, 2868, 1599 (CO), 1577, 1563, 1480, 1446, 1384, 1353, 1278, 1219, 1173, 1160, 1088, 1042, 1000, 968, 873, 771, 752, 621, 497. $\mu_{eff} = 4.32\ \mu_B$ (Evans' Method, CD_3CN, 298K). λ_{max}(ε, $M^{-1}cm^{-1}$) (DMF): 524(128), 581(150), 653(72).

$K(Ph_4P)[Fe(L^{iPr})]_2$

To a stirred solution of H_3L^{iPr} (153 mg, 0.31 mmol) in DMF (3 mL) was added KH (40 mg, 1.01 mg) as a solid. When H_2 evolution ceased, $Fe(OAc)_2$ (53 mg, 0.31 mmol) and Ph_4PCl (115 mg, 0.31 mmol) were added together as a DMF (1 mL) solution. After stirring for 2h, MeCN (3 mL) was added to precipitate K(OAc). The reaction mixture was filtered over Celite, and the filtrate was concentrated to dryness. X-ray quality crystals were obtained by vapor diffusion of diethyl ether into a concentrated DMF solution of $K(Ph_4P)[Fe(L^{iPr})]_2$ (179 mg, 78%). ^{1}H NMR (δ, DMSO-d_6, 400 MHz): 25.58, 15.31, 13.92, 12.96, 8.96, 7.90(bs, 4H, Ph_4P), 7.75(bs, 8H, Ph_4P), 7.69(d, 8H, Ph_4P), 6.51, 1.00, 0.71, -0.16, -1.45. FTIR (KBr, cm^{-1}) ν: 3056, 3023, 2989, 2928, 1596, 1583, 1556 (CO), 1473, 1441, 1354, 1269, 1234, 1108, 1041, 997, 914, 799, 755, 723, 688, 622, 592, 527, 485. μ_{eff} = 7.27 μ_B (Evans' Method, DMSO-d_6, 298K). Anal. Calcd (found) for $K(Ph_4P)[Fe(L^{iPr})]_2$: C, 66.94 (66.82); H, 6.03 (6.07); N, 8.43 (8.44).

$K_2[Zn(L^{iPr})]_2$

To a stirred solution of H_3L^{iPr} (158 mg, 0.32 mmol) in DMF (3 mL) was added KH (42 mg, 1.04 mg) as a solid. When H_2 evolution ceased, $Zn(OAc)_2$ (58 mg, 0.32 mmol) was added as a solid. After stirring for 22h, the reaction mixture was filtered over Celite, and the filtrate was set up for recrystallization by layering diethyl ether on top of the filtrate. X-ray quality crystals were obtained by vapor diffusion of diethyl ether into a concentrated DMF solution of $K_2[Zn(L^{iPr})]_2$ (82 mg, 43%). ^{1}H NMR (δ, DMSO-d_6, 400 MHz): 7.41(bs, ArH), 6.79(t, 3H, ArH), 6.62(t, 3H, ArH), 0.632(bs, 18H, CH_3). FTIR (KBr, cm^{-1}) ν: 3060, 2962, 2928, 2867, 1597, 1553 (CO), 1523, 1485, 1449, 1413, 1309, 1264, 1221, 1091, 1037, 948, 747, 661, 622, 474.

NMR Mixing Experiment

A DMSO-d_6 (0.60 mL) solution of $K_2[Zn(L^{iPr})]_2$ (11.3 mg, 0.01 mmol) and $K(Ph_4P)[Fe(L^{iPr})]_2$ (10.9 mg, 0.01 mmol) was prepared by slowly dissolving the two salts in a small vial. Upon complete dissolution of the salt, the solution was transferred to an NMR tube. A ^{1}H NMR spectrum was acquired of the sample (400 MHz, 25 °C) and compared to reference spectra. The spectrum showed only the peaks that were present in the two reference spectra of the starting materials, with no indication of any mixing of the dimeric iron species with the zinc complex.

$Ph_4P[Fe(L^{Mod})]$

To a stirred solution of $K(Ph_4P)[Fe(L^{iPr})]_2$ (210 mg, 0.14 mmol) in DMF was added iodosylbenzene (62 mg, 0.28 mmol) as a solid. The pale yellow solution turned deep red as the solid dissolved. After 4h of stirring, solvent was removed in vacuo. The deep red solid was taken up in MeCN, filtered, and the filtrate was concentrated to dryness. X-ray quality crystals were obtained by vapor diffusion of diethyl ether into a concentrated DMF solution of $Ph_4P[Fe(L^{Mod})]$ (55 mg, 86%). ^{1}H NMR (δ, DMSO-d_6, 400 MHz): 66.10, 37.77, 33.63, 29.25, 13.70, 7.93(bs, 4H, Ph_4P), 7.70(bs, 16H, Ph_4P), -7.68, -11.37. FTIR (KBr, cm^{-1}) ν: 3058, 3024, 2965, 2927, 2868, 1611 (CO), 1585, 1479, 1438, 1384, 1268, 1215, 1161, 1108, 1042, 971, 888, 767, 725, 691, 659, 610, 527, 493, 446. μ_{eff} = 5.86 μ_B (Evans' Method, DMF-d_7, 298K). λ_{max}(ε, M^{-1}cm^{-1}) (DMF): 450(3000). Anal. Calcd (found) for $Ph_4P[Fe(L^{Mod})]_2$: C, 69.79 (69.65); H, 6.06 (6.09); N, 7.14 (7.15).

Dioxygen activation

A solution of K(Ph_4P)[Fe(L^{iPr})]$_2$ (50 mg, 0.03 mmol) in DMF was sealed in a Schlenk tube under vacuum in a dry box. The reaction flask was transferred to a fume hood where dry O_2 was added via gastight syringe. After 2h of stirring, solvent was removed in vacuo and the crude solid was brought into the dry box once more. The solid was taken up in MeCN, filtered, and concentrated to dryness. Crystalline Ph_4P[FeL^{Mod}] was obtained as above (3 mg, 10%).

$^{18}O_2$-labeling experiment

A DMF (5 mL) solution of K(Ph_4P)[FeL^{iPr}]$_2$ (87 mg, 0.06 mmol) was sealed under vacuum in a 10 mL Schlenk tube. Excess ^{18}O-labeled dioxygen was added via volume displacement from a 25 mL breakseal ampoule. Upon addition, there was an immediate color change from pale yellow to deep red. After two hours of stirring, the reaction flask was placed under vacuum to remove the excess O_2, and the reaction mixture was worked up as above. Spectral analysis of the purified material by HRESI-MS confirmed ^{18}O incorporation into the product.

Ph_4P[Fe(L^{Ph})(MeCN)]

To a stirred solution of H_3L^{Ph} (224 mg, 0.37 mmol) in DMF (5 mL) was added KH (46 mg, 1.15 mmol) as a solid. When H_2 evolution ceased, Fe(OAc)$_2$ (65 mg, 0.37 mmol) was added as a solid. The pale yellow solution turned bright gold. After 10 minutes of stirring, Ph_4PBr (156 mg, 0.37 mmol) was added as a solid. After 30 minutes of stirring, solvent was removed in vacuo. The resultant dark yellow oil was taken up in acetonitrile (20 mL) and filtered to remove KBr. The filtrate was concentrated to ~15 mL and the resultant golden solution was cooled to -30 °C to give yellow crystals of $Ph_4P[Fe(L^{Ph})(MeCN)]$ (251 mg, 91%). X-ray quality crystals were obtained by vapor diffusion of diethyl ether into a concentrated acetonitrile solution of the complex. ^1H NMR (δ, CD_3CN, 300 MHz): 28.47, 13.94, 12.50, 6.66, 5.73, 4.90, 2.99. FTIR (KBr, cm^{-1}) ν: 3056, 3022, 2926, 2248 (MeCN), 1654, 1597, 1583, 1558, 1473, 1441, 1354, 1269, 1235, 1204, 1109, 1072, 1041, 924, 863, 799, 755, 723, 689, 622, 527, 481. $\mu_{eff} = 5.47\ \mu_B$ (Evans' Method, CD_3CN, 298K). Anal. Calcd (found) for $Ph_4P[CoN(o\text{-}PhNC(O)Ph)_3(MeCN)]$: C, 73.69 (74.12); H, 4.98 (5.05); N, 8.39 (8.77).

Crystallography

Suitable crystals were coated with Paratone-N oil, suspended on a small fiber loop and placed in a cooled nitrogen gas stream at 173K on a Bruker D8 APEX II CCD sealed tube diffractometer with graphite monochromated Mo-Ka (0.71073 Å) radiation, except in the cases of $K(Ph_4P)[Fe(L^{iPr})]_2\cdot DMF\cdot 0.5MeCN$ and $Ph_4P[Fe(L^{Mod})]\cdot DMF$ in which Cu-Ka (1.54178 Å) radiation was utilized. Data were measured using a series of combinations of phi and omega scans with 10 s frame exposures and 0.5° frame widths. Data collection, indexing and initial cell refinements were all carried out using APEX II software.[131] Frame integration and final cell refinements were done using SAINT software.[132] The final cell parameters were determined from least-squares refinement on 2159 reflections. The structure was solved using Direct methods and difference Fourier techniques (SHELXTL, V6.12).[133] Hydrogen atoms were placed in their expected chemical positions using the HFIX command and were included in the final cycles of least squares refinement using a riding model. All non-hydrogen atoms were refined anisotropically. Scattering factors and anomalous dispersion corrections are taken from the *International Tables for X-ray Crystallography*.[134] Structure solution, refinement, graphics and generation of publication materials were performed using SHELXTL, V6.12 software.[133]

Table 5-5. Crystal data and structure refinement for solid-state structures.

	$Et_4N[Co(L^{Mod})]_2$ ·DMF	$K(Ph_4P)[Fe(L^{iPr})]_2$ ·DMF·0.5MeCN	$K_2[Zn(L^{iPr})]_2$ ·0.5DMF
Empirical formula	$C_{41}H_{57}CoN_6O_5$	$C_{88}H_{94.5}Fe_2KN_{9.5}O_7P$	$C_{121.5}H_{132}K_4N_{16.5}O_{12.5}Zn_4$
Formula weight	772.86	1579.00	2445.32
T (K)	173(2)	173(2)	173(2)
λ (Å)	0.71073	1.54178	0.71073
Crystal System	Monoclinic	Monoclinic	Triclinic
Space group	P2(1)/n	P2(1)/c	P-1
a (Å)	10.6572(2)	13.7113(3)	19.9019(18)
b (Å)	21.7676(4)	21.1287(4)	20.7796(18)
c (Å)	17.8714(3)	28.9991(7)	21.527(2)
α (°)	90	90	64.875(2)
β (°)	102.7570(10)	93.5360(10)	81.773(2)
γ (°)	90	90	68.754(2)
V ($Å^3$)	4043.50(13)	8385.1(3)	7511.8(12)
Z	4	4	2
ρ_{calc} (Mg/m^3)	1.270	1.251	1.081
GOF on F^2	1.167	1.079	1.008
R	0.0718	0.0651	0.0908
wR	0.1872	0.1953	0.2576

	$Ph_4P[Fe(L^{Mod})]\cdot DMF$	$Ph_4P[Fe(L^{Ph})(MeCN)]$ $\cdot 2MeCN$
Empirical formula	$C_{57}H_{59}FeN_5O_5P$	$C_{69}H_{56}FeN_7O_3P$
Formula weight	980.91	1118.03
T (K)	173(2)	173(2)
λ (Å)	1.54178	0.71073
Crystal System	Monoclinic	Monoclinic
Space group	C2/c	P2(1)/c
a (Å)	24.3796(5)	10.8922(9)
b (Å)	13.1251(2)	26.118(2)
c (Å)	35.6256(8)	20.0064(16)
α (°)	90	90
β (°)	94.694(1)	90.541(5)
γ (°)	90	90
V (Å^3)	11361.4(4)	5691.2(8)
Z	8	4
ρ_{calc} (Mg/m^3)	1.147	1.305
GOF on F^2	1.028	1.038
R	0.0893	0.0967
wR	0.2740	0.2764

Chapter 6: Facile C-F Bond Activation by Fe(II) Complexes Using Dioxygen as Terminal Oxidant and Oxygen Atom Source

Section 6-1. Introduction

The chemical inertness of fluorocarbon C–F bonds (up to ~150 kcal/mol in fluoroarenes) makes them a much sought after target for chemical manipulations.[250] The ability to activate and/or functionalize these bonds would allow for the degradation of environmentally malignant fluorocarbons, as well as the ability to produce fine chemicals from existing fluorinated compounds. The manipulation of C–F bonds has become increasingly important in the pharmaceutical and agrochemical industries, where F-containing compounds make up approximately 20% and 30% of all products in their respective industries.[251] Known examples of organometallic, metal-mediated C–F cleavage of fluoroarenes proceed by oxidative addition, bond metathesis, hydrodefluorination, or nucleophilic attack pathways (Scheme 6-1).[252]

(i) oxidative addition $[M] + R\text{—}F \longrightarrow R\text{—}[M]\text{—}F$

(ii) bond metathesis $L\text{—}[M] + R\text{—}F \longrightarrow R\text{—}[M] + L\text{—}F$

(iii) hydrodefluorination $H\text{—}[M] + R\text{—}F \longrightarrow F\text{—}[M] + R\text{—}H$

(iv) nucleophilic attack $[M]^{-} + R\text{—}F \longrightarrow R\text{—}[M] + F^{-}$

Scheme 6-1. Known organometallic pathways of metal-mediated C–F cleavage (L = H, R_3Si).

Nucleophilic substitutions, in particular, most often occur at electron-rich, late transition metal centers and require forcing conditions or more expensive 4d and 5d metals.[253-258] Jones and coworkers reported a half-sandwich rhodium complex, Cp*Rh(PMe_3)H_2, and its ability to activate aryl C–F bonds (Figure 6-1).[258] The metal is activated toward nucleophilic attack by first deprotonating the metal complex with pyridine, and the reaction was determined to be autocatalytic as the F^- produced in the reaction was found to also be an efficient enough base to continue the catalytic cycle.

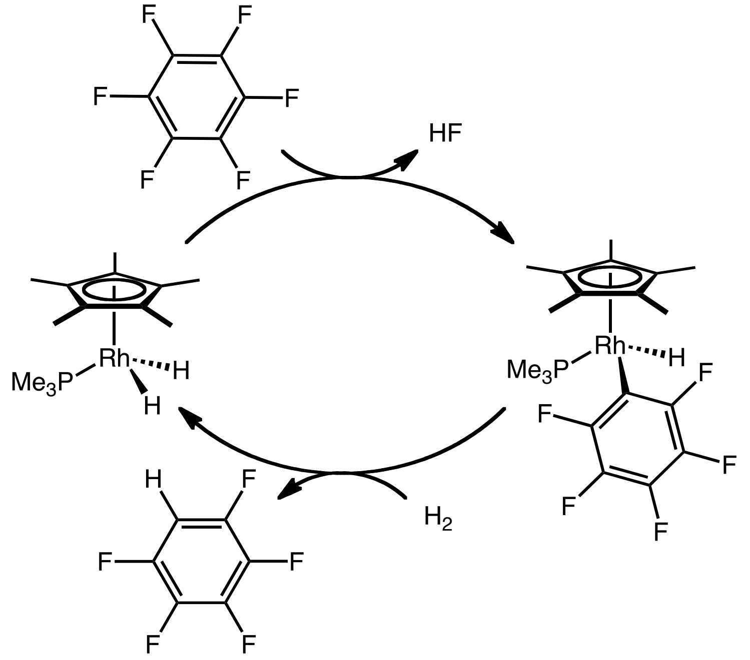

Figure 6-1. Rhodium half-sandwich complex from Jones, et al. shown to attack aryl C–F bonds.[258]

In another study by the Bergman lab, a deprotonated iridium half-sandwich, Li[Cp*Ir(PMe_3)H], was shown to be effective for attack on aryl and vinyl fluorocarbons.[257] These two studies represent rare examples of metal centers basic enough to act as strong nucleophiles. C–F activation by organometallic processes are rarely catalytic, however, due to the inability to effect turnover as a result of the strength of the intermediate M–F bonds. Many known examples of metal-mediated aryl C–F cleavage exist, but functionalization of the carbon atom is usually limited to C–H and C–C bond formation, and only a few examples of C–O bond formation exist.[259-261] The C–O bond forming reactions all involve the nucleophilic attack of a metal-bound hydroxide ion on the aryl C–F bond.

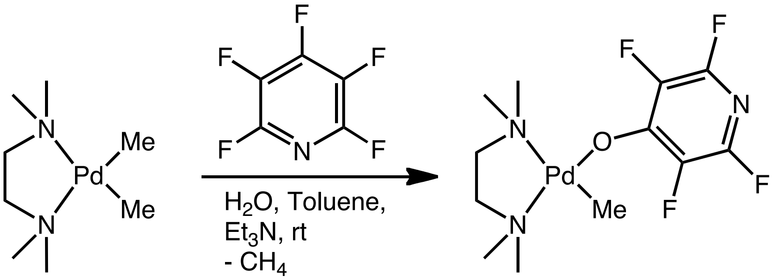

Scheme 6-2. Representative C–F hydroxylation reaction from Stammler, et al.[259]

The reactions are mediated by more expensive, electron-rich 4d and 5d metals such as, osmium(III),[261] palladium(II),[259] and platinum(II),[260] and examples of this type of reactivity by cheaper first-row metals have not been published.

An interesting strategy toward catalytic nucleophilic addition of oxygen fragments into organic substrates is to generate metal species with nucleophilic oxo ligands. While examples of nucleophilic oxo ligands are rare, they have been utilized in substitution reactions,[262-268] as well as in 1,2- and cycloaddition[269-273] reactions. All of these reactions were performed at high-valent, early transition metal centers; however, one example of nucleophilic attack by a late metal-oxo moiety has been reported. Borovik and coworkers reported the isolation of an Fe(III) oxo complex that was shown to generate the corresponding Fe(III) methoxide complex in the presence of MeI, a potent electrophile.[7] To the best of our knowledge, despite the previously mentioned examples of nucleophilic attack by later metal-hydroxides, there have been no reports of nucleophilic attack on weaker electrophiles by later transition metal-oxo fragments. It is important to note that, while there are very few examples of C–F bond activation mediated by iron centers, the aforementioned work by Borovik, et al. indicates that iron may be able to generate metal-oxo fragments reactive enough to attack weaker, C–F bond-containing electrophiles.

Examples of C–F bond activation by iron are few, but those that exist operate by diverse mechanisms. In an example from Pétillon and Muir, it was shown that the terminal vinyl fluorine atoms in the diiron(I) complex, $[(Fe(CO)_3)_2(\mu\text{-}C(SMe)(CF_3)C{=}CF_2)]$, were susceptible to attack by exogenous substrates due to the enhanced electrophilicity at the vinyl α-carbon that resulted from coordination of the alkene to one of the iron centers.[274] This allowed for the functionalization of the C–F bonds to generate new aliphatic C–X bonds (X = N, S, H, and O). In separate studies by Stone and Bisnette, the monoanionic Fe(0) complex, $Na[CpFe(CO)_2]$ was found to react with polyfluoroaromatics to produce the corresponding fluoroaryl complexes (i.e., the reaction with perfluorobenzene produced the complex, $[CpFe(C_6F_5)(CO)_2]$).[275, 276] These complexes are thought to proceed via nucleophilic aromatic substitution mechanisms, involving attack of the iron atom on the aryl ring. Work by Green and coworkers showed that the Fe(II) complex, $[CpFe(Me)(CO)_2]$, reacts with the Lewis acid, $B(C_6F_5)_3$, to produce the fluoroaryl complex, [CpFe(C_6F_4-2-C(O)Me)$(CO)_2$] (Scheme 6-3).[277] They suggested that the reaction begins by coordination of the boron atom of $B(C_6F_5)_3$ to the carbonyl ligand. This interaction results in a ligand rearrangement that involves the addition of the Fe ion into the aryl C–F bond.

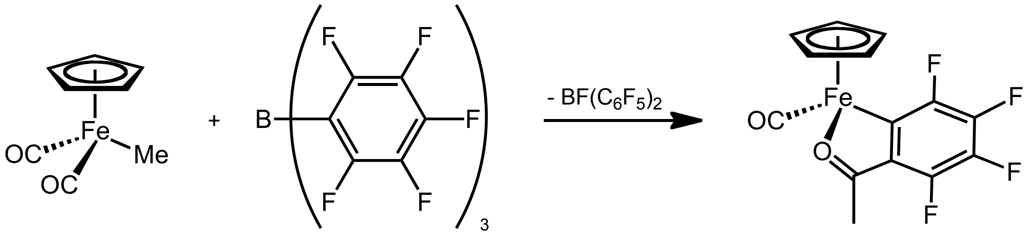

Scheme 6-3. C–F cleavage by Fe(II) half-sandwich complex, [CpFe(Me)$(CO)_2$], reported by Green and coworkers.[277]

The newly formed acyl ligand migrates into the benzyne intermediate, concomitant with loss of $FB(C_6F_5)_2$ to produce the isolated product. The last example, reported by Willemsen, et al., showed that the bisalkylidyne cluster, $Fe_3(CO)_9(\mu_3\text{-CF})_2$, reacts with 1,1-difluoroallene to produce a pair of complexes that both result from reduction of the coordinated allene.[278] It appears that one product is produced by attack of the methylidyne ligand on the coordinated allene, coupled with a 1,3-fluorine migration, and the second product is a result of attack of both methylidyne ligands, coupled with a 1,4-fluorine migration on the five-carbon fragment.

The utilization of nucleophilic metal-oxo fragments to attack weaker electrophiles (i.e., fluorocarbons) would represent a new strategy in the functionalization of C–F bonds. This strategy would not only result in scission of C–F bonds without the intermediacy of a stable M–F bond, it would also result in functionalization at the carbon atom. In this chapter, I report that the Fe(II) complex, K[Fe(L^{C6F5})(MeCN)], undergoes facile intramolecular C–F bond cleavage in the presence of an oxygen-atom transfer reagent to form an Fe(III) phenoxide species, K[Fe(L^{Mod})]. It is shown that dioxygen can act as a suitable oxygen atom source for this transformation, as confirmed by labeling studies. A high-valent Fe-oxygen adduct is implicated in the substitution reaction, which is a rare example of nucleophilic behavior by an Fe-oxo moiety.

Section 6-2. Results and Discussion

In chapters 2 and 3, I reported on the Co(II) and Ni(II) complexes of a novel tris(amidato)amine ligand platform, H_3L^R, developed in our lab.[113, 279] It was demonstrated that, through variation of the acyl substituents on the ligand arms, control of ligand binding to the open axial coordination site of the metal ion could be achieved. We felt that because of the strong donor ability of the electron-rich amidate ligands, this scaffold should also allow for the support of high-valent metal ions. By combining these characteristics, we hoped to develop Fe(II) complexes of this ligand system for use as size-selective C–H hydroxylation catalysts (Figure 6-2).

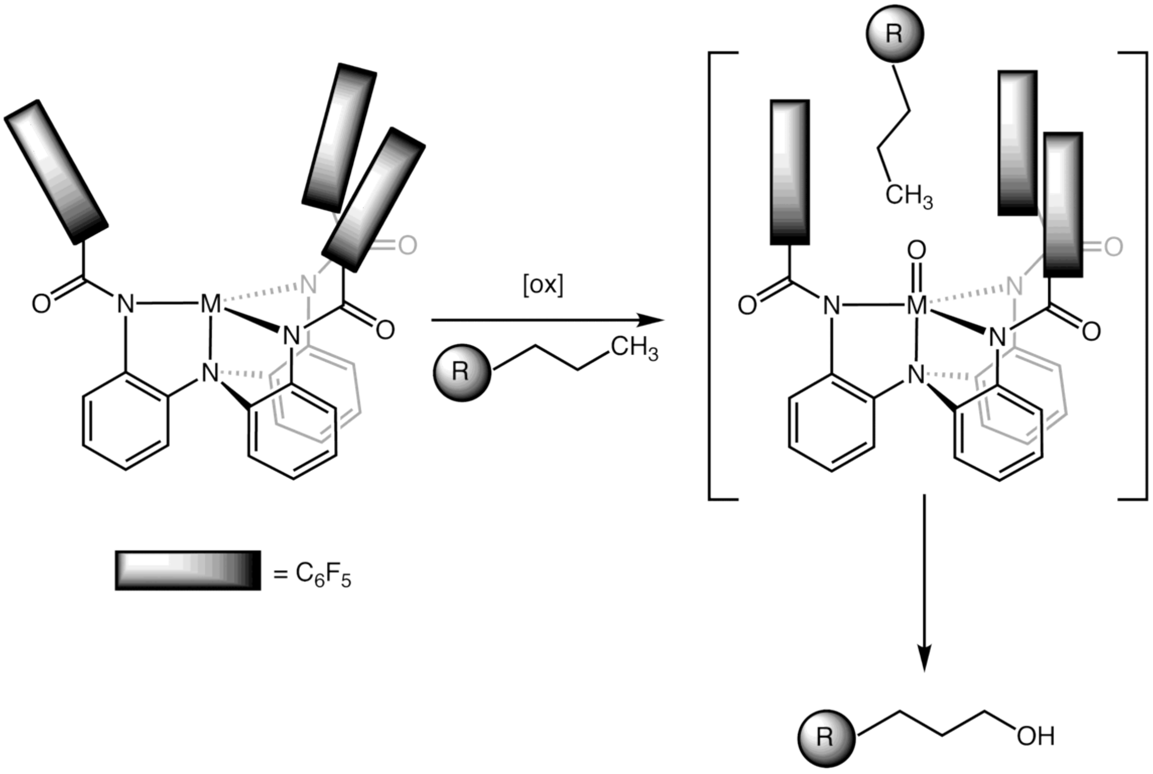

Figure 6-2. Proposed size-selective C–H hydroxylation reaction (see chapter 5 for detailed explanation.

With that in mind, the trisamine precursor, L^{NH2}, was acylated with perfluorobenzoyl chloride to form the tris(perfluorophenylamido)amine derivative, H_3L^{C6F5}. The absence of C–H bonds in the ligand arms is intended to prevent intramolecular C–H activation in the presence of a terminal oxidant (see chapter 5 for further details), while the reducing nature of the amidate donor atoms will destabilize the reactive intermediate toward atom-transfer reactions.

A strategy was then developed in order to generate an Fe(II) complex. Initially, one equivalent of KH is added in order to deprotonate one of the nitrogens of the three amide arms of H_3L^{C6F5}. Addition of $Fe(HMDS)_2(THF)$ to the singly deprotonated ligand results in deprotonation of the remaining two amide nitrogens, concomitant with loss of $HN(TMS)_2$ and the formation of the desired five-coordinate complex, K[Fe(L^{C6F5})(MeCN)], in moderate yield (Scheme 6-4). Subsequent workup and recrystallization by slow diffusion of diethyl ether into an MeCN solution of the crude product gives crystals of K[Fe(L^{C6F5})(MeCN)] suitable for X-ray diffraction (Figure 6-3).

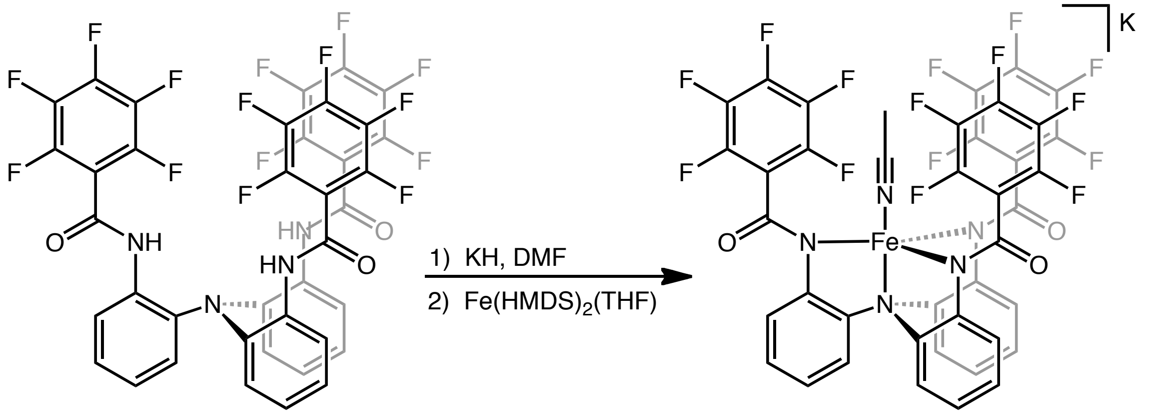

H_3L^{C6F5}

K[Fe(L^{C6F5})(MeCN)]
yellow, 75%
FTIR (KBr, cm^{-1}): ν(CO): 1602
μ_{eff} = 5.15 μ_B (Evans' Method, $(CD_3)_2SO$, 298K)

Scheme 6-4. Synthesis of K[Fe(L^{C6F5})(MeCN)].

The solid-state structure of the complex displays an Fe(II) ion in a trigonal bipyramidal geometry (Figure 6-3). The equatorial plane is comprised of three *N*-amidate donors, while a tertiary amine donor and an acetonitrile solvent molecule occupy the axial sites.

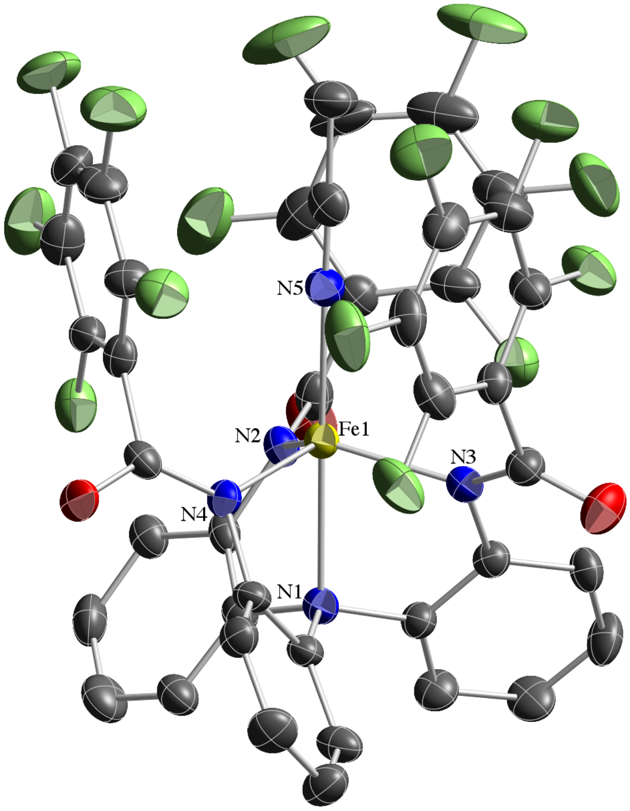

Figure 6-3. Solid-state structure of K[Fe(L^{C6F5})(MeCN)]. Hydrogen atoms and counterion have been omitted for clarity. Thermal ellipsoids shown at 50% probability.

The paramagnetically-shifted ^{1}H NMR of K[Fe(L^{C6F5})(MeCN)] contains four signals, indicating that the complex maintains C_3-symmetry in solution. Solution-state magnetic moment measurements give a μ_{eff} of 5.15 μ_{B} (Evans' method, DMSO-d_6, 25 °C), consistent with the assignment of a high-spin (S = 2) Fe(II) center.

Table 6-1. Selected bond lengths and angles for K[Fe(L^{C6F5})(MeCN)].

	K[Fe(L^{C6F5})(MeCN)]
Fe–N_{amide} (ave.)	2.076(5) Å
Fe–N_{amine}	2.291(4) Å
Fe–N_{MeCN}	2.125(5) Å
N_{amine}–Fe–N_{MeCN}	179.10(18)°

The electrochemical properties of K[Fe(L^{C6F5})(MeCN)] were investigated by cyclic voltammetry experiments, but the complex did not display any significant or reversible electrochemical events at 25 °C in DMF with *n*-tetrabutylammonium hexafluorophosphate ($TBAPF_6$) as the supporting electrolyte. As such, the CV was attempted once more in the presence of ~1 equivalent of Et_4NCN, added directly to the electrochemical cell. As was the case for K(Ph_4P)[Fe(L^{iPr})]$_2$ and Ph_4P[(FeL^{Ph})(MeCN)], the addition of cyanide ion to K[Fe(L^{C6F5})(MeCN)] gave rise to a reversible electrochemical event at $E_{1/2}$ = -0.310 V (ΔE_p = 0.073 V; i_{pc}/i_{pa}^{-1} = 0.89) vs. Fc/Fc$^+$. The shift to more positive potentials relative to that observed for the cyanide adducts of K(Ph_4P)[Fe(L^{iPr})]$_2$ and Ph_4P[(FeL^{Ph})(MeCN)], is consistent with the change in acyl substituents from electron-rich isopropyl and phenyl groups to strongly electron withdrawing perfluorinated phenyl groups. As was the case for [Fe(L^{iPr})(CN)]$^{2-}$ and [Fe(L^{Ph})(CN)]$^{2-}$, the signal is tentatively assigned to the Fe(II)/Fe(III) couple for the currently uncharacterized cyanide adduct, [Fe(L^{C6F5})(CN)]$^{2-}$.

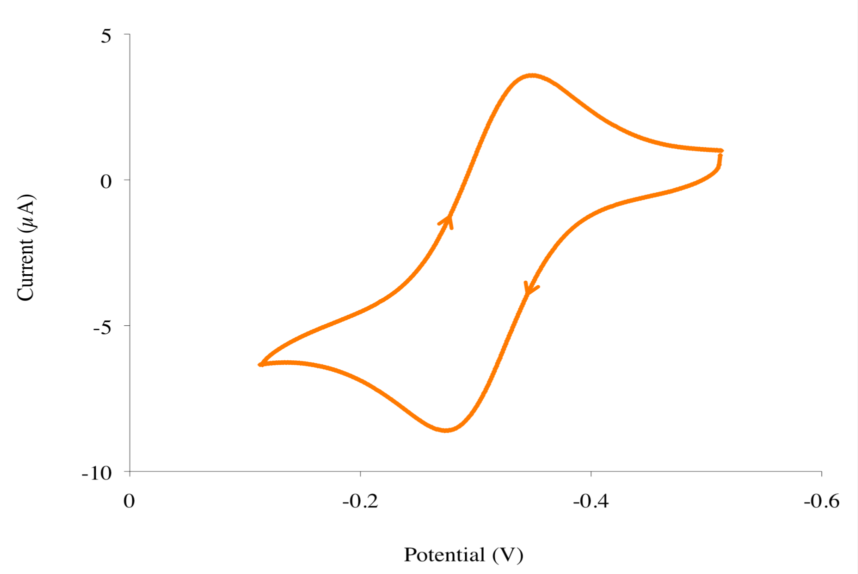

Figure 6-4. Cyclic voltammogram of cyanide adduct, $[Fe(L^{C6F5})(CN)]^{2-}$, recorded at 0.1 V/s.

Iron(II) complex in hand, we sought to explore the reactivity of this species with oxygen atom transfer reagents. Exposure of solutions of $K[Fe(L^{C6F5})(MeCN)]$ to one equivalent of iodosylbenzene or pyridine *N*-oxide results in the formation of an approximately 50:50 mixture of complexes identified as an Fe(III)phenoxide, $K[Fe(L^{Mod})]$, and an Fe(III)fluoride species, $K[Fe(L^{C6F5})(F)]$ (Scheme 6-5).

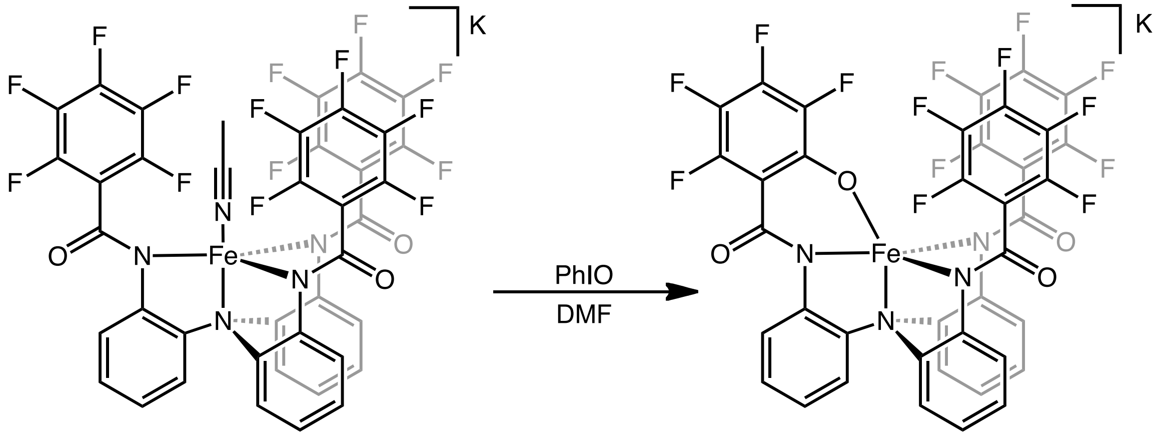

K[Fe(L^{C6F5})(MeCN)]

K[Fe(L^{Mod})]
purple, 45%
FTIR (KBr, cm^{-1}): ν(CO) 1608
μ_{eff} = 5.83 μ_B (Evans' Method, CD_3CN, 298K)

Scheme 6-5. Synthesis of Fe(III) phenoxide, K[Fe(L^{Mod})].

X-ray quality crystals of K[Fe(L^{Mod})]can be grown by slow diffusion of diethyl ether into an acetonitrile solution of the complex (Figure 6-5).

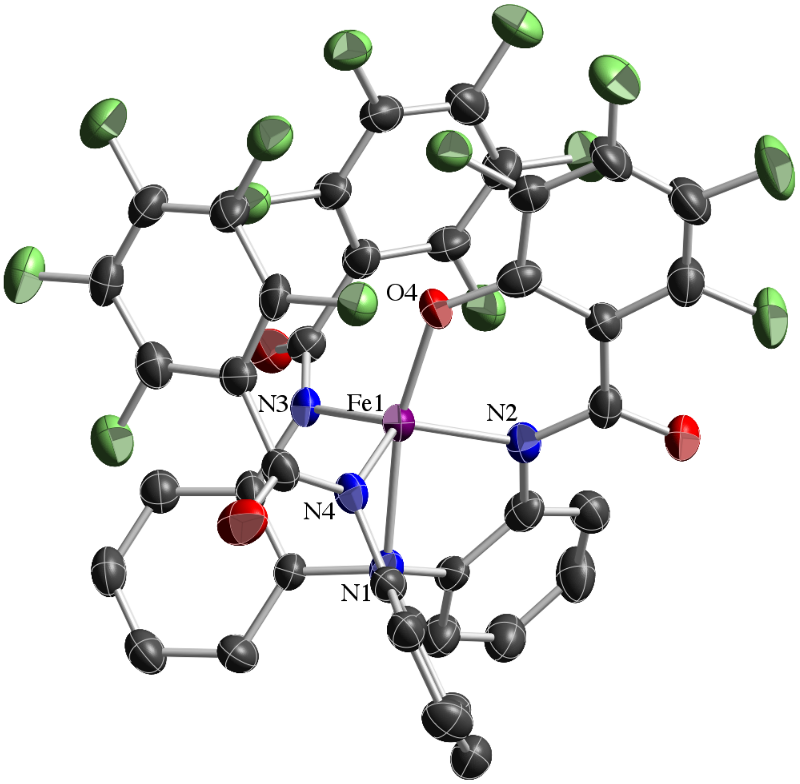

Figure 6-5. Solid-state structure of K[Fe(L^{Mod})]. Hydrogen atoms and counterion have been omitted for clarity. Thermal ellipsoids shown at 30% probability.

The solid-state structure of the Fe(III)phenoxide complex displays a five-coordinate metal ion coordinated to a now pentadentate ligand in which the C-F bond *ortho* to the acyl group on one the perfluorophenyl ligand arms has been replaced with a C-O bond.[13] The Fe-O bond length of 1.863(5) Å is consistent with an Fe(III) ion bound to a phenoxide unit.[280] In the *trans* position to the phenoxide ligand, the tertiary amine of the chelate is coordinated (Fe–N$_{ax}$ = 2.234(5) Å), and the three remaining equatorial sites are filled by the *N*-donors of the amidate arms (average Fe–N$_{eq}$ = 1.981(6) Å), which, all together, result in a distorted trigonal bipyramidal geometry around the iron center (τ_5 =

0.74).[120] The shorter Fe-N bonds, compared to the Fe(II) starting material, are also indicative of a formal oxidation state change from Fe(II) to Fe(III).

The UV-Visible spectrum shows an absorption at λ_{max} = 530 nm (Figure 6-6). This value, along with a large extinction coefficient (ε = 6133 $M^{-1}cm^{-1}$) are also consistent with an Fe(III)phenoxide species.[245] The solution state magnetic data (μ_{eff} = 5.83 μ_B, S = 5/2) support the assignment of this species as a high spin Fe(III) complex.

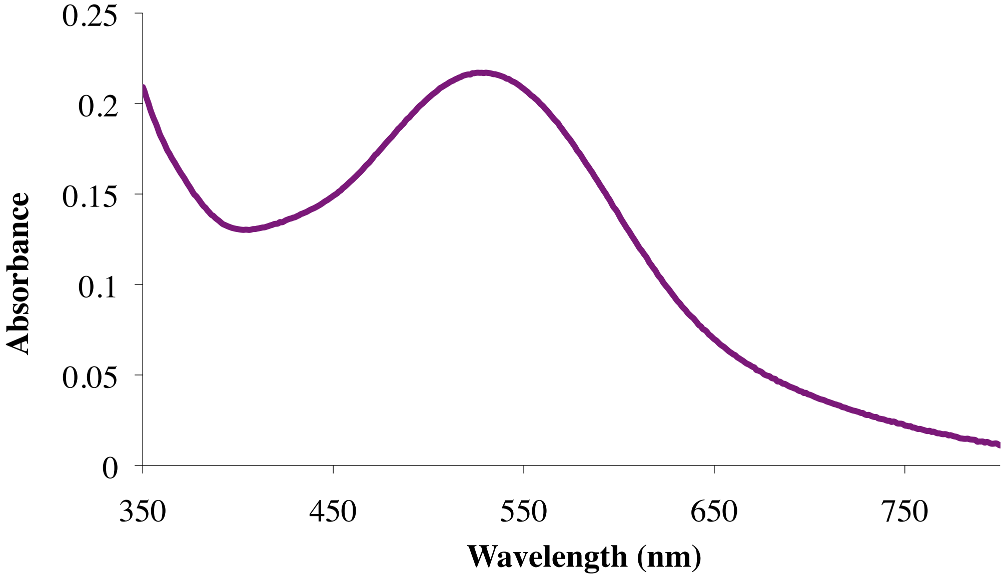

Figure 6-6. UV-Vis absorption data for K[Fe(L^{Mod})] (3.50 x 10^{-5} M in MeCN).

The FTIR spectrum of K[Fe(L^{Mod})] shows a peak at 1008 cm^{-1}, consistent with the C–O stretch of an electron deficient aryloxide (Figure 6-7).

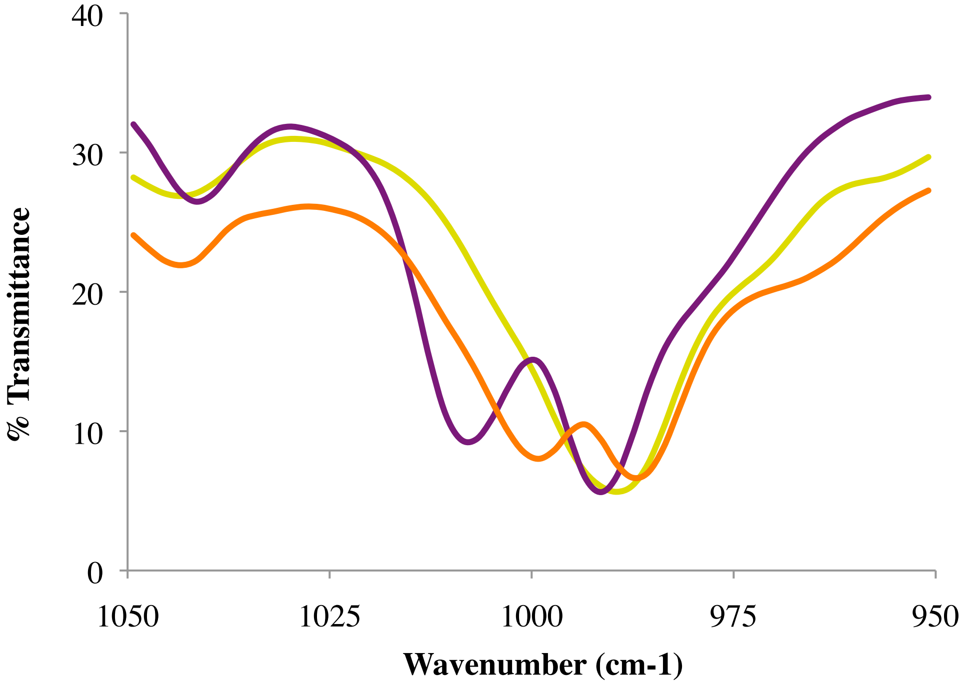

Figure 6-7. Overlay of FTIR region showing aryloxide ν(C-O) stretches. yellow, K[Fe(L^{C6F5})]; purple, K[Fe(L^{Mod})] (ν(C-O) 1008 cm^{-1}); orange, $(Et_4N)_2$[Fe(L^{Mod})] (ν(C-O) 999 cm^{-1}).

Analysis of K[Fe(L^{Mod})] by cyclic voltammetry (25 °C, DMF, 0.2 M $TBAPF_6$) gives rise to a single, reversible event at $E_{1/2}$ = -0.754 (ΔE_p = 0.067 V; i_{pc}/i_{pa}^{-1} = 0.87) vs. Fc/Fc^+. This feature is tentatively assigned to the Fe(II)/Fe(III) couple. This data further supports the necessity for an anionic, fifth ligand in order to gain access to Fe(III) complexes of the $[(L^R)]^{3-}$ ligand scaffold.

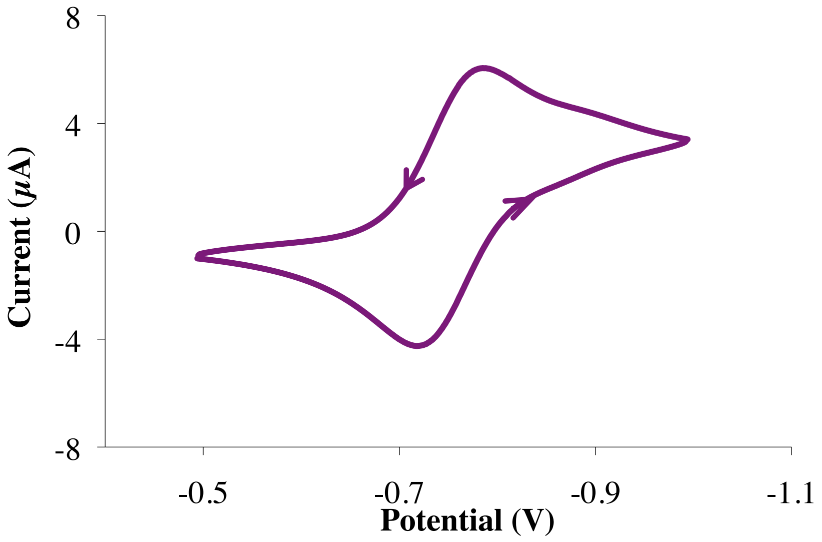

Figure 6-8. Cyclic voltammogram of K[Fe(L^{Mod})] recorded at 10 mV/s.

The second product, K[Fe(L^{C6F5})(F)], forms as a result of the reaction of the other half of the Fe(II) species with the fluoride ion lost in the C-F cleavage reaction. The species was identified in the ESI-MS as one of two major species in the crude reaction mixture ([Fe(L^{C6F5})(F)]$^-$ *m/z* 944). We have been unable to isolate this species from our crude reaction mixtures, however, we are able to validate the identity of the species through independent synthesis. Addition of two equivalents of tetramethylammonium fluoride to an acetonitrile solution of K[Fe(L^{C6F5})(MeCN)], followed by one electron oxidation with ferrocenium tetrafluoroborate results in the formation of Me_4N[Fe(L^{C6F5})(F)] (Scheme 6-6). The negative mode ESI-MS spectrum of this species shows an [M-1] peak at m/z 944, consistent with the species seen in the crude reaction mixture containing the C-F activated product. The UV-visible spectrum of the complex shows an absorption band at 493 nm, which would account for the blue-shifted absorption maximum observed in the spectrum of the reaction mixture, relative to the spectrum of pure K[Fe(L^{Mod})]. The IR spectrum of $Me_4N[Fe(L^{C6F5})(F)]$ shows a ν(CO) stretch at 1615 cm^{-1}, which is also present in the crude solid isolated from the C–F hydroxylation reaction.

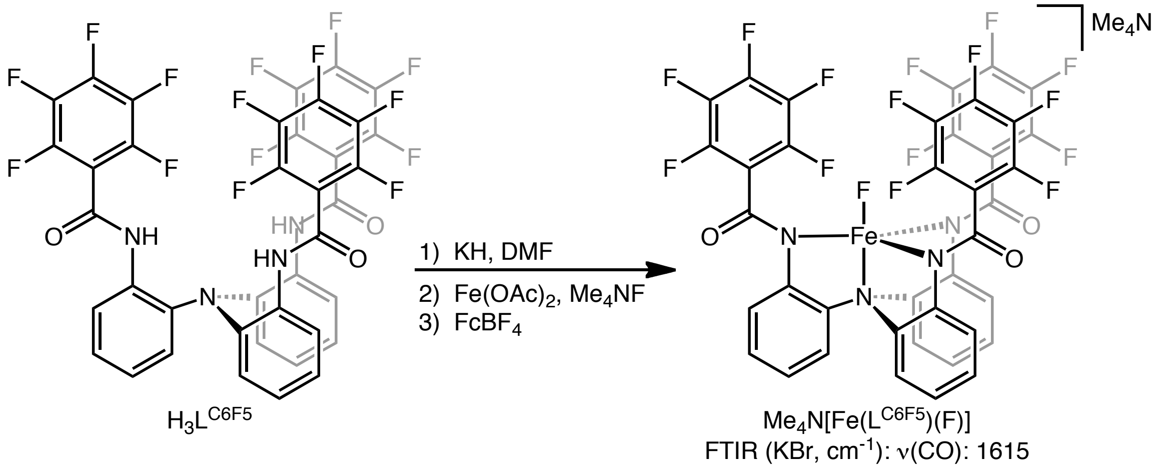

Scheme 6-6. Synthesis of $Me_4N[Fe(L^{C6F5})(F)]$.

As stated above, the cyclic voltammogram of K[Fe(L^{Mod})] shows a reversible event at $E_{1/2}$ = -753 mV that we have assigned to the Fe(II)/Fe(III) couple. This finding indicates that the corresponding Fe(II) phenoxide should be able to be isolated. Accordingly, the addition of one equivalent of potassium hydroxide to a DMF solution of K[Fe(L^{C6F5})(MeCN)] produces an orange species in solution as the KOH dissolves. Salt metathesis is achieved by addition of two equivalents of Et_4NBr, concomitant with loss of two equivalents of KBr. Recrystallization of the isolated orange solid by diffusion of diethyl ether into an MeCN solution of the solid affords orange crystals in approximately 50% yield (Scheme 6-7). These crystals have been formulated as $(Et_4N)_2[Fe(L^{Mod})]$.

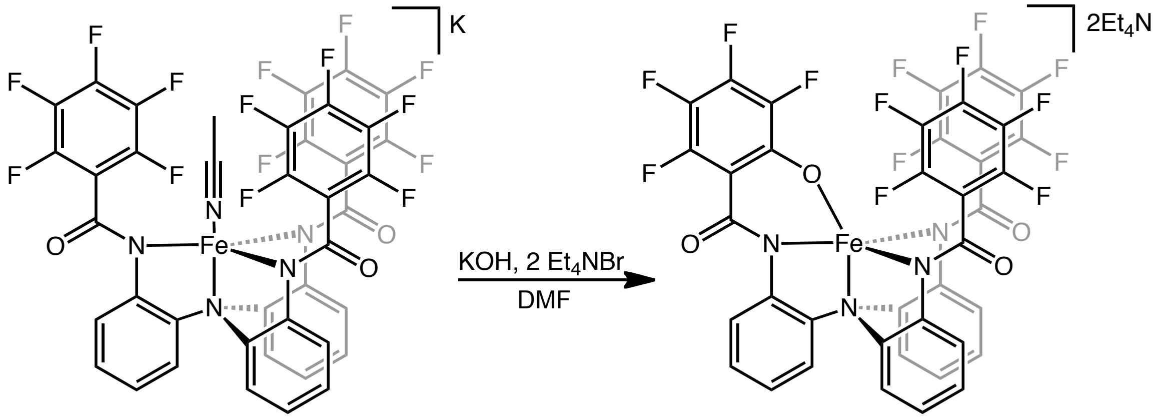

K[Fe(L^{C6F5})(MeCN)]

(Et$_4$N)$_2$[Fe(L^{Mod})]
orange, 50%
FTIR (KBr, cm^{-1}): ν(CO) 1600
μ_{eff} = 5.10 μ_B (Evans' Method, CD$_3$CN, 298K)

Scheme 6-7. Synthesis of (Et$_4$N)$_2$[Fe(L^{Mod})].

It seems likely that the reaction to generate this species proceeds via attack of a coordinated hydroxide ligand on the *ortho*-position of the ligand aryl ring in an S$_N$Ar reaction (Scheme 6-8). The lost F$^-$ could then deprotonate the phenol, which would result in the loss of HF, coupled with the formation of the Fe(II)-phenoxide adduct.

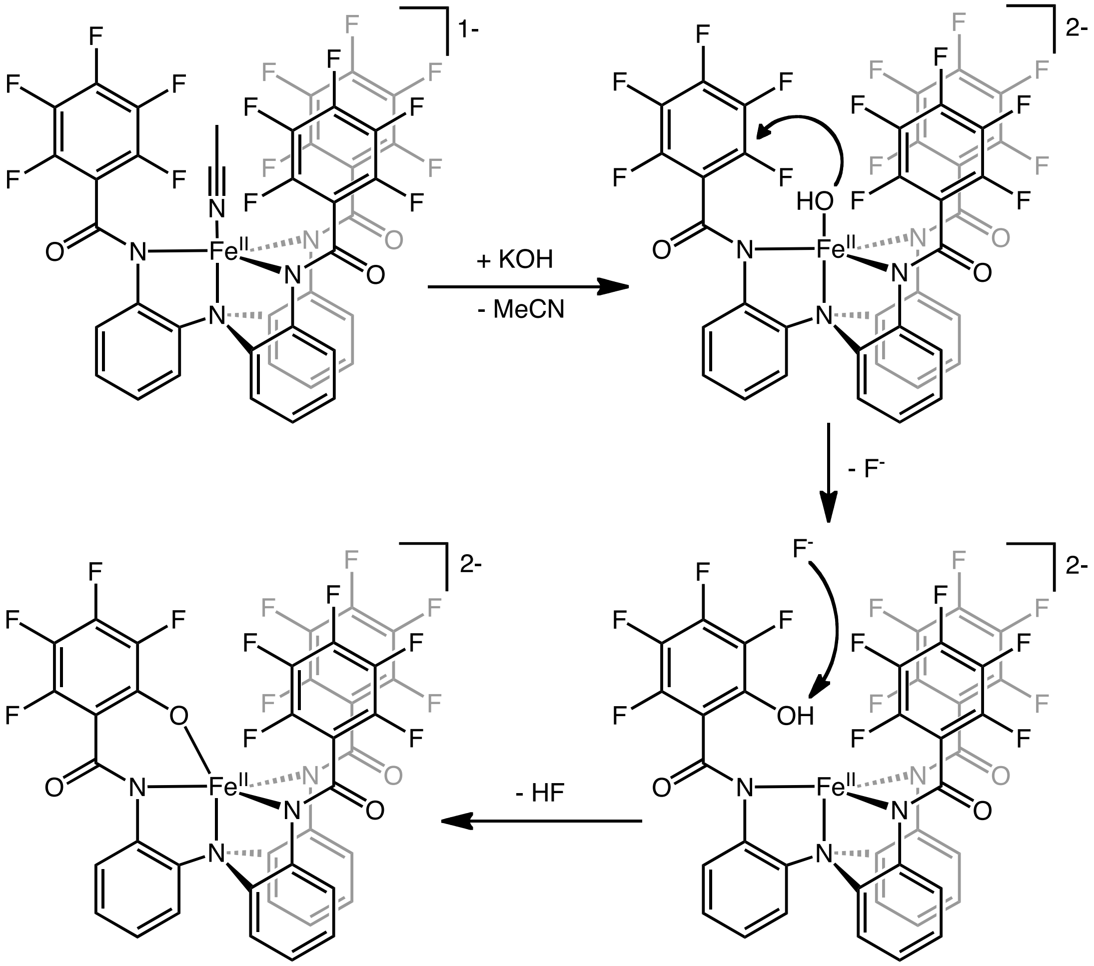

Scheme 6-8. Proposed mechanism for C–F hydroxylation by Fe(II)-hydroxide adduct.

The HF could possibly react with the remaining unreacted complex, which would explain our inability to isolate the product in greater than 50% yield. X-ray quality crystals of $(Et_4N)_2[Fe(L^{Mod})]$ can be obtained by vapor diffusion of diethyl ether into an acetonitrile solution of the complex (Figure 6-9).

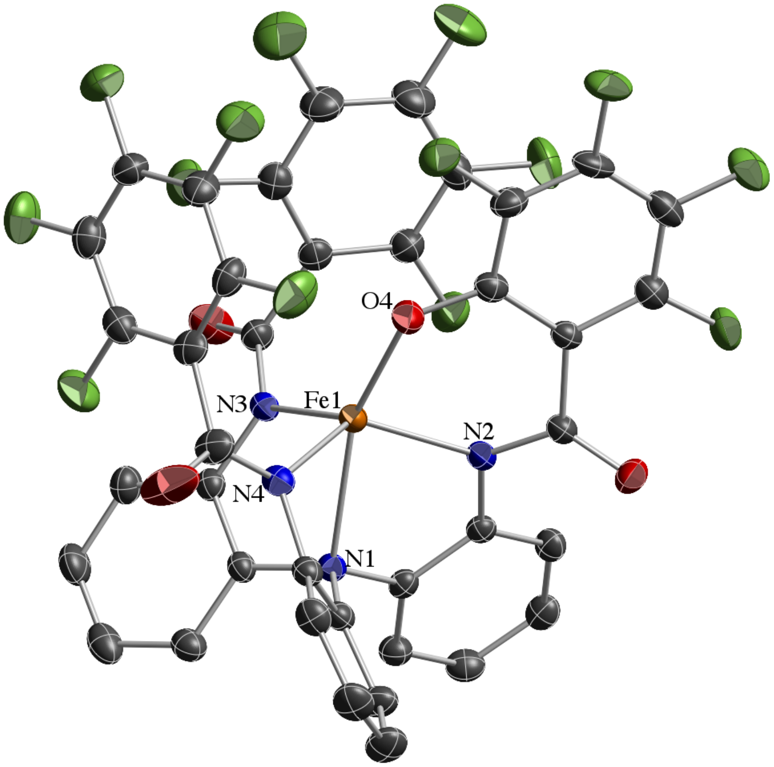

Figure 6-9. Solid-state structure of $(Et_4N)_2[Fe(L^{Mod})]$. Counterions and hydrogen atoms are omitted for clarity. Thermal ellipsoids are shown at 40% probability.

The solid-state structure of $(Et_4N)_2[Fe(L^{Mod})]$ reveals a monomeric complex in which, much like $K[Fe(L^{Mod})]$, hydroxylation has occurred at one of the *ortho*-C–F bonds of the perfluorophenyl substituents, resulting in a five-coordinate complex with a phenoxide ligand. The short Fe–O bond length (1.974(2) Å) is consistent with the assignment of an phenoxide ligand. In the *trans* position, the tertiary amine of the chelate is coordinated ($Fe–N_{ax}$ = 2.323 Å), and the three remaining sites are filled by the *N*-donors of the amidate arms (average $Fe–N_{eq}$ = 2.084(2) Å), which all together result in an intermediate geometry around the iron center ($\tau_5 = 0.51$).

Table 6-2. Selected bond lengths and angles for K[Fe(L^{Mod})] and $(Et_4N)_2$[Fe(L^{Mod})].

	K[Fe(L^{Mod})]	$(Et_4N)_2$[Fe(L^{Mod})]
Fe–N_{amide} (ave.)	1.981(6) Å	2.084(2) Å
Fe–N_{amine}	2.234(5) Å	2.323(2) Å
Fe–O	1.863(5) Å	1.974(2) Å
N_{amine}–Fe–O	167.2(2)°	157.20(9)°
N_{amide}–Fe–O	90.6(2)°	89.64(9)°
τ_5	0.74	0.51

The longer bond lengths about the metal ion relative to K[Fe(L^{Mod})], along with the magnetic data ($\mu_{eff} = 5.10\ \mu_B$, $S = 2$) support the assignment of this species as a high spin Fe(II)-phenoxide complex. Cyclic voltammetry experiments on $(Et_4N)_2$[Fe(L^{Mod})] further support its relationship to its Fe(III) analogue (Figure 6-10). The voltammogram of the Fe(II) adduct shows a reversible electrochemical event at $E_{1/2}$ = -0.751 (ΔE_p = 0.074 V; i_{pc}/i_{pa}^{-1} = 0.96) vs. Fc/Fc$^+$. This feature is nearly identical to the Fe(II)/Fe(III) couple observed in K[Fe(L^{Mod})], confirming the predicted one-electron difference between the two anions.

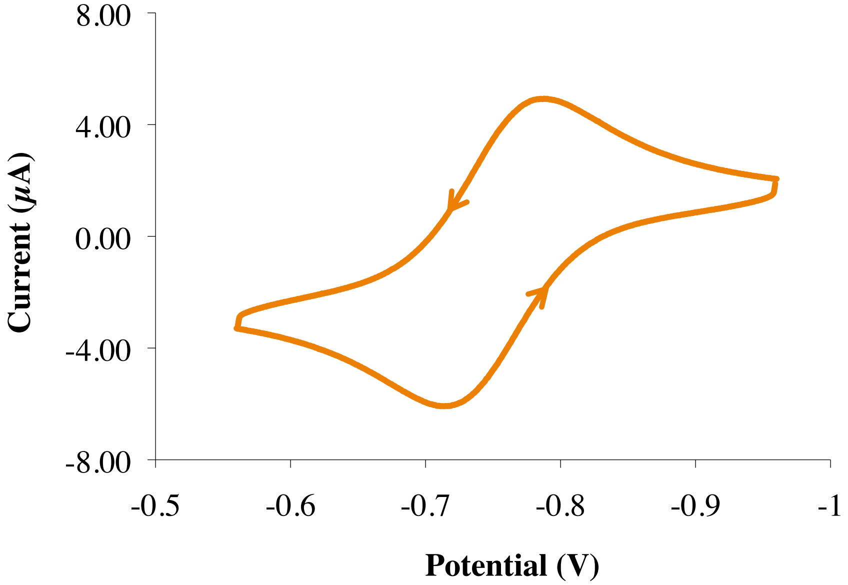

Figure 6-10. Cyclic voltammogram of $(Et_4N)_2[Fe(L^{Mod})]$ recorded in DMF (0.2 M $TBAPF_6$) at 0.1 V/s.

Interestingly, addition of dioxygen to a THF solution of $K[Fe(L^{C6F5})(MeCN)]$ results in formation of a purple species that is identical to $K[Fe(L^{Mod})]$, as confirmed by HRESI-MS, FTIR, and UV-vis analysis of the recrystallized material (Scheme 6-9). This result indicates that dioxygen is being activated at the Fe(II) center of the metal complex and the oxygen atom is, in turn, used to activate the ligand C-F bond.

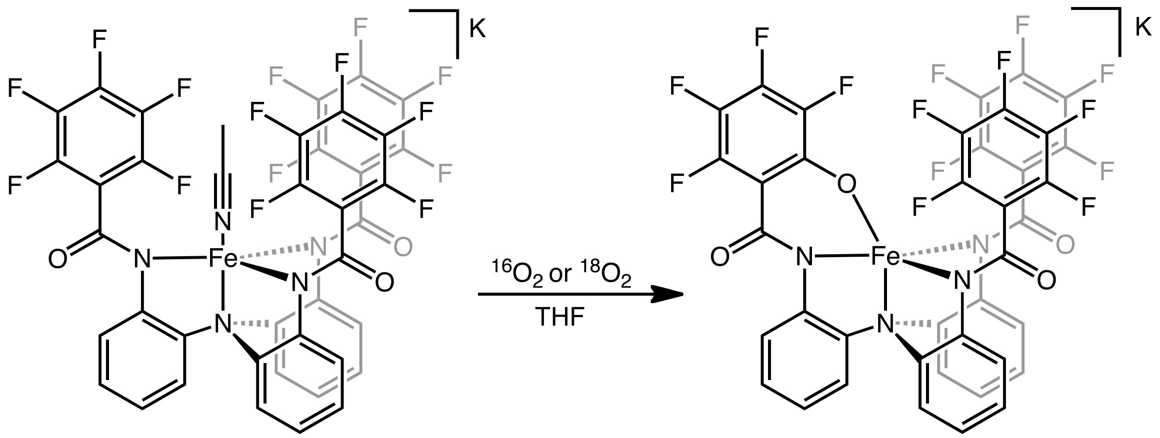

K[Fe(L^{C6F5})(MeCN)]

K[Fe(L^{Mod})]
FTIR (KBr, cm^{-1}): ν(CO) 1608

Scheme 6-9. Synthesis of K[Fe(L^{Mod})] using dioxygen as the oxidant/*O*-atom source.

The role of dioxygen in this reaction was confirmed by labeling studies using ^{18}O-labeled dioxygen (98% enriched). Performing the oxygenation reaction with the enriched dioxygen gives a purple reaction mixture that yields purple crystals after performing workups and recrystallization steps identical to those for the reaction employing naturally abundant dioxygen. The high resolution ESI-MS spectrum of the crystalline product shows a mass peak at m/z of 924, which is upshifted by two mass units from the spectrum of the coordinate anion ([Fe(L^{Mod})]$^-$ *m*/*z* = 922) of the product generated from $^{16}O_2$, verifying incorporation of an O_2-derived oxygen atom into the product.

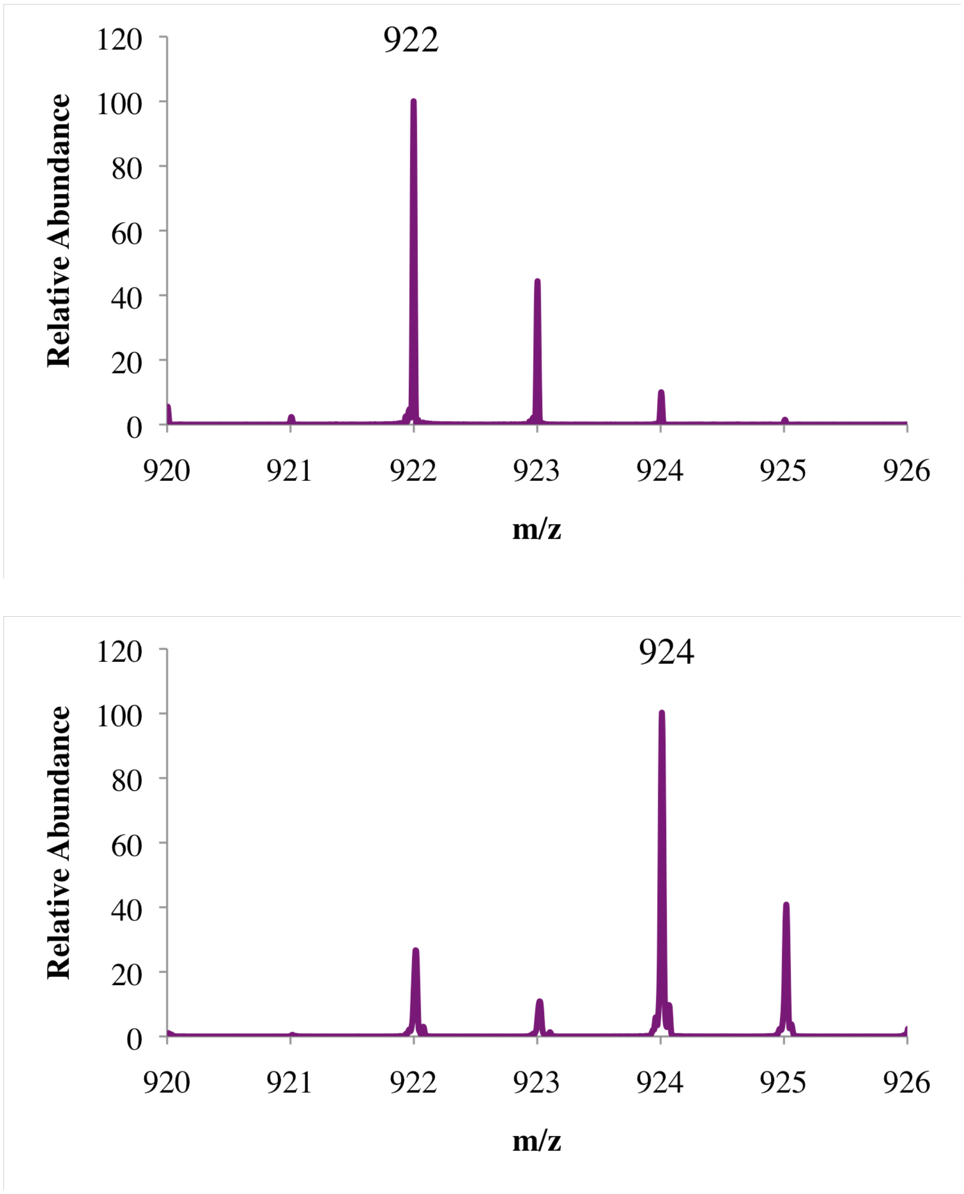

Figure 6-11. HRESI-MS spectra showing [Fe(L^{Mod})]$^-$ made using $^{16}O_2$ (top) and ^{18}O-labeled O_2 (bottom).

Given the known transformations that result in C-F bond cleavage to form C-O bonds, it is reasonable to suggest that the Fe(III)phenoxide species is formed via a nucleophilic attack pathway. Deprotonation of H_3L^{C6F5} with three equivalents of potassium hydride results in the formation of the triply deprotonated ligand, $K_3[(L^{C6F5})]$. Addition of PhIO to a DMF solution of $K_3[(L^{C6F5})]$ results in no reaction, as seen by ^1H NMR. This observation indicates that the C-F activation with PhIO does not proceed without the presence of iron in the ligand cavity, implicating a high valent Fe-oxo intermediate. This Fe-oxo could attack the fluoroarene, resulting in fluorine loss and product formation (Scheme 6-10, a).

a)

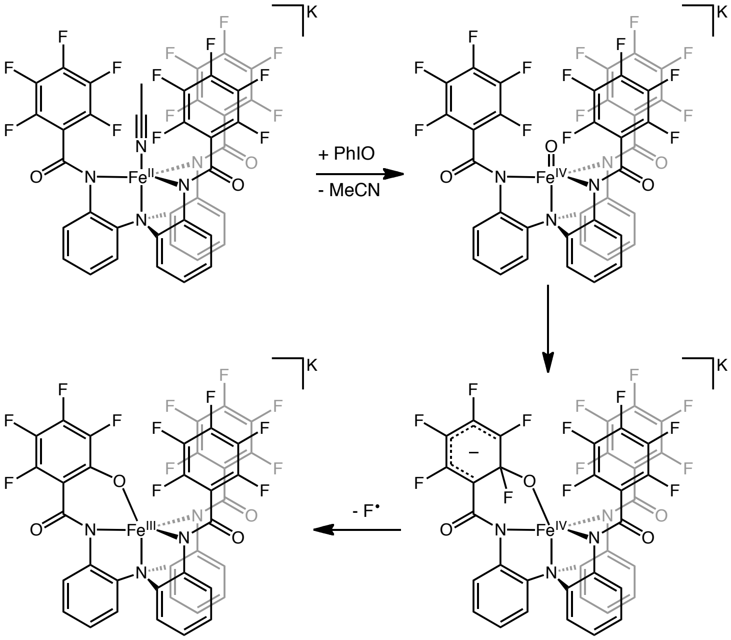

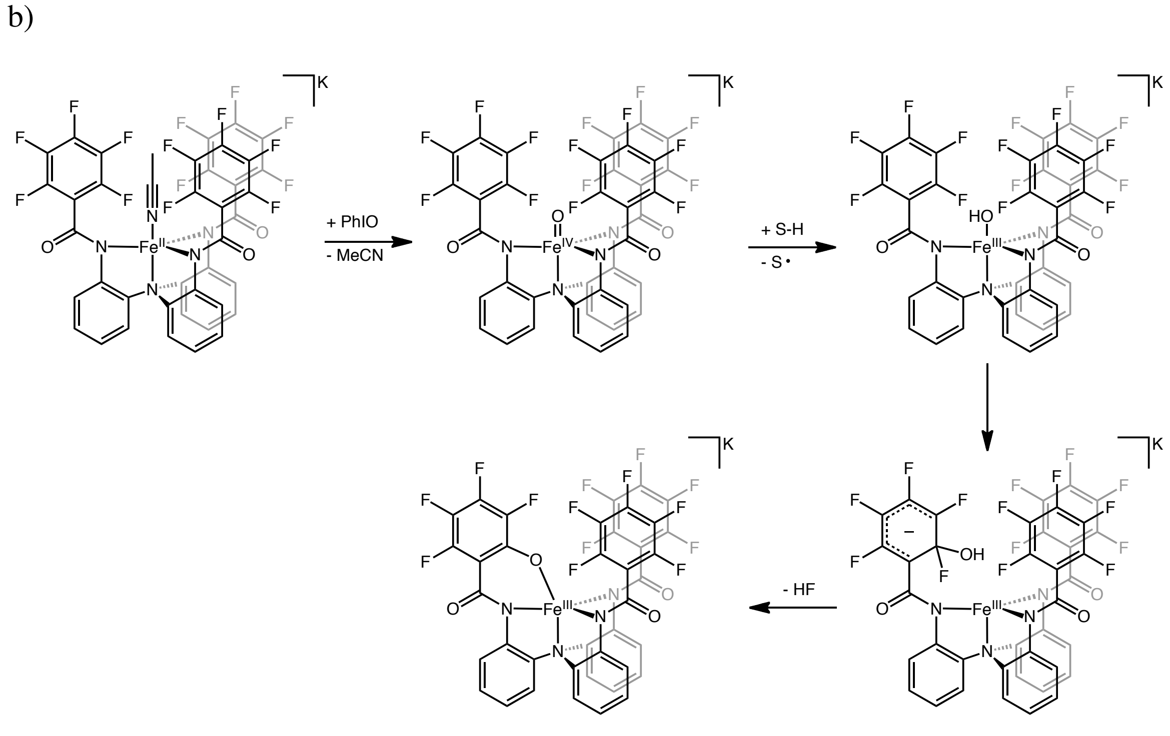

Scheme 6-10. Mechanisms of C-F activation that have been disproven.

This mechanism, however, is not supported experimentally. Addition of either excess triethylsilane or tetraethylsilylium tetrakis(pentafluorophenyl)borate does not result in Si-F bond formation as would be expected in the presence of F^-. Also, addition of as much as 100 equivalents of methyl iodide, a potent electrophile, does not result in Me-O bond formation, as observed by ESI-MS. An alternative mechanism would have the Fe(IV)=O unit abstract an H atom from solvent to form an Fe(III)-OH that could then attack the ring, resulting in loss of HF (Scheme 6-10, b). This mechanism has also been precluded by experimental evidence. If hydrogen atom abstraction occurs, the lower BDE of 9,10-dihydroanthracene versus tetrahydrofuran should result in preferential formation of anthracene. However, addition of excess 9,10-dha to the reaction prior to the addition of oxidant does not result in the formation of anthracene, as confirmed by ^{1}H NMR. In addition, the presence of amine bases like triethylamine and Proton Sponge (1,8-bis(dimethylamino)naphthalene) does not result in the formation of their respective hydrofluoride salts.[258] Also, if the reactive intermediate in C-F cleavage is an Fe(III)hydroxide, the intermediate should be able to be prepared through a different route, which would also result in immediate phenoxide formation. However, attempting to synthesize the Fe(III)-OH intermediate via addition of potassium hydoxide to a putative Fe(III) species, [Fe(L^{C6F5})], in DMF only results in the formation of iron oxides over the course of days. Due to the inability to trap the fluorine byproduct of C-F activation, we propose a mechanism that proceeds via a bridged diiron intermediate (Scheme 6-11).

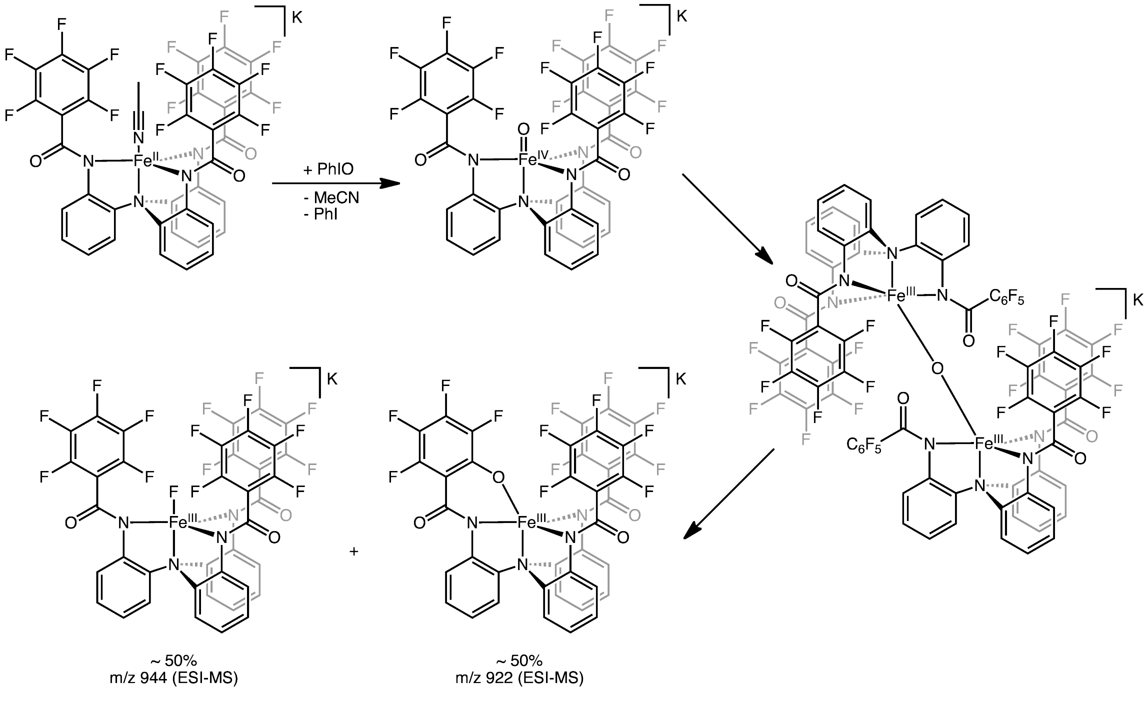

Scheme 6-11. Proposed dinuclear mechanism of C-F activation.

The formation of an oxo-bridged diiron(III) intermediate would prohibit the ability to trap the fluoride ion prior to the formation of the Fe(III) fluoride product. A dinuclear mechanism could proceed by a transient Fe(IV) oxo bridging with one of the unreacted Fe(II) molecules to form a bridged diiron(III) complex. This would be followed by attack on the aryl carbon by the μ-oxo intermediate. The lost F^- would then bind to the open Fe site, generating the two observed products.

In another attempt to generate a ligand backbone robust enough to effect intermolecular C–H activation, the parent trisamine ligand was acylated with heptafluorobutyryl chloride, using the standard acylating procedure. The resultant perfluoropropyl-substituted ligand, H_3L^{C3F7}, features aliphatic C–F bonds that are not susceptible to substitution reactions, and therefore should be more robust than the previous alkyl and fluoroaryl iterations of the ligand. A strategy was then developed in order to generate an Fe(II) complex. The ligand is first deprotonated with three equivalents of potassium hydride (Scheme 6-12). The ligand is then transmetallated with $Fe(OAc)_2$ to generate the desired five-coordinate complex, $K[Fe(L^{C3F7})(MeCN)]$, in moderate yield.

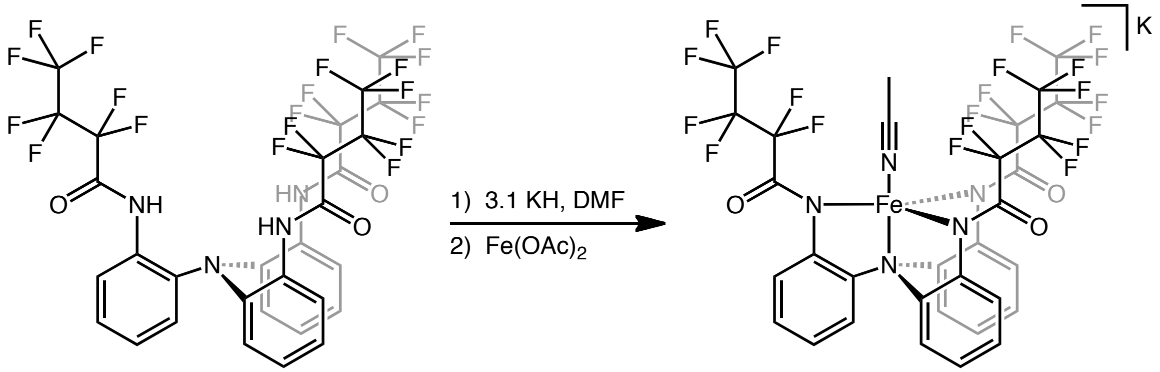

Scheme 6-12. Synthesis of Fe(II) complex, $K[Fe(L^{C3F7})(MeCN)]$.

Subsequent workup and recrystallization by slow diffusion of diethyl ether into an MeCN solution of the crude product gives crystals of K[Fe(L^{C6F5})(MeCN)] suitable for X-ray diffraction (Figure 6-12). The solid state structure of the complex displays an Fe(II) ion in a trigonal bipyramidal geometry (τ_5 = 0.96). The equatorial plane is comprised of three *N*-amidate donors, while a tertiary amine donor and an acetonitrile solvent molecule occupy the axial sites.

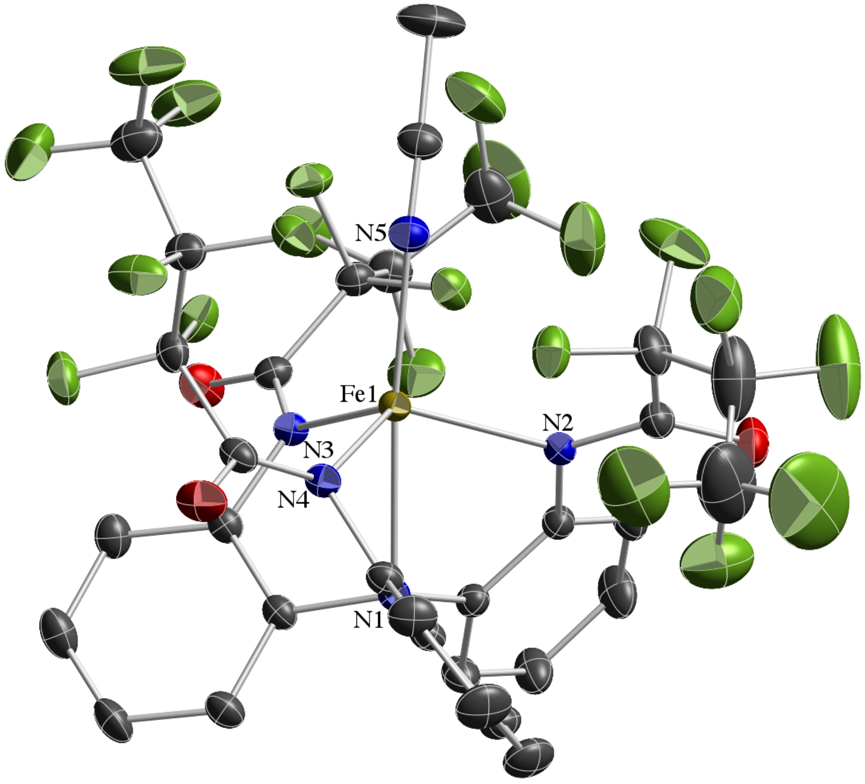

Figure 6-12. Solid-state structure of K[Fe(L^{C3F7})(MeCN)]. Counterion and hydrogen atoms are omitted for clarity. Thermal ellipsoids are shown at 40% probability.

The paramagnetically-shifted ^{1}H NMR of K[Fe(L^{C3F7})(MeCN)] contains four signals, indicating that the complex maintains C_3-symmetry in solution. The FTIR of K[Fe(L^{C3F7})(MeCN)] shows a ν(CO) stretch of 1629 cm^{-1}. While this stretch is much higher than those observed for the other Fe(II) complexes of this ligand scaffold, the value is consistent with the shift to more electron-rich perfluoropropyl groups.

Table 6-3. Selected bond lengths and angles for K[Fe(L^{C3F7})(MeCN)].

	K[Fe(L^{C3F7})(MeCN)]
Fe–N_{amide} (ave.)	2.113(2) Å
Fe–N_{amine}	2.326(2) Å
Fe–N_{MeCN}	2.100(2) Å
N_{amine}–Fe–N_{MeCN}	173.91(7)°
τ_5	0.96

The electrochemical properties of K[Fe(L^{C3F7})(MeCN)] were investigated by cyclic voltammetry experiments, but the complex did not display any significant or reversible electrochemical events at 25 °C in DMF with *n*-tetrabutylammonium hexafluorophosphate (TBAPF$_6$) as the supporting electrolyte. The CV was then acquired in the presence of ~1 equivalent of Et$_4$NCN, added directly to the electrochemical cell. Like the other Fe(II) complexes of this ligand scaffold, the addition of cyanide ion to K[Fe(L^{C3F7})(MeCN)] gave rise to an electrochemical event (Figure 6-13).

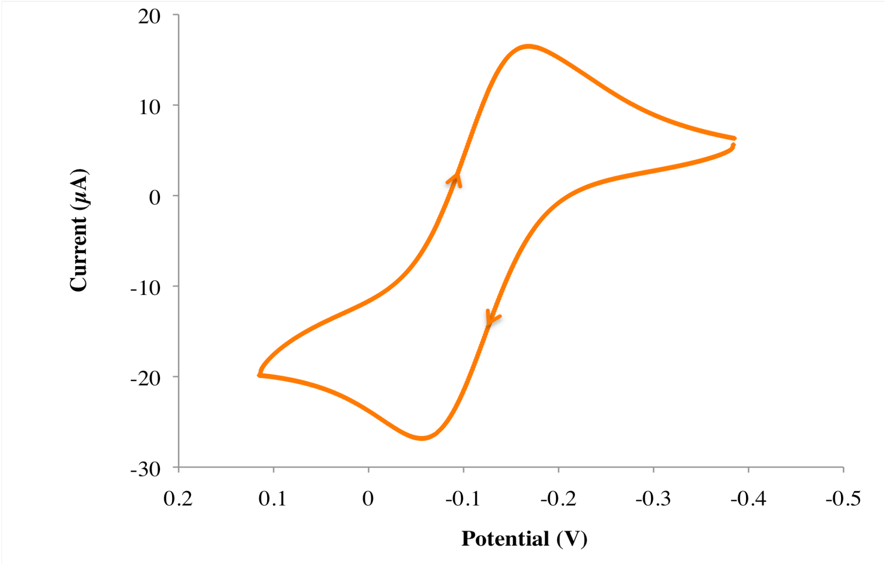

Figure 6-13. Cyclic voltammogram of K[Fe(L^{C3F7})(MeCN)] recorded in DMF (0.2 M $TBAPF_6$) at 0.1 V/s.

The cyanide adduct of K[Fe(L^{C3F7})(MeCN)] displays an irreversible event at $E_{1/2}$ = -0.112 V (ΔE_p = 0.113 V; i_{pc}/i_{pa}^{-1} = 0.73) vs. Fc/Fc^+. The shift of this signal to more positive potentials relative to that observed for the cyanide adducts of the other $[(L^R)]^{3-}$ (R = iPr, Ph, C_6F_5) ligand derivatives is consistent with the change in acyl substituents to the strongly electron-withdrawing perfluorinated propyl groups. With the Fe(II) complex in hand, we sought to explore the reactivity of this species with dioxygen. It was discovered, however, that addition of dioxygen to solutions of K[Fe(L^{C3F7})(MeCN)] in either MeCN or DMF results in no reaction. This observation, along with the observed $E_{1/2}$, indicates that K[Fe(L^{C3F7})(MeCN)] is too stable towards oxidation to react with dioxygen.

In summary, I have reported a new mode of C-F activation in which a nucleophilic Fe-oxo unit cleaves an intramolecular aryl C-F bond to form a phenoxide.

This reactivity can be achieved with artificial oxidants, as well as with dioxygen. The lack of reactivity of these complexes with fluorine anion/radical trapping reagents implicates a diiron species as the active intermediate in C-F cleavage. It is noteworthy that not only is this transformation mediated by inexpensive, environmentally benign Fe ions and dioxygen, it also proceeds quickly at room temperature. Future studies will focus on modulating our ligand system to effect intermolecular C-F bond activation, as well as in depth studies toward understanding the mechanism of this reaction.

Section 6-3. Experimental

General Considerations

All manipulations were carried out using standard Schlenk techniques or conducted in an MBraun Labmaster 130 drybox under a nitrogen atmosphere. All reagents used were purchased from commercial vendors and used as received unless otherwise noted. Anhydrous solvents were purchased from Sigma-Aldrich and further purified by sparging with Ar gas followed by passage through activated alumina columns. Deuterated dimethyl sulfoxide (DMSO-d_6) was purchased from Aldrich and degassed and dried according to standard procedures[127] prior to use. Labeled dioxygen gas (^{18}O, 98%) was obtained from ICON Isotopes, Summit, NJ. Elemental analyses were performed by Atlantic Microlab, Inc., Norcross, GA and Midwest Microlabs, Indianapolis, IN. Fe(HMDS)$_2$(THF) was prepared according to a published procedure.[281] ^1H NMR spectra were recorded on a Varian Inova 400 MHz spectrometer at ambient temperature. Chemical shifts were referenced to residual solvent peaks. Infrared spectra were recorded as KBr pellets on a Varian Scimitar 800 Series FT-IR spectrophotometer. UV-Visible absorption spectra were recorded on a Cary 50 spectrophotometer using 1.0 cm quartz cuvettes. Solution state magnetic moments were measured using Evans' method.[128] Mass spectra were recorded in the Mass Spectrometry Center at Emory University on a JEOL JMS-SX102/SX102A/E mass spectrometer. X-ray diffraction studies were carried out in the X-ray Crystallography Laboratory at Emory University on a Bruker Smart 1000 CCD diffractometer. Cyclic voltammetric experiments were carried out using a CH Instruments (Austin, TX) Model 660C potentiostat. All experiments were conducted in DMF with 0.20 M tetrabutylammonium hexafluorophosphate as the supporting electrolyte. Electrochemical experiments were conducted in a three-component cell consisting of a Pt auxiliary electrode, a non-aqueous reference electrode ($Ag/AgNO_3$), and a glassy carbon working electrode. All electrochemical measurements are referenced and reported versus the ferrocene/ferrocenium couple.

$K[Fe(L^{C6F5})(MeCN)]$

To a stirred solution of H_3L^{C6F5} (259 mg, 0.30 mmol) in DMF (7 mL) was added KH (12 mg, 0.30 mmol) as a solid. After an hour of stirring, $Fe(HMDS)_2(THF)$ (133 mg, 0.30 mmol) was added as a solid. The yellow solution turned light brown, and two hours later solvent was removed in vacuo. The resultant beige solid was taken up in acetonitrile, filtered, and concentrated in vacuo. Yellow, x-ray quality crystals were obtained by vapor diffusion of diethyl ether into a concentrated MeCN solution (120 mg, 44%). ^1H NMR (δ, $(CD_3)SO$, 400 MHz): 20.88, 17.49, 16.36, 14.68, 14.10, 13.00, 12.30, 11.32, 6.53, -5.50. FTIR (KBr, cm^{-1}) ν: 3068, 2936, 2884, 1669, 1654, 1604

(CO), 1570, 1518, 1497, 1386, 1241, 1117, 1089, 989, 874, 789, 754, 669, 566. μ_{eff} = 5.15 μ_B (Evans' Method, $(CD_3)_2SO$, 298K). λ_{max}(ε, $M^{-1}cm^{-1}$) (MeCN): 251(50,526), 289(sh). Anal. Calcd (found) for $K[FeN(o\text{-}PhNC(O)C_6F_5)_3(MeCN)]$: C, 50.37 (50.13); H, 2.52 (2.27); N, 7.50 (7.53).

$K[Fe(L^{Mod})]$

To a stirred solution of H_3L^{C6F5} (255 mg, 0.29 mmol) in DMF (3 mL) was added KH (39 mg, 0.97 mmol) as a solid. After an hour of stirring, $Fe(OAc)_2$ (51 mg, 0.29 mmol) was added as a solid. The yellow solution turned light brown, and one hour later, solvent was removed in vacuo. The resultant oil was taken up in THF, and the mixture was filtered over Celite to remove KOAc. To the filtrate was added PhIO (64 mg, 0.29 mmol) as a solid. The yellow solution turned purple instantly. After 2 hours of stirring, solvent was removed in vacuo. The resultant purple oil was taken up in acetonitrile and filtered over Celite. Deep purple, x-ray quality crystals were obtained by slow diffusion of diethyl ether into acetonitrile (123 mg, 44%). ^1H NMR (δ, CD_3CN, 300 MHz): 60.20, 36.04, 29.78, 12.11, -0.71, -2.78, -5.21, -18.31. FTIR (KBr, cm^{-1}) ν: 3070, 2978, 2936, 2878, 1608 (CO), 1590, 1520, 1500, 1463, 1364, 1282, 1225, 1117, 1088, 1008, 991, 881, 809, 789, 753, 667, 621, 568. μ_{eff} = 5.83 μ_B (Evans' Method, CD_3CN, 298K). λ_{max}(ε, $M^{-1}cm^{-1}$) (MeCN): 530(6133). HRESI-MS: $C_{39}H_{12}O_4N_4F_{14}Fe$ *m/z* Calcd. 921.99899 Found 921.99838. Anal. Calcd (found) for $K[FeN(o\text{-}NC(O)C_6F_5)_2(o\text{-}NC(O)C_6F_4O)]$: C, 50.04 (50.13); H, 1.68 (2.16); N, 5.84 (5.86).

$(Et_4N)_2[Fe(L^{Mod})]$

To a stirred solution of H_3L^{C6F5} (92 mg, 0.11 mmol) in DMF (3 mL) was added KH (14 mg, 0.35 mmol) as a solid. After an hour of stirring, $Fe(OAc)_2$ (18 mg, 0.11 mmol) was added as a solid. The yellow solution turned light brown, and one hour later, solvent was removed in vacuo. The resultant oil was taken up in THF, and the mixture was filtered over Celite to remove KOAc. To the filtrate was added KOH (6 mg, 0.11 mmol) and Et_4NBr (44 mg, 0.21 mmol) consecutively, as solids. The yellow solution turned orange as the solids dissolved. After 24 hours of stirring, solvent was removed in vacuo. The resultant orange oil was taken up in acetonitrile and filtered over Celite. Orange, x-ray quality crystals were obtained by slow diffusion of diethyl ether into acetonitrile (61 mg, 49%). ^1H NMR (δ, CD_3CN, 300 MHz): 35.00, 24.60, 23.30, 19.27, 19.01, 5.95, 0.16, -4.03, -5.90, -6.26. FTIR (KBr, cm^{-1}) ν: 3059, 2989, 1638, 1600 (CO), 1566, 1518, 1496, 1460, 1370, 1330, 1173, 1085, 999, 987, 872, 786, 757, 621, 565. $\mu_{eff} = 5.10\ \mu_B$ (Evans' Method, CD_3CN, 298K). $\lambda_{max}(\varepsilon, M^{-1}cm^{-1})$ (MeCN): 450(sh). Anal. Calcd (found) for $(Et_4N)_2[FeN(o\text{-}NC(O)C_6F_5)_2(o\text{-}NC(O)C_6F_4O)]$: C, 55.94 (56.04); H, 4.53 (4.44); N, 8.01 (8.02).

Synthesis of an Fe(III) fluoride adduct

To a stirred solution of H_3L^{C6F5} (95 mg, 0.11 mmol) in DMF (2 mL) was added KH (13 mg, 0.33 mmol) as a solid. After an hour of stirring, $Fe(OAc)_2$ (19 mg, 0.11 mmol) was added as a solid. The yellow solution turned light brown, and one hour later solvent was removed in vacuo. The resultant yellow oil was taken up in THF, filtered over Celite to remove KOAc, and concentrated to dryness. The yellow oil was taken up in acetonitrile and Me_4NF was added as a solid (20 mg, 0.22 mmol). After 1 hour of stirring the mixture was filtered and concentrated to dryness. The yellow oil was dissolved in acetonitrile and ferrocenium tetrafluoroborate (30 mg, 0.11 mmol) was added as an acetonitrile solution. After 20 minutes of stirring, solvent was removed in vacuo. The resultant dark red oil was washed with 2 x 5 mL portions of diethyl ether before being dissolved in THF and filtered over Celite. The crude product was isolated by concentration in vacuo. FTIR (KBr, cm^{-1}): ν(CO) 1615. λ_{max}(ε, $M^{-1}cm^{-1}$) (MeCN): 493(1547), 583(sh). HRMS(ESI): $[Fe(L^{C6F5})F]^-$ *m/z* Calcd. 944.00033 Found 943.99670 $[M-1]^+$.

Synthesis of K[FeL^{Mod}] with Dioxygen

A THF (8 mL) solution of K[Fe(L^{C6F5})(MeCN)] (50 mg, 0.05 mmol) was sealed under vacuum in a 25 mL Schlenk tube. Excess dry O_2 (20 mL) was added via gastight syringe. Upon addition, there was an immediate color change from pale yellow to deep reddish-purple. After two hours of stirring, the reaction flask was placed under vacuum to remove the excess O_2, and the reaction mixture was worked up as above. Spectral analysis of the crude product by IR, UV-Vis, and ESI-MS confirmed product formation.

^{18}O Labeling Study

A THF (5 mL) solution of K[Fe(L^{C6F5})(MeCN)] (115 mg, 0.11 mmol) was sealed under vacuum in a 10 mL Schlenk tube. Excess ^{18}O-labeled dioxygen was added via volume displacement from a 25 mL breakseal ampoule. Upon addition, there was an immediate color change from pale yellow to deep reddish-purple. After two hours of stirring, the reaction flask was placed under vacuum to remove the excess O_2, and the reaction mixture was worked up as above. Spectral analysis of the purified material by HRESI-MS confirmed ^{18}O incorporation into the product.

N(*o*-PhNHC(O)C_3F_7)$_3$ (H_3L^{C3F7})

A suspension of L^{NH2} (4.00 g, 13.8 mmol) in dichloromethane (DCM, 120 mL) was cooled to 0°C under an atmosphere of N_2. Triethylamine (6.28 mL, 42.8 mmol) was then added, followed by the dropwise addition of heptafluorobutyryl chloride (6.39 mL, 42.8 mmol). The mixture was allowed to warm to room temperature and stirred for 12 hours. The reaction mixture was washed with saturated aqueous $NaHCO_3$ (3 x 100 mL), dried over magnesium sulfate, and filtered. Solvent was removed in vacuo, and the resulting pale yellow oil was washed triturated in hexanes (~50 mL) until a white solid was produced. The white solid was collected by filtration, washed with copious amounts of diethyl ether, and dried in vacuo (8.55 g, 71%). ^1H NMR (δ, CD_3CN, 400 MHz): 9.37 (s, 3H, NH), 7.65 (d, 3H, *J* = 4.0 Hz, ArH), 7.26 (td, 6H, ArH), 6.88 (td, 3H, *J* = 4 Hz, ArH). ^{13}C NMR (δ, CD_3CN, 400 MHz): 156.10, 139.34, 129.65, 129.22, 127.09, 126.78, 125.71, 109.22. ^{19}F NMR (δ, CD_3CN, 400 MHz): -92.05, -131.05, -138.26.

K[Fe(L^{C3F7})(MeCN)]

To a stirred solution of H_3L^{C3F7} (285 mg, 0.32 mmol) in DMF (6 mL) was added KH (40 mg, 1.01 mmol) as a solid. After an hour of stirring, $FeBr_2$ (70 mg, 0.32 mmol) was added as a solid. The yellow solution turned near colorless, and two hours later solvent was removed in vacuo. The resultant brown solid was taken up in acetonitrile, filtered, and concentrated in vacuo. Colorless, x-ray quality crystals were obtained by vapor diffusion of diethyl ether into a concentrated MeCN solution of the complex (267 mg, 85%). ^{1}H NMR (δ, CD_3CN, 400 MHz): 22.38, 9.12, 6.59, 3.77. FTIR (KBr, cm^{-1}) ν: 3067, 3027, 2297, 2259, 1629 (CO), 1590, 1483, 1454, 1392, 1338, 1233, 1115, 892, 749, 652, 598, 534, 462.

Crystallography

Suitable crystals were coated with Paratone-N oil, suspended on a small fiber loop and placed in a cooled nitrogen gas stream at 173K on a Bruker D8 APEX II CCD sealed tube diffractometer with graphite monochromated Mo-Ka (0.71073 Å) radiation. Data were measured using a series of combinations of phi and omega scans with 10 s frame exposures and 0.5° frame widths. Data collection, indexing and initial cell refinements were all carried out using APEX II software.[131] Frame integration and final cell refinements were done using SAINT software.[132] The final cell parameters were determined from least-squares refinement on 2159 reflections. The structure was solved using Direct methods and difference Fourier techniques (SHELXTL, V6.12).[133] Hydrogen atoms were placed in their expected chemical positions using the HFIX command and were included in the final cycles of least squares refinement using a riding model. All non-hydrogen atoms were refined anisotropically. Scattering factors and anomalous dispersion corrections are taken from the *International Tables for X-ray Crystallography*.[134] Structure solution, refinement, graphics and generation of publication materials were performed using SHELXTL, V6.12 software.[133]

Table 6-4. Crystal data and structure refinement for solid-state structures.

	K[Fe(L^{C6F5})(MeCN)]·Et_2O ·2MeCN	K[Fe(L^{Mod})]
Empirical formula	$C_{49}H_{31}F_{15}FeKN_7O_4$	$C_{39}H_{12}F_{14}FeKN_4O_4$
Formula weight	1161.76	961.48
T (K)	173(2)	173(2)
λ (Å)	0.71073	1.54178
Crystal System	Orthorhombic	Monoclinic
Space group	P2(1)2(1)2(1)	P2(1)/n
a (Å)	10.5151(4)	11.1224(8)
b (Å)	19.7084(7)	25.1294(14)
c (Å)	23.9822(10)	15.9176(9)
α (°)	90	90
β (°)	90	103.789(4)
γ (°)	90	90
V (Å^3)	4970.0(3)	4320.7(5)
Z	4	4
ρ_{calc} (Mg/m^3)	1.553	1.478
GOF on F^2	1.015	1.026
R	0.0649	0.0863
wR	0.1207	0.2385

	$(Et_4N)_2[Fe(L^{Mod})]\cdot 0.8MeCN$	$K[Fe(L^{C3F7})(MeCN)]\cdot MeCN$
Empirical formula	$C_{56.60}H_{54.40}F_{14}FeN_{6.80}O_4$	$C_{34}H_{15}F_{21}FeKN_6O_3$
Formula weight	1215.72	1049.47
T (K)	173(2)	173(2)
λ (Å)	0.71073	0.71073
Crystal System	Monoclinic	Triclinic
Space group	P(2)1/c	P-1
a (Å)	11.087(3)	11.076(9)
b (Å)	12.113(3)	11.514(9)
c (Å)	40.937(11)	17.989(14)
α (°)	90	81.401(11)
β (°)	91.748(4)	84.720(11)
γ (°)	90	62.818(10)
V ($Å^3$)	5495(3)	2017(3)
Z	4	2
ρ_{calc} (Mg/m^3)	1.469	1.728
GOF on F^2	1.019	1.074
R	0.0592	0.0529
wR	0.1438	0.1348

References

1. Kraatz, H.-B.; Metzler-Nolte, N., *Concepts and Models in Bioinorganic Chemistry*. Wiley-VCH: Weinheim, 2006.
2. Bertini, I.; Gray, H. B.; Stiefel, E. I.; Valentine, J. S., *Biological Inorganic Chemistry*. University Science Books: 2007.
3. Friedle, S.; Reisner, E.; Lippard, S. J., *Chem. Soc. Rev.* **2010,** *39* (8), 2768-2779.
4. Mandal, S. K.; Que, L., *Inorg. Chem.* **1997,** *36*, 5424-5425.
5. Dougherty, W. G.; Rangan, K.; O'Hagan, M. J.; Yap, G. P. A.; Riordan, C. G., *J Am. Chem. Soc.* **2008,** *130* (41), 13510-13511.
6. Borovik, A. S., *Acc. Chem. Res.* **2005,** *38* (1), 54-61.
7. MacBeth, C. E.; Golombek, A. P.; Young, V. G., Jr.; Yang, C.; Kuczera, K.; Hendrich, M. P.; Borovik, A. S., *Science* **2000,** *289* (5481), 938-941.
8. Chirik, P. J.; Wieghardt, K., *Science* **2010,** *327*, 794-795.
9. Bolm, C., *nature chemistry* **2009,** *1*, 420.
10. Enthaler, S.; Junge, K.; Beller, M., *Angew. Chem., Int. Ed.* **2008,** *47*, 3317-3321.
11. Trovitch, R. J.; Lobkovsky, E.; Chirik, P. J., *Inorg. Chem.* **2006,** *45* (18), 7252-7260.
12. Archer, A. M.; Bouwkamp, M. W.; Cortez, M.-P.; Lobkovsky, E.; Chirik, P. J., *Organometallics* **2006,** *25* (18), 4269-4278.
13. Bart, S. C.; Hawrelak, E. J.; Lobkovsky, E.; Chirik, P. J., *Organometallics* **2005,** *24* (23), 5518-5527.
14. Bart, S. C.; Lobkovsky, E.; Chirik, P. J., *J Am. Chem. Soc.* **2004,** *126* (42), 13794-13807.

15. Casey, C. P.; Guan, H., *J Am. Chem. Soc.* **2007,** *129* (18), 5816-5817.
16. Bullock, R. M., *Angew. Chem., Int. Ed.* **2008,** *47*, 3317-3321.
17. Sui-Seng, C.; Freutel, F.; Lough, A. J.; Morris, R. H., *Angew. Chem., Int. Ed.* **2008,** *47* (5), 940-943.
18. Nishiyama, H.; Furuta, A., *Chem. Comm.* **2007,** *7*, 760.
19. Enthaler, S.; Erre, G.; Tse, M. K.; Junge, K.; Beller, M., *Tetrahedron Lett.* **2006,** *47* (46), 8095-8099.
20. Shaikh, N. S.; Enthaler, S.; Junge, K.; Beller, M., *Angew. Chem., Int. Ed.* **2008,** *47* (13), 2497-2501.
21. Legros, J.; Bolm, C., *Angew. Chem., Int. Ed.* **2003,** *42* (44), 5487-5489.
22. Legros, J.; Bolm, C., *Chem.--Eur. J.* **2005,** *11* (4), 1086-1092.
23. Legros, J.; Bolm, C., *Angew. Chem., Int. Ed.* **2004,** *43* (32), 4225-4228.
24. Korte, A.; Legros, J.; Bolm, C., *Synlett* **2004,** (13), 2397-2399.
25. Bryliakov, K. P.; Talsi, E. P., *Angew. Chem.* **2004,** *116*, 5340.
26. Egami, H.; Katsuki, T., *J Am. Chem. Soc.* **2007,** *129* (29), 8940-8941.
27. Pavan, C.; Legros, J.; Bolm, C., *Adv. Synth. Catal.* **2005,** *347* (5), 703-705.
28. Nakanishi, M.; Bolm, C., *Adv. Synth. Catal.* **2007,** *349* (6), 861-864.
29. Rose, E.; Ren, Q.-z.; Andrioletti, B., *Chem.--Eur. J.* **2004,** *10* (1), 224-230.
30. Gelalcha, F. G.; Bitterlich, B.; Anilkumar, G.; Tse, M. K.; Beller, M., *Angew. Chem., Int. Ed.* **2007,** *46* (38), 7293-7296.
31. Schröder, K.; Tong, X.; Bitterlich, B.; Tse, M. K.; Gelalcha, F. G.; Brückner, A.; Beller, M., *Tetrahedron Lett.* **2007,** *48*, 6339-6342.

32. Anilkumar, G.; Bitterlich, B.; Gelalcha, F. G.; Tse, M. K.; Beller, M., *Chem. Commun.* **2007,** (3), 289-291.

33. Bitterlich, B.; Anilkumar, G.; Gelalcha, F. G.; Spilker, B.; Grotevendt, A.; Jackstell, R.; Tse, M. K.; Beller, M., *Chem. Asian J.* **2007,** *2*, 514-520.

34. Oldenburg, P. D.; Shteinman, A. A.; Que, L., Jr., *J Am. Chem. Soc.* **2005,** *127* (45), 15672-15673.

35. Bukowski, M. R.; Comba, P.; Lienke, A.; Limberg, C.; Lopez de Laorden, C.; Mas-Balleste, R.; Merz, M.; Que, L., Jr., *Angew. Chem., Int. Ed.* **2006,** *45* (21), 3446-3449.

36. Oldenburg, P. D.; Ke, C.-Y.; Tipton, A. A.; Shteinman, A. A.; Que, L., *Angew. Chem., Int. Ed.* **2006,** *45* (47), 7975-7978.

37. Chen, M. S.; White, M. C., *Science* **2007,** *318* (5851), 783-787.

38. Correa, A.; Bolm, C., *Angew. Chem., Int. Ed.* **2007,** *46* (46), 8862-8865.

39. Correa, A.; Bolm, C., *Adv. Synth. Catal.* **2008,** *350* (3), 391-394.

40. Correa, A.; Carril, M.; Bolm, C., *Angew. Chem., Int. Ed.* **2008,** *47* (15), 2880-2883.

41. Bistri, O.; Correa, A.; Bolm, C., *Angew. Chem., Int. Ed.* **2008,** *47* (3), 586-588.

42. Plietker, B., *Angew. Chem., Int. Ed.* **2006,** *45* (36), 6053-6056.

43. Harrop, T. C.; Mascharak, P. K., Model Complexes of Ni-Containing Enzymes. In *Concepts and Models in Inorganic Chemistry*, Kraatz, H.-B.; Metzler-Nolte, N., Eds. Wiley-VCH: Weinheim, 2006; pp 309-329.

44. Jackson, T. A.; Que, L., Structural and Functional Models for Oxygen-Activating Nonheme Iron Enzymes In *Concepts and Models in Inorganic Chemistry*, Kraatz, H.-B.; Metzler-Nolte, N., Eds. Wiley-VCH: Weinheim, 2006; pp 239-286.

45. Barondeau, D. P.; Kassmann, C. J.; Bruns, C. K.; Tainer, J. A.; Getzoff, E. D., *Biochemistry* **2004,** *43*, 8038-8047.

46. Darnault, C.; Volbeda, A.; Kim, E. J.; Legrand, P.; Vernede, X.; Lindahl, P. A.; Fontecilla-Camps, J. C., *Nature Struc. Biol.* **2003,** *10*, 271-279.

47. Minor, W.; Steczko, J.; Stec, B.; Otwinowski, Z.; Bolin, J. T.; Walter, R.; Axelrod, B., *Biochemistry* **1996,** *35*, 10687-10701.

48. Roach, P. L.; Clifton, I. J.; Fülöp, V.; Harlos, K.; Barton, G. J.; Hajdu, J.; Andersson, I.; Schofield, C. J.; Baldwin, J. E., *Nature* **1995,** *375*, 700-704.

49. Roach, P. L.; Clifton, I. J.; Hensgen, C. M. H.; Shibata, N.; Schofield, C. J.; Hajdu, J.; Baldwin, J. E., *Nature* **1997,** *387*, 827-830.

50. Shigehiro, N.; Nakasako, M.; Dohmae, N.; Tsujimara, M.; Takio, K.; Odaka, M.; Yohda, M.; Kamiya, N.; Endo, I., *Nature Struc. Biol.* **1998,** *5* (5), 347-351.

51. Sami, M.; Brown, T. J. N.; Roach, P. L.; Schofield, C. J.; Baldwin, J. E., *FEBS Lett* **1997,** *405* (2), 191-194.

52. Landman, O.; Borovok, I.; Aharonowitz, Y.; Cohen, G., *FEBS Lett* **1997,** *405* (2), 172-174.

53. Kramer, J. A.; Johnson, K. R.; Dunham, W. R.; Sands, R. H.; Funk, M. O., Jr., *Biochemistry* **1994,** *33* (50), 15017-22.

54. Barnes, S. J.; Weitzman, P. D., *FEBS Lett.* **1986,** *201* (2), 267-270.

55. Kim, A.-R.; Rylett, R. J.; Shilton, B. H., *Biochemistry* **2006,** *45* (49), 14621-14631.

56. Lindahl, P. A., *Biochemistry* **2002,** *41*, 2097-2105.

57. Lee, A. V.; Schafer, L. L., *Eur. J. Inorg. Chem.* **2007,** (16), 2243-2255.

58. Ray, M.; Yap, G. P. A.; Rheingold, A. L.; Borovik, A. S., *J. Chem. Soc., Chem. Commun.* **1995,** (17), 1777-8.

59. Bossu, F. P.; Chellappa, K. L.; Margerum, D. W., *J Am. Chem. Soc.* **1977,** *99* (7), 2195-203.

60. Thomson, R. K.; Zahariev, F. E.; Zhang, Z.; Patrick, B. O.; Wang, Y. A.; Schafer, L. L., *Inorg. Chem.* **2005,** *44* (24), 8680-8689.

61. Kannan, S.; Barnes, C. L.; Duval, P. B., *Chem. Commun.* **2005,** (48), 5997-5998.

62. Ray, M.; Golombek, A. P.; Hendrich, M. P.; Yap, G. P. A.; Liable-Sands, L. M.; Rheingold, A. L.; Borovik, A. S., *Inorg. Chem.* **1999,** *38* (13), 3110-3115.

63. Hammes, B. S.; Ramos-Maldonado, D.; Yap, G. P. A.; Liable-Sands, L.; Rheingold, A. L.; Young, V. G., Jr.; Borovik, A. S., *Inorg. Chem.* **1997,** *36* (15), 3210-3211.

64. Bossu, F. P.; Margerum, D. W., *J Am. Chem. Soc.* **1976,** *98* (13), 4003-4.

65. Margerum, D. W., *Pure Appl. Chem.* **1983,** *55* (1), 23-34.

66. Kimura, E., *Pure Appl. Chem.* **1989,** *61* (5), 823-8.

67. Kimura, E., *J. Coord. Chem.* **1986,** *15* (1), 1-28.

68. Kushi, Y.; Machida, R.; Kimura, E., *J. Chem. Soc., Chem. Commun.* **1985,** (4), 216-18.

69. Kimura, E.; Machida, R.; Kodama, M., *J Am. Chem. Soc.* **1984,** *106* (19), 5497-505.

70. Harrop, T. C.; Mascharak, P. K., *Coord. Chem. Rev.* **2005,** *249* (24), 3007-3024.

71. Harrop, T. C.; Olmstead, M. M.; Mascharak, P. K., *Inorg. Chem.* **2006,** *45* (8), 3424-3436.

72. Afshar, R. K.; Eroy-Reveles, A. A.; Olmstead, M. M.; Mascharak, P. K., *Inorg. Chem.* **2006,** *45* (25), 10347-10354.

73. Afshar, R. K.; Patra, A. K.; Bill, E.; Olmstead, M. M.; Mascharak, P. K., *Inorg. Chem.* **2006,** *45* (9), 3774-3781.

74. Afshar, R. K.; Patra, A. K.; Olmstead, M. M.; Mascharak, P. K., *Inorg. Chem.* **2004,** *43* (18), 5736-5743.

75. Collins, T. J., *Acc. Chem. Res.* **2002,** *35* (9), 782-790.

76. Tiago de Oliveira, F.; Chanda, A.; Banerjee, D.; Shan, X.; Mondal, S.; Que, L., Jr.; Bominaar, E. L.; Muenck, E.; Collins, T. J., *Science* **2007,** *315* (5813), 835-838.

77. Collins, T. J.; Kostka, K. L.; Münck, E.; Uffelman, E. S., *J Am. Chem. Soc.* **1990,** *112*, 5637-5639.

78. Sen Gupta, S.; Stadler, M.; Noser, C. A.; Ghosh, A.; Steinhoff, B.; Lenoir, D.; Horwitz, C. P.; Schramm, K.-W.; Collins, T. J., *Science* **2002,** *296* (5566), 326-328.

79. Ghosh, A.; Gupta, S. S.; Bartos, M. J.; Hangun, Y.; Vuocolo, L. D.; Steinhoff, B. A.; Noser, C. A.; Horner, D.; Mayer, S.; Inderhees, K.; Horwitz, C. P.; Spatz, J.;

Ryabov, A. D.; Mondal, S.; Collins, T. J., *Pure Appl. Chem.* **2001,** *73* (1), 113-118.

80. Ellis, W. C.; Tran, C. T.; Roy, R.; Rusten, M.; Fischer, A.; Ryabov, A. D.; Blumberg, B.; Collins, T. J., *J Am. Chem. Soc.* **2010,** *132* (28), 9774-9781.
81. Mankad, N. P.; Whited, M. T.; Peters, J. C., *Angew. Chem., Int. Ed.* **2007,** *46* (30), 5768-5771.
82. Tsay, C.; Mankad, N. P.; Peters, J. C., *J Am. Chem. Soc.* **2010,** *132* (40), 13975-13977.
83. Lee, Y.; Mankad, N. P.; Peters, J. C., *nature chemistry 2* (7), 558-565.
84. Whited, M. T.; Mankad, N. P.; Lee, Y.; Oblad, P. F.; Peters, J. C., *Inorg. Chem.* **2009,** *48* (6), 2507-2517.
85. MacBeth, C. E.; Harkins, S. B.; Peters, J. C., *Can. J. Chem.* **2005,** *83* (4), 332-340.
86. Frye, C. L.; Vincent, G. A.; Hauschildt, G. L., *J Am. Chem. Soc.* **1966,** *88* (12), 2727-30.
87. Redshaw, C.; Rowan, M. A.; Homden, D. M.; Dale, S. H.; Elsegood, M. R. J.; Matsui, S.; Matsuura, S., *Chem. Commun.* **2006,** (31), 3329-3331.
88. Michalczyk, L.; de Gala, S.; Bruno, J. W., *Organometallics* **2001,** *20* (26), 5547-5556.
89. Niemoth-Anderson, J. D.; Clark, K. A.; George, T. A.; Ross, C. R., II, **2000,** *122* (16), 3977-3978.
90. Hu, X.; Meyer, K., *J. Organomet. Chem.* **2005,** *690* (24-25), 5474-5484.
91. Blackman, A. G., *Polyhedron* **2005,** *24* (1), 1-39.

92. Schrock, R. R., *Acc. Chem. Res.* **1997,** *30* (1), 9-16.

93. Cummins, C. C.; Lee, J.; Schrock, R. R.; Davis, W. M., *Angew. Chem.* **1992,** *104* (11), 1510-12 (See also Angew Chem , Int Ed Engl , 1992, 31(11), 1501-3).

94. Pinkas, J.; Wang, T.; Jacobson, R. A.; Verkade, J. G., *Inorg. Chem.* **1994,** *33* (19), 4202-10.

95. Verkade, J. G., *Acc. Chem. Res.* **1993,** *26* (9), 483-9.

96. Roussel, P.; Errington, W.; Kaltsoyannis, N.; Scott, P., *J. Organomet. Chem.* **2001,** *635* (1-2), 69-74.

97. Filippou, A. C.; Schneider, S.; Schnakenburg, G., *Inorg. Chem.* **2003,** *42* (22), 6974-6976.

98. Cummins, C. C.; Schrock, R. R., *Inorg. Chem.* **1994,** *33* (2), 395-6.

99. Freundlich, J. S.; Schrock, R. R.; Cummins, C. C.; Davis, W. M., *J Am. Chem. Soc.* **1994,** *116* (14), 6476-7.

100. MacBeth, C. E.; Gupta, R.; Mitchell-Koch, K. R.; Young, V. G., Jr.; Lushington, G. H.; Thompson, W. H.; Hendrich, M. P.; Borovik, A. S., *J Am. Chem. Soc.* **2004,** *126* (8), 2556-2567.

101. Yandulov, D. V.; Schrock, R. R., *Science* **2003,** *301* (5629), 76-78.

102. Ritleng, V.; Yandulov, D. V.; Weare, W. W.; Schrock, R. R.; Hock, A. S.; Davis, W. M., *J Am. Chem. Soc.* **2004,** *126* (19), 6150-6163.

103. Chen, J.; Woo, L. K., *J. Organomet. Chem.* **2000,** *601* (1), 57-68.

104. Ray, M.; Golombek, A.; Hendrich, M. P.; Young, V. G., Jr.; Borovik, A. S., *J Am. Chem. Soc.* **1996,** *118* (25), 6084-6085.

105. Mederos, A.; Dominguez, S.; Hernandez-Molina, R.; Sanchiz, J.; Brito, F., *Coord. Chem. Rev.* **1999,** *193-195*, 857-911.

106. Zanello, P., Metal Complexes Containing Redox-active Ligands. In *Inorganic Electrochemistry: Theory, Practice, and Application*, Royal Society of Chemistry: Cambridge, U.K., 2003; pp 325-74.

107. Fleischer, E. B.; Gebala, A. E.; Tasker, P. A., *Inorg. Chim. Acta* **1972,** *6* (1), 72-6.

108. Silyl-substituted derivatives of the ligand have been investigated with early transition metals. See Baumann, R. Group 4 Complexes Containing Tridentate Diamido Donor Ligands. Organometallic Chemistry and Catalysis. Ph.D Thesis, Massachusetts Institute of Technology, Cambridge, MA, Feb 1999.

109. Celenligil-Cetin, R.; Paraskevopoulou, P.; Lalioti, N.; Sanakis, Y.; Staples, R. J.; Rath, N. P.; Stavropoulos, P., *Inorg. Chem.* **2008,** *47* (23), 10998-11009.

110. Celenligil-Cetin, R.; Paraskevopoulou, P.; Dinda, R.; Staples, R. J.; Sinn, E.; Rath, N. P.; Stavropoulos, P., *Inorg. Chem.* **2008,** *47* (3), 1165-1172.

111. Celenligil-Cetin, R.; Paraskevopoulou, P.; Dinda, R.; Lalioti, N.; Sanakis, Y.; Rawashdeh, A. M.; Staples, R. J.; Sinn, E.; Stavropoulos, P., *Eur. J. Inorg. Chem.* **2008,** (5), 673-677.

112. Jones, M. B.; MacBeth, C. E., *Inorg. Chem.* **2007,** *46* (20), 8117-8119.

113. Jones, M. B.; Newell, B. S.; Hoffert, W. A.; Hardcastle, K. I.; Shores, M. P.; MacBeth, C. E., *Dalton Trans.* **2010,** *39*, 401-410.

114. Jones, M. B.; Hardcastle, K. I.; MacBeth, C. E., *Polyhedron* **2010,** *29* (1), 116-119.

115. Cummins, C. C.; Schrock, R. R.; Davis, W. M., *Angew. Chem.* **1993,** *105* (5), 758-61 (See also Angew Chem , Int Ed Engl , 1993, 32(5), 756-9).

116. Schrock, R. R., *Philos. Trans. R. Soc. London, Ser. A* **2005,** *363* (1829), 959-969.

117. Ray, M.; Hammes, B.; Yap, G. P. A.; Rheingold, A. L.; Borovik, A. S., *Inorg. Chem.* **1998,** *37* (7), 1527-1532.

118. Silyl-substituted derivatives of the ligand have been investigated with early transition metals. See Baumann, R. Group 4 Complexes Containing Tridentate Diamido Donor Ligands. Organometallic Chemistry and Catalysis. Ph.D Thesis, Massachusetts Institute of Technology, Cambridge, MA, Feb 1999.

119. Gorvin, J. H., *J. Chem. Soc., Perkin Trans. 1* **1988,** *6*, 1331-1335.

120. Addison, A. W.; Rao, T. N.; Reedijk, J.; Van Rijn, J.; Verschoor, G. C., *J. Chem. Soc., Dalton Trans.* **1984,** (7), 1349-56.

121. Yang, L.; Powell, D. R.; Houser, R. P., *Dalton Transactions* **2007,** (9), 955-964.

122. Sacconi, L.; Orlandini, A.; Midollini, S., *Inorg. Chem.* **1974,** *13* (12), 2850-9.

123. Hu, X.; Castro-Rodriguez, I.; Meyer, K., *J Am. Chem. Soc.* **2004,** *126* (41), 13464-13473.

124. Mani, F.; Mealli, C., *Inorg. Chim. Acta* **1981,** *63*, 97-106.

125. Nakamoto, K., *Infrared and Raman Spectra of Inorganic and Coordination Compounds, Part B: Applications in Coordination, Organometallic, and Bioinorganic Chemistry*. 5th ed. ed.; Wiley: New York, 1997.

126. Kluge, K. Manuscript in Preparation

127. Armarego, W. L. F.; Chai, C. L. L., *Purification of Laboratory Chemicals*. 5th ed.; Butterworth-Heinemann: New York, 2003.

128. Evans, D. F., *J. Chem. Soc.* **1959**, 2003-5.

129. Vosburgh, W. C.; Cooper, G. R., *J Am. Chem. Soc.* **1941,** *63*, 437-42.

130. Connors, K. A., *Binding Constants: The Measurement of Molecular Complex Stability*. John Wiley & Sons: New York, 1987.

131. *Apex II*, Bruker AXS Inc., Analytical X-ray Systems: Madison, WI, 2005.

132. *SAINT v 6.45A*, Bruker AXS Inc., Analytical X-Ray Systems: Madison, WI, 2003.

133. Sheldrick, G. M., *Acta Crystallogr., Sect. A: Found. Crystallogr.* **2008,** *A64* (1), 112-122.

134. *International Tables for X-ray Crystallography*. Academic Publishers: Dordrecht, The Netherlands, 1992; Vol. C.

135. Collins, T. J.; Nichols, T. R.; Uffelman, E. S., *J Am. Chem. Soc.* **1991,** *113* (12), 4708-9.

136. Sharma, S. K.; Upreti, S.; Gupta, R., *Eur. J. Inorg. Chem.* **2007,** (20), 3247-3259.

137. Kruger, H. J.; Peng, G.; Holm, R. H., *Inorg. Chem.* **1991,** *30* (4), 734-42.

138. Shearer, J.; Zhao, N., *Inorg. Chem.* **2006,** *45* (24), 9637-9639.

139. Neupane, K. P.; Shearer, J., *Inorg. Chem.* **2006,** *45* (26), 10552-10566.

140. Sovago, I.; Osz, K., *Dalton Transactions* **2006,** (32), 3841-3854.

141. Bossu, F. P.; Margerum, D. W., *J Am. Chem. Soc.* **1976,** *98* (13), 4003-4.

142. Bossu, F. P.; Margerum, D. W., *Inorg. Chem.* **1977,** *16* (5), 1210-14.

143. Singh, J.; Hundal, G.; Gupta, R., *Eur. J. Inorg. Chem.* **2008,** (12), 2052-2063.

144. Ottenwaelder, X.; Aukauloo, A.; Journaux, Y.; Carrasco, R.; Cano, J.; Cervera, B.; Castro, I.; Curreli, S.; Munoz, M. C.; Rosello, A. L.; Soto, B.; Ruiz-Garcia, R., *Dalton Transactions* **2005,** (15), 2516-2526.

145. Lassalle-Kaiser, B.; Guillot, R.; Sainton, J.; Charlot, M.-F.; Aukauloo, A., *Chem.--Eur. J.* **2008,** *14* (14), 4307-4317.

146. Hammes, B. S.; Ramos-Maldonado, D.; Yap, G. P. A.; Rheingold, A. L.; Young, V. G.; Borovik, A. S., *Coord. Chem. Rev.* **1998,** *174*, 241-253.

147. Ingle, G. K.; Makowska-Grzyka, M. M.; Arif, A. M.; Berreau, L. M., *Eur. J. Inorg. Chem.* **2007,** (33), 5262-5269.

148. Rudzka, K.; Arif, A. M.; Berreau, L. M., *J Am. Chem. Soc.* **2006,** *128* (51), 17018-17023.

149. Sur, S. K., *J. Magn. Reson.* **1989,** *82* (1), 169-73.

150. Drago, R. S., *Physical Methods in Chemistry*. W. B. Saunders Company: Philidelphia, 1977.

151. Ciampolini, M., *Inorg. Chem.* **1966,** *5* (1), 35-41.

152. Herrera, A. M.; Staples, R. J.; Kryatov, S. V.; Nazarenko, A. Y.; Rybak-Akimova, E. V., *Dalton Transactions* **2003,** (5), 846-856.

153. Sacconi, L.; Nannelli, P.; Nardi, N.; Campigli, U., *Inorg. Chem.* **1965,** *4* (7), 943-9.

154. Chohan, B. S.; Shoner, S. C.; Kovacs, J. A.; Maroney, M. J., *Inorg. Chem.* **2004,** *43* (24), 7726-7734.

155. Banci, L.; Benelli, C.; Gatteschi, D., *Inorg. Chem.* **1984,** *23* (20), 3262-3.

156. Mathew, M.; Palenik, G. J., *J Am. Chem. Soc.* **1969,** *91* (17), 4923-4.

157. Sacconi, L.; Ciampolini, M.; Speroni, G. P., *J Am. Chem. Soc.* **1965,** *87* (14), 3102-6.

158. Nakamoto, K., *Infrared and Raman Spectra of Inorganic and Coordination Compounds, Part B: Applications, in Coordination, Organometallic, and Bioinorganic Chemistry*. 5th ed.; Wiley: New York, 1997.

159. Toernroos, K. W.; Chernyshov, D.; Hostettler, M.; Buergi, H. B., *Acta Crystallogr., Sect. C: Cryst. Struct. Commun.* **2005,** *C61* (10), m450-m452.

160. Brefuel, N.; Duhayon, C.; Shova, S.; Tuchagues, J.-P., *Chem. Commun.* **2007,** (48), 5223-5225.

161. Purcell, W.; Basson, S. S.; Leipoldt, J. G.; Roodt, A.; Preston, H., *Inorg. Chim. Acta* **1995,** *234* (1-2), 153-6.

162. Holz, R. C.; Thompson, L. C., *Inorg. Chem.* **1993,** *32* (23), 5251-6.

163. Palaniandavar, M.; Butcher, R. J.; Addison, A. W., *Inorg. Chem.* **1996,** *35* (2), 467-71.

164. Lennartson, A.; Hakansson, M.; Jagner, S., *New J. Chem.* **2007,** *31* (3), 344-347.

165. Raymond, K. N.; Corfield, P. W. R.; Ibers, J. A., *Inorg. Chem.* **1968,** *7* (7), 1362-72.

166. Dean, P. A. W.; Vittal, J. J.; Craig, D. C.; Scudder, M. L., *Inorg. Chem.* **1998,** *37* (7), 1661-1664.

167. Pal, S.; Nandi, A. K., *Macromolecules* **2003,** *36* (22), 8426-8432.

168. Ma, H.; Chattopadhyay, S.; Petersen, J. L.; Jensen, M. P., *Inorg. Chem.* **2008,** *47* (18), 7966-7968.

169. Beltran, L. M. C.; Long, J. R., *Acc. Chem. Res.* **2005,** *38* (4), 325-334.

170. Funck, K. E.; Hilfiger, M. G.; Berlinguette, C. P.; Shatruk, M.; Wernsdorfer, W.; Dunbar, K. R., *Inorg. Chem.* **2009,** *48* (8), 3438-3452.

171. Zhong, C.; Zhao, M.; Stern, C.; Barrett, A. G. M.; Hoffman, B. M., *Inorg. Chem.* **2005,** *44* (23), 8272-8276.

172. Shores, M. P.; Sokol, J. J.; Long, J. R., *J Am. Chem. Soc.* **2002,** *124* (10), 2279-2292.

173. Shatruk, M.; Avendano, C.; Dunbar, K. R., *Prog. Inorg. Chem.* **2009,** *56*, 155-334.

174. Dunbar, K. R.; Heintz, R. A., *Prog. Inorg. Chem.* **1997,** *45*, 283-391.

175. Li, D.; Ruschman, C.; Parkin, S.; Clerac, R.; Holmes, S. M., *Chem. Commun.* **2006,** (38), 4036-4038.

176. Shatruk, M.; Chambers, K. E.; Prosvirin, A. V.; Dunbar, K. R., *Inorg. Chem.* **2007,** *46* (13), 5155-5165.

177. Orpen, A. G.; Brammer, L.; Allen, F. H.; Kennard, O.; Watson, D. G.; Taylor, R., *J. Chem. Soc., Dalton Trans.* **1989,** (12), S1-S83.

178. Meyer, F.; Winter, R. F.; Kaifer, E., *Inorg. Chem.* **2001,** *40* (18), 4597-4603.

179. Sarkar, S.; Datta, A.; Mondal, A.; Chopra, D.; Ribas, J.; Rajak, K. K.; Sairam, S. M.; Pati, S. K., *J. Phys. Chem. B* **2006,** *110* (1), 12-15.

180. Kersting, B.; Steinfeld, G., *Chem. Commun.* **2001,** (15), 1376-1377.

181. Gressenbuch, M.; Kersting, B., *Eur. J. Inorg. Chem.* **2007,** (1), 90-102.

182. Lozan, V.; Kersting, B., *Inorg. Chem.* **2008,** *47* (12), 5386-5393.

183. Steinfeld, G.; Lozan, V.; Kersting, B., *Angew. Chem., Int. Ed.* **2003,** *42* (20), 2261-2263.

184. Zinn, P. J.; Sorrell, T. N.; Powell, D. R.; Day, V. W.; Borovik, A. S., *Inorg. Chem.* **2007,** *46* (24), 10120-32.

185. Gressenbuch, M.; Lozan, V.; Steinfeld, G.; Kersting, B., *Eur. J. Inorg. Chem.* **2005,** (11), 2223-2234.

186. Bond, A. D.; Derossi, S.; Harding, C. J.; McInnes, E. J. L.; McKee, V.; McKenzie, C. J.; Nelson, J.; Wolowska, J., *Dalton Transactions* **2005,** (14), 2403-2409.

187. Lu, T.; Zhuang, X.; Li, Y.; Chen, S., *J Am. Chem. Soc.* **2004,** *126* (15), 4760-4761.

188. Heinrich, J. L.; Berseth, P. A.; Long, J. R., *Chem. Commun.* **1998,** (11), 1231-1232.

189. Lescouezec, R.; Toma, L. M.; Vaissermann, J.; Verdaguer, M.; Delgado, F. S.; Ruiz-Perez, C.; Lloret, F.; Julve, M., *Coord. Chem. Rev.* **2005,** *249* (23), 2691-2729.

190. Bill, E. *JulX 1.4.1 A Program for the Simulation and Analysis of Magnetic Susceptibility Data*, http: // ewww.mpi-muelheim.mpg.de/bac/logins/bill/julX_en.php.

191. Benbellat, N.; Gavrilenko, K. S.; Le Gal, Y.; Cador, O.; Golhen, S.; Gouasmia, A.; Fabre, J.-M.; Ouahab, L., *Inorg. Chem.* **2006,** *45* (26), 10440-10442.

192. Wu, D.; Guo, D.; Song, Y.; Huang, W.; Duan, C.; Meng, Q.; Sato, O., *Inorg. Chem.* **2009,** *48* (3), 854-860.

193. Berseth, P. A.; Sokol, J. J.; Shores, M. P.; Heinrich, J. L.; Long, J. R., *J Am. Chem. Soc.* **2000,** *122* (40), 9655-9662.

194. Karadas, F.; Schelter, E. J.; Shatruk, M.; Prosvirin, A. V.; Bacsa, J.; Smirnov, D.; Ozarowski, A.; Krzystek, J.; Telser, J.; Dunbar, K. R., *Inorg. Chem.* **2008,** *47* (6), 2074-2082.

195. Stanlake, L. J. E.; Beard, J. D.; Schafer, L. L., *Inorg. Chem.* **2008,** *47* (18), 8062-8068.

196. Huang, B.-H.; Yu, T.-L.; Huang, Y.-L.; Ko, B.-T.; Lin, C.-C., *Inorg. Chem.* **2002,** *41* (11), 2987-2994.

197. Huang, Y.-L.; Huang, B.-H.; Ko, B.-T.; Lin, C.-C., *J. Chem. Soc., Dalton Trans.* **2001,** (8), 1359-1365.

198. Davies, R. P.; Linton, D. J.; Snaith, R.; Wheatley, A. E. H., *Chem. Commun.* **2000,** (3), 193-194.

199. Klemp, A.; Uson, I.; Ahlemann, J.-T.; Belgardt, T.; Storre, J.; Roesky, H. W., *Main Group Chem.* **1995,** *1* (1), 127-38.

200. Fischer, P.; Graef, R.; Stezowski, J. J.; Weidlein, J., *J Am. Chem. Soc.* **1977,** *99* (18), 6131-2.

201. Jennings, J. R.; Wade, K.; Wyatt, B. K., *J. Chem. Soc., A* **1968,** (10), 2535-8.

202. Horder, J. R.; Lappert, M. F., *J. Chem. Soc., A* **1968,** (8), 2004-8.

203. Tabernero, V.; Mosquera, M. E. G.; Cuenca, T., *Organometallics* **2010,** *29*, 3642-3646.

204. Kai, Y.; Yasuoka, N.; Kasai, N.; Kakudo, M., *Bull. Chem. Soc. Jap.* **1972,** *45* (11), 3388-96.

205. Power, M. B.; Bott, S. G.; Clark, D. L.; Atwood, J. L.; Barron, A. R., *Organometallics* **1990,** *9* (12), 3086-97.

206. Eldred, S. E.; Stone, D. A.; Gellman, S. H.; Stahl, S. S., *J Am. Chem. Soc.* **2003,** *125* (12), 3422-3423.

207. Hoerter, J. M.; Otte, K. M.; Gellman, S. H.; Cui, Q.; Stahl, S. S., *J Am. Chem. Soc.* **2008,** *130* (2), 647-654.

208. Hoerter, J. M.; Otte, K. M.; Gellman, S. H.; Stahl, S. S., *J Am. Chem. Soc.* **2006,** *128* (15), 5177-5183.

209. Vivanco, M.; Ruiz, J.; Floriani, C.; Chiesi-Villa, A.; Rizzoli, C., *Organometallics* **1993,** *12* (5), 1794-801.

210. Ruiz, J.; Vivanco, M.; Floriani, C.; Chiesi-Villa, A.; Guastini, C., *J. Chem. Soc., Chem. Commun.* **1991,** (11), 762-4.

211. Vivanco, M.; Ruiz, J.; Floriani, C.; Chiesi-Villa, A.; Rizzoli, C., *Organometallics* **1993,** *12* (5), 1802-10.

212. Akitt, J. W., *Prog. NMR Spec.* 1989; Vol. 21.

213. Robinson, G. H., *Coordination Chemistry of Aluminum*. VCH Publishers, Inc.: New York, 1993.

214. Donaldson, P. B.; Tasker, P. A.; Alcock, N. W., *J. Chem. Soc., Dalton Trans.* **1977,** (12), 1160-5.

215. Fleischer, E. B.; Gebala, A. E.; Swift, D. R.; Tasker, P. A., *Inorg. Chem.* **1972,** *11* (11), 2775-84.

216. Larsen, E.; LaMar, G. N.; Wagner, B. E.; Parks, J. E.; Holm, R. H., *Inorg. Chem.* **1972,** *11* (11), 2652-68.

217. Stiefel, E. I.; Brown, G. F., *Inorg. Chem.* **1972,** *11* (2), 434-6.

218. Kepert, D. L., *Inorg. Chem.* **1972,** *11* (7), 1561-3.

219. Abrahamson, H.; Heiman, J. R.; Pignolet, L. H., *Inorg. Chem.* **1975,** *14* (9), 2070-5.

220. Verkade, J. G., *Coord. Chem. Rev.* **1994,** *137*, 233-95.

221. Pinkas, J.; Gaul, B.; Verkade, J. G., *J Am. Chem. Soc.* **1993,** *115* (10), 3925-31.

222. Benn, R.; Rufinska, A.; Janssen, E.; Lehmkuhl, H., *Organometallics* **1986,** *5* (4), 825-7.

223. Nam, W., *Acc. Chem. Res.* **2007,** *40* (7), 522-531.

224. Comba, P.; Kerscher, M.; Schiek, W., *Prog. Inorg. Chem.* **2007,** *55*, 613-704.

225. Kovacs, J. A.; Brines, L. M., *Acc. Chem. Res.* **2007,** *40* (7), 501-509.

226. Costas, M.; Mehn, M. P.; Jensen, M. P.; Que, L., Jr., *Chem. Rev.* **2004,** *104* (2), 939-986.

227. Carson, E. C.; Lippard, S. J., *J Am. Chem. Soc.* **2004,** *126* (11), 3412-3413.

228. Moreira, R. F.; Tshuva, E. Y.; Lippard, S. J., *Inorg. Chem.* **2004,** *43* (14), 4427-4434.

229. Soo, H. S.; Komor, A. C.; Iavarone, A. T.; Chang, C. J., *Inorg. Chem.* **2009,** *48* (21), 10024-10035.

230. Shook, R. L.; Borovik, A. S., *Chem. Commun.* **2008,** (46), 6095-6107.

231. Korendovych, I. V.; Kryatov, S. V.; Rybak-Akimova, E. V., *Acc. Chem. Res.* **2007,** *40* (7), 510-521.

232. Thallaj, N. K.; Rotthaus, O.; Benhamou, L.; Humbert, N.; Elhabiri, M.; Lachkar, M.; Welter, R.; Albrecht-Gary, A.-M.; Mandon, D., *Chem.--Eur. J.* **2008,** *14* (22), 6742-6753.

233. Korendovych, I. V.; Kryatova, O. P.; Reiff, W. M.; Rybak-Akimova, E. V., *Inorg. Chem.* **2007,** *46* (10), 4197-4211.

234. Kimura, E.; Kodama, M.; Machida, R.; Ishizu, K., *Inorg. Chem.* **1982,** *21* (2), 595-602.

235. Thibon, A.; England, J.; Martinho, M.; Young, V. G.; Frisch, J. R.; Guillot, R.; Girerd, J.-J.; Muenck, E.; Que, L., Jr.; Banse, F., *Angew. Chem., Int. Ed.* **2008,** *47* (37), 7064-7067.

236. Kim, S. O.; Sastri, C. V.; Seo, M. S.; Kim, J.; Nam, W., *J Am. Chem. Soc.* **2005,** *127* (12), 4178-4179.

237. Hong, S.; Lee, Y.-M.; Shin, W.; Fukuzumi, S.; Nam, W., *J Am. Chem. Soc.* **2009,** *131* (39), 13910-13911.

238. Lee, Y.-M.; Hong, S.; Morimoto, Y.; Shin, W.; Fukuzumi, S.; Nam, W., *J Am. Chem. Soc.* **2010,** *132* (31), 10668-10670.

239. Lee, D.; Lippard, S. J., *J Am. Chem. Soc.* **1998,** *120* (46), 12153-12154.

240. Hagadorn, J. R.; Que, L.; Tolman, W. B., *J Am. Chem. Soc.* **1998,** *120*, 13531-13532.

241. Tolman, W. B.; Que, L., *J. Chem. Soc., Dalton Trans.* **2002**, 653-660.

242. Tshuva, E.; Lippard, S. J., *Chem. Rev.* **2004,** *104*, 987-1012.

243. Carson, E. C.; Lippard, S. J., *J. Inorg. Biochem.* **2006,** *100* (5-6), 1109-1117.

244. Thyagarajan, S.; Incarvito, C. D.; Rheingold, A. L.; Theopold, K. H., *Chem. Commun.* **2001**, 2198-2199.

245. Jensen, M. P.; Lange, S. J.; Mehn, M. P.; Que, E. L.; Que, L., *J Am. Chem. Soc.* **2003,** *125*, 2113-2128.

246. Harman, W. H.; Chang, C. J., *J Am. Chem. Soc.* **2007,** *129* (49), 15128-15129.

247. Herold, S.; Lippard, S. J., *J Am. Chem. Soc.* **1997,** *119* (1), 145-156.

248. Lee, D.; Lippard, S. J., *Inorg. Chem.* **2002,** *41* (10), 2704-2719.

249. Taktak, S.; Kryatov, S. V.; Rybak-Akimova, E. V., *Inorg. Chem.* **2004,** *43* (22), 7196-7209.

250. Smart, B. E., *Mol. Struct. Energ.* 1986; Vol. 3.

251. Müller, K.; Faeh, C.; Diederich, F., *Science* **2007,** *317* (5846), 1881-1886.

252. Perutz, R. N.; Braun, T., Transition Metal-mediated C-F Bond Activation. In *Comprehensive Organometallic Chemistry III*, Crabtree, R. H.; Mingos, D. M. P., Eds. Elsevier: Oxford, 2007.

253. King, R. B.; Bisnette, M. B., *J. Organomet. Chem.* **1964,** *2*, 38-44.

254. Bruce, M. I.; Stone, F. G. A., *Journal of the Chemical Society A* **1966**, 1837-1842.

255. Artamkina, G. A.; Mil'Chenko, A. Y.; Beletskaya, I. P.; Reutov, O. A., *J. Organomet. Chem.* **1986,** *311*, 199-206.

256. Edelbach, B. L.; Jones, W. D., *J. Am. Chem. Soc.* **1997,** *119* (33), 7734-7742.

257. Peterson, T. H.; Golden, J. T.; Bergman, R. G., *Organometallics* **1999,** *18*, 2005-2020.

258. Edelbach, B. L.; Jones, W. D., *J Am. Chem. Soc.* **1997,** *119* (33), 7734-7742.

259. Braun, T.; Rothfeld, S.; Schorlemer, V.; Stammler, A.; Stammler, H.-G., *Inorg. Chem. Commun.* **2003,** *6*, 752-755.

260. Park, S.; Pontier-Johnson, M.; Roundhill, D. M., *J Am. Chem. Soc.* **1989,** *111*, 3101-3103.

261. Arroyo, M.; Bernes, S.; Ceron, M.; Cortina, V.; Mendoza, C.; Torrens, H., *Inorg. Chem.* **2007,** *46* (12), 4857-4867.

262. Chen, C.-T.; Kuo, J.-H.; Ku, C.-H.; Weng, S.-S.; Liu, C.-Y., *J. Org. Chem.* **2005,** *70* (4), 1328-1339.

263. Chen, C.-T.; Kuo, J.-H.; Li, C.-H.; Barhate, N. B.; Hon, S.-W.; Li, T.-W.; Chao, S.-D.; Liu, C.-C.; Li, Y.-C.; Chang, I. H.; Lin, J.-S.; Liu, C.-J.; Chou, Y. C., *Org. Lett.* **2001,** *3* (23), 3729-3732.

264. Chen, C.-T.; Kuo, J.-H.; Pawar, V. D.; Munot, Y. S.; Weng, S.-S.; Ku, C.-H.; Liu, C.-Y., *J. Org. Chem.* **2005,** *70* (4), 1188-1197.

265. Chen, C.-T.; Lin, J.-S.; Kuo, J.-H.; Weng, S.-S.; Cuo, T.-S.; Lin, Y.-W.; Cheng, C.-C.; Huang, Y.-C.; Yu, J.-K.; Chou, P.-T., *Org. Lett.* **2004,** *6* (24), 4471-4474.

266. Figueroa, J. S.; Piro, N. A.; Clough, C. R.; Cummins, C. C., *J Am. Chem. Soc.* **2006,** *128* (3), 940-950.

267. Partyka, D. V.; Staples, R. J.; Holm, R. H., *Inorg. Chem.* **2003,** *42* (24), 7877-7886.

268. Cross, W. B.; Anderson, J. C.; Wilson, C. S., *Dalton Trans.* **2009**, 1201-1205.

269. Housmekerides, C. E.; Ramage, D. L.; Kretz, C. M.; Shontz, J. T.; Pilato, R. S.; Geoffroy, G. L.; Rheingold, A. L.; Haggerty, B. S., *Inorg. Chem.* **1992,** *31* (22), 4453-68.

270. Howard, W. A.; Waters, M.; Parkin, G., *J Am. Chem. Soc.* **1993,** *115* (11), 4917-18.

271. Hanna, T. A.; Baranger, A. M.; Bergman, R. G., *J. Org. Chem.* **1996,** *61* (14), 4532-4541.

272. Pilato, R. S.; Housmekerides, C. E.; Jernakoff, P.; Rubin, D.; Geoffroy, G. L.; Rheingold, A. L., *Organometallics* **1990,** *9* (8), 2333-41.

273. Parkin, G.; Bercaw, J. E., *J Am. Chem. Soc.* **1989,** *111* (1), 391-3.

274. Guennou de Cadenet, K.; Rumin, R.; Petillon, F. Y.; Yufit, D. S.; Muir, K. W., *Eur. J. Inorg. Chem.* **2002**, 639-657.

275. Bruce, M. I.; Stone, F. G. A., *J. Chem. Soc. A* **1966**, 1837-1842.

276. King, R. B.; Bisnette, M. B., *J. Organomet. Chem.* **1964,** *2*, 38-43.

277. Chernega, A. N.; Grahm, A. J.; Green, M. L. H.; Haggitt, J.; Lloyd, J.; Mehnert, N.; Souter, J., *J. Chem. Soc., Dalton Trans.* **1997**, 2293-2303.

278. Lentz, D.; Willemsen, S., *J. Organomet. Chem.* **2002,** *641*, 215-219.

279. Jones, M. B.; MacBeth, C. E., *Inorg. Chem.* **2007,** *46* (20), 8117-8119.

280. Pyrz, J. W.; Pan, X.; Doyle, B.; Que, L., *Inorg. Chem.* **1991,** *30* (18), 3461-3464.

281. Olmstead, M. M.; Power, P. P.; Shoner, S. C., *Inorg. Chem.* **1991,** *30*, 2547-2551.